Universidad Politécnica de Madrid

Escuela Técnica Superior de Ingenieros Industriales

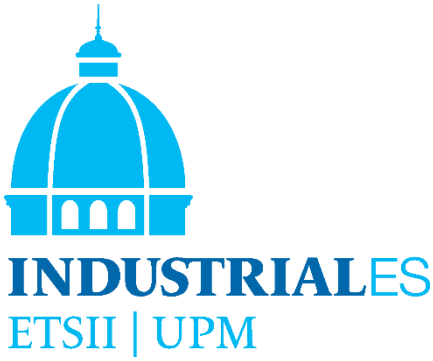

FIELD QUALITY IN Nb_3Sn SUPERCONDUCTING ACCELERATOR MAGNETS

TESIS DOCTORAL

Susana Izquierdo Bermúdez

Ingeniero Industrial por la Universidad Carlos III de Madrid (UC3M)

2023

Universidad Politécnica de Madrid

Escuela Técnica Superior de Ingenieros Industriales

Doctorado en Ingeniería Eléctrica y Electrónica

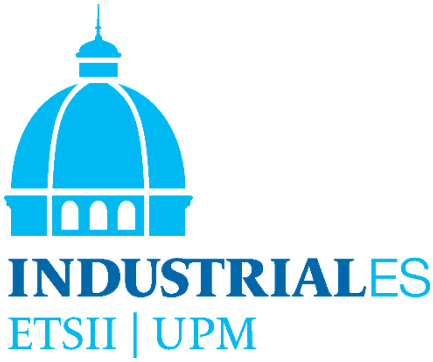

TESIS DOCTORAL

FIELD QUALITY IN NB_3SN SUPERCONDUCTING ACCELERATOR MAGNETS

Texto para la obtención del grado de Doctor

Autor:

Susana Izquierdo Bermúdez

Ingeniero Industrial por la Universidad Carlos III de Madrid (UC3M)

Directores:

Luca Bottura

European Center of Nuclear Research (CERN)

Fernando Toral Fernández

Doctor Ingeniero Industrial por la Universidad Pontificia de Comillas (ETSI-ICAI)

2023

UNIVERSIDAD POLITÉCNICA DE MADRID

Escuela Internacional de Doctorado

Escuela Técnica Superior de Ingenieros Industriales

TESIS DOCTORAL

Field Quality in Nb_3Sn Superconducting Accelerator Magnets

Autor: Susana Izquierdo Bermudez

Directores: Luca Bottura y Fernando Toral Fernández

Tribunal nombrado por el Sr. Rector Magfco. de la Universidad Politécnica de Madrid, el día ….. de …….. de 20….

TRIBUNAL

PRESIDENTE:	D. Presidente:	_____
VOCALES:	D. Vocal 1:	_____
	D. Vocal 2:	_____
	D. Vocal 3:	_____
SECRETARIO:	D. Secretario:	_____
SUPLENTES:	D. _____...____	
	D. _____...____	

Realizado el acto de defensa y lectura de la Tesis el día.....de.....de 20…

en la Escuela técnica Superior de Ingeniería Industrial.

Calificación ……..

EL PRESIDENTE LOS VOCALES

EL SECRETARIO

Para Hugo y Eva,
por iluminar mi vida.

ABSTRACT

Colliders of highly energetic particle beams are a crucial tool for high energy physics (HEP) and accelerator magnets are an essential component to steer and focus the particle beam. To enable highest energy hadron colliders, reliable and cost-effective magnet technologies are fundamental. Today Nb_3Sn is the superconductor that reached a level of maturity enough to be considered as a candidate material to reach field levels above 10 T. This pursuit of higher magnetic fields translates into challenges for the magnet design. A major milestone for the technology will be the first-time implementation of Nb_3Sn quadrupole accelerator magnets in the High Luminosity Upgrade of the Large Hadron Collider (HL-LHC). After more than 20 years of development, the production of the first mini-series of Nb_3Sn accelerator-quality magnets is ongoing, paving the path towards the next generation magnets. The work presented in this thesis is focused on the magnetic performance, contributing to a better understanding of these magnets, needed to define targets for future generation accelerator magnets.

HL-LHC Nb_3Sn magnets are exploring an unprecedented operating current density in the strand of 700–800 A/mm^2 and a magnetic energy density 50 % higher than the NbTi main dipoles of the LHC. In addition, fabrication of Nb_3Sn coils requires a heat treatment to 650ºC after winding to form the superconducting phase. The formation of the superconducting phase produces a volume expansion leading to radial, azimuthal, and axial dimensional changes of the conductor. The position of the conductors must be controlled with a precision greater than 0.1 mm. Compared to the Nb-Ti, state-of-the-art Nb_3Sn conductor features larger filament size and higher critical current density resulting on a strand magnetization about one order of magnitude larger, which has an impact on the field errors in particular at injection. A superconducting magnet is therefore a complex electro-magnetic-mechanical system and HL-LHC marks the start of a new era in particle accelerators.

The aim of this work is to study the magnetic behaviour of the Nb_3Sn magnets for the HL-LHC upgrade in order to stablish a solid background for future accelerators. Special focus is given to the intrinsic difficulties of Nb_3Sn technology. After a brief introduction, the second chapter will describe the challenges to reach the 12 T field level and the main design features of the MBH-11 T dipoles and MQXF quadrupoles. Chapter three focuses on the geometric field errors with an assessment of the precision in the positioning of the conductors within the magnet cross section. Later on, the contribution of ferromagnetic materials is discussed including the capabilities to correct field errors through magnetic shimming. The last two chapters address the magnetization and coupling current effects (field distortions and AC losses), including the dynamic effects at injection (decay and snapback).

RESUMEN

Los colisionadores de partículas de alta energía son una herramienta crucial para la física de altas energías y los imanes son un componente esencial para dirigir y enfocar el haz de partículas. Imanes superconductores eficientes y fiables son fundamentales para la construcción de colisionadores de protones de alta energía. Hoy en día, el Nb_3Sn es el superconductor que ha alcanzado la madurez suficiente para ser utilizado en imanes de más de 10 T. La búsqueda de campos magnéticos más altos se traduce en desafíos en el diseño del imán. Un hito importante para esta tecnología será la implementación por primera vez de imanes de Nb_3Sn para el aumento de la luminosidad del LHC, proyecto conocido como HL-LHC (High Luminosity Upgrade of the Large Hadron Collider). Después de más de 20 años de desarrollo, se está llevando a cabo la producción de la primera miniserie de imanes Nb_3Sn para acelerador. Esta tesis estudia el comportamiento magnético de estos imanes.

Los imanes de Nb_3Sn para el HL-LHC están explorando una densidad de corriente en la sección metálica del cable sin precedentes de 700–800 A/mm^2 y una densidad de energía un 50 % más alta que los dipolos principales de NbTi del LHC. Además, la fabricación de bobinas de Nb_3Sn requiere un tratamiento térmico a 650 ºC después del bobinado para formar la fase superconductora. La formación de la fase superconductora produce una expansión de volumen que conduce a cambios dimensionales radiales, azimutales y axiales del conductor. La posición de los conductores debe controlarse con una precisión superior a 0.1 mm. En comparación con el Nb-Ti, el conductor Nb_3Sn presenta un tamaño de filamento más grande y una densidad de corriente crítica más alta, lo que da como resultado una magnetización del superconductor un orden de magnitud mayor, lo que tiene un impacto en los errores de campo, en particular al nivel de energía en el que se inyecta el haz. Por lo tanto, un imán superconductor es un sistema electro-mecánico-magnético complejo y el HL-LHC marca el comienzo de una nueva era en los aceleradores de partículas.

El objetivo de este trabajo es estudiar el comportamiento magnético de los imanes Nb_3Sn para HL-LHC con el fin de establecer una base sólida para futuros aceleradores. Se presta especial atención a las dificultades intrínsecas de la tecnología de Nb_3Sn. Después de una breve introducción, el segundo capítulo describirá los desafíos para alcanzar el nivel de campo de 12 T y las principales características de diseño de los dipolos MBH-11 T y los cuadrupolos MQXF. El capítulo tres se centra en los errores geométricos del campo magnético con una evaluación de la precisión en el posicionamiento de los conductores dentro de la sección transversal del imán. Más adelante, se analiza la contribución de los materiales ferromagnéticos. Los dos últimos capítulos abordan los efectos de la magnetización y las corrientes de acoplamiento, incluyendo los efectos dinámicos en la inyección (‘decay and snapback’).

ACKNOWLEDGEMENTS

I would like to thank my supervisors, family, and friends, who made possible this thesis and accompanied my efforts over the last years. Thanks to Luca Bottura and Fernando Toral, my two supervisors. Thanks for providing me the positive support I needed, pushing me to reach my dreams. I value the insights and guidance you provide.

This work would have not been possible without the help of colleagues and friends, with whom I shared more than ten years of fantastic work. I would like to acknowledge Paolo Ferracin, Ezio Todesco, Juan Carlos Perez and Jose Ferradas Troitino, for everything I learnt not only about magnet design and technology, but also on how important is to feel at home when you are at work. Thanks for taking care of me and helping me to grow. Special acknowledgements to Lucio Fiscarelli, for all his magnetic measurements and kindness, it has been a great pleasure! I am also grateful to Franco J. Mangiarotti, G. Willering, M. Bajko, C. Petrone, B. Bordini, M. Guinchard and many others that have contributed to this journey. I wish to extend my special thanks to my supervisors over the last years: Paolo Fessia for seeing in me the potential to contribute to the magnet community, Gijs de Rijk for his mentoring and Attilio Milanese for being rigours and always supportive.

I also want to express my gratitude to my friends in Geneva, in particular to Miguel, Marta, Ada and Anité, living near you gives me the stability I need to lead my life far from home. Also, thanks to my friends from childhood, for accepting my decision to move abroad and still be part of my life. Isa, you helped make me into what I am today. And the last, but also the most important, thanks to my family. Hugo and Eva, you put upside down our lives, filling every single corner of love and happiness. I am lucky of having the best mate for life one could imagine, Alejandro, thanks for being always there. I love you. Words cannot express my gratitude to my parents and my sister, for giving me your love and your unconditional support. You are the reason behind my successes and the inspiration behind my endeavours. Finally, thanks also Cristina and Miguel Angel for being always present.

Thank you all form the bottom of my heart.

Susana

AGRADECIMIENTOS

Quisiera agradecer a mis directores, familiares y amigos, a todos los que han acompañado mis esfuerzos durante los últimos años y han hecho posible esta tesis. Gracias a Luca Bottura y Fernando Toral, mis dos supervisores. Gracias por creer en mí, por todo vuestro apoyo y por guiarme por este camino.

No estaría aquí sin la ayuda de compañeros y amigos, con quienes he compartido más de diez años de emocionante trabajo. Muchas gracias, Paolo Ferracin, Ezio Todesco, Juan Carlos Perez y Jose Ferradas Troitino, por todo lo que he aprendido no solo sobre el diseño y la tecnología de los imanes, sino también sobre la importancia de sentirse como en casa cuando se está en el trabajo. Gracias por cuidarme y ayudarme a crecer. Y por supuesto, gracias a Lucio Fiscarelli, por todas sus todas sus medidas magnéticas y amabilidad, ¡ha sido un gran placer! Muchas gracias, Franco J. Mangiarotti, G. Willering, M. Bajko, C. Petrone, B. Bordini, M. Guinchard y gracias a muchos otros que habéis contribuido a este viaje. Deseo extender mi agradecimiento a mis supervisores en los últimos años: Paolo Fessia por ver en mí el potencial para contribuir a la comunidad de los imanes superconductores, Gijs de Rijk por guiarme en mis primeros años y Attilio Milanese por su rigurosidad y apoyo.

También quiero expresar mi agradecimiento a mis amigos de Ginebra, en particular a Miguel, Marta, Ada y Anité, vivir cerca de vosotros me da la estabilidad que necesito para llevar mi vida lejos de casa. Gracias también a mis amigos de la infancia y la universidad, por aceptar mi decisión vivir fuera y seguir formando parte de mi camino. Isa, me ayudaste a convertirme en lo que soy hoy. Y para finalizar, gracias a mi familia, sin duda lo más importante en mi vida. Hugo y Eva, pusisteis nuestras vidas patas arriba, llenando cada rincón de amor y felicidad. Tengo la suerte de tener a mi lado al mejor compañero de vida que uno pueda imaginar, Alejandro, gracias por estar siempre ahí. Te quiero. Es imposible expresar con palabras mi gratitud a mis padres y a mi hermana, gracias por brindarme vuestro amor y apoyo incondicional. Sois la razón detrás de mis éxitos y la inspiración detrás de mis esfuerzos. Por último, gracias también a Cristina y Miguel Ángel por estar siempre presentes.

Gracias a todos de corazón.

Susana

CONTENTS

LIST OF ABBREVIATIONS AND ACRONYMS

HEP	High Energy Physics
LHC	Large Hadron Collider
HL-LHC	High Luminosity upgrade of the LHC
HTS	High Temperature Superconductor
ROXIE	Routine for the Optimization of magnet X-sections, Inverse field calculation and coil End design
CERN	European Center of Nuclear Research
LBNL	Lawrence Berkley National Lab
FCC	Future Circular Collider

1 INTRODUCTION

The performance of high energy colliders is strongly dependent on their magnet system: arc dipoles for energy reach, and interaction region quadrupoles for luminosity. For the main ring dipole magnets of a hadron collider, the linear relationship between beam energy, ring radius, and magnetic field strength provides the basis for facility optimization for physics reach and for cost. A reasonable estimate for the beam energy is $E = 0.3 \cdot B \cdot R$, with energy E in TeV, field B in T, and radius R in km. The maximum affordable dipole field, together with the dimension of the tunnel, set the maximum achievable energy, so the focus is set on the development of cost-effective high-field accelerator dipoles. In the insertion and straight section regions, where the experiments are housed, special magnets are needed for the strong focusing of the beam in the interaction point or for the crossing in the beam. To avoid as much as possible beam orbit perturbations, the magnetic field provided by the magnets is required to have a high level of homogeneity. Nb_3Sn is today the natural reference for future collider magnets, and the magnets produced for the High Luminosity Upgrade of the LHC is the first application of accelerator-quality Nb_3Sn magnet technology in an operating particle accelerator. Precise control of the magnetic field uniformity will however remain a must. The author of this thesis aims at providing a comprehensive description of the experience gained with the production of the HL-LHC Nb_3Sn magnets to improve the understanding and set field quality targets for future accelerators.

1.1 The need of Nb_3Sn Magnets for Particles Accelerators

Particle accelerators were invented in the 1930s in order to study the basic constituents of matter and the forces involved in their interactions. Charged elementary particles such as electrons, positrons or ionized atoms are accelerated to high kinetic energy. In circular accelerators, the particle energy and momentum increase with every pass around the track. To force the beams into circular orbits, dipole magnets providing a homogeneous magnetic field are necessary. The increase of particle energy and magnetic field is synchronized to ensure that the particles circulate in the same path every time. The main magnetic elements in a circular accelerator are:

- dipoles, which create the main vertical magnetic field, perpendicular to the particle direction, used to deflect particle motions onto circular trajectories;
- quadrupoles, which produce a field that is null at the centre of the vacuum chamber and linearly dependent on the distance to the centre, whose purpose is to focus the beam.

They are in general electro-magnets, and depending on the field strength several designs are possible:

- low field (up to 2 T) iron-dominated magnets;

- super-ferric magnets;
- superconducting magnets.

In iron-dominated magnets the peak magnetic field is limited by the iron saturation at about 2 T. The field shape depends principally on the shape of the iron yoke, which determines the good field region where the beam can travel safely. In most of the cases, such magnets are resistive, although there are examples of iron-dominated superconducting magnets, where the yoke can remain either at ambient or at cryogenic temperature. For fields above 2 T, the magnets should be superconducting to be sufficiently compact and limit power consumption, and the coil should produce the additional magnetic flux. In this case, the coil becomes larger and the placement of the conductors determines the shape and the quality of the field. The coil is in general placed in a cylindrical shell around the magnet bore. This coil configuration is called the $\cos\theta$ configuration, since the current distribution in the cylindrical shell approximately varies as the cosine of the angle from the mid plane. Dipoles with the $\cos\theta$ configuration and Nb-Ti cables have been built for the following accelerators:

- Tevatron at Fermilab ([1.1][1.2], Chicago, USA: 4.4T;
- HERA at DESY ([1.3][1.4][1.5], Hamburg, Germany: 4.7T;
- RHIC at Brookhaven ([1.6][1.7], New York, USA: 3.5T;
- LHC at CERN ([1.8], Geneva, Switzerland: 8.3T at 1.9K.

The LHC is the end of the evolution for Nb-Ti ($B \approx 8$ T) and accelerator magnets of the next generation will make use of Nb_3Sn to achieve peak fields in the coil beyond the reach of the ubiquitous Nb-Ti. The development of a new generation of accelerator magnets based on Nb_3Sn superconductor with operation fields up to 15-16 T has shown in the last two decades a good progress in the USA, EU and Asia. High Temperature Superconductors (HTS) materials are opening the path to higher fields and improved energy efficiency through operation at higher cryogenic temperature, or helium free configurations. This technology is still at its early stage. Much work needs to be done on the way to realize the potential of HTS materials, starting from their basic conductor characteristics through cable and magnet design, technology and quench protection, including their mass production and cost optimization issues.

On the short term, within the next five years, Nb_3Sn technology will be implemented in HL-LHC [1.9] by using large-aperture high-gradient final-focus quadrupoles in ATLAS and CMS experiments and 12 T dipoles in the dispersion suppression region. On the longer term, dipole and quadrupole magnets with nominal operation fields up to 16 T are under discussion for FCC-hh [1.10]. The two HL-LHC Nb_3Sn magnets operating in the range of 12 T peak field that are being produced, which are a demonstration of the state-of-the-art technology are:

- **MBH-11T Dipoles**: In order to create space for the installation of collimators in the dispersion suppressors, few standard 14.3-m-long LHC NbTi dipoles (MB) will be replaced with 2x5.5-m-long-Nb_3Sn magnets with a field of 11.2 T in the aperture [1.11]. A higher field allows for shorter magnets and room for collimator units, to reduce beam losses in the magnets due to the higher beam intensity. Ten units were initially foreseen; successive studies, complemented by data from LHC operation, reduced the need to two units to be initially installed in 2020, now delayed.
- **MQXF Quadrupoles**: In order to increase the probability of collision, new large aperture magnets around ATLAS and CMS will replace the present triplets, denoted as Q1, Q2a, Q2b, and Q3, to decrease the size of the beam by a factor 2. In the present LHC, the triplet quadrupoles use Nb-Ti superconducting coils to generate a gradient of 215 T/m in a 70 mm aperture, with a magnetic length of 6.3

m for Q1 and Q3[1.12], and 5.5 m for Q2 [1.13], and with a conductor peak field of 7.7 and 8.6 T, respectively. The new triplet magnets, called MQXF [1.14], will feature an aperture of 150 mm, will operate at a gradient of 132.2 T/m and a conductor peak field of 11.3 T. The aperture also includes a 16-mm-thick tungsten absorber to bring the heat load and the radiation damage on the magnets in the HL-LHC era back to the LHC values. The lay-out of the LHC and of the HL-LHC interaction regions are compared in Figure 1 [1.15]. Thanks to the Nb_3Sn technology, the triplet aperture can be doubled keeping the total length increase within 40% (from 25 to 35 m). The magnetic length is 8.4 m for Q1/Q3 and 7.15 m for Q2a and Q2b [1.14]. The US collaboration, in charge of Q1/Q3, decided to split the magnet in two 4.2 m long parts, to minimize the risks due to the length increase with respect to the longest Nb_3Sn accelerator magnet manufactured by the US LHC Accelerator Research Program [1.16].

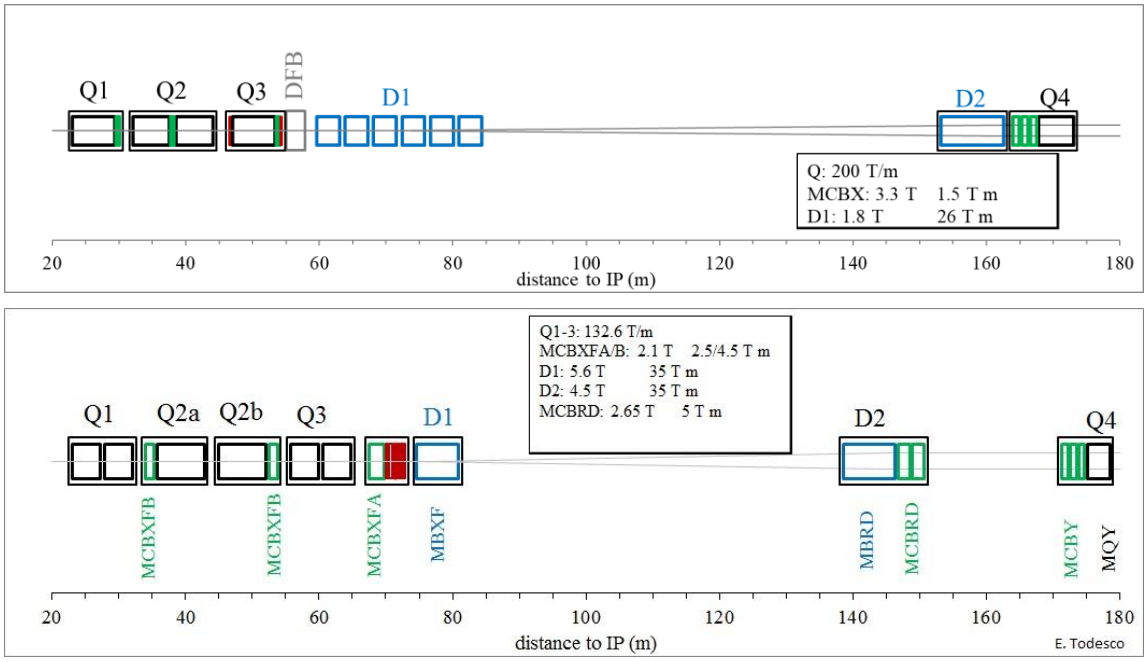

Figure 1. The lay-out of the LHC interaction region (upper part) and of the HL-LHC interaction region (lower part). Thick boxes are magnets, and thin ones are cryostats. Courtesy of Ezio Todesco.

The MBH dipoles and MQXF quadrupoles constitute the best database for the definition of the target field quality for future Nb_3Sn accelerator magnets.

1.2 Magnetic Field in Accelerator Magnets

Within a cylinder carrying uniform current density j_0, the field is perpendicular to the radial direction and proportional to the distance from the center r:

$$\vec{B} = -\frac{\mu_0 j_0 \vec{r}}{2} \qquad \textit{Eq. 1}$$

Combining the effect of two intersecting cylinders, the field in the common space can be written in Cartesian coordinates as:

$$B_x = \frac{\mu_0 j_0 r}{2}\{-r_1 \sin\theta_1 + r_2 \sin\theta_2\} = 0$$

$$B_y = \frac{\mu_0 j_0 r}{2}\{-r_1 \cos\theta_1 + r_2 \cos\theta_2\} = -\frac{\mu_0 j_0}{2} w \qquad \textit{Eq. 2}$$

A similar proof can be found for intercepting ellipses [1.17]. Although the result is interesting, the geometry results in a no circular aperture not easy to reproduce in a real winding with a flat cable and not practical for accelerator magnets. A current shell distribution in a circular aperture, easier to build, proportional to the angle ($j(\theta)=j_o cos(\theta)$) also results also in a perfect dipolar field in the aperture:

$$B_y = -4\frac{\mu_0 j_0}{2\pi}\int_0^{\pi/2}\int_r^{r+w}\frac{cos^2(\theta)}{\rho}\rho d\rho d\theta = -\frac{\mu_0 j_0}{2} w \qquad \textit{Eq. 3}$$

It can be seen from Eq. 3, that for a dipole sector coil of aperture r and coil width *w*, we have that

- the field is proportional to the current density j_0;
- the field is proportional to the coil width *w*;
- the field is independent of the coil aperture *r*.

Analogously, four intercepting circles/ellipses and a cos2θ current distribution generate a perfect quadrupole field. The field is equal to zero at the center and increases linearly with the radius. The gradient, defined as the ratio between the field and the radius is:

$$G = \frac{B_y}{r} = -\frac{\mu_0 j_0}{2}\log\left(1+\frac{w}{r}\right) \qquad \textit{Eq. 4}$$

This means that,

- the gradient is proportional to the current density j_0;
- the gradient depends on the ratio of the coil width w and the aperture *r*;
- for large coil width, the gradient increases only with the logarithm of the coil width w.

For illustration, Figure 2 shows perfect cosθ and cos2θ current distributions.

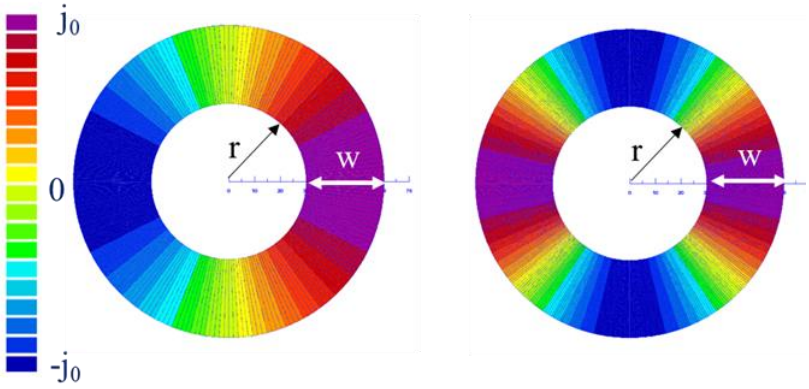

Figure 2. Perfect cosθ and cos2θ current distribution

In a real winding, the perfect *cos(nθ)* current distribution can by approximated by a sector coil with layers and wedges. In the case of a dipole, this means that there is a maximal current at the midplane, with opposite sign on the left and right sides of the aperture, and zero current at 90° and 270°. Figure 3, shows the block layout in the 11 T MBH and MQXF coil.

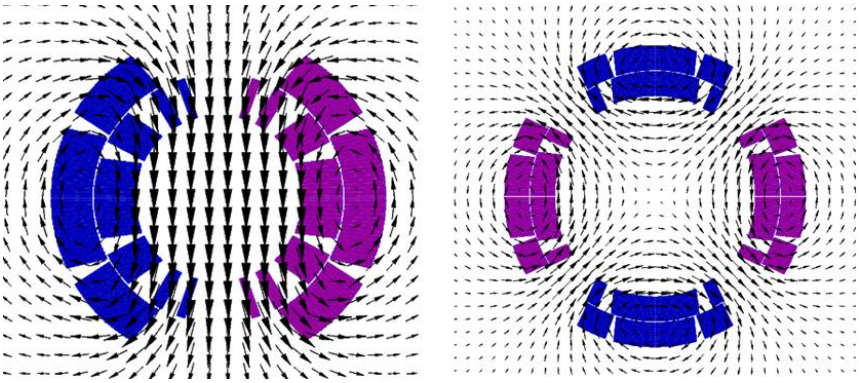

Figure 3. Dipole (left) and quadrupole (right) sector coil layout with wedges and two layers

In a circular accelerator, in order to guarantee a beam stable during the operation, the magnetic field errors must be controlled at levels of the order of less than 10^{-4} of the main field. The field quality in the aperture is described in a standard form as harmonics coefficients defined by the series expansion (further details of the derivation of this expression will be given in Section 3.1),

$$B_y + iB_x = B_{ref} \cdot 10^{-4} \sum (b_n + ia_n) \left(\frac{x+iy}{R_{ref}}\right)^{n-1} \qquad \textit{Eq. 5}$$

where B_x and B_y are the field components in Cartesian coordinates, B_{ref} is the reference field (B_1 in case of a dipole, B_2 in the case of a quadrupole), and b_n and a_n are the normalized harmonics coefficients at the reference radius R_{ref} (17 mm in MBH, as for the LHC main dipoles; 50 mm in MQXF).

Magnetic field errors in superconducting magnets can have several origins: (i) Geometric field errors, resulting from the deviation of the real current distribution in the coils from the ideal current distribution that is needed to generate the desired magnetic field; (ii) Deviations caused due to the non-linear saturation of the iron yoke (iii) Persistent current effects, due to the diamagnetic properties of the superconducting material (iv) Decay and snapback, dynamic effects at injection due to the current imbalance among the strands in the Rutherford cables.

The main field and transfer function, defined as the ratio between the main field and the current, are used to illustrate geometric and the iron saturation effect. In an electromagnet, in the absence of ferromagnetic material or before reaching the saturation field, the field is proportional to the current (dashed black line in Figure 4, geometric component which depends on the coil geometry). For the specific case illustrated in Figure 4, for a current level above 5 kA, the ratio of the field and the current starts decreasing due to the saturation of the iron. At the maximum current level, the transfer function decreases by 5 % due to the non-linear iron saturation.

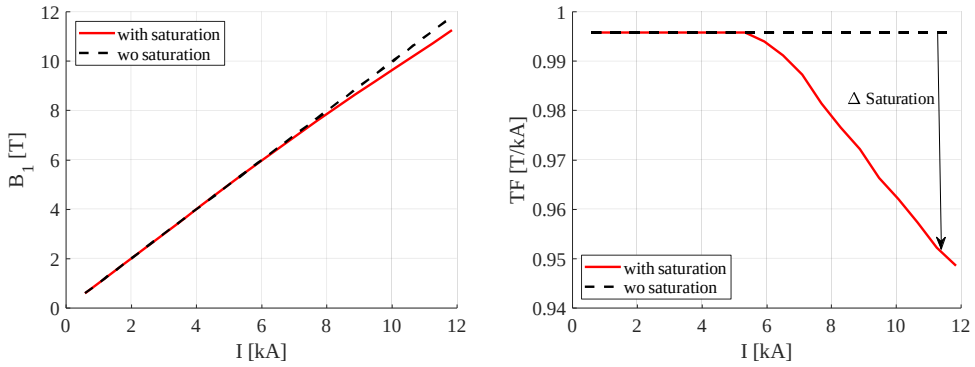

Figure 4. Iron saturation effect in the main field (left) and transfer function (right) in the MBH dipole

During the magnet ramp, long-lasting currents flowing within the superconducting filaments in a strand subjected to an external field change have also an impact on the generated field. The filament bears a memory of the field changes seen, and the resulting magnetization is hysteretic (see Figure 5, left). Once stablished, the persistent currents can be considered frozen in time. Magnetization changes can be induced by current redistribution, the so-called *decay* and the ensuing *snap-back*. Figure 5, right, zooms in the decay and snapback in the MBH 11 T dipole during the injection plateau at 760 A.

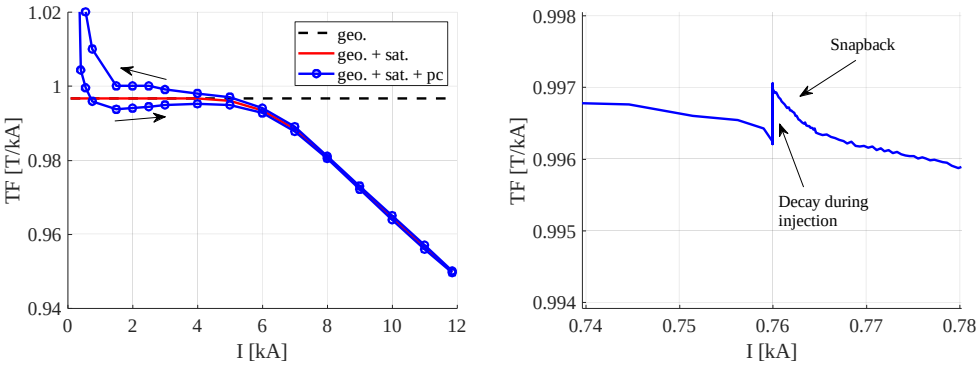

Figure 5. Left: Transfer function as a function of current in the MBH-11 T dipole considering only the geometric component (black line), geometric and iron saturation effect (red continuous line) and geometric, iron saturation and persistent currents (blue line with circles). Right: decay and snapback during the injection plateau in a MBH-11 T short model dipole.

The same effects described above are also present in the harmonics. In Figure 6 the behaviour of the normal sextupole component b_3 in an MBH short model is shown as a function of the current, during a so-called 'machine' current cycle. During up-ramps the sextupole follows the lower branch of the hysteresis curve. The persistent current effects strongly decrease with increasing field, and the curve approaches the value of the geometric sextupole field error. For fields above 6 T also the yoke saturation is visible. When lowering the dipole field, the sextupole follows the down-ramp branch of the hysteresis curve.

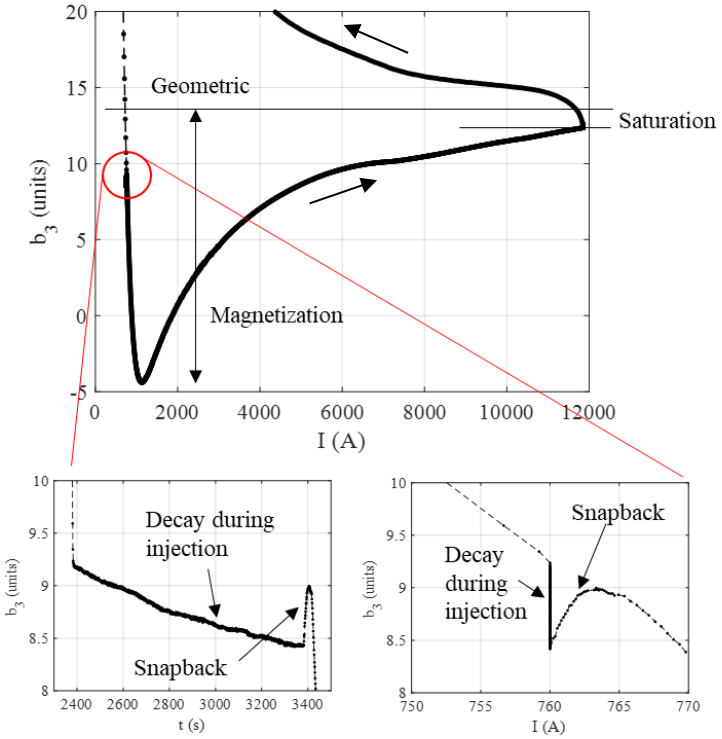

Figure 6.Measured sextupole component of the field during a ramp in a MBH-11T short model magnet, with a zoom of the decay and snapback during the injection plateau.

1.3 Scope of the thesis

Compared to the Nb-Ti magnets currently operating in particle accelerators, state-of-the-art Nb_3Sn conductor features larger filament size and higher critical current density resulting on a strand magnetization about one order of magnitude larger. In addition, fabrication of Nb_3Sn coils requires heat treatment after winding. The formation of the superconducting phase Nb_3Sn during heat treatment produces a volume expansion leading to radial, azimuthal and axial dimensional changes of the conductor. In order to prevent residual strain from altering superconducting performances, the tooling must provide the adequate space for these dimensional changes. The position of the conductors must be controlled with a precision better than 0.1 mm, meaning that the best compromise between performance and field quality needs to be found. After reaction, coils are impregnated with epoxy resin. In the case of cosθ magnets, the final arc length of the coil is a critical parameter to allow reaching both the nominal pre-stress as well as the nominal geometry, i.e., field quality. An additional challenge of Nb_3Sn is that the conductor is brittle, and the coil elastic modulus is about 3 times the stiffness of the NbTi non-impregnated coils, meaning that the same relative variation on coil size gives larger effect on pre-stress. The assembly process is delicate and must be well controlled to avoid degradation on the stress sensitive Nb_3Sn conductor.

A superconducting magnet is therefore a complex mechanical-magnetic system and HL-LHC marks the start of a new era in particle accelerators, as it is the first-time magnets relying on Nb_3Sn conductors are installed in an accelerator. The aim of this work is to study the magnetic behaviour of the Nb_3Sn magnets in a particle accelerator, focusing on the intrinsic difficulties of Nb_3Sn technology. The study has been performed by means of:

- Modeling of the magnet behaviour with analytical and numerical models.

- Analysis of the magnetic measurements performed at ambient and cryogenic temperature.
- Analysis of conductor magnetization, coil geometry and stress measurements, to evaluate and describe the source of the measured effects in the field.

This thesis consists of the following main parts:

Magnet design: challenges and features

Chapter 2 presents the main features of the design of a Nb_3Sn accelerator magnet, showing as application the cases of the MBH and MQXF magnets. The chapter starts with an overview of the main magnet parameters and challenges to reach the 12 T field level. After a description of the strand and cable used for each magnet, the author provides a description of the electromagnetic and mechanical design with a special emphasis in the description of the two different mechanical concepts.

Geometric field components

In Chapter 3 the study of the geometric field errors is presented. The chapter starts with a description of the intrinsic challenges of Nb_3Sn and an assessment of the precision in the positioning of the conductors in MBH and MQXF magnets using a Monte-Carlo analysis. After a description of the modeling approach to describe the effect of coil shimming and mechanical deformation on the field, magnetic measurements at ambient and cryogenic temperature are analyzed. In particular, the following effects are studied:

- Effect of coil shimming and mechanical deformation on the collared coil and coil pack assemblies, including an estimate of the coil waviness, systematic and random field errors.
- Effect of the magnet assembly, to evaluate the impact of the coil deformation and iron yoke.
- Effect of the cool down, since a high degree of cold-warm correlation is important in order to detect and compensate geometrical errors before the final assembly.
- Effect of the electromagnetic forces during powering, to evaluate if there is a signature of coil un-loading in the field measurements.
- Effect of the powering cycles, to determine if there is a trace of plastic deformation on the coils visible on the geometric multipoles.

Finally, faulty assembly procedures identified through magnetic measurements are presented.

Ferromagnetic materials contribution

Next Chapter focuses on the contribution of the ferromagnetic materials, with the very non-linear behavior of the iron. Special attention is given to the transfer function and integral field which needs to be precisely known. Capabilities to correct field errors through magnetic shimming are also discussed in this chapter. The contribution of the beam screen to the field errors is computed numerically and compared to measurements. Finally, faulty assembly procedures identified through magnetic measurements where ferromagnetic materials were present are summarized.

Persistent and coupling currents effects

Chapter 5 analyses the field generated by magnetization currents (the so-called persistent currents), leading to field distortions that degrade the accelerator performance, in particular at the injection energy. Flux jumps in Nb_3Sn at 1.9 K introduce a degree of uncertainty in the contribution of the magnetization. Taking as starting point the semi-analytical model to describe the filament magnetization in the LHC NbTi dipoles, an approach to account for the flux jumps through a reduction of the effective filament size

is discussed and validated. As an additional application, the calculation of hysteresis losses arising from the superconductor magnetization of the filaments is presented and compared to the measurements.

Decay and snapback

The last section of the Thesis is dedicated to the so-called dynamic effects at injection, important due to their relatively large amplitude and strong time dependence. The database and understanding of the field "decay" and the following "snap-back" is quite well established for magnets built with Nb-Ti cables. While we would expect the basic mechanisms to be identical in Nb_3Sn cables, only little data is available. Systematic measurements to study the dependence of decay and snapback on the injection field level, powering history and temperature were performed. The main attention is restricted to the first allowed multipoles for which the effects are systematic.

1.4 References

[1.1] K. Koepke, et al., "Fermilab doubler magnet design and fabrication techniques", IEEE Trans. Magn., Vol. MAG-15, No. l, January 1979.

[1.2] FT. Cole et al, editors, A Report on the Design of the FNAL Superconducting Accelerator, May 1979.

[1.3] HERA, A Proposal for a Large Electron-Proton Colliding Beam Facility at DESY, DESY HERA 81-10, 1981

[1.4] S. Wolff, Superconducting Magnets for HERA, Proceedings of the XIII International Conference on High Energy Particle Accelerators, Novosibirsk, Aug. 1986, Vol. 2, p. 29, DESY HERA 1986-12

[1.5] H. Kaiser, Design of Superconducting Dipole for HERA, Proceedings of the XIII International Conference on High Energy Particle Accelerators, Novosibirsk, Aug. 1986, Vol. 2, p. 49. DESY HERA 1986-14

[1.6] Conceptual Design of the Relativistic Heavy Ion Collider, RHIC, Report No. BNL51932, Brookhaven National Laboratory, Upton NY. 1986, latest version of magnet design received from A. Greene, BNL, private communication

[1.7] M. Anerella, et al., "The RHIC magnet system ", Nucl. Instrum. Meth. A499 (2003) 280-315.

[1.8] O. Brüning, et al., LHC Design Report, Geneva: CERN, 2004. - 548 p., doi: 10.5170/CERN-2004-003-V-1.

[1.9] O. Brüning, et al., "High-Luminosity Large Hadron Collider (HL-LHC): Technical design report," CERN 2020-010, DOI 10.23731/CYRM-2020-0010

[1.10] Future Circular Collider Study. Volume 3: The Hadron Collider (FCC-hh) Conceptual Design Report, preprint edited by M. Benedikt et al. CERN accelerator reports, CERN-ACC-2018-0058, Geneva, December 2018. Published in Eur. Phys. J. ST.

[1.11] F. Savary et al., "Status of the 11 T Nb3Sn Dipole Project for the LHC," in IEEE Transactions on Applied Superconductivity, vol. 25, no. 3, pp. 1-5, June 2015, Art no. 4003205, doi: 10.1109/TASC.2014.2375914.

[1.12] S. Feher et al., "Production and installation of the LHC low-β triplets," IEEE Trans. Appl. Supercond., vol. 16, no. 2, pp. 437–440, Jun. 2006.

[1.13] A. Yamamoto et al., "Production and measurement of the MQXA series of LHC low-β insertion quadrupoles," IEEE Trans. Appl. Supercond., vol. 15, no. 2, pp. 1084–1089, Jun. 2005.

[1.14] P. Ferracin et al., "Magnet design of the 150 mm aperture low-β quadrupoles for the high luminosity LHC," IEEE Trans. Appl. Supercond., vol. 24, no. 3, Jun. 2014, Art. no. 4002306.

[1.15] E. Todesco et al., 'The High Luminosity LHC interaction region magnets towards series production,' Superconductor Science and Technology, 2021, https://dx.doi.org/10.1088/1361-6668/abdba4
[1.16] S. A. Gourlay et al., "Magnet R&D for the US LHC accelerator research program," IEEE Trans. Appl. Supercond., vol. 16, no. 2, pp. 324–327, Jun. 2006.
[1.17] M. N. Wilson, Superconducting Magnets, Plenum Press, 1983.

2 MAGNET DESIGN: CHALLENGES AND FEATURES

2.1 The 12 T Challenge

The field generated by a dipole is proportional to the current density j_0 and the coil width w (see Eq. 3). In a quadrupole, the gradient is proportional to the current density j_0 and the natural logarithm of the width ($log(1+w/r)$, see Eq. 4). A higher field or gradient can be achieved by increasing the current density and/or the coil width. The drawback of the second path is the need of a larger quantity of superconductor and a less compact design. The increase of the current density is the most critical path since it hits the physical limits for protection, mechanical structure and stresses, and stability. Large current densities provide more compact magnets, but as can be observed from examining the history of accelerator magnets, most cases range between 300 and 600 A/mm^2 (see Figure 7).

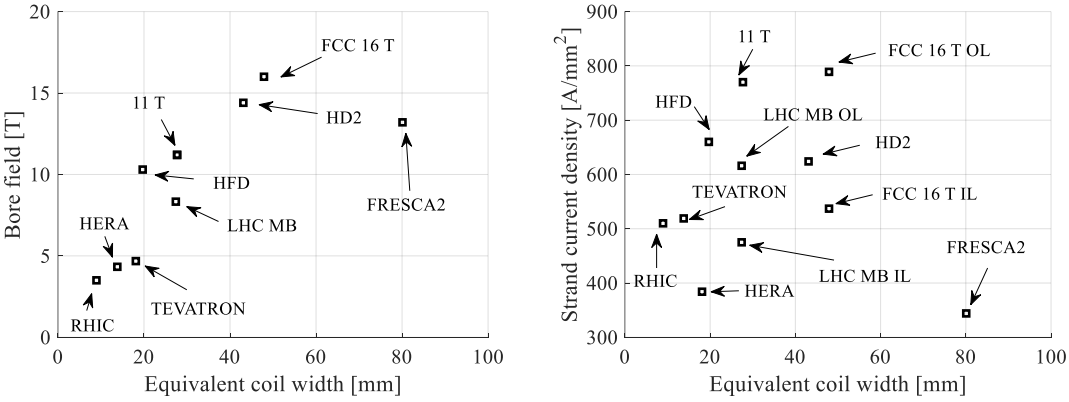

Figure 7. Equivalent coil width versus bore field and strand current density for Nb-Ti and Nb_3Sn dipole magnets.

To fix orders of magnitude, the typical value of the strand current density (also called engineering current density, ratio between the current and the metal surface of the strand, excluding insulation) at nominal operating conditions in the cables of the large superconducting accelerators built and operated to date varies from 380 A/mm^2 for the HERA dipole cable to 620 A/mm^2 in the LHC outer layer dipole cable, while the energy stored per unit volume of strands ranges from 30 J/cm^3 in the HERA dipole to 70 J/cm^3 in the LHC dipole. Both values will increase further in the next generation of superconducting accelerator magnets, reaching respectively 770 A/mm^2 and 125 J/cm^3 in the 11 T dipoles to be installed in the LHC as a part of the High-Luminosity upgrade

project. The values for a 16 T Nb_3Sn dipole under design for the Future Circular Collider [2.1] would reach nearly 800 A/mm^2 and 200 J/cm^3, respectively. Figure 8 shows the strand energy and current density for different dipole magnets built in the past, in construction, and being designed for future accelerators. The trend towards increasing stored energy per unit volume of strand vs. bore field is very clear and is accompanied by a somewhat more modest and scattered increase of the strand current density vs. bore field.

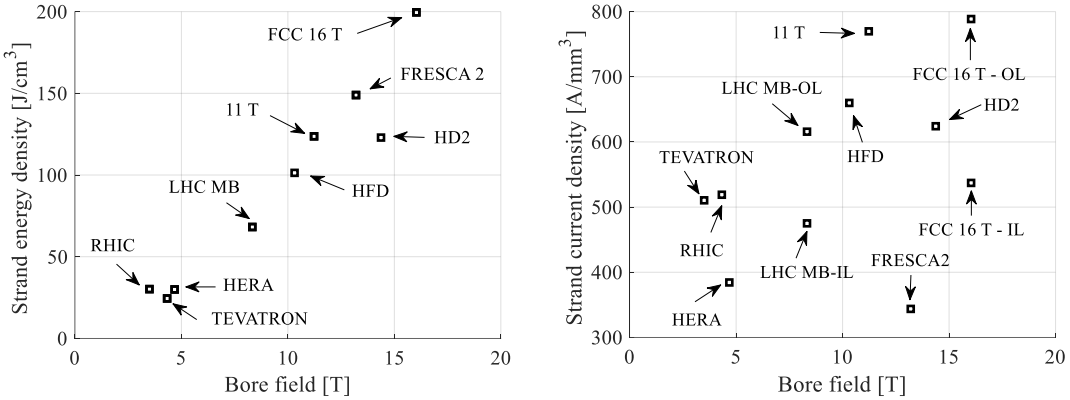

Figure 8. Bore field versus strand energy density and strand current density (also called engineering current density) for Nb-Ti and Nb_3Sn magnets.

Due to the brittle nature of Nb_3Sn, respecting the mechanical limits at which Nb_3Sn superconductors can safely operate is critical. The Lorentz forces in an n-pole magnet tend to push the coil (see Figure 9 and Figure 10):

- towards the mid plane in the vertical/azimuthal direction (F_y, $F_\theta < 0$ in the first quadrant for a dipole, first octant for a quadrupole);
- outwards in the radial–horizontal direction (F_x, $F_r > 0$ in the first quadrant for a dipole, first octant for a quadrupole);
- in the coil ends, the electromagnetic forces tend to push the coil outwards in the longitudinal direction ($F_z > 0$ for the coil end at $z > 0$)

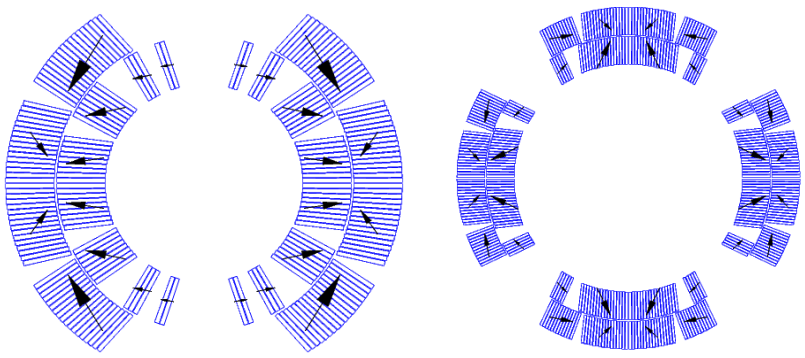

Figure 9. Electromagnetic forces in the MBH 11 T dipole (left) and MQXF quadrupole (right)

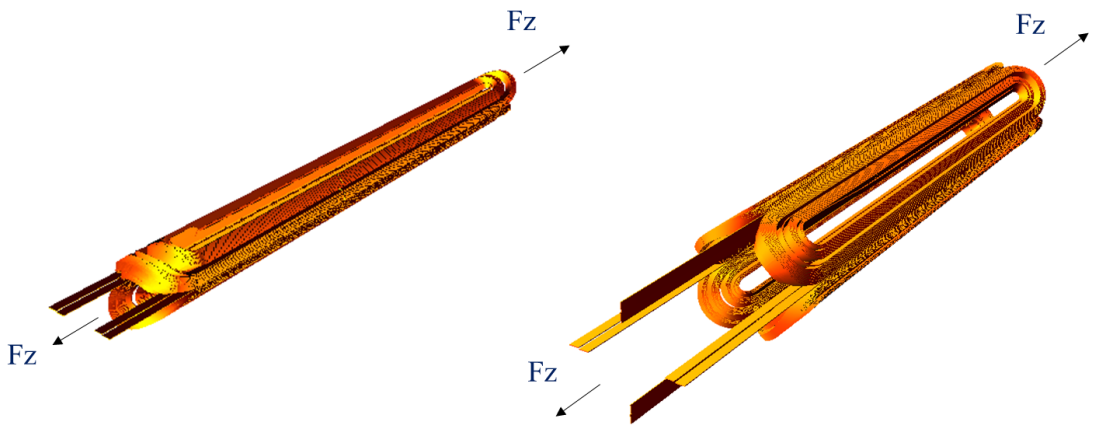

Figure 10. Axial electromagnetic forces in the MBH 11 T dipole (left) and MQXF quadrupole (right)

Approximating the coil by a thin shell placed at a radius a, the electromagnetic forces in a dipole providing a bore field B_y can be derived analytically [2.2],

$$F_x = -F_y = \frac{B_y^2}{2\mu_0}\frac{4}{3}a \qquad \textit{Eq. 6}$$

$$F_z = \frac{B_y^2}{2\mu_0}2\pi a^2 \qquad \textit{Eq. 7}$$

Thus, the x/y electromagnetic force on a dipole coil varies

- with the square of the bore field
- linearly with the bore radius.

The axial force on a dipole coil varies

- with the square of the bore field
- with the square of the bore radius

In the case of a quadrupole, the electromagnetic forces under the thin shell approximation are [2.2]:

$$F_x = \frac{B_y^2}{2\mu_0}a\frac{4\sqrt{2}}{15} = \frac{G^2}{2\mu_0}a^3\frac{4\sqrt{2}}{15} \qquad \textit{Eq. 8}$$

$$F_y = -\frac{B_y^2}{2\mu_0}a\frac{4\sqrt{2}+8}{15} = -\frac{G^2}{2\mu_0}a^3\frac{4\sqrt{2}+8}{15} \qquad \textit{Eq. 9}$$

$$F_z = \frac{B^2}{2\mu_0}\pi a^2 = \frac{G^2a^2}{2\mu_0}\pi a^2 \qquad \textit{Eq. 10}$$

Thus, the x/y electromagnetic force on a quadrupole coil varies

- with the square of the gradient or coil field
- with the cube of the aperture radius (for a fixed gradient)
- keeping the peak field constant, the force is proportional to the aperture.

The axial force on a quadrupole coil varies

- with the square of the gradient, i.e., with the square of the coil peak field since the gradient is proportional to the field.
- with the fourth power of the aperture radius (for a fixed gradient).

Being the peak field and aperture the same, a quadrupole has half of the longitudinal electromagnetic forces of a dipole. The axial electromagnetic force in the LHC-MB dipole at nominal current is 265 kN. In the MBH-11 T dipole axial force is almost a factor 2 due to the higher field, with an axial force per aperture of 450 kN, whereas in MQXF due to the large aperture the electromagnetic forces are 1200 kN per aperture.

In the azimuthal direction, a simple way of comparing forces in magnet design, independently of the mechanical structure, is the sum of the azimuthal components of the forces in the coil, divided by the coil width. This gives an indication of the compression in the midplane induced by the electromagnetic forces, ignoring friction, structure deformation, prestress etc. In the LHC dipoles, the accumulation of the electromagnetic forces compresses the coil in the midplane with 70 MPa. This value is increased by 50% to ~100 MPa for the 11 T dipole and for the MQXF. To avoid the detachment of the coil from the pole, coils are pre-stressed during assembly. This goal is reached through two different structures The 11 T dipole imposes a fixed dimension through collaring, with main load applied at room temperature. The MQXF imposes a force through bladder and keys, and around half of the load is applied during the cool down through the thermal contraction of the Al shell. Short model magnets were tested under a wide range of azimuthal pre-load to define the target pre-load for the series magnets [2.4],[2.5]. Figure 11 shows the evolution of the measured difference in the azimuthal pole stress for the MQXF and collar stress for the 11 T during powering, measured with the strain gauges on the titanium pole and the stainless-steel collars, respectively. Initially, the stress linearly decreases with the applied forces (proportional to the square of the current). After a certain level, the linear behavior is lost: this is considered an indication of detachment of the coil from the pole. The pre-stress target for MQXF series magnets at cold is 100-110 MPa, corresponding to a pole un-loading at ~ 90 % of the nominal current [2.6]. For the 11 T magnet, the strategy was to limit the mid-plane stress during collaring to avoid conductor degradation, corresponding to a pole un-loading at ~ 50 % of the nominal current [2.3].

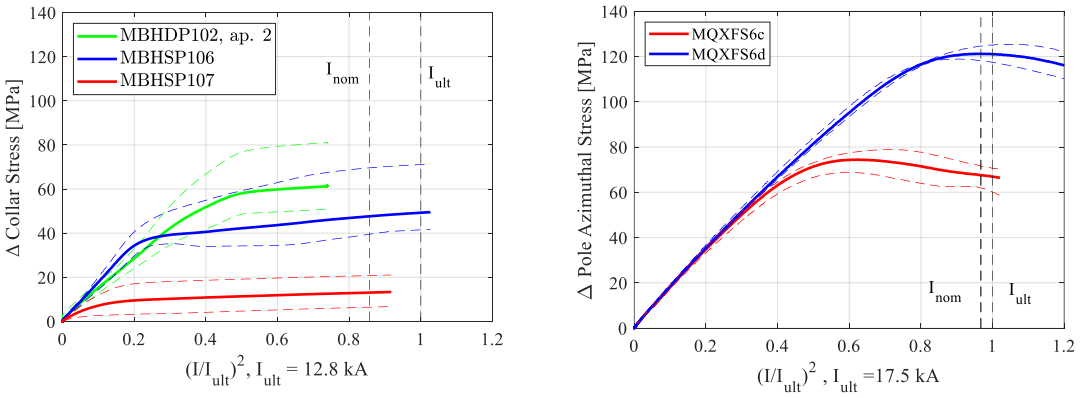

Figure 11. Collar nose stresses in SP106, SP107 and DP102 during powering in the straight section of the magnet. The dashed line marks indicate the spread among the coils in the same longitudinal section. Pole stresses in MQXFS6b and MQXFS6c during powering in the straight section of the magnet. The dashed line marks indicate the spread among the coils in the same longitudinal section.

The handling of the electromagnetic forces is one of the biggest challenges in Nb_3Sn accelerators magnets, but not the only one. Some other challenges of the technology are:

- *Cabling and winding:* Both magnets make use of 40 strand cable with moderate keystone angle. The large aspect ratio of this cable required a careful optimization of the cable parameters [2.6]; final choice was a trade-off between a good compaction (needed to avoid strand pop out during winding [2.7]) and a low

deformation of the strands (to avoid the degradation of the critical current). Both 11 T dipole and MQXF makes use of a special tool to avoid strand pop up when winding coil ends, developed in LBNL. The MQXF cable dimensions were iterated at the beginning of the short model phase, reducing the keystone angle from 0.55 to 0.4 to reduce the critical current degradation. In the 11 T the keystone angle was also reduced from 0.79 to 0.5 for the PIT short model magnet. In addition, the conductor insulation must withstand a heat treatment at 650˚C so the polyimide insulation traditionally used for NbTi magnets is not suitable. In state-of-the-art Nb_3Sn accelerator magnets, the conductor is insulated with fiber glass. After the heat treatment to form the superconducting phase, the coil is impregnated with an epoxy resin .

- *Length*: The management of thermal contractions and dilatations (from 1.9 K during magnet operation to 650 °C during coil reaction) of the different magnet components is one of the main challenges of the Nb_3Sn technology; they scale with the magnet length. One-meter-long models were built since the 90's [2.9],[2.10]. In 2008, LARP successfully proved the technology up to 3.4-m-long coils [2.12]. The extension was not trivial, requiring a segmentation of the Al shells to minimize the accumulation of longitudinal stresses and several iterations in the tooling. HL-LHC magnets will bring this range to 7 m; the final target for FCC is 15 m long dipoles as in the LHC. The MQXF program consists of a 7.2-m-long Q2 built at CERN, whereas the US program went for a split Q1/Q3 magnet made of two 4.2-m-long units to mitigate the risks related to long coils.

- *Protection*: The hot spot temperature in the Nb_3Sn magnets for the HL-LHC is around 100 K higher than in the MB magnets operating in the LHC. It is interesting to note here that in spite of the great increase of current density in the copper (from 600 A/mm^2 in HERA dipoles to 1400 A/mm^2 in the 11 T dipoles) the increase of the hot spot temperature is moderate thanks to a great improvement on the time required to detect, validate and initiate a quench. This delay is around 200 ms for HERA dipoles [2.13], 160 ms for Tevatron dipoles [2.14], 90 ms for the LHC-MB dipoles [2.15] and 40 ms for HL-LHC Nb_3Sn magnets. In MQXF, thanks to the use a novel protection system based on Coupling Loss Induced Currents (CLIQ) [2.16], the hot spot in normal operation decreases from ≈ 300 K to 250 K. The bulk temperature of the coil can be derived from the overall current density [2.17], going from 80 K in the LHC MB magnets to 110 K in the HL-LHC Nb_3Sn magnets. It is important to recall that if the coil is not impregnated and operates in superfluid helium, the contribution of HeII to the specific heat is very large below the transition temperature so it plays a major role. Flux jumps require a variable threshold for detection that has been made possible through a new hardware development.

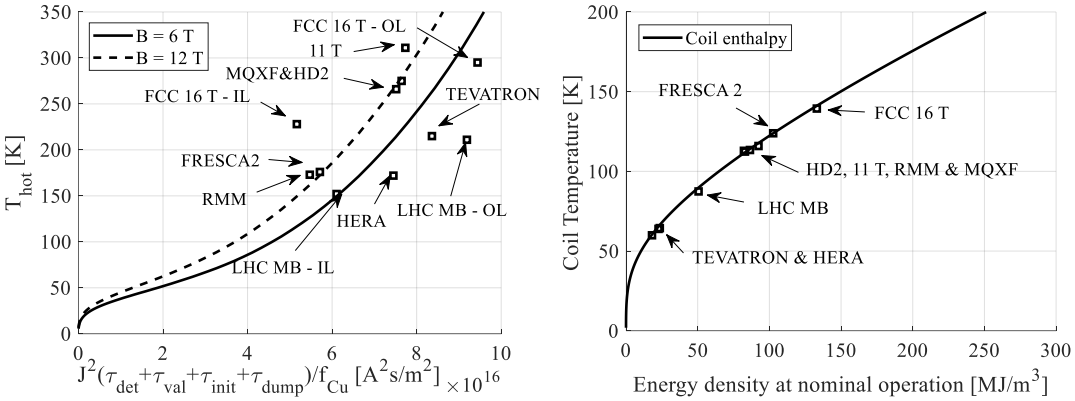

Figure 12. Left: Relation between the integral of the square of the current density and the temperature rise in the conductor for different magnets (symbols), assuming 40 ms for detection, validation and initiation in Nb3Sn magnets, 90 ms in the LHC dipoles [2.15], 160 ms in Tevatron [2.14] and 200 ms in Hera [2.13], compared to the adiabatic increase of temperature (lines) assuming that 1/3 of the coil is copper, 1/3 is superconductor and 1/3 is insulation. Two values of initial field were taken to give sense for the intrinsic spread. Right: Relation between the energy density and bulk temperature of the coil for different magnets (symbols), compared to the coil enthalpy (solid line) assuming that 1/3 of the coil is copper, 1/3 is superconductor and 1/3 is insulation.

- *Field quality*: The field quality in Nb_3Sn magnets is the focus of this thesis. Compared to the Nb-Ti magnets currently operating in the LHC, state-of-the-art Nb_3Sn conductor features larger filament size and higher critical current density resulting on a strand magnetization about one order of magnitude larger. This has important implications for the field quality at injection energy. In addition, fabrication of Nb_3Sn coils requires heat treatment after winding. The formation of the superconducting phase Nb_3Sn during heat treatment produces a volume expansion leading to radial, azimuthal, and axial dimensional changes of the conductor. In order to prevent residual strain from altering superconducting performances, the tooling must provide the adequate space for these dimensional changes. The position of the conductors must be controlled with a precision greater than 0.1 mm, meaning that the best compromise between performance and field quality needs to be found.

This section summarizes the main design features of the MBH-11 T and MQXF magnets, as application cases of the aforementioned challenges. The main parameters of the magnets are summarized in Table 1. Both magnets make use of 40 strands Rutherford cable and are designed to operate approximately at 80 % of the short sample limit. The coil fabrication process is similar in the two cases, based on the wind-and-react technology, where the superconducting phase is formed after winding and during coil heat treatment. After reaction, the coils are impregnated with epoxy CTD-101K resin. A relevant difference is the impregnation: in the 11 T dipole the pole is not impregnated with the coil, leaving the possibility of an additional degree of freedom for shimming and allowing the detachment of the coil from the pole during powering. This technology follows the one developed for the CERN-Elin dipole [2.27]. The MQXF has a pole impregnated with the coil, following the LARP design [2.12].

Table 1. Main parameters of the 11 T and MQXF magnets

Parameters	Unit	MBH 11T	MQXF
Strand diameter	mm	0.7	0.85
Number of strands	--	40	40
Copper to superconductor ratio (cu/SC)	--	1.1 ± 0.1	1.2 ± 0.1
Nominal magnet current (I_{nom})	kA	11.85	16.23
Conductor peak field at I_{nom}	T	11.7	11.3
Engineering (strand) current density at I_{nom}	A/mm^2	770	715
Engineering (strand) energy density at I_{nom}	J/cm^2	124	120
Equivalent coil width (w)	mm	30	36
Magnetic length	m	1.7/5.3	1.2/7.2
Stored energy at I_{nom}	MJ/m	0.899	1.15
Mid-plane stress due to e.m forces at I_{nom}	MPa	97	101

2.2 MBH-11T dipole

The MBH-11T dipole features an aperture of 60 mm and provides a nominal aperture field of 11.2 T. The 11 T coils are made with a Rutherford-type cable composed of 40 strands of 0.70 mm diameter. The cable incorporates a 12 mm wide stainless-steel core of 25 μm thickness to reduce inter-strand coupling currents. Each coil has 56 turns, 22 in the inner layer and 34 in the outer layer. The magnetic length is 1.7 m for the short model magnet and 5.3 m for the full-size magnets. The mechanical design of the 11 T relays on separate stainless-steel collars for each aperture and a vertically split iron yoke, surrounded by a welded stainless-steel shell (see Figure 13). Two different concepts for coil pre-load were explored. In FNAL design, poles are impregnated with the coil and the pre-load is provided thorough coil-mid-plane shimming and horizontal deformation of the collared coils during the cold mass assembly [2.19]. CERN pursued a solution with removable poles [2.21], allowing the loading at the poles similarly to the conventional collared Nb-Ti accelerator magnets ([2.22]-[2.26]1.[2.22]) and some earlier Nb_3Sn magnets ([2.27][2.28]).

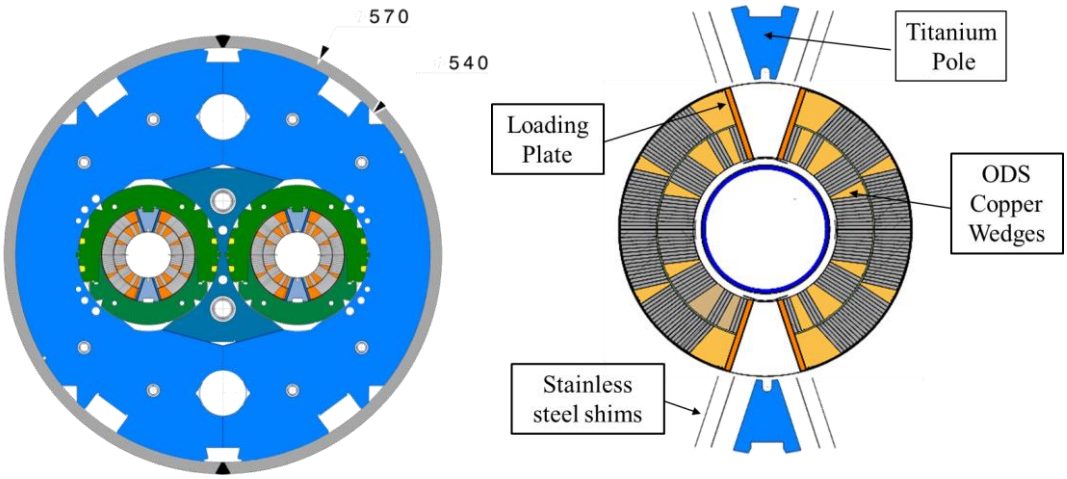

Figure 13. MBH-11 T magnet cross section (left). 11 T coil package, CERN design, including removable pole and loading shims (right).

2.2.1 Conductor and cable

MBH-11 T coils are made with a Rutherford-type cable composed of 40 strands of 0.70 mm diameter, with a Cu/non-Cu ratio of 1.1 and a minimum non-Cu J_c of 2450 A/mm^2 at 12 T of applied magnetic field and 4.2 K (see strand specifications in Table 2). CERN supported the development of two strand technologies, namely the RRP strand by OST (then Bruker-OST) with 108 sub elements and PIT strand by Bruker-EAS, with 120 sub elements [2.29]. PIT conductor has been used for the construction of one short model double aperture magnet.

Table 2. 11 T strand parameters (RRP & PIT strand)

Parameters	Unit	
Strand diameter	mm	0.7
Sub-element diameter	μm	< 50
Cu/SC	--	1.1 ± 0.1
RRR	--	> 150
I_c (12 T, 4.2 K), no self-field correction	A	> 438
Non-Cu Jc (12 T, 4.2 K), no self-field	A/mm^2	> 2450

The bare superconducting cable is 14.700 mm wide and 1.250 mm thick, with a keystone angle of 0.79˚. For the coil design and the field quality computation, an increase of width and mid-thickness of 1 % and 4.5% respectively was assumed. The cable incorporates a 12-mm-wide 25-μm-thick stainless-steel core to reduce inter-strand coupling currents. RRP 108/127 strands from Bruker-OST were used for the series magnets, all built using the first-generation design. A short model magnet using PIT strand was built using the second-generation design, where the keystone angle was reduced from 0.79˚ to 0.50˚ to limit the current degradation due to cabling [2.30]. Table 3 summarizes the cable parameters for the first- and second-generation design. The cable insulation consists of a C-shaped glass/mica foil folded around the cable and braided with S-2 11-Tex glass fibre. A similar insulation scheme was used in [2.28]. The target insulation thickness is 100 μm.

Table 3. 11 T cable parameters

Parameters	Unit	1st Generation	2nd Generation
Un-reacted bare cable width	mm	14.700	14.700
Un-reacted bare cable mid-thickness	mm	1.250	1.250
Un-reacted cable keystone angle	˚	0.79	0.50
Reacted bare cable width	mm	14.850	14.850
Reacted bare cable mid-thickness	mm	1.307	1.288
Reacted cable keystone angle	˚	0.81	0.50
Cable insulation thickness at 5 MPa	mm	0.1	0.1

2.2.2 Magnetic design

The MBH-11 T coil features 56 turns, 22 in the inner layer and 34 in the outer layer, wound around a titanium alloy pole and subdivided in 6 blocks per quadrant. The magnets will be connected in series with the MBs and have to be compatible with the LHC lattice and main systems. Consequently, the new magnets must: 1) be double-aperture magnets with the same beam separation distance of 194 mm, and 2) have a central field of about 11 T to produce the integrated field of 119 Tm at 11.85 kA as one MB. Due to the differences in iron saturation between the MB and the MBH 11T, in order to have the same integral of the transfer function across the entire range of current during ramping up to nominal current, a dedicated trim power converter is added. Although the final magnet will have a two-in-one structure like the MBs, single aperture models were made in order to maximize the overall effectiveness of the development activities. As the coils are individually collared, a single aperture model is good enough to test most of the features of a two-in-one magnet. A set of modifications were introduced in the design which have an impact on the integral field:

- Magnetic iron laminations on the magnet extremities were replaced by non-magnetic laminations to reduce the peak field on the coil ends
- The outer radius of the iron yoke was reduced from 275 mm to 270 mm in order to have the same outer diameter of the cold mass. The aim of this change it was to be able to re-use the existing tooling from the MB production.

The main operational parameters of the double aperture magnet are summarized in Table 4 and Figure 14 shows the coil cross section.

Table 4. Main 11 T parameters for operation at 1.9 K (double aperture magnet).

Parameters	Unit	Nominal[a]	Short Sample[b]
Current	kA	11850	14650
I/I_{SSL}	%	81	100
Central field	T	11.23	13.64
Coil peak field	T	11.77	14.32
Differential inductance	mH/m	11.92	11.70
Stored energy	MJ/m	0.899	1.327
Current sharing temp.	K	6.4	1.9
Overall current density [c]	A/mm^2	522	645
Engineering current density [d]	A/mm^2	770	952
Copper current density	A/mm^2	1439	1779
F_x/F_y per quadrant	MN/m	3.64/-1.86	5.37/2.74
F_θ layer1/layer2 per quadrant	MN/m	1.26/1.69	1.86/2.50
F_z (per aperture)	MN	0.45	0.65

[a] Nominal current is for LHC operation at 7 TeV per beam

[b] Short Sample Limit (SSL) is for minimal conductor requirement

[c] Current density in whole coil pack (conductor (non-Cu and Cu) and insulation)

[d] Current density in whole conductor (non-Cu and Cu)

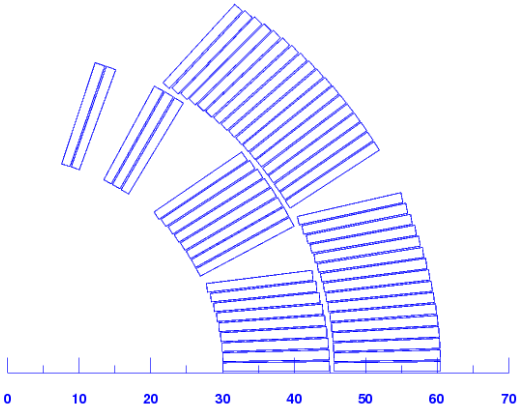

Figure 14. MBH-11 T coil cross section

After the construction of the first prototype coils, the coil length was adjusted to fit the requirements in terms of integrated field at nominal current. Details will be treated in Section 4.2.1. The field in the aperture is described in the standard form of harmonics coefficients in a series expansion (see Eq. 5). Electromagnetic design included both 2D and 3D computations. The conductor lay out in the coil ends was optimized to minimize the integrated field harmonics, computed according to the following convention,

$$\bar{b}_n = \frac{\int_{z_0}^{z_{end}} B_n(I,z)dz}{B_0^{ss} l_{mag}(I)} \qquad \textit{Eq. 11}$$

where B_n are the harmonic coefficient at the reference radius (further details will be given in Section 3.1), B_0^{ss} is the main field in the straight section and l_{mag} is the magnetic length of the integrated section. Integrating limits are ± ∞ when providing the total integral of the harmonics content.

$$l_{mag}(I) = \frac{1}{B_0^{ss}(I)} \int_{z_0}^{z_{end}} B_2(I,z)dz \qquad \textit{Eq. 12}$$

Magnetic length and harmonics are summarized in Table 5, providing the local contribution of the magnet connection side (c.s), non-connection side (n.c.s) and total integral. In the coil connection side, the Nb_3Sn to NbTi splice has an important contribution to the sextupole field component.

Table 5. 11 T field harmonics at nominal current (2 in 1 configuration).

	Units	Straight part	Ends		Integral
			c.s	n.c.s	
Magnetic length, m	m	--	0.237	0.148	5.323
b_2	units	-13.09	-2.29	-6.94	-12.44
b_3	units	7.66	40.52	7.22	9.11
b_5	units	0.34	4.28	1.16	0.54
a_2	units	-0.26	-3.24	0.00	-0.39
a_4	units	-0.01	1.26	0.00	0.05

2.2.3 Mechanical design

The MBH-11 T support structure relays on separate stainless-steel collars for each aperture and a vertically split iron yoke, surrounded by a welded stainless-steel shell. The pre-load results mainly from the interference of a removable pole, made up of titanium, with the *coil package* (see Figure 13, right), which consists of the coil and of lateral stainless-steel shims of adjustable thickness. The role of the laminated collars is to fix and close the coils in a precise cavity.

Collars are placed around the coil pack. The role of the laminated collars is to fix and close the coils in a precise cavity providing a pre-compression. In order to obtain the clearance required to insert the keys, the collared coil is placed within a collaring tool, composed by a top and a bottom block, engaging the collars in two indentations per quadrant. Compressed by pistons, the tool pushes the top long collar towards the bottom long collar, until the necessary key slot clearance is achieved. To limit misalignment of the collaring tools and avoid overstressing the coils, two stoppers are placed close to the key slots. Ideally, the tooling is in contact with the stoppers when keys are inserted. The experience from different collaring operations executed with various coils segments showed that the typical clearance required to insert the keys is about +0.15 mm. This process leads to an overshoot of stresses in the collar-coil assembly, with respect to the targeted prestress at room temperature. It is at this time that the coil midplane turns experience the highest stress [2.34]. Figure 15 illustrates the collared coil assembly at the different assembly steps.

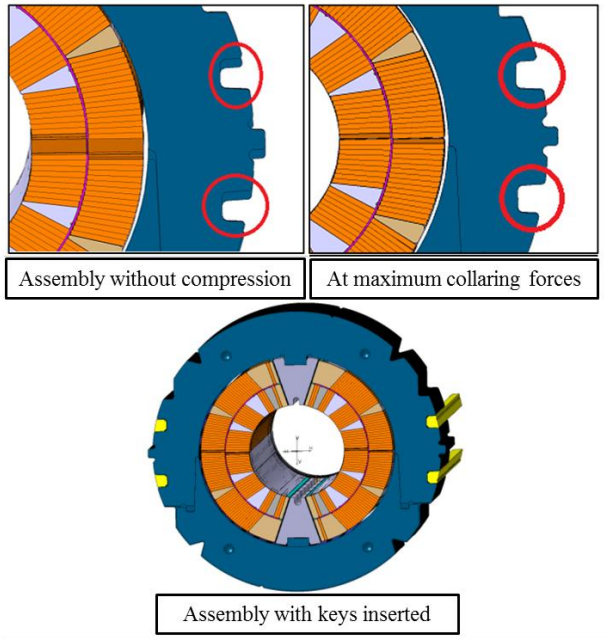

Figure 15. Illustration of the collared coil assembly without compression, with an interference of the key slots of 0.15 mm and the assembly under compression with the keys inserted.

After collaring, yoke laminations are placed around the collared coils, and the assembly is enclosed in stainless steel shells of 10 mm for single aperture and 15 mm for the double aperture magnets. The final step in the magnet assembly is the welding of the end plates followed by longitudinal loading. In the short model program, the coils are loaded longitudinally by 30-60 kN per aperture (7-14 % of the longitudinal electromagnetic force at nominal current) with the purpose of maintaining a contact between the coil and the end plate after cooling down, providing a rigid longitudinal support to the coil (that will tend to expand due to the axial component of the Lorentz force).

2.3 MQXF Low-β Quadrupole

MQXF coils are made with a Rutherford-type cable composed of 40 strands of 0.85 mm diameter, with 50 turns wound in 2 layers around a titanium alloy pole and subdivided in 4 blocks per octant. The design of the MQXF quadrupole magnet (described in detail in [2.4]) relies on an aluminium cylinder pre-stressed at room temperature with water pressurized bladders and interference keys, i.e. the bladder and key technology that has been demonstrated in the previous successful series of LARP magnets [2.9]. The magnet features an aperture of 150 mm and provides a nominal field gradient of 132.2 T/m.

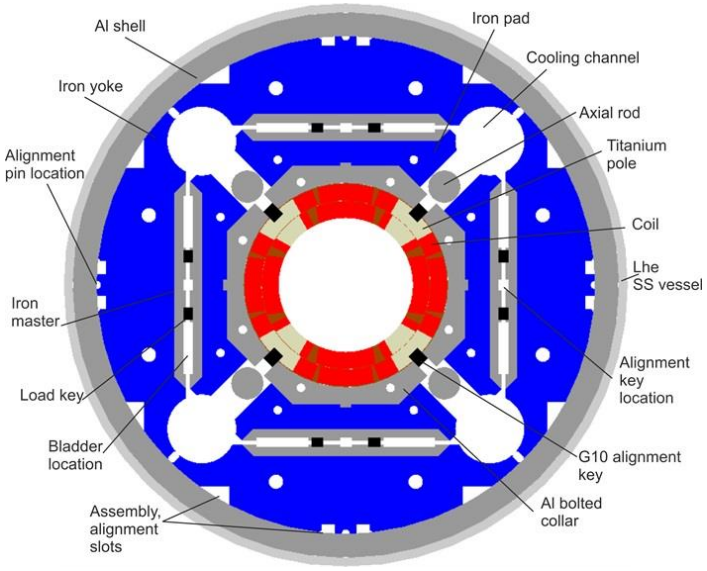

Figure 16. Magnet cross-section

2.3.1 Conductor and cable

MQXF coils are made with a Rutherford-type cable composed of 40 strands of 0.85 mm diameter, with a Cu/non-Cu ratio of 1.2 and a minimum non-Cu J_c of 2450 (1400) A/mm^2 at 12 (15) T of applied magnetic field and at 4.2 K (see strand specifications in Table 6). CERN supported the development of two strand technologies: Restacked Rod Process (RRP) by OST [2.33] (later Bruker-OST) and Powder in Tube (PIT) by Bruker [2.29]. PIT conductor has been used for the construction of two short models and five MQXFB coils.

Table 6. MQXF strand parameters

Parameters	Unit	RRP 108/127	PIT 192
Strand diameter	mm	0.85	
Sub-element diameter	μm	< 55	
Cu/SC	--	1.2 ± 0.1	
Wire twist pitch	mm	19 ± 3	
RRR	--	> 150	
I_c (12 T, 4.2 K), no self-field correction	A	> 632	> 590
I_c (15 T, 4.2 K), no self-field correction	A	> 331	> 331
Non-Cu Jc (12 T, 4.2 K), no self-field	A/mm^2	> 2450	> 2290
Non-Cu Jc (15 T, 4.2 K), no self-field	A/mm^2	> 1280	> 1280

The bare superconducting cable is 18.150 mm wide and 1.525 mm thick, with a keystone angle of 0.4°. The angle was reduced from the "first-generation" value of 0.55° to bring the critical current degradation due to cabling to < 5% in the PIT conductor and < 3% in the RRP conductor. For the coil design and the field quality computation, an increase of width and mid-thickness of 1.2% and 4.5% respectively was assumed, with the same keystone angle, as observed by dimensional measurements performed on cross-section of first-generation. The cable incorporates a 12 mm wide 25 μm thick stainless-steel core to reduce inter-strand coupling currents. RRP 108/127 strands from Bruker-OST will be used for all MQXFA and MQXFB series magnets. The design assumes a critical current degradation due to cabling of 5 %. The average degradation of the RRP cables is 3 %, whereas in the PIT cables the degradation is 7-14 %. R&D is on-going at CERN to reduce cabling degradation in PIT cables [2.6].

Table 7. MQXF cable parameters

Parameters	Unit	1st Generation	2nd Generation
Un-reacted bare cable width	mm	18.150	18.150
Un-reacted bare cable mid-thickness	mm	1.525	1.525
Reacted bare cable width	mm	18.513	18.363
Reacted bare cable mid-thickness	mm	1.594	1.594
Cable keystone angle	°	0.550	0.400
Cable insulation thickness at 5 MPa	mm	0.150	0.145

2.3.2 Magnetic design

The MQXF coils features 50 turns wound in 2 layers around a titanium alloy pole and subdivided in 4 blocks octant. MQXF is basically a scale-up in radius of HQ [2.10]. Coil cross section was optimized for stress distribution among layers and field quality [2.11]. The nominal gradient (7 TeV collision energy) was decreased from 140 T/m to 132.6 T/m in 2015 to increase the margin, decreasing the peak field in the coil from 12.1 T to 11.4 T. The reduction of the operation gradient was compensated by increasing the magnetic length from 4.00 to 4.20 m for Q1/Q3 and from 6.80 to 7.15 m for Q2a/Q2b [2.4]. In the original design, nominal current was defined neglecting the radial coil deformation due to loading and cool down, which according to the model was increasing the field by 1 %. In 2020 and based on the measurements from the short model magnet and first prototypes, the nominal current was reduced from 16.47 kA to 16.23 kA, which corresponds to a nominal gradient of 132.2 T/m. The magnetic length was also adjusted to 7.17 m for MQXFB and 4.21 m for MQXFA, keeping the same integral gradient as in the original design (557 T for MQXFA and 948 T for MQXFB). The main operational parameters of the magnet are summarized in Table 8 and Figure 17 shows the conductor layout in the coil cross section.

Table 8. Main MQXF parameters for operation at 1.9 K.

Parameters	Unit	Nominal[a]	Short Sample[b]
Current	kA	16.23	21.24
I/I_{SSL}	%	76	100
Gradient	T/m	132.2	168.1
Coil peak field	T	11.3	14.5
Differential inductance	mH/m	8.26	8.13
Stored energy	MJ/m	1.15	1.89
Current sharing temp.	K	7.0	1.9
Overall current density[c]	A/mm^2	462	604
Engineering current density[d]	A/mm^2	715	936
Copper current density	A/mm^2	1311	1716
F_x/F_y per octant	MN/m	2.41/-3.41	3.83/-5.68
F_θ layer1/layer 2 per octant	MN/m	-1.81/-2.1	-2.98/-3.46
F_z (whole magnet)	MN	1.2	1.9

[a] Nominal current is for LHC operation at 7 TeV per beam

[b] Short Sample Limit (SSL) is for minimal conductor requirement

[c] Current density in whole coil pack (conductor (non-Cu and Cu) and insulation)

[d] Current density in whole conductor (non-Cu and Cu)

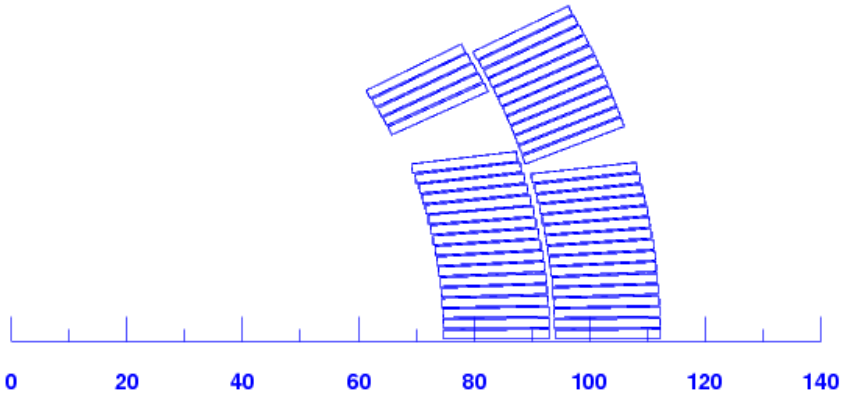

Figure 17. MQXF Coil cross-section

Due to the large beam size and orbit displacement in the final focusing triplet, these magnets have challenging targets for field quality requirements at nominal operating current. The coil cross section is optimized such that all allowed harmonics are within one unit at 6.5 TeV. Field quality is optimized at 123 T/m (6.5 TeV) because the triplet will operate between 100% and 90% of the maximum gradient [2.31]. The main concerns in terms of field quality are: 1) a systematic deviation on the first allowed harmonic, b_6, as the target range is only 1 unit; 2) the control of the low order, not allowed multipole (mainly b_3, a_3, b_4, a_4) stemming from assembly or component asymmetries. The design accounted for the possibility to correct the first allowed harmonic by shims at the level of the coil; the non-allowed harmonics are corrected by ferromagnetic shims allocated in the yoke. This will be treated in Chapter 3 (Geometric field components) and Chapter 4 (Ferromagnetic materials contribution). The conductor lay out in the coil ends was optimized to minimize the integrated field harmonics. The contribution of each magnet

end is also provided in a separate column in Table 9. As it can be observed, even if the integral of b_6 over the connection side of 400 mm length is close to 9 units, the total integral is 0.32 units for Q1/Q3 and - 0.07 units for Q2a/b. The rest of the harmonics are also summarized in the table, providing the local contribution on the magnet connection side (c.s.), non-connection side (n.c.s.) and the total integral. The large a_2 in the connection side of the magnet is mainly due to the layer jump. A detailed description of the 3D magnetic field optimization is available in [2.32].

Table 9. MQXF field harmonics at collision energy

	Units	Straight part	Ends		Integral	
			c.s	n.c.s	Q1/Q3	Q2a/b
Magnetic length	m	-0.64	0.40	0.34	4.27	7.17
b_6	units	-0.11	8.94	-0.03	0.32	-0.07
b_{10}	units	-0.87	-0.19	-0.82	-0.18	-0.15
b_{14}	units	0.00	-0.55	-1.08	-0.86	-0.86
a_2	units	0.00	31.34	0.00	-2.98	-1.75
a_6	units	0.22	2.21	0.00	0.21	0.12

2.3.3 Mechanical design

The design of the MQXF quadrupole support structure relies on an aluminium cylinder pre-stressed at room temperature with bladders and interference keys (i.e. bladder and key technology). The design of the structure comprises the shell-yoke sub-assembly, composed by four iron yokes surrounded by a 29 mm thick aluminium shell, and the coil-pack sub-assembly, which consists of four aluminium collars and iron pads bolted around the coils with G11 pole alignment keys. The aluminium collars are made of about 50 mm thick laminations assembled with tie rods. For MQXFB, the iron yoke and the iron pads are made of 5.6 mm-thick laminations with a 50 mm thick lamination every ≈ 600 mm. In the case of MQXFA, yokes and iron pads are made of about 50 mm thick laminations. In the end coil regions, the iron pad laminations are replaced by stainless steel pad laminations to reduce the conductor peak field in the ends. Between each pad and yoke, the master package on each quadrant contains two interference keys to balance the azimuthal tension in the outer shell with the azimuthal compression in the inner coils. Three structures were built for the short model program. At CERN, MQXFSD2 (thick laminations) and MQXFSD3 structure (thin laminations) were used for the assembly of all the short model magnets. The longitudinal electromagnetic forces are kept by four tensioned rods, made of aluminium for the short model magnets and of stainless steel for MQXFA and MQXFB. The rods are placed within the pads' gaps and connected to the end plates.

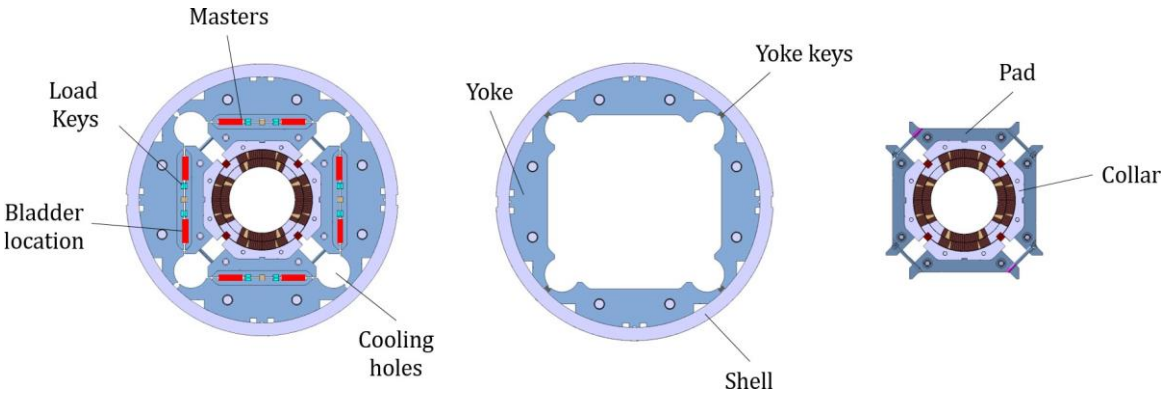

Figure 18. MQXF magnet assembly: Full magnet (left), yoke-shell sub-assembly (middle) and coil-pack sub-assembly(right). The most relevant components are labelled accordingly. The position of the bladders is highlighted using red rectangles.

Maintaining contact between the coils and poles pieces at all stages is achieved by the azimuthal pre-load applied on the shell. The pre-load is obtained by a system of water-pressurized bladders and keys which pre-compress the coil-pack and pre-tension the aluminium shell at room temperature. During the pre-load operation, the pressurized bladders open the master package and allow inserting the load keys with shims of the designed thickness, thus creating an interference between the coil-pack and the shell-yoke sub-assembly when the bladders are deflated and removed. The final pre-load is achieved during the cool-down phase, when the tensioned aluminium shell increases its stress because of its high thermal contraction. Figure 19 shows the different pre-load steps with the deformed shape of the magnet cross-section and Figure 20 shows how the forces are distributed withing the shell and coil and how they compare to the electromagnetic force. The markers indicate the ratio between the azimuthal electromagnetic force per octant, and the mechanical azimuthal forces imparted by the shell (in tension) and received by the coil (in compression). At room temperature, when the keys are inserted, 40% of the force provided by the shell is transferred to the coil, which increases to 87% of the electromagnetic forces at nominal current for the target pre-stress of 80 MPa peak coil azimuthal stress after room temperature loading.

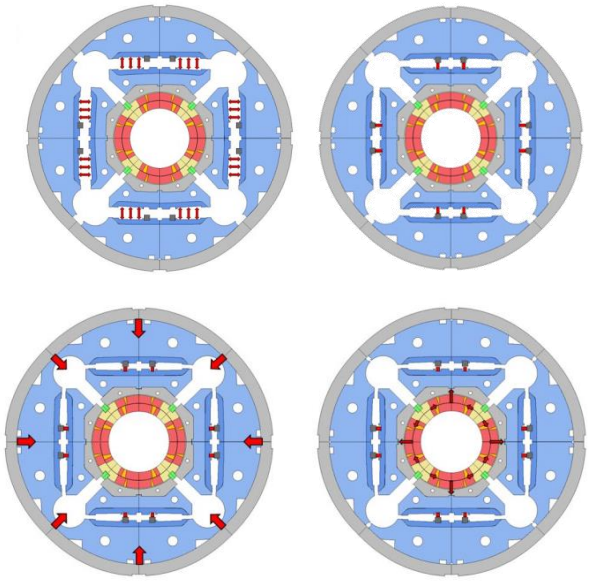

Figure 19. Loading sequence for MQXF with deformed shape: bladder pressurization (top left), key insertion (top right), cool down (bottom left) and nominal gradient (bottom right).

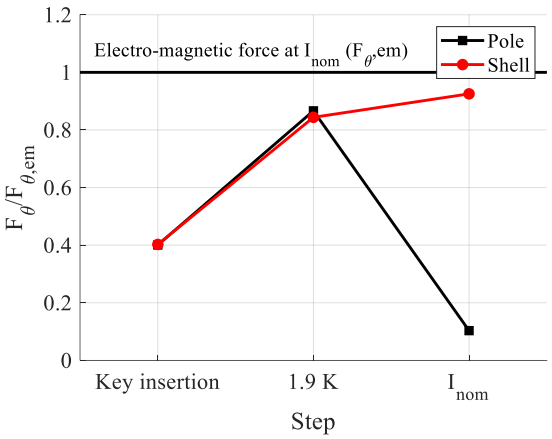

Figure 20. Ratio between azimuthal total electromagnetic force per octant and the azimuthal force provided by the shell and received by the coil.

In terms of peak stress, for the target pre-load the coil reaches a maximum compression of – 86 MPa in the pole region which increases to -125 MPa after cooling down. During powering, due the electromagnetic forces, the peak stress in the mid-plane is -110 MPa at nominal current and -120 at ultimate current. The cool down doubles the average stress in the inner layer pole turn whereas the peak coil stress increases by 40 %. Figure 21 and Table 10 show the coil azimuthal stress at the different assembly and operation steps.

Table 10. Azimuthal stress in the coil at the different assembly and operation steps.

		Bladder pressurization	Key insertion	Cool down	Powering (I_{nom}/I_{ult})
Average σ_θ, inner layer pole	MPa	-58	-52	-97	-6/-2
Peak σ_θ, inner layer pole turn	MPa	-72	-86	-113	-14/-8
Peak σ_θ, coil	MPa	-72	-86	-124	-109/-120

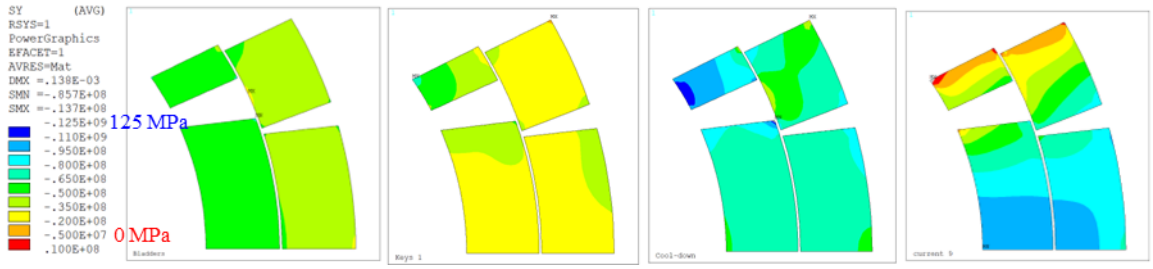

Figure 21. Coil azimuthal stress in Pa, from left to right: bladder pressurization, key insertion, cool down and nominal gradient.

After loading, two 8-mm thick stainless-steel (SS) half shells are welded around the magnet (see Figure 22). The cold mass assembly is completed with the welding of the end covers to the main cylinder formed by the welded half shells. Due to the impossibility to access the reverse side of the longitudinal weld of the shrinkage cylinders, a permanent backing strip is installed, in order to provide support for a fully penetrated root pass. The backing strip is linked to the magnet through tack welding blocks every 0.6 m that can slide in the direction of the magnet axis to compensate for the different in thermal contraction among the different components. The target pre-stress in the SS shell is 75 MPa to assure that SS shell is still in contact with the magnet aluminium shell after cool-down. This corresponds to an increase of the coil stress of 8 MPa ± 8 MPa. After the cold powering test results of the first two MQXFB prototypes welding requirements were modified, to assure no coupling of the SS vessel to the magnet, with a target increase of

coil pre-stress of 0 MPa and a maximum allowable increase of 8 MPa [2.35]. Figure 22 shows the full magnet length magnet assembly and a cross section of the magnet highlighting the relevant elements for cold mass assembly.

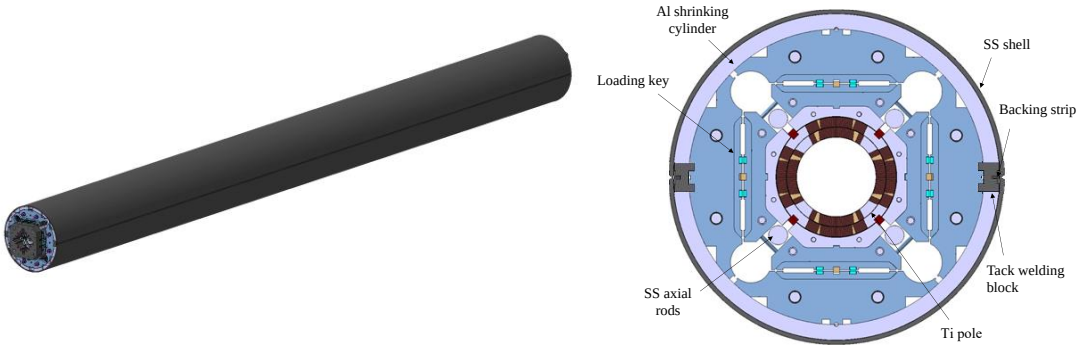

Figure 22. View of MQXFB magnet including axial support system and stainless-steel shell (left). Cross section of the MQXF magnet including stainless steel shell, backing strip and tack welding blocks.

2.4 Conclusions

The Nb_3Sn magnets for the HL-LHC are exploring an unprecedented strand current density of 700–800 A/mm^2 with an operating peak field of around 11.5 T. The overall energy density in the coil is 125 J/cm^2, almost two times the value of the LHC-MB dipoles (70 J/cm^2) with 50 % higher accumulated stress due to electromagnetic forces in the mid plane (100 MPa in the 11 T and MQXF vs 70 MPa in the LHC-MB). The protection, management of thermal contractions, dimensional tolerances, and control of pre-stress during assembly and powering are challenging. MBH-11 T and MQXF relay in very similar technology in terms of conductor strand, cable and coil fabrication. The MBH-11 T mechanical structure is based on a traditional collared structure, whereas MQXF relies on an aluminium cylinder pre-stressed at room temperature with water pressurized bladders and interference keys. After more than 20 years of development, the production of the first mini-series of Nb_3Sn accelerator-quality magnets is ongoing, paving the path towards the next generation magnets. The work presented in this thesis is focused on the magnetic performance, contributing to a better understanding of these magnets, needed to define targets for future generation accelerator magnets. The specific contribution of the author to the design of the 11 T and MQXF magnets are:

- 2D&3D electromagnetic design of MQXF coil, including iterations on the coil end-spacers geometry and update of the design with the second-generation cable.
- Fine tuning of the 11 T electromagnetic design, with the modification of the iron yoke geometry and coil length. 2D electromagnetic design with the second-generation cable.
- Design of the quench protection heater geometry both for MBH-11T and MQXF.
- Study of the magnetic, mechanical and quench protection performance analysing test results.

2.5 References

[2.1] D. Tommasini, et al., “Status of the 16 T Dipole Development Program for a Future Hadron Collider,” IEEE Transactions on Applied Supercond., vol. 28, no. 3, pp. 4001305, 2018.

[2.2] Bailey, R (ed.), “CAS - CERN Accelerator School: Course on Superconductivity for Accelerators,” Geneva CERN-2014-005, CERN Yellow Reports: School Proceedings, arXiv:1502.02950 ;

[2.3] S. Izquierdo Bermudez et al., "Mechanical analysis of the Nb_3Sn 11 T dipole short models for the High Luminosity Large Hadron Collider," Superconductor Science and Technology, July 2019, https://dx.doi.org/10.1088/1361-6668/ab1f39

[2.4] P. Ferracin, et al., "The HL-LHC Low-β Quadrupole Magnet MQXF: From Short Models to Long Prototypes," IEEE Trans. Appl. Supercond., vol. 29, no. 5, Aug. 2019, Art. no. 4001309.

[2.5] S. Izquierdo Bermudez et al., "Performance of a MQXF Nb3Sn Quadrupole Magnet Under Different Stress Level," in IEEE Transactions on Applied Superconductivity, vol. 32, no. 6, pp. 1-6, Sept. 2022, Art no. 4007106, doi: 10.1109/TASC.2022.3167369.

[2.6] P. Ferracin et al., "Assembly and Pre-Loading Specifications for the Series Production of the Nb3Sn MQXFA Quadrupole Magnets for the HL-LHC," in IEEE Transactions on Applied Superconductivity, vol. 32, no. 6, pp. 1-6, Sept. 2022, Art no. 4000306, doi: 10.1109/TASC.2022.3148971.

[2.7] J. Fleiter, A. Ballarino, A. Bonasia, B. Bordini and D. Richter, "Optimization of Nb3Sn Rutherford Cables Geometry for the High-Luminosity LHC," in IEEE Transactions on Applied Superconductivity, vol. 27, no. 4, pp. 1-5, June 2017, Art no. 4004305, doi: 10.1109/TASC.2017.2672903.

[2.8] I. Aviles Santillana, S. Sgobba et al., " Advanced Examination of Nb3Sn Coils and Conductors for the LHC Luminosity Upgrade: A Methodology Based on Computed Tomography and Materialographic Analyses", SUST-105443

[2.9] P. Wanderer, "Overview of LARP Magnet R&D," in IEEE Transactions on Applied Superconductivity, vol. 19, no. 3, pp. 1208-1211, June 2009, doi: 10.1109/TASC.2009.2017917.

[2.10] S. Caspi, " Design of a 120 mm Bore 15 T Quadrupole for the LHC Upgrade Phase II," in IEEE Transactions on Applied Superconductivity, vol. 20, no. 3, pp. 144 - 147, February 2010, doi: 10.1109/TASC.2010.2040147

[2.11] F. Borgnolutti et al., "Magnetic Design Optimization of a 150 mm Aperture Nb_3Sn Low-Beta Quadrupole for the HiLumi LHC," in IEEE Transactions on Applied Superconductivity, vol. 24, no. 3, pp. 1-5, June 2014, Art no. 4000405, doi: 10.1109/TASC.2013.2279905.

[2.12] G. Ambrosio et al., "LARP Long Nb_3Sn Quadrupole Design," in IEEE Transactions on Applied Superconductivity, vol. 18, no. 2, pp. 268-272, June 2008, doi: 10.1109/TASC.2008.922277.

[2.13] D. Bonmann, et al., "Heater-Induced Quenches in a Superconducting Hera Test Dipole", IEEE Transactions on Applied Supercond., vol. 24, no. 2, pp 1555-1558, March 1988.

[2.14] P. S. Martin, "Design and Operation of the Quench Protection System for the Fermilab Tevatron", TM-1398 1790.000.

[2.15] A. Danner, F. Sonnemann, "Review of quench simulations for the protection of LHC main dipole magnets", LHC ICP-Internal Note 00-199.

[2.16] E. Ravaioli, "CLIQ," Ph.D. dissertation, Univ. Twente, 2015

[2.17] S. Izquierdo Bermudez et al., " Analytical method for the prediction of quench initiation and development in accelerator magnets, Cryogenics, Volume 95, 2018, Pages 102-109, ISSN 0011-2275, https://doi.org/10.1016/j.cryogenics.2018.09.004.

[2.18] Rossi L 2012 J. Cryog. Supercond. Soc. Japan 47

[2.19] G. Ambrosio, "Nb3Sn High Field Magnets for the High Luminosity LHC Upgrade Project," in IEEE Transactions on Applied Superconductivity, vol. 25, no. 3, pp. 1-7, June 2015, Art no. 4002107, doi: 10.1109/TASC.2014.2367024.

[2.20] A. V. Zlobin et al., “Design and fabrication of a single-aperture 11 T Nb3Sn dipole model for LHC upgrades,” IEEE Trans. Appl. Supercond., vol. 22, no. 3, p. 4001705, 2012.
[2.21] M. Karppinen, et al., “Design of 11 T Twin-Aperture Dipole Demonstrator Magnet for LHC Upgrades”, IEEE Transactions on Applied Superconductivity, vol. 22, no. 3, 4901504, 2012.
[2.22] S. Wolff, “Superconducting magnet design”, *AIP Conference* Proceedings 249, edited by M. Month and M. Dienes, 1992, p. 1160-1197.
[2.23] M. Anerella, et al., “The RHIC magnet system“, Nucl. Instrum. Meth. A499 (2003) 280-315.
[2.24] A. Devred, “About the mechanics of SSC dipole magnet prototypes,” AIP Conference Proceedings 249, 1309 (1992); doi: 10.1063/1.41955
[2.25] T. Ogitsu, et al., “Mechanical performance of 5-cm-aperture, 15-m-long SSC dipole magnet prototypes”, IEEE Trans. Appl. Supercond., Vol. 3, No. l, March 1993, p. 686-691.
[2.26] O. Brüning, et al., LHC Design Report, Geneva: CERN, 2004. - 548 p., doi: 10.5170/CERN-2004-003-V-1.
[2.27] A. Asner et al., “First , 1 m Long superconducting dipole model magnets for LHC break the 10 tesla field threshold,” in proceedings of MT-11, Tsukuba, Japan, 1989.
[2.28] A. den Ouden et al., “An experimental 11.5 T LHC type dipole magnet,” IEEE Trans. Mag., vol. 30, p. 2320, 1994.
[2.29] B. Bordini et al., "The Bundle-Barrier PIT Wire Developed for the HiLumi LHC Project," in IEEE Transactions on Applied Superconductivity, vol. 27, no. 4, pp. 1-6, June 2017, Art no. 6000706, doi: 10.1109/TASC.2016.2640760.
[2.30] E. Nilsson et al., "Design Optimization of the Nb3Sn 11 T Dipole for the High Luminosity LHC," in IEEE Transactions on Applied Superconductivity, vol. 27, no. 4, pp. 1-5, June 2017, Art no. 4001005, doi: 10.1109/TASC.2016.2635121.
[2.31] S. Izquierdo Bermudez et al., "Second-Generation Coil Design of the Nb3Sn low-β Quadrupole for the High Luminosity LHC," in IEEE Transactions on Applied Superconductivity, vol. 26, no. 4, pp. 1-5, June 2016, Art no. 4001105, doi: 10.1109/TASC.2016.2519002.
[2.32] S. Izquierdo Bermudez et al., "Coil End Optimization of Nb_3Sn Quadrupole for the High Luminosity LHC," in IEEE Transactions on Applied Superconductivity, vol. 25, no. 3, pp. 1-4, June 2015, Art no. 4001504, doi: 10.1109/TASC.2014.2370100.
[2.33] G. De Marzi et al., "Magnetic and Electromechanical Characterization of a High-J_C RRP Wire for the HL-LHC MQXF Cable," in IEEE Transactions on Applied Superconductivity, vol. 32, no. 6, pp. 1-5, Sept. 2022, Art no. 6001505, doi: 10.1109/TASC.2022.3167655.
[2.34] P. Ferracin et al., "Mechanical Analysis of the Collaring Process of the 11 T Dipole Magnet," in IEEE Transactions on Applied Superconductivity, vol. 29, no. 5, pp. 1-5, Aug. 2019, Art no. 4002705, doi: 10.1109/TASC.2019.2899284.
[2.35] S. I. Bermudez et al., "Status of the MQXFB Nb3Sn Quadrupoles for the HL-LHC," in IEEE Transactions on Applied Superconductivity, vol. 33, no. 5, pp. 1-9, Aug. 2023, Art no. 4001209, doi: 10.1109/TASC.2023.3237503.

3 GEOMETRIC FIELD ERRORS

3.1 Introduction

In an empty space, free of any currents and magnetised materials, the magnetic field fulfils the following two Maxwell equations:

$$\vec{\nabla} \cdot \vec{\mathrm{B}} = 0, \vec{\nabla} \times \vec{\mathrm{B}} = 0 \qquad \textit{Eq. 13}$$

In the central part of a superconductor accelerator magnet, the conductors are parallel to the beam pie. Under these conditions, one can consider the magnetic field is two dimensional. Defining a complex magnetic field,

$$\vec{\mathrm{B}} = B_y + iB_x \qquad \textit{Eq. 14}$$

it can be proven than $\vec{\mathrm{B}}$ is analytical since it satisfies the Cauchy-Riemann conditions and can be expanded in a power series, obtaining,

$$B_y(x,y) + iB_x(x,y) = \sum_{n=1}^{\infty} (B_n + iA_n)(x+iy)^{n-1} \qquad \textit{Eq. 15}$$

To avoid coefficients with physical dimensions depending on the order of the multipoles, a reference radius (R_{ref}) is defined, which is typically 2/3 of the aperture. Moreover, the main component is factorized so that the normalized multipoles (b_n, a_n) become dimensionless,

$$B_y(x,y) + iB_x(x,y) = 10^{-4} B_{ref} \sum_{n=1}^{\infty} (b_n + ia_n) \left(\frac{x+iy}{R_{ref}}\right)^{n-1} \qquad \textit{Eq. 16}$$

B_{ref} is the reference field, B_1 in a dipole, B_2 in a quadrupole. For an accelerator magnet, typical acceptable field quality deviations from the ideal field are of the order of 0.01% at 2/3 of the aperture radius. This is why a 10^{-4} is also factorized, such that the normalized multipoles have values of the order of unit.

The magnetic field in $z = x + iy$ of a single current in the position $z_0 = x_0 + iy_0$ can be written, using the Biot-Savart law in complex notation

$$B(z) = \frac{\mu_0 I}{2\pi(z - z_0)}; \vec{\mathrm{B}} = B_y + iB_x \qquad \textit{Eq. 17}$$

where μ_0 is the magnetic permeability in the vacuum. The above formulation, based on complex notation, can be expressed in terms of a multipolar expansion:

$$\mathrm{B}(z) = \frac{\mu_0 I}{2\pi(z - z_0)} = -\frac{\mu_0 \mathrm{I}}{2\pi z_0}\frac{1}{\left(1 - \frac{z}{z_0}\right)} == -\frac{\mu_0 \mathrm{I}}{2\pi z_0}\sum_{n=1}^{\infty}\left(\frac{z}{z_0}\right)^{n-1} \qquad \textit{Eq. 18}$$

Comparing Eq. 16 and Eq. 18, the main field of a current line expressed in terms of multipoles are,

$$B_n + iA_n = -\frac{I\mu_0}{2\pi z_0}\left(\frac{R_{ref}}{z_0}\right)^{n-1} \qquad \textit{Eq. 19}$$

$$b_n + ia_n = -\frac{I\mu_0}{2\pi z_0}\frac{10^4}{B_{ref}}\left(\frac{R_{ref}}{z_0}\right)^{n-1} \qquad \textit{Eq. 20}$$

The requirements on field quality can be translated into the requirements on the positioning of the current lines in the cross-section; typically, the required precision for a superconducting magnet in a circular collider is of the order of 0.1 mm. The multipole variation created by a misplacement Δz_0 of the current line is given by

$$\Delta(B_n + iA_n) = \mathrm{n}\frac{I\mu_0}{2\pi z_0^2}\left(\frac{R_{ref}}{z_0}\right)^{n-1} \cdot \Delta z_0 \qquad \textit{Eq. 21}$$

and has the same power law decay as a current line. This implies that the random components of the field quality due to the position of the current lines also have a power law decay as it can be seen in Figure 23 where the random components of the measured field errors in the first MQXFB prototype magnet are compared with the decay of multipoles of a current line according to Biot-Savart law.

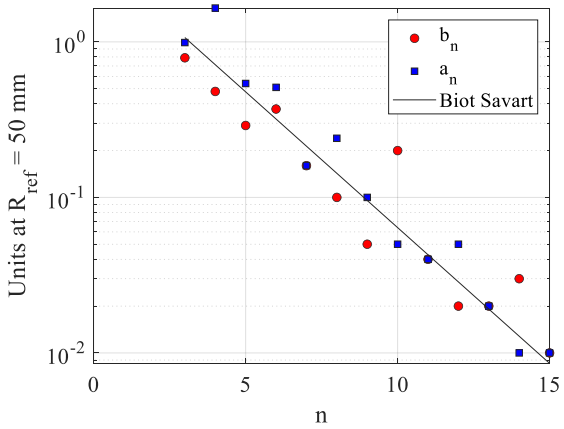

Figure 23. Random components of the measured field errors in the first MQXFB prototype magnet compared with the decay of multipoles of a current line with order plotted on a semi-logarithmic scale.

The geometric multipoles, field errors originating from misplacements of conductors, depend on the position of the coil turns at operating conditions, i.e. once assembled in the collars, enclosed in the iron yoke, cooled down to operating temperature and energized. The geometric field quality at operating conditions is mainly determined by:

- placement of the conductors as defined by the magnetic design, which is typically optimized in accelerator magnets to few units of the main field.

- accuracy on the conductor position within the coil, due to manufacturing tolerances on components and coil production process,
- the initial size of the impregnated coil and the shims used during the collaring or coil-pack assembly,
- the deformation during magnet assembly and cool-down, and
- the coil deformation under electromagnetic loading.

A change of 0.05 mm at the pole gives a change of b_3 of ~ 1.5 units in the MBH-11T dipole and a change of b_6 of ~ 2 units for the MQXF quadrupole; in both cases these changes are at the limit of the field quality requirements. A systematic offset in the position of the coil is easy to cure through a fine tuning of the cross-section. This was done in MQXF after the production of the first short model and prototype magnets, and it will be explained in section 3.5.4. On the other hand, very little can be done for the random variations of the position of the coil, which is mainly due to the reproducibility of the coil manufacturing and assembly. Random fluctuations of cable positioning can be analyzed through Monte Carlo methods [3.1]. The measurements of Nb-Ti magnets during the past 30 years have shown that this spread ranges from 0.06 to 0.01 mm ([3.2],[3.3]). These data refer to a stable production of the same object, with the number of pieces ranging from 10 to 1000. Nb_3Sn coil have a very different manufacturing process than NbTi. The conductor expands during heat treatment and the coil is at least 3 times more rigid than non-impregnated NbTi coils. Very little statistics are available for Nb_3Sn. In [3.4], a series of six 43.5 mm aperture HFDA dipoles and six 90 mm TQ quadrupoles were studied, deriving a spread of 0.13 mm for the dipoles and 0.14 mm for the quadrupoles. Nevertheless, this analysis was based in a small production of short models and HL-LHC provides the opportunity to assess the capability to control field quality in a mini-series production. This chapter will first describe the main features of Nb_3Sn coil fabrication process relevant for field quality, and assess the precision of the placement of the conductor along the magnet axis and within the coil cross section comparing the different magnets produced so far. A significant improvement is present from the short model to prototypes and series magnets, indicating the importance of having a stable production before the assessment of the reachable level of precision with a new technology. The main deformation modes during assembly are discussed, to justify the large field errors in some specific cases. Afterwards, the impact of assembly, cool down and powering is discussed to conclude with the main findings from the production monitoring.

3.2 Overall reproducibility of the coil positioning

The coil geometry is the result of assembling stacks of conductors, 20 to 35 per layer in the case of MQXF and MBH, which are produced with stringent, but not infinitely small, tolerances (in large cables the best that can be achieved nowadays is of the order of ± 0.0025 mm on the thickness) and insulated by braiding with S2 glass fiber, which can be industrially produced with a few micrometres (± 5 μm) tolerance on their thickness. Moreover, in the case of Nb_3Sn magnets, the coils undergo a heat treatment step after winding. During this stage, coils radially expand and longitudinally contract due to the Nb_3Sn phase change. In order to prevent residual strain from altering superconducting performances, the tooling must provide the adequate space for these dimensional changes. An overall volume dilatation during reaction of about 4 % has been observed for unconstrained strands. However, in Rutherford cables, the compaction of the strands, the remaining stress, the friction between strands and with the surrounding insulation, can lead to different longitudinal contractions. For instance, the fiber-glass sleeves are potentially looser than fiberglass tightly braided on the cables, allowing the cable to

expand more transversally and contract more longitudinally [3.5]. Inside coils, the conditions are even more stringent. Since it was suggested in previous projects that the transversal over-compaction was a potential cause of degraded performances [3.6], conservative assumptions were taken for the design of the reaction tooling to let the cable expand during reaction. MBH assumed 4.5 % expansion in thickness and 1 % in width. The same 4.5 % expansion in thickness was assumed for MQXF design, and 2.1 % in width. Measurements of coil cross sections were taken from the first MQXF practice coils. Different analysis methods show very consistent results for the two coils, with a thickness expansion of about 3.0% and only 0.15% expansion in width. As a consequence, conductors are aligned on the outer diameter and the ≈ 600 μm of free radial space due to the overestimation in cable width expansion are filled with epoxy in a non-uniform way (see Figure 24), which will have a negative impact on field quality.

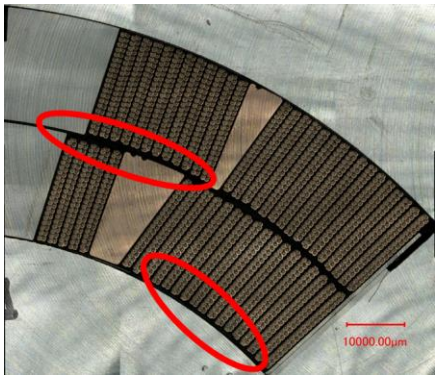

Figure 24. Image of an MQXF coil cross section showing free radial space in the radial dimension due to the overestimation in cable width expansion in the first-generation design.

Based on this analysis, and in order to find the best compromise between performance and field quality, it was decided in the second generation MQXF coil design to: 1) reduce the radial space in the tooling to accommodate for a cable width expansion of 1.2% instead of 2%; 2) keep the same azimuthal space, corresponding to a thickness expansion of 4.5%. Table 11 summarizes the average dimensional changes of the conductor assumed for the design of the reaction and impregnation tooling in MQXF and MBH-11T coils. For the case of the 11 T, the target insulation thickness was 0.1 mm but the measured insulation thickness at 5 MPa was 130 - 135 μm for the first coils, which translates to an over-thickness per coil quadrant in the azimuthal direction of 2 mm in the outer layer and 1.3 mm in the inner layer. This over-thickness resulted in difficulties in closing the heat treatment and vacuum impregnation molds and in the observations of large coil spring back at the opening of the heat treatment mold. The effective room for expansion for the conductor during heat treatment was -0.8 % due to the insulation over-thickness. The insulation parameters were optimized in 2018 to leave sufficient space to the conductor during reaction [3.7]. From these examples one can understand how difficult is to obtain in superconducting magnets a field quality comparable to that of classical lower field magnets, where the field distribution is determined by the iron-pole profiles which can be produced with a hundredth-millimetre precision. The problem of expansion during heat treatment is intrinsic to Nb_3Sn technology and it was not present in NbTi accelerator magnets.

Table 11. Average dimensional changes of the conductor assumed for the design of the reaction and impregnation tooling

	Thickness [%]	Width [%]
MBH-11 T 1st Generation Design, old insulation	-0.8	0.6
MBH-11 T 1st Generation, new insulation	4.5	1
MQXF 1st Generation Design	4.5	2.1
MQXF 2nd Generation Design	4.5	1.2

After impregnation, the geometry of each coil is measured. The deviation of the azimuthal dimensions with respect to the nominal values is estimated by aligning the data on the nominal outer radius (60.8 mm for MBH and 113.376 mm for MQXF) [3.8]. In Figure 25, the azimuthal deviations (left + right mid-plane) of the MBH and MQXF short model coils with respect to nominal dimensions are given in the form of a box plot: the horizontal lines indicate the minimum, the 25% percentile, the median, the 75% percentile, and the maximum deviations of the measurements performed on each coil. The median ranges from 0.1 mm to 0.6 mm and -0.4 to 0.3 mm in MBHS and MQXFS coils, respectively. For the case of the MBH-11T, the conductor insulation thickness was ≈ 0.135 mm in coils 106-117. After the optimization of the insulation parameters to reach the ≈ 0.100 mm target thickness, coil azimuthal size was closer to nominal, with a significant reduction of the spread of coil azimuthal size along the length, with the exception of coil 119 where the impregnation fixture was not correctly closed before impregnation. Reaching a 0.1 mm control on the azimuthal coil size is one of the main challenges for Nb_3Sn. For series production long coils, the average size and variation along the straight section length stabilized to ± 0.125 mm. Figure 26 shows the azimuthal coil size deviation for MBH coils, with a great improvement from the prototype to the series coils mainly driven by the reduction of the insulation thickness by ≈ 30 μm ([3.7]). In MQXFB program, the coil size stabilizes after the production of eight coils (see Figure 27).

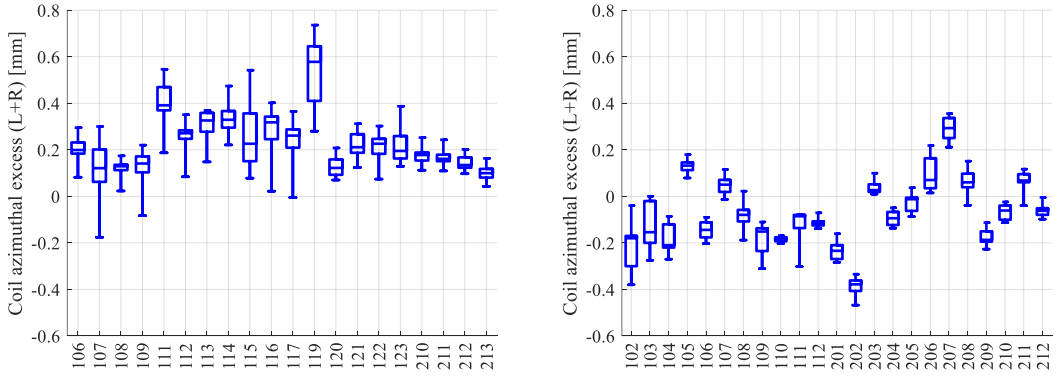

Figure 25 Azimuthal coil size deviation (left + right mid-plane) with respect to nominal dimension for MBHS-11 T (left) and MQXFS (right) short model coils.

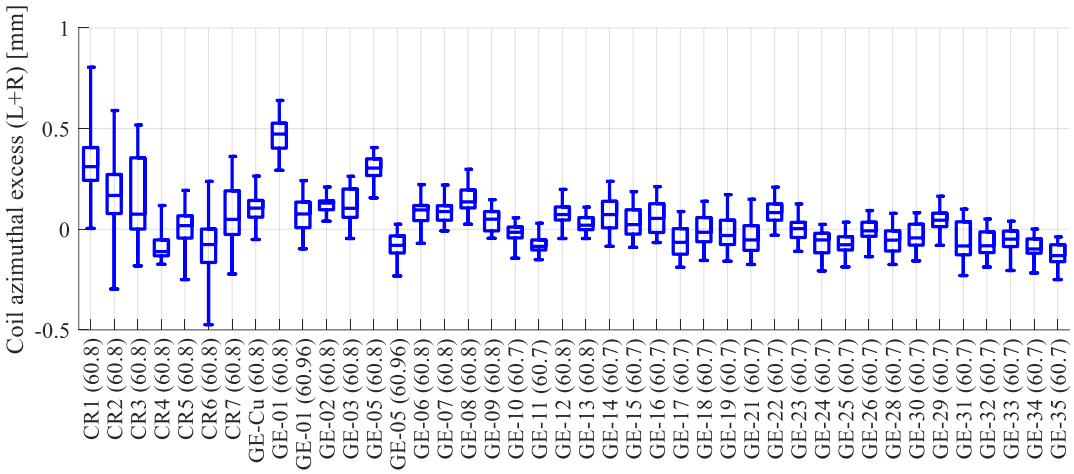

Figure 26 Azimuthal coil size deviation (left + right mid-plane) with respect to nominal dimension for MBH-11 T prototype (CR) and series (GE) coils.

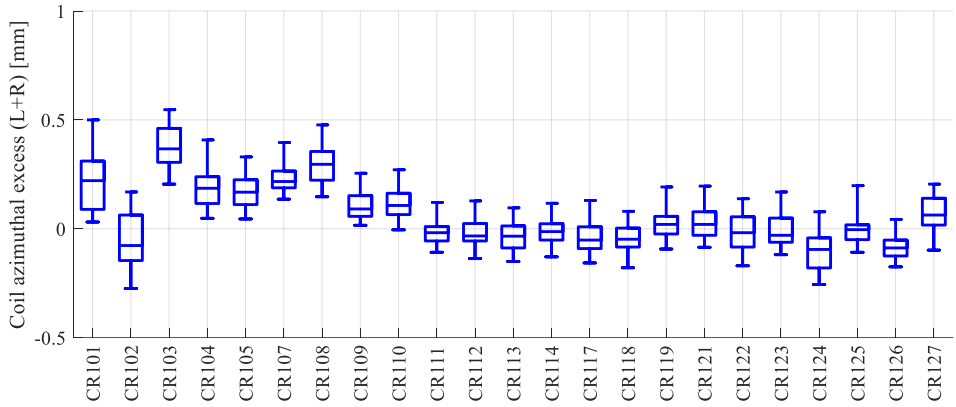

Figure 27. Azimuthal coil size deviation (left + right mid-plane) with respect to nominal dimension for MQXFB coils.

The spread on the harmonics along the magnet length can be used to derive the accuracy of the positioning of the turns in the coil, using the Monte-Carlo approach described in [3.1]. The coil blocks are assumed to be rigid bodies, characterized by three degrees of freedom: the radial displacement (r), the angular displacement (Φ) and the coil block rotation (α).

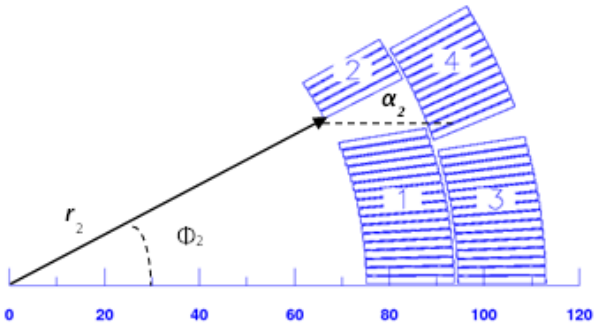

Figure 28. One octant of MQXF coil block (x-dimension in mm) including the degrees of freedom definition for random coil block displacements

A random displacement with rms amplitude d is equally shared by the block degrees of freedom, with an average displacement of zero and a rms of $d/\sqrt{3}$:

- Radial displacement. $r_{min} = r - d$ and $r_{max} = r + d$.
- Angular displacement. $\Delta\varphi = d / (r + w_{cable}/2)$. $\varphi_{min} = \varphi - \Delta\varphi$ and $\varphi_{max} = \varphi + \Delta\varphi$.
- Coil block rotation. $\Delta\alpha = 2d / w_{cable}$. $\alpha_{min} = \alpha - \Delta\alpha$ and $\alpha_{max} = \alpha + \Delta\alpha$.

The resulting rms of the coil blocks displacements is d:

$$\sigma_b = \sqrt{\sigma_r^2 + \sigma_\varphi^2 + \sigma_\alpha^2} = d, \text{ where } \sigma_r = \frac{d}{\sqrt{3}}, \sigma_\varphi = \frac{d}{\sqrt{3}}, \sigma_\alpha = \frac{d}{\sqrt{3}}.$$

Once such random movements are assigned to the cross-section, the magnetic field is computed for this new configuration. The simulation is repeated for 100–1000 cases, and an average $\mu_n(d)$ and standard deviation $\sigma_n(d)$ of the field harmonics is estimated for a given amplitude d. The standard deviation represents the impact of the spread of the coil position on the field harmonics. The spread in the multipoles is proportional to the spread in the position d and decays with the multiple order n as $(R_{ref}/r)^n$. The sigma obtained for a Monte-Carlo analysis on the MQXF coil cross section for an amplitude of displacement of d = 0.03 mm, d = 0.05 mm and d = 0.10 mm is shown in Figure 29. The numerical data can be fitted using a simple power law. The fitting constant for different values of the amplitude rms d are given in Table 12.

$$\sigma_n(d) = d\alpha\beta^n \qquad \textit{Eq. 22}$$

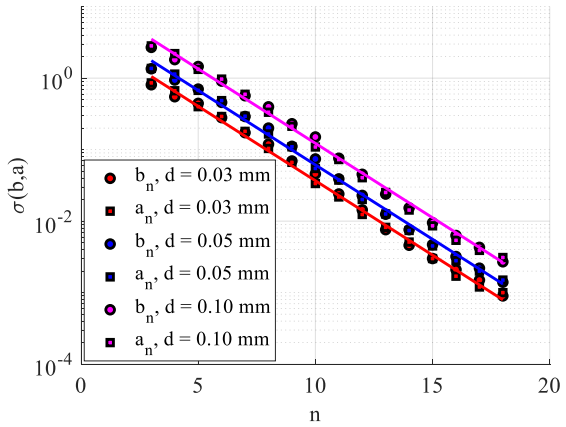

Figure 29. Numerical estimate (markers) and fit (solid line) of the geometric random multipoles due to random block displacement of amplitudes d for the four-block MQXF coil.

Table 12. Fitting constants α and β for random multipoles generated by random block displacements for MQXF quadrupole.

d (mm)	α (mm^{-1})	β
0.10	150.4	0.6175
0.05	149.8	0.6182
0.03	145.2	0.6219
Average	148.5	0.6192

MQXFB magnets are measured along 13 consecutive positions with a 0.6 m rotating coil. The first and last are discarded in this analysis because they cover the ends. The rms of the 11 data points along the magnet axis in MQXFB prototypes and first series are shown in Figure 30, which can be fitted with a rigid random displacement of blocks with rms of 0.04 mm. Short model magnets were measured with 0.130 mm length probes. The derived displacement of the blocks is d = 0.03 mm.

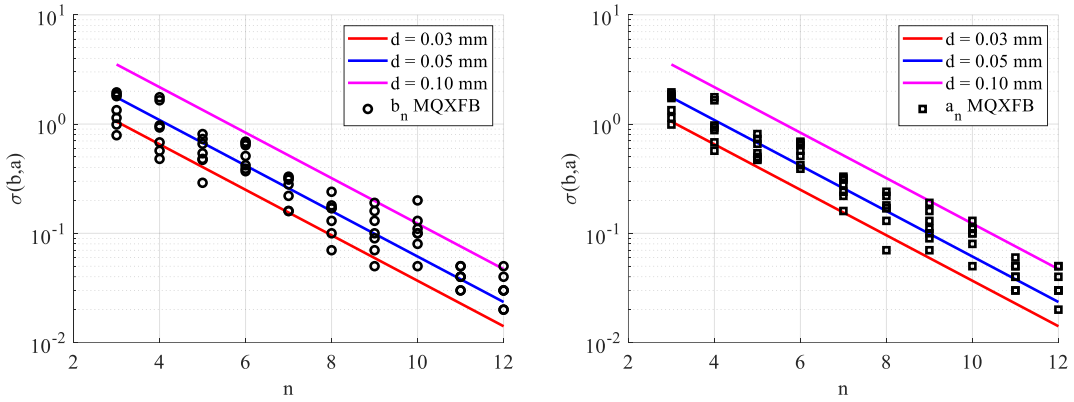

Figure 30. rms of the multipoles along the axis for MQXFBP1, BP2, BP3 and B02 and scaling law for different amplitudes of random displacements d (solid line). The plot on the left represents the normal multipoles and the plot on the right the skew multipoles.

The same approach can be used for a dipole, using the fitting equation 23 [3.1]. The nonlinear term γ^{n^2} provides a correction to the power law that gives a faster decrease of the higher order terms. In general, the larger the blocks, the faster the reduction of the high order multipoles with respect to the power law. Figure 31 shows the numerical estimate (markers) and fit (solid line) of the geometric random multipoles due to random block displacement of amplitudes d for the MBH coil. The fitting parameters are α = 90 mm^{-1}, β = 0.59 and $\gamma = 0.993$. The rms of the harmonics along the axis of MBH-11T series collared coils (11 collared coils were built so far) is shown in Figure 32. The magnet is measured using eight 0.75-m-long segments, so the magnet straight section is covered with six rotating coils. For harmonic orders n>8 the measurements flatten, the data no longer follow the Biot-Savart decay, which is an indication of reaching the measurement precision. Experimental data are consistent with rigid random displacements of blocks with rms of 0.039 mm, consistent with the findings in MQXFB and slightly larger than the value found in [3.1] for the LHC-MB dipoles where the estimate of the reproducibility on the coil positioning along the magnet axis was 0.025 mm. The short model magnets were measured using a 0.130 mm probe and the estimate of the reproducibility on the coil positioning along the axis is 0.050 mm.

$$\sigma_n(d) = d\alpha\beta^n\gamma^{n^2} \qquad \textit{Eq. 23}$$

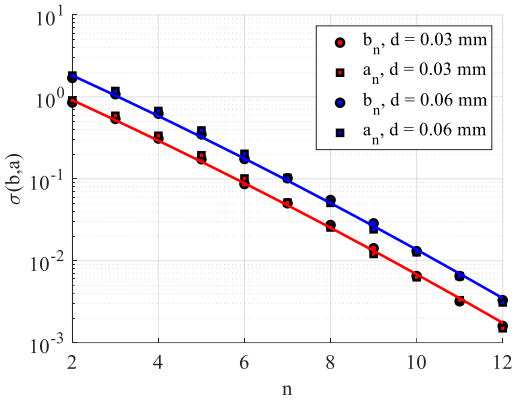

Figure 31. Numerical estimate (markers) and fit (solid line) of the geometric random multipoles due to random block displacement of amplitudes d for the MBH coil.

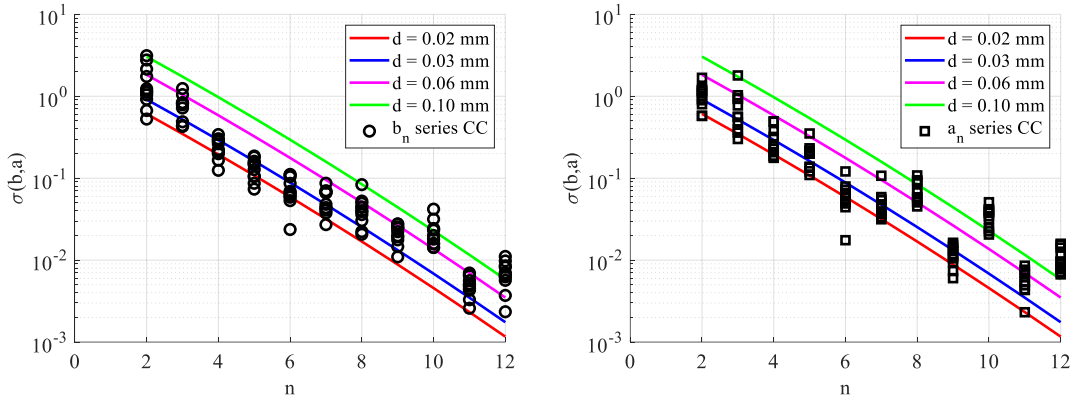

Figure 32. rms of the multipoles along the axis for the 11 MBH series collared coils and scaling law for different amplitudes of random displacements d (solid line).

The estimate of the reproducibility of the coil positioning along the axis for the LHC-MB NbTi dipoles and the Nb_3Sn magnets for the HL-LHC is shown in Table 13. The 0.025 mm of accuracy in the NbTi main bending dipoles is close to the 0.030 – 0.050 mm found in MQXF and MBH-11T. It is important to point out that we are comparing a production of a stable series production of a well-stablished technology with a new technology used in few magnets, so the results are very encouraging for Nb_3Sn technology.

Table 13. Estimate on the reproducibility of the coil positioning along the axis, including the information of the number of apertures analyzed, the length of the rotating coil and the magnet length

	# Apertures	L_{probe} (m)	$L_{magnetic}$ (m)	d (mm)
LHC-MB dipoles [3.1]	-	0.60	14.3	0.025
MBH (series)	11	0.75	5.3	0.039
MBHS (short models)	5	0.13	1.7	0.050
MQXFS (short models)	7	0.13	1.2	0.030
MQXFB (prototypes and series)	4	0.5/0.6	7.2	0.040
TQ [3.4]	4	0.10	0.8	0.047

The same analysis can be used to assess the reproducibility of the coil positioning over the production. Given a set of magnets, the spread in the measured multipoles can be interpreted as a spread in the position of the coil using the Monte-Carlo simulation described before. The measurements of Nb-Ti magnets during the past 30 years have shown that this spread ranges from 0.06 to 0.01 mm (one sigma). These data refer to a stable production of the same object, with the number of pieces ranging from 10 to 1000. Figure 33 shows the measured harmonics after loading at room temperature in MQXFS and MQXFB magnets compared with the target field quality which assumes a random distribution of the coil blocks of d=0.030 mm for the non-allowed harmonics and d = 0.060 mm for the allowed harmonics. A very remarkable improvement can be appreciated from the short models, where the different parameters are being optimized, and the stable production for the long MQXFB magnets. The measured integral harmonics after collaring at room temperature in MBH series collared coils are shown in Figure 34. Measurements show a systematic b_3 of 5.7 units (deformation due to collaring, see next chapter) that was not corrected along the production in order to have a better share of the sextupole component between injection and nominal energy due to the persistent current effects (see Chapter 5).

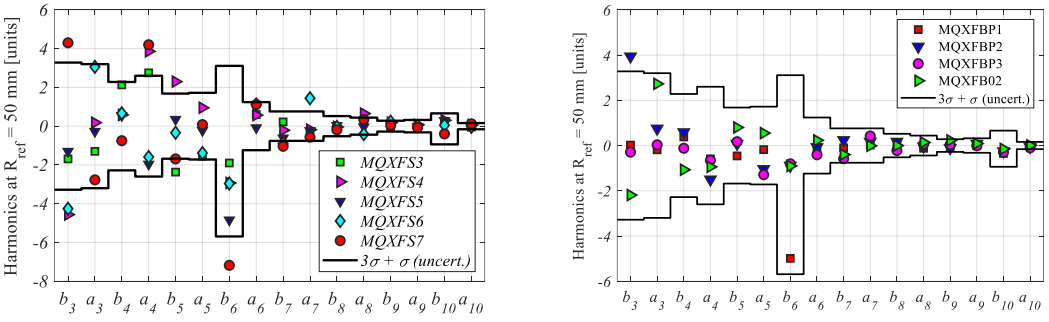

Figure 33. Harmonics after loading at room temperature in MQXFS and MQXFB magnets compared with target field quality which assumes a random distribution of the coil blocks of d=0.030 mm for the non-allowed harmonics and d = 0.060 mm for the allowed harmonics.

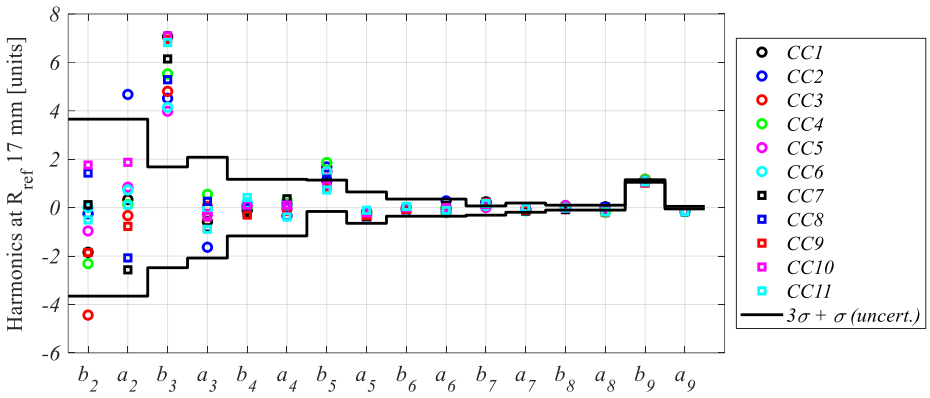

Figure 34. Integral harmonics after collaring at room temperature in MBH series collared coils compared with target field quality which assumes a random distribution of the coil blocks of d=0.030 mm.

The random movements are not equally spread along the different degrees of freedom: one systematically observes that the spread in odd normal multipoles is 2–3 times larger than in the skew, and vice versa for the even ones ([3.1]-[3.3]). In Table 14, the spread of the integral harmonics measured over the production of Tevatron, HERA, RHIC and LHC [3.9] is compared to the spread in the six Nb_3Sn High Field Dipoles (HFD) built in FNAL [3.4] and the MBH short models (MBHS, 8 apertures) and series (MBH, 11 apertures) collared coils. The estimate spread of the coil positioning on MBHS short magnets is 0.209 mm, almost 2 times larger than the obtained for HFDA. The MBHS magnets use different pole shims to optimize the pre-stress, and different radial insulation in the coil outer radius to optimize the quench heater performance, which introduce a large spread among magnets. This will be treated in detail in Section 3.3. For the series collared coils, the spread is 0.057 mm, similar than the one obtained for the Tevatron and HERA dipoles and about 2 times larger than the LHC. Here, we have to point out that we are comparing a stable series production of a well-established technology with a new technology used in a few magnets, showing that Nb_3Sn can target the same requirements in terms of geometric field errors than NbTi magnets, in spite of the aforementioned challenges.

Table 14. Estimate of the reproducibility of the coil positioning in the production of superconducting dipoles (d in mm), average values and split among the different multipole families.

	b_{2n+1}	$b_{2(n+1)}$	a_{2n+1}	$a_{2(n+1)}$	all
Tevatron	0.128	0.052	0.070	0.052	0.065
HERA	0.122	0.020	0.024	0.058	0.041
RHIC	0.052	0.006	0.008	0.032	0.016
LHC-MB	0.054	0.001	0.018	0.026	0.025
HFDA	0.274	0.124	0.047	0.180	0.130
MBHS	0.274	0.144	0.176	0.263	0.209
MBH	0.099	0.054	0.032	0.054	0.057

For the MQXF quadrupoles, the estimate of the spread in coil positioning is 0.079 mm for the short model magnets (5 magnets), a factor 2 times better than the TQ Nb_3Sn quadrupoles [3.4] and 3 times worse than the LHC MQ. In the long MQXFB magnets (4 magnets) the estimated spread is 0.040 mm, only 25 % worse than the LHC MQ. Table 15 summarizes the estimate of reproducibility of the coil positioning for different superconductor quadrupoles.

Table 15. Estimate of the reproducibility of the coil positioning in the production of superconducting quadrupoles (d in mm).

Magnet	d (mm)	Magnet	d (mm)
RHIC MQ	0.022	LHC MQXB	0.016
RHIC MQY	0.018	TQ	0.144
LHC MQ	0.029	MQXFS	0.079
LHC MQY	0.025	MQXFB	0.040
LHC MQXA	0.010		

For completeness, Figure 35 shows the standard deviation of the measured multipoles in the 5 MQXFS, 6 MQXFB, 9 MBHS and 11 MBH. For MQXFBP1, b_6 is corrected to account for the change on cross section to compute the standard deviation among magnets, with a remarkable low spread of b_6 among magnets. Data is compared to the scaling law for different amplitudes of random displacement of the coil blocks. The spread of the integral harmonics over a set of magnets will be the sum of the spread along the axis, plus the spread from coil to coil. For example, in the LHC 14.3-m-long dipoles the spread along the axis measured with 125-mm-long mole correspond to about 0.030 mm of spread in the coil position. In the hypothesis of a Gaussian distribution of the spreads along the axis, this gives a negligible contribution (about 0.003 mm) to the spread along 14.3 m. For a 1-m-long model of the LHC dipole, the contribution of the spread along the axis would be 0.012 mm, i.e. still small but not negligible w.r.t. 0.025 mm spread from coil to coil.

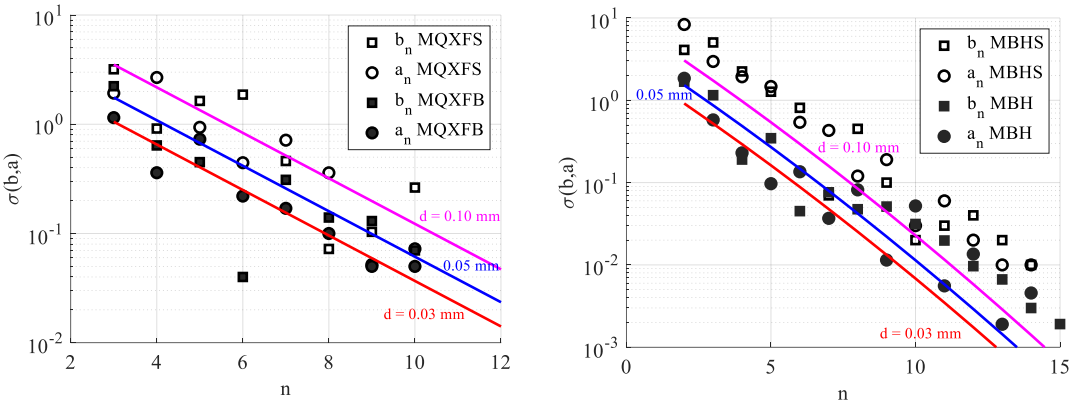

Figure 35. rms of the multipoles for the MQXFS (5 apertures), MQXFB (4 apertures), MBHS (8 apertures) and MBH (11 apertures) production and scaling law for different amplitudes of random displacements d (solid line).

3.3 Analysis of field errors due to coil fabrication and assembly

The previous section put in evidence the significant improvement in terms of field quality when going from short models, where coil and pre-load parameters are being optimized, to series production. This section describes the expected impact on field quality of the different deformation modes and validates the computation with examples from production. MQXF and MBH magnets rely on a different pre-load concept. In the case of the MBH, the pre-load results mainly from the interference of a removable pole, made up of titanium, with the coil package, which consists of the coil and of lateral stainless-steel shims of adjustable thickness. The coil package is enclosed in the fixed cavity imposed by the shape of the stainless-steel collars. Non-nominal shim sizes are applied when coil

size difference from nominal is larger than 0.025-0.050 mm to achieve uniform pre-load. Magnetic measurements are performed after collaring, meaning that at the stage of the measurements the main pre-load is already applied. In MQXF, the coils are not enclosed in a cavity and the pre-load results from the interference of the yoke loading keys and the shrinkage of the external aluminium shell. For more details, see Chapter 2. In MQXF, magnetic measurements are performed after bolting, when the coils are not pre-loaded, after centring the coil pack in the yoke-shell subassembly and once the loading keys are inserted.

As explained in previous sections, coil displacement results in a change of geometric multipoles. For small amplitude of a deformation *d*, the multipoles changes are linearly dependent on the amplitude, i.e.:

$$\Delta b_n^{m,q}(d) = \delta b_n^{m,q}(d)\ d$$
$$\Delta a_n^{m,q}(d) = \delta a_n^{m,q}(d)\ d$$

where the coefficients $\delta b_n^{m,q}$ and $\delta a_n^{m,q}$ represent the *Jacobian coefficients* of the change in normal and skew multipoles with respect to the amplitude of the deformation mode *m* considered. In order to achieve a general result, the calculations are quadrant by quadrant in the case of a dipole (*q*), octant by octant for a quadrupole, i.e. neglecting any symmetry in the magnet for the modes of deformation described in the following sections. Once the Jacobians of a mode are computed for the first quadrant, it is then possible to derive the Jacobians for the same mode applied to the other quadrants of the coil using symmetry rules. In this section, the main deformation modes during assembly of MBH and MQXF coils are described, providing examples to assess the impact of the deformations in field errors.

3.3.1 Coil deformation modes in MBH

The coil displacement modes considered for a MBH collared coil are shown in Figure 36. The first two modes correspond to the change of azimuthal coil length as caused by a pole shim or a midplane shim. The third mode describes the effect of a pure radial compression, and the fourth mode corresponds to an elliptic deformation of the coil, as would result from a deformation of the collars under the collaring load.

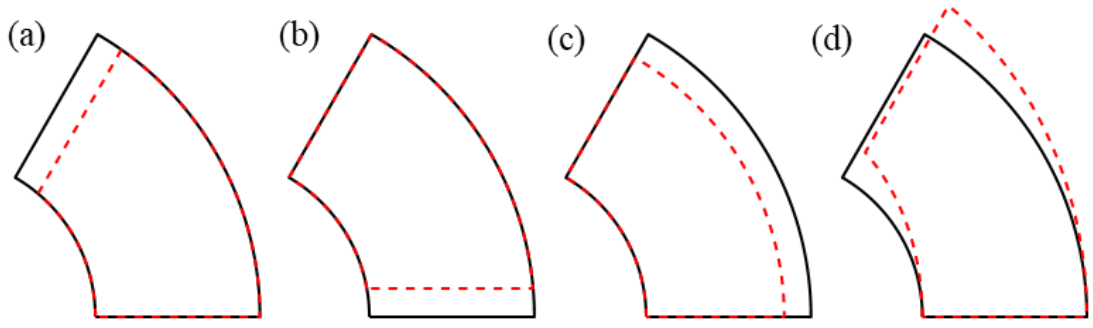

Figure 36. Coil displacement modes in MBH. (a) mode 1, compression at the pole surface; (b) mode 2, compression at the midplane; (c) mode 3, compression on the outer contour; (d) mode 4, elliptic collaring deformation. The mode amplitude is considered positive in the direction indicated by the arrows.

The Jacobian coefficient for each deformation mode is computed in ROXIE. Deformation associated with modes 1 and 2 (pole and midplane shims) is assumed to take place in the cable insulation only, meaning that the change of azimuthal side is uniformly distributed among the cables reducing the thickness of the insulation, keeping the wedge and bare cable size constant. For mode 3, the deformation is assumed to take place in the conductor

insulation and inter-layer insulation. For mode 4, the inner edge of the conductor is placed in an elliptical aperture instead of a round aperture. The multipole Jacobians are given in Table 16 and Table 17 per 1 mm of coil deformation applied to the first quadrant of a dipole aperture.

Table 16. The normal multipole Jacobian in units at a reference radius of 17 mm per 1 mm of coil deformation for the modes considered here applied to quadrant 1.

Mode	δb_1	δb_2	δb_3	δb_4	δb_5
1	19.38	20.00	6.95	-0.11	-0.67
2	-13.23	-17.53	-11.80	-5.88	-2.62
3	16.68	-0.38	-3.29	-1.14	0.07
4	-12.35	5.41	8.58	3.16	-0.24

Table 17. The skew multipole Jacobian in units at a reference radius of 17 mm per 1 mm of coil deformation for the modes considered here applied to quadrant 1.

Mode	δa_1	δa_2	δa_3	δa_4	δa_5
1	20.30	0.61	-6.73	-3.52	-0.48
2	-34.37	-19.97	-7.16	-1.99	-0.58
3	-26.78	-16.86	-4.74	-0.42	0.01
4	19.81	16.36	2.97	-2.38	-1.45

The Jacobians for the same mode applied to the other quadrants of the coil can be derived using the symmetry rules reported in Table 18. The symmetries are reflections, whose sign depend on the symmetry of the mode and on the type and order of the multipole generated. Using the symmetry rules, it is also possible to compute the multipoles generated by deformation modes that do not have mirror symmetry in the four quadrants. In the following sections, specific cases in the MBH will be discussed, including the experience from the short model program and the series construction.

Table 18. Symmetry rules for odd and even, normal and skew multipoles (n=0...∞) generated by the modes considered here and applied to the four quadrants of a dipole coil. The modes for quadrants 2,3 and 4 are intended as obtained by mirror symmetry of the mode in the first quadrant. A "+" entry in the table means that the multipole generated has the same signs as the one computed for the first quadrant, a "-" entry means that the multipole generated in the quadrant has the same amplitude as the one computed for the first quadrant, but inverted sign.

Quadrant	b_{2n+1}	a_{2n+1}	$b_{2(n+1)}$	$a_{2(n+1)}$
1	+	+	+	+
2	+	-	-	+
3	+	+	-	-
4	+	-	+	-

3.3.1.1 Correlation between field harmonics and pole shift (deformation mode 1)

In case the same deformation mode 1 is applied to all the quadrants, in this specific case a change of the pole shimming, the resulting Jacobians are as follows:

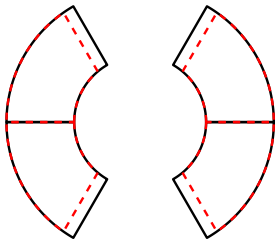

$$\boldsymbol{\delta b^{m}_{2n+1} = \delta b^{1,1}_{2n+1} + \delta b^{1,2}_{2n+1} + \delta b^{1,3}_{2n+1} + \delta b^{1,4}_{2n+1} = 4\delta b^{1,1}_{2n+1}}$$

$$\boldsymbol{\delta a^{m}_{2n+1} = \delta a^{1,1}_{2n+1} + \delta a^{1,2}_{2n+1} + \delta a^{1,3}_{2n+1} + \delta a^{1,4}_{2n+1} = 0}$$

$$\boldsymbol{\delta b^{m}_{2(n+1)} = \delta b^{1,1}_{2(n+1)} + \delta b^{1,2}_{2(n+1)} + \delta b^{1,3}_{2(n+1)} + \delta b^{1,4}_{2(n+1)} = 0}$$

$$\boldsymbol{\delta a^{m}_{2(n+1)} = \delta a^{1,1}_{2(n+1)} + \delta a^{1,2}_{2(n+1)} + \delta a^{1,3}_{2(n+1)} + \delta a^{1,4}_{2(n+1)} = 0}$$

The deformed coil geometry still respects the initial dipole symmetry, and therefore only allowed multipoles are generated. The result is reported in Table 19 and Table 20. A 0.1 mm pole shim generates 2.8 units of b_3 and -0.7 units of b_5.

Table 19. The normal multipole Jacobian in units at a reference radius of 17 mm per 1 mm of pole shim applied in the four quadrants.

δb_1	δb_2	δb_3	δb_4	δb_5	δb_6	δb_7
77.53	0.00	27.78	0.00	-2.68	0.00	0.46

Table 20. The skew multipole Jacobian in units at a reference radius of 17 mm per 1 mm of pole shim applied in the four quadrants.

δa_1	δa_2	δa_3	δa_4	δa_5	δa_6	δa_7
0.00	0.00	0.00	0.00	0.00	0.00	0.00

In order to understand the impact of the pole shim in the multipoles, we study the collared coil aperture SP105b, where the coils assembled and tested in SP105 were re-collared with a 0.05 mm thinner shim in the pole. Measurements show a decrease of 1.2 units of the sextupole, close to the 1.4 units predicted by the Jacobian (see Table 21).

Table 21. Measured and predicted change of the allowed multipoles for a 0.05 mm decrease of the pole shims, symmetrically applied in all the quadrants of the aperture.

		b_3	b_5
Measured	SP105	-4.11	1.14
	SP105b	-5.31	1.39
	Δ (SP105b- SP105)	-1.20	0.25
Predicted Δ for -0.05 pole shim		-1.39	0.13

In the 11 T dipole the stress sensitive Nb_3Sn conductor operates with both high stresses on the mid plane and nearly no compression at the pole when powered. Through the short model program, it has become clear that there is a risk of over compressing the coils during the collaring procedure. Measurements on conductor samples, which have been submitted to room temperature transverse stress cycles representative of what they experience during the collaring process have shown that performance degradation starts to occur when exceeding 150 MPa. The risk has been minimized by a revisited collaring procedure and a reduced target excess, ensuring that the coils are assembled without over compressing the conductor [3.10]. In order to cope with the variation of the azimuthal size along the coil length, in the series collared coils the pole shims have variable thickness along the length with a granularity of 0.025 mm. Right and left limb of the coil pack has different dimensions, which is compensated with different pole shim thickness in the two sides (top/bottom symmetric) in order to have the same level of pre-stress. Figure 37 shows the coil quadrant azimuthal excess, coil pack azimuthal excess and pole shim thickness for the right and left limb of the first series collared coil aperture.

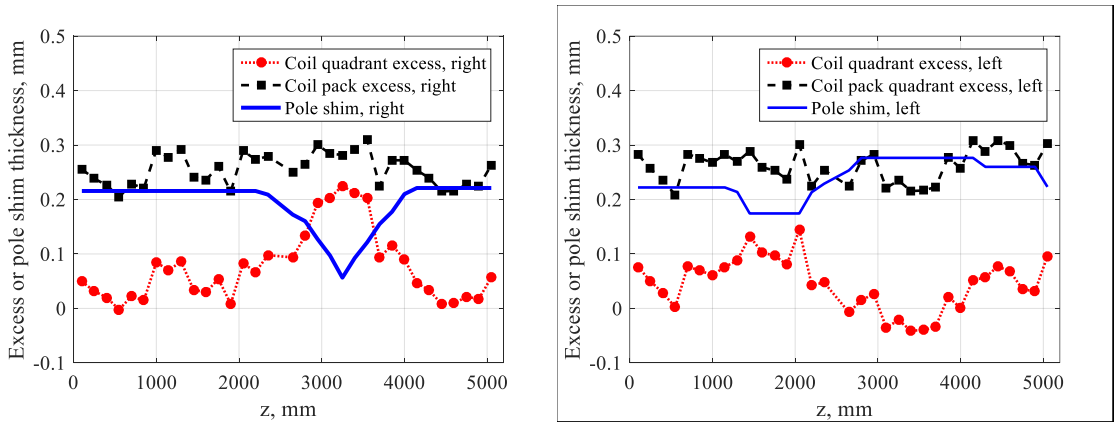

Figure 37. Coil quadrant excess, coil pack excess and pole shim thickness for the right and left limb of the first series collared coil.

The associated deformation mode is top/bottom symmetric and right/left antisymmetric. In this case the composition rule is the following:

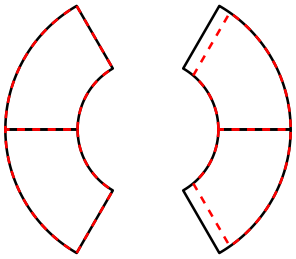

$$\delta b^{m}_{2n+1} = \delta b^{1,1}_{2n+1} + \delta b^{1,4}_{2n+1} = 2\delta b^{1,1}_{2n+1}$$

$$\delta a^{m}_{2n+1} = \delta a^{1,1}_{2n+1} + \delta a^{1,4}_{2n+1} = 0$$

$$\delta b^{m}_{2(n+1)} = \delta b^{1,1}_{2(n+1)} + \delta b^{1,4}_{2(n+1)} = 2\delta b^{1,1}_{2(n+1)}$$

$$\delta a^{m}_{2(n+1)} = \delta a^{1,1}_{2(n+1)} + \delta a^{1,4}_{2(n+1)} = 0$$

The resulting Jacobian for this case, in units at 17 mm per 1 mm left-right asymmetry in the pole shim thickness is shown in Table 22 and Table 23. In Figure 38 shows the expected variation of the normal quadrupole and sextupole components along the collared coil length for the left right asymmetry on the pole shims installed in the first series collared coil and the measured multipoles. The same variation is shown in Figure 39 for the third series collared coil aperture. The expected effect of 0.2 mm of left-right asymmetry in the pole shim is 8 units of b_2, closed to the measured value. In order to quantify the impact on b_3, both the coil quadrant excess (see section 3.3.1.1) and the left-right asymmetry has to be taken into account. In relax state and assuming perfect conductor placing in the coil cross-section, the expected b_3 is -0.4 units. The average coil quadrant excess in this specific collared coil is 0.250 mm, which corresponds to 7 units

of b_3 (see Table 19). A right-left asymmetry on the pole shim of 0.2 mm is expected to generate 2.8 units of b_3. The measured effect is about half of this value.

Table 22. The normal multipole Jacobian in units at a reference radius of 17 mm per 1 mm left-right asymmetry of the pole shim (top/bottom symmetric).

δb_1	δb_2	δb_3	δb_4	δb_5	δb_6	δb_7
38.76	40.00	13.89	-0.23	-1.34	0.11	0.23

Table 23. The skew multipole Jacobian in units at a reference radius of 17 mm per 1 mm left-right asymmetry of the pole shim (top/bottom symmetric).

δa_1	δa_2	δa_3	δa_4	δa_5	δa_6	δa_7
0.00	0.00	0.00	0.00	0.00	0.00	0.00

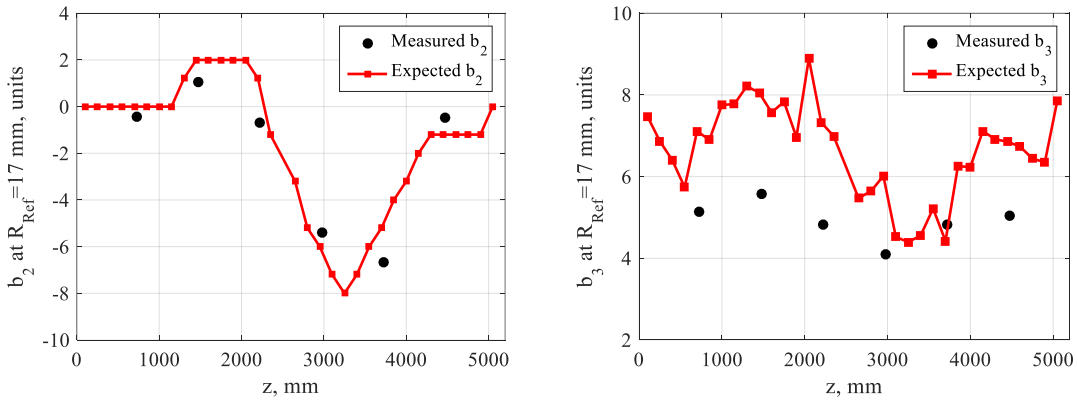

Figure 38. Measured and expected normal quadrupole and sextupole components along the collared coil length for the left right asymmetry on the pole shims installed in the first series collared coil.

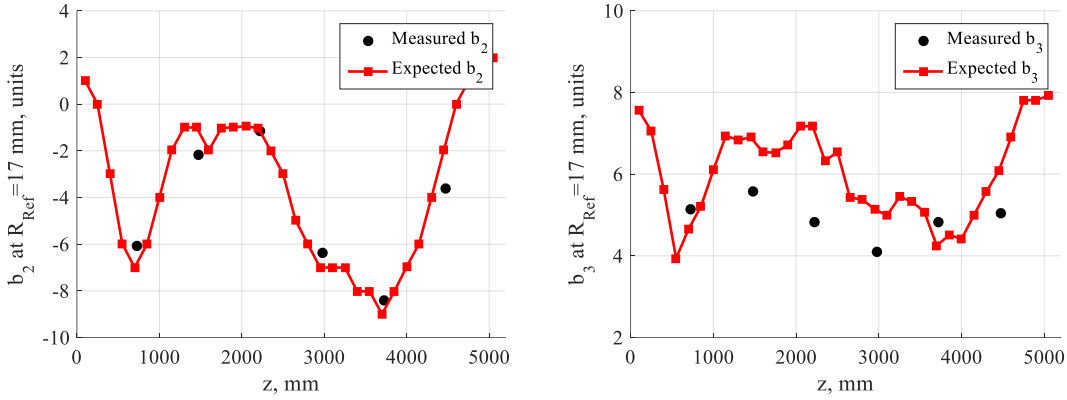

Figure 39. Measured and expected normal quadrupole and sextupole components along the collared coil length for the left right asymmetry on the pole shims installed in the third series collared coil.

3.3.1.2 Correlation between field harmonics and mid-plane shift (deformation mode 2)

Different coil sizes in the upper and lower pole of a collared coil aperture, with a top bottom symmetric pole shim result in a shift of the coil midplane. The composition rule and the resulting Jacobian (Table 24 and Table 25) are:

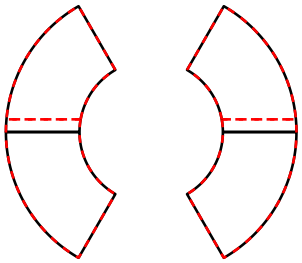

$$\delta b^{m}_{2n+1} = \delta b^{2,1}_{2n+1} + \delta b^{2,2}_{2n+1} - \delta b^{2,3}_{2n+1} - \delta b^{2,4}_{2n+1} = 0$$

$$\delta a^{m}_{2n+1} = \delta a^{2,1}_{2n+1} + \delta a^{2,2}_{2n+1} - \delta a^{2,3}_{2n+1} - \delta a^{2,4}_{2n+1} = 0$$

$$\delta b^{m}_{2(n+1)} = \delta b^{2,1}_{2(n+1)} + \delta b^{2,2}_{2(n+1)} - \delta b^{2,3}_{2(n+1)} - \delta b^{2,4}_{2(n+1)} = 0$$

$$\delta a^{m}_{2(n+1)} = \delta a^{2,1}_{2(n+1)} + \delta a^{2,4}_{2(n+1)} - \delta a^{2,3}_{2(n+1)} - \delta a^{2,4}_{2(n+1)} = 4\delta a^{2,1}_{2(n+1)}$$

Table 24. The normal multipole Jacobian in units at a reference radius of 17 mm per 1 mm midplane shift (left/right symmetric).

δb_1	δb_2	δb_3	δb_4	δb_5	δb_6	δb_7
0.00	0.00	0.00	0.00	0.00	0.00	0.00

Table 25. The skew multipole Jacobian in units at a reference radius of 17 mm midplane shift (left/right symmetric).

δa_1	δa_2	δa_3	δa_4	δa_5	δa_6	δa_7
0.00	-79.89	0.00	-7.97	0.00	-0.93	0.00

The series collared coil assembly 2, which is the one with larger skew dipole is used as study case to validate this deformation mode. Figure 40 shows the expected a_2 for the mid-plane shift in the collared coil assembly. The average value is well captured. Field harmonics are measured using a 750 mm probe, geometrical measurements are available every 150 mm meaning that in case of sharp transition magnetic measurements provide only the average value.

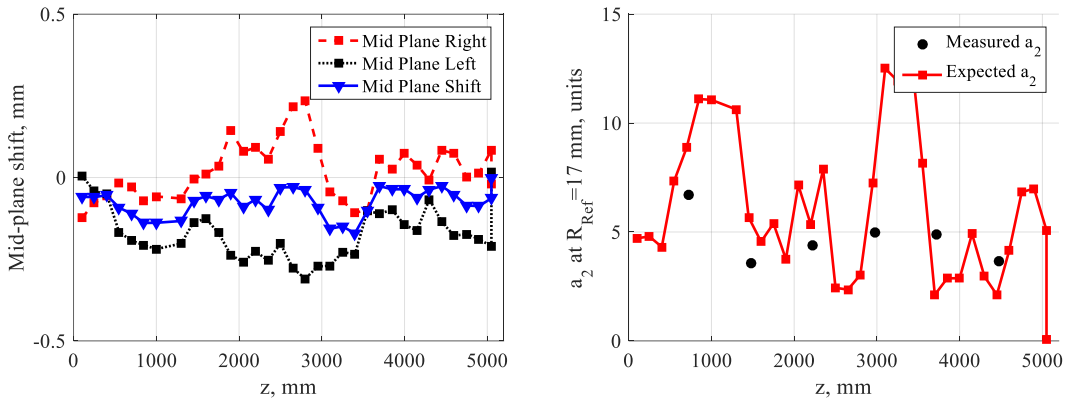

Figure 40. Left: Mid plane shift in the second MBH series collared coil assembly. Right: Measured and expected skew dipole along the collared coil length for the mid-plane shift in the second series collared coil assembly.

3.3.1.3 Correlation between field harmonics and mid-plane rotation (deformation mode 2)

Different coil sizes in the upper and lower pole of a collared coil assembly, with a top bottom symmetric pole shim result in a rotation of the coil midplane. The composition rule is:

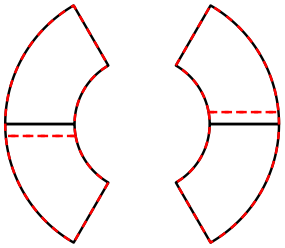

$$\delta b^{m}_{2n+1} = \delta b^{2,1}_{2n+1} - \delta b^{2,2}_{2n+1} + \delta b^{2,3}_{2n+1} - \delta b^{2,4}_{2n+1} = 0$$

$$\delta a^{m}_{2n+1} = \delta a^{2,1}_{2n+1} - \delta a^{2,2}_{2n+1} + \delta a^{2,3}_{2n+1} - \delta a^{2,4}_{2n+1} = 4\delta a^{2,1}_{2n+1}$$

$$\delta b^{m}_{2(n+1)} = \delta b^{2,1}_{2(n+1)} - \delta b^{2,2}_{2(n+1)} + \delta b^{2,3}_{2(n+1)} - \delta b^{2,4}_{2(n+1)} = 0$$

$$\delta a^{m}_{2(n+1)} = \delta a^{2,1}_{2(n+1)} - \delta a^{2,2}_{2(n+1)} + \delta a^{2,3}_{2(n+1)} - \delta a^{2,4}_{2(n+1)} = 0$$

The resulting Jacobian is shown in Table 26 and Table 27. The series collared coil assembly number 2 is the one selected to validate this deformation mode since it is the one with the largest mid-plane rotation. Figure 41 shows that both the amplitude and the shape of the measured skew sextupole correlates with the mid-plane rotation of the collared coil assembly.

Table 26. The normal multipole Jacobian in units at a reference radius of 17 mm per 1 mm mid-plane rotation

δb_1	δb_2	δb_3	δb_4	δb_5	δb_6	δb_7
0.00	0.00	0.00	0.00	0.00	0.00	0.00

Table 27. The skew multipole Jacobian in units at a reference radius of 17 mm per 1 mm mid-plane rotation

δa_1	δa_2	δa_3	δa_4	δa_5	δa_6	δa_7
-137.9	0.00	-28.64	0.00	-2.33	0.00	-0.45

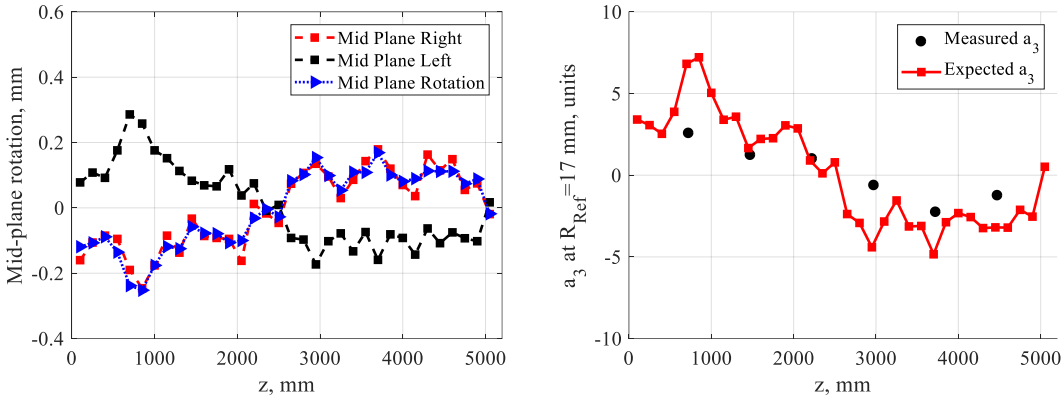

Figure 41. Left: Mid plane rotation in the second MBH series collared coil assembly. Right: Measured and expected the skew sextupole along the collared coil length for the mid-plane rotation in the second series collared coil assembly.

3.3.1.4 Correlation between field harmonics top/bottom radial asymmetry (deformation mode 3)

One of the main challenges in the initial phase of the MBH development was the high compaction in the coils due to the insulation over-thickness [3.7]. In order to provide more room for the conductor, two coils were produced without the S2-glass protection sheet that is typically installed in the outer diameter of the coil before impregnation. Since the size of the impregnation cavity was kept the same, mode 3 describes the displacements applied to the conductor turns. These coils were installed in two different apertures,

SP102 and SP103 (see Appendix 1), generating a top/bottom radial asymmetry. The composition rule for the multipole Jacobians of Table 16 and Table 17 following the symmetric rules of Table 18 is:

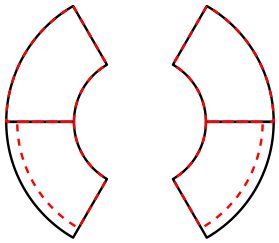

$$\delta b^{m}_{2n+1} = \delta b^{3,3}_{2n+1} + \delta b^{3,4}_{2n+1} = 2\delta b^{3,1}_{2n+1}$$
$$\delta a^{m}_{2n+1} = \delta a^{3,3}_{2n+1} + \delta a^{3,4}_{2n+1} = 0$$
$$\delta b^{m}_{2(n+1)} = \delta b^{3,3}_{2(n+1)} + \delta b^{3,4}_{2(n+1)} = 0$$
$$\delta a^{m}_{2(n+1)} = \delta a^{m3,3}_{2(n+1)} + \delta a^{3,4}_{2(n+1)} = -2\delta a^{3,1}_{2(n+1)}$$

The result of the calculations above is reported in Table 28 and Table 29. Odd normal and even skew multipoles are generated. A 0.1 mm top-bottom radial asymmetry generates 3.4 units of a_2 and 0.7 units of b_3. Figure 42 shows the correlation between the top/bottom radial insulation asymmetry and the average measured a_2 in the straight section. The measured skew dipole in SP102 and SP103 is 8.7 units and 8.0 units respectively, which is larger than the predicted skew dipole by the deformation mode. Nevertheless, measurements are around 4 units larger than the values measured in SP105 and the series collared coil CC02 (note that in CC02 the source of the large measured a_2 can be explained through the mid plane shift (see section 3.3.1.2)). Deformation mode 3 assumes that the radial difference takes place in the conductor insulation and inter-layer insulation. If instead one assumes that the coil turns are aligned in the outer radius and most of the radial difference is concentrated in the inner radius of the coil, measurements and computations would be in closer agreement.

Table 28. The normal multipole Jacobian in units at a reference radius of 17 mm per 1 mm of top/bottom radial asymmetry.

δb_1	δb_2	δb_3	δb_4	δb_5	δb_6	δb_7
33.35	0.00	-6.58	0.00	0.13	0.00	0.07

Table 29. The skew multipole Jacobian in units at a reference radius of 17 mm per 1 mm of top/bottom radial asymmetry.

δa_1	δa_2	δa_3	δa_4	δa_5	δa_6	δa_7
0.00	33.73	0.00	0.84	0.00	0.30	0.00

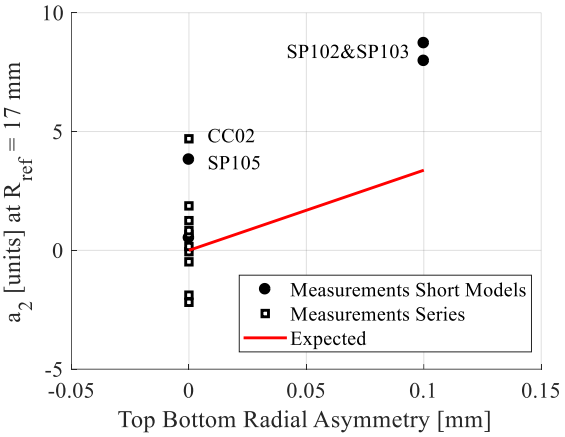

Figure 42. Average a_2 in the straight section for all measured collared apertures from the short model and series program.

3.3.1.5 Correlation between field harmonics and radial deformation (deformation mode 3)

The first 11 T coil was impregnated in a cavity with a radial dimension of 60.96 mm instead of the nominal 60.8 mm. This results in a coil deformation in radial direction. A second coil was fabricated in the same cavity to be paired in the second series collared coil assembly. The effect of a radial deformation, top/bottom symmetric for 1 mm radial deformation is shown in Table 30 and Table 31.

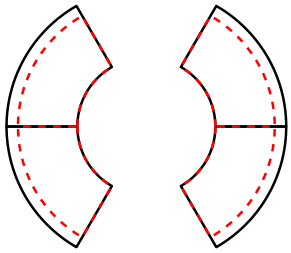

$$\boldsymbol{\delta b^{m}_{2n+1} = \delta b^{3,1}_{2n+1} + \delta b^{3,2}_{2n+1} + \delta b^{3,3}_{2n+1} + \delta b^{3,4}_{2n+1} = 4\delta b^{3,1}_{2n+1}}$$

$$\boldsymbol{\delta a^{m}_{2n+1} = \delta a^{3,1}_{2n+1} + \delta a^{3,2}_{2n+1} + \delta a^{3,3}_{2n+1} + \delta a^{3,4}_{2n+1} = 0}$$

$$\boldsymbol{\delta b^{m}_{2(n+1)} = \delta b^{3,1}_{2(n+1)} + \delta b^{3,2}_{2(n+1)} + \delta b^{3,3}_{2(n+1)} + \delta b^{3,4}_{2(n+1)} = 0}$$

$$\boldsymbol{\delta a^{m}_{2(n+1)} = \delta a^{3,1}_{2(n+1)} + \delta a^{3,2}_{2(n+1)} + \delta a^{3,3}_{2(n+1)} + \delta a^{3,4}_{2(n+1)} = 0}$$

Table 30. The normal multipole Jacobian in units at a reference radius of 17 mm per 1 mm radial deformation.

δb_1	δb_2	δb_3	δb_4	δb_5	δb_6	δb_7
66.70	0.00	-13.17	0.00	0.27	0.00	0.13

Table 31. The skew multipole Jacobian in units at a reference radius of 17 mm per 1 mm radial deformation.

δa_1	δa_2	δa_3	δa_4	δa_5	δa_6	δa_7
0.00	0.00	0.00	0.00	0.00	0.00	0.00

The main field of the series collared coil apertures is used in order to evaluate the impact of radial compression. The expected difference in the main field (b_1) of collared coil

aperture 2, assembled with coils impregnated in a 0.160 mm larger cavity is 12 units of b_1. Figure 43 shows that the measured difference is in between 18 and 30 units, around a factor 2 larger than expected. As explained in section 3.3.1.4, measurements and computations would be in close agreement if the coil is aligned in the outer radius and most of the radial difference concentrated in the inner radius of the coil.

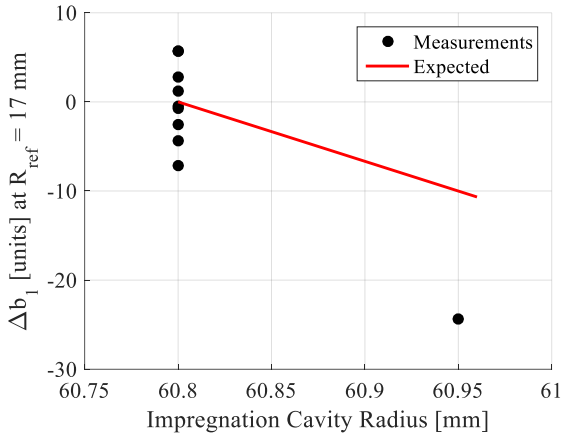

Figure 43. Difference in the main field with respect to the average field in the series MBH collared coil apertures as a function of the impregnation cavity radius.

3.3.1.6 Correlation between field harmonics and collared coil vertical deflection (deformation mode 4)

The coils produced in the 11 T program have a significant variation of their azimuthal size along the coil length; therefore, it is crucial to study its effect on the pre-stress in the various assembly steps. As SP105 is the assembly with most varying coil package azimuthal size, it is used as a study case for the consequences of its size variation by analysis of geometrical and magnetic data. The coil package of SP105 have a local azimuthal excess of 0.450 mm per quadrant in the centre of the magnet (at z=650 mm, where z is the position in the straight section relative to the pole key). The size decreases significantly towards the ends by over 150 μm. At z=50 mm, the coil package oversize per quadrant is 0.300 mm. The vertical deflection of the collared coil is expected to be larger in the regions with larger coil pack excess. Figure 44 compares the measured coil package azimuthal excess per quadrant with the measured vertical deflection of the collared coil and the measured sextupole component (b_3) of the field.

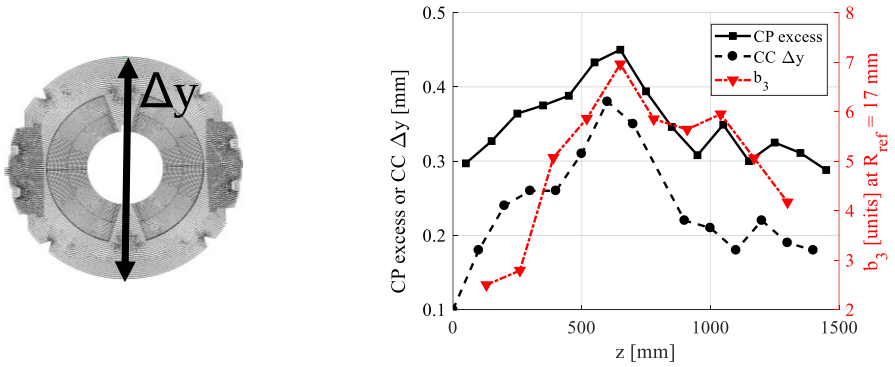

Figure 44. Measured coil package (CP) azimuthalexcess per quadrant, collared coil vertical deflection (CC Δy) and the sextupole component (b_3) of the field harmonics in SP105 along the magnet axis.

These measurements are used to validate the deformation mode 4. In case the same deformation mode is applied to all the quadrants', only allowed multiples are generated:

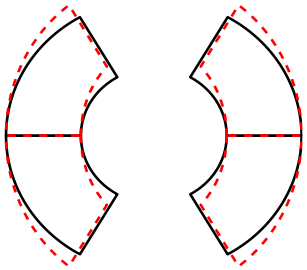

$$\delta b^{m}_{2n+1} = \delta b^{4,1}_{2n+1} + \delta b^{4,2}_{2n+1} + \delta b^{4,3}_{2n+1} + \delta b^{4,4}_{2n+1} = 4\delta b^{4,1}_{2n+1}$$

$$\delta a^{m}_{2n+1} = \delta a^{4,1}_{2n+1} + \delta a^{4,2}_{2n+1} + \delta a^{4,3}_{2n+1} + \delta a^{4,4}_{2n+1} = 0$$

$$\delta b^{m}_{2(n+1)} = \delta b^{4,1}_{2(n+1)} + \delta b^{4,2}_{2(n+1)} + \delta b^{4,3}_{2(n+1)} + \delta b^{4,4}_{2(n+1)} = 0$$

$$\delta a^{m}_{2(n+1)} = \delta a^{4,1}_{2(n+1)} + \delta a^{4,2}_{2(n+1)} + \delta a^{4,3}_{2(n+1)} + \delta a^{4,4}_{2(n+1)} = 0$$

Table 32 and Table 33 show the results of the above computations assuming that the inner radius of the coil follows an elliptical aperture with a semi-major axis 1 mm longer than the semi minor-axis. In Figure 45 the expected variation of the sextupole for the measured coil package excess (deformation mode 1) and collared coil vertical deflection (deformation mode 4) is compared with the measurements. Field measurements were performed on the cold mass assembly meaning that even in the surrounding structure (yoke and shell), the shape of the collared coil remains. Therefore, the cold mass assembly has a negligible effect on the relative pre-stress along the magnet axis. Without this feature in the cold mass assembly, stresses would be more elevated in the high azimuthal excess regions. The elliptic deformation of the collared coils with the final pre-load target for the series collared coils introduced a systematic b_3 of 5.7 units (Figure 34).

Table 32. The normal multipole Jacobian in units at a reference radius of 17 mm per 1 mm vertical deflection of the collared coils.

δb_1	δb_2	δb_3	δb_4	δb_5	δb_6	δb_7
-49.40	0.00	34.32	0.00	-0.97	0.00	0.09

Table 33. The skew multipole Jacobian in units at a reference radius of 17 mm per 1 mm vertical deflection of the collared coils.

δa_1	δa_2	δa_3	δa_4	δa_5	δa_6	δa_7
0.00	0.00	0.00	0.00	0.00	0.00	0.00

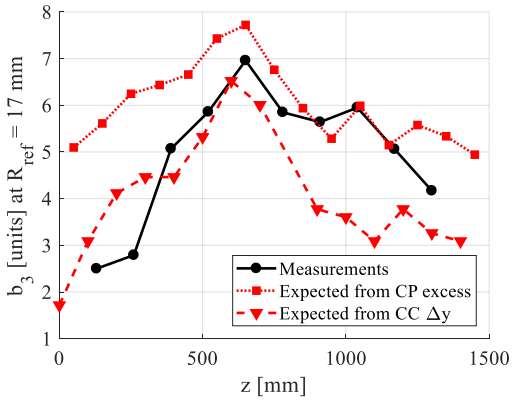

Figure 45. Comparison of the measured sextupole component of the field harmonics in SP105 compared to the expected values based on the coil package excess and collared coil vertical deflection. Correlation between field harmonics and left-right asymmetry.

3.3.2 Coil deformation modes in MQXF

3.3.2.1 Coil pack assembly

In MQXF, the aim of the coil shimming is to compensate for the difference in the azimuthal size among the four coils assembled in the coil pack. Figure 46 shows the coil deformation modes considered in MQXF. The first mode compensates the azimuthal coil under-size with mid-plane shims. The second mode compensates the azimuthal under-size with radial shimming. In both cases, the azimuthal length corresponds to the coil arc-length in relax state since the coils are only loaded after magnet assembly.

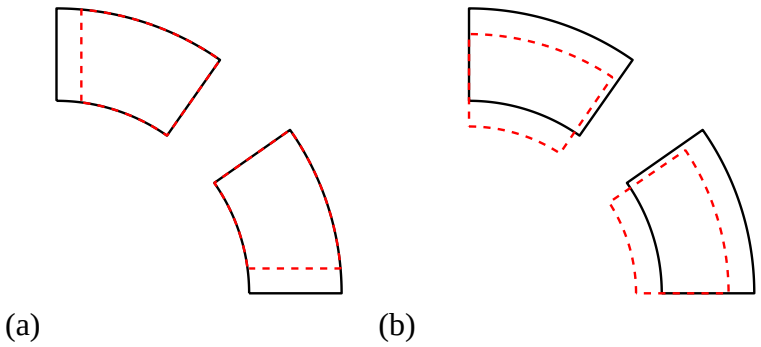

Figure 46. Coil deformation modes in MQXF (a) mode 1, mid-plane shimming to compensate for coil azimuthal under-size; (b) mode 2, radial shimming to compensate for coil azimuthal under-size

The Jacobian coefficient for each deformation mode are computed in ROXIE. The change of azimuthal size is uniformly distributed among the cables, keeping the wedges and the pole size constant. The multipole Jacobians are given in Table 34 and Table 35 per 1 mm of coil size deviation applied to the first quadrant of the quadrupole. As an example, a 0.1 mm undersize coil can be shimmed with 0.050 mm mid-plane shim per side (mode 1) or 0.064 mm ($4 \cdot 0.1/(2 \cdot \pi)$) radial shim (mode 2). In case the coil is shimmed in the mid-plane, a normal and skew sextuple of 0.25 and -0.25 units respectively will be generated. If the coils are shimmed in the radius, the expected normal and skew sextupole would be 2.00 and -2.00 units. As it can be seen from Table 34 and Table 35, for field homogeneity, a good alignment of the inner diameter of the coil turns is important since the strands close to the aperture are the ones with a larger contribution to the field errors. This good alignment of the inner diameter of the coil turns is achieved by compensating the coils size difference among coils through mid-plane shims instead of radial shims.

Table 34. The normal multipole Jacobian in units at a reference radius of 50 mm per 1 mm of coil deviation for the modes considered here applied to quadrant 1.

Mode	δb_2	δb_3	δb_4	δb_5	δb_6
1	0.00	2.50	0.00	-4.55	-3.42
2	45.24	20.00	0.00	-4.44	0.00

Table 35. The skew multipole Jacobian in units at a reference radius of 50 mm per 1 mm of coil deviation for the modes considered here applied to quadrant 1.

Mode	δa_2	δa_3	δa_4	δa_5	δa_6
1	0.00	-2.50	-7.58	-4.55	0.00
2	0.00	-20.00	-17.06	-4.45	0.00

As discussed in Section 3.3.1, the Jacobians for the same mode applied to the other quadrants of the coil can be derived using the symmetry rules. For the case of a quadrupole, the symmetry rules are summarized in Table 36

Table 36. Symmetry rules for odd and even, normal and skew multipoles (n=0...∞) generated by the modes considered here and applied to the four quadrants of a quadrupole. The modes for quadrants 2,3 and 4 are intended as obtained by mirror symmetry of the mode in the first quadrant. A "+" entry in the table means that the multipole generated has the same signs as the one computed for the first quadrant, a "-" entry means that the multipole generated in the quadrant has the same amplitude as the one computed for the first quadrant, but inverted sign

Quadrant	b_{2n+1}	a_{2n+1}	$b_{2(n+1)}$	$a_{2(n+1)}$
1	+	+	+	+
2	-	+	+	-
3	-	-	+	+
4	+	-	+	-

Using the symmetry rules the expected multipoles due to asymmetric coil shimming in MQXF assemblies can be estimated and compared to the measurements. In particular, the following sections describe the case of MQXFS3a. In order to demonstrate the importance of a good alignment of the inner diameter of the coils, two coil packs assemblies were performed. For the first assembly, the coil size deviations were corrected by shimming the coil outer radius. In the second assembly, shims were placed on the mid-plane (azimuthal shimming).

3.3.2.1.1 Correlation between field harmonics and radial shift (deformation mode 2)

In the first coil pack assembly of MQXFS3a, the size difference among coils was compensated through radial shims. Table 37 summarizes the coil excess and the shimming layout. Coil 105 was the biggest coil, with an azimuthal excess (Left + Right) of 0.150 mm. The rest of the coils were shimmed radially to achieve good matching of the outer diameter of the coils and the inner diameter of the collars, important to assure a proper pre-load. The smallest coil, coil 106, was shimmed with a 0.200 mm polyimide foil in the outer surface, whereas the other two coils were shimmed with 0.075 mm thick

foil. Figure 47 shows a pictorial view of the deformed shaped and compares the measured and expected multipoles. The agreement is good, especially in the odd normal and skew multipoles.

Table 37. MQXFS3a coil lay-out, azimuthal excess and shimming lay-out in the first coil pack assembly.

Q.	Coil	Azimuthal excess (L+R), mm (actual)	Azimuthal excess (L+R), mm (rounded)	Mid-plane shim per coil branch, mm	Radial shim, mm
1	106	-0.145	-0.150	0	0.200
2	7	0.030	0.050	0	0.075
3	105	0.130	0.150	0	0.000
4	107	0.047	0.050	0	0.075

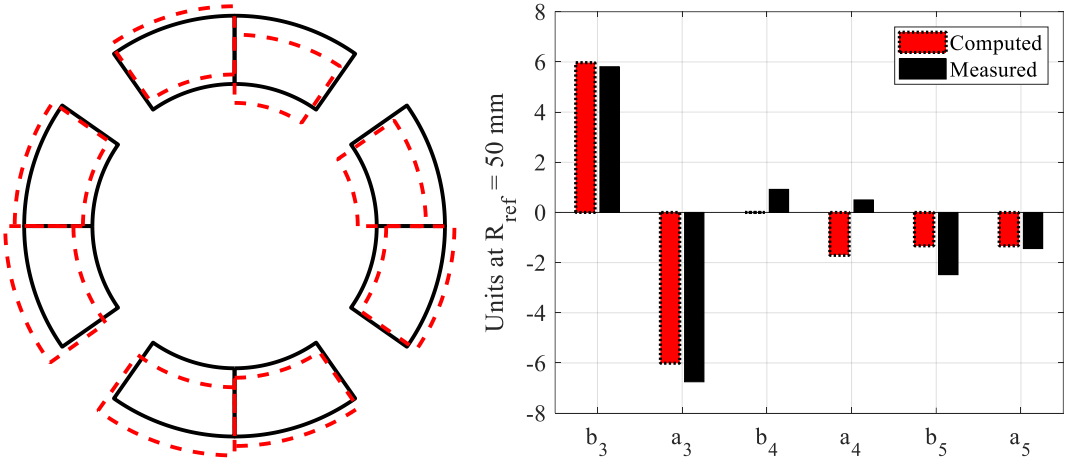

Figure 47. Coil deformed shape for the first coil pack assembly of MQXFS3a (left) and measured and computed field errors (right)

3.3.2.1.2 Correlation between field harmonics and mid-plane shift (deformation mode 1)

The second MQXFS3a coil pack assembly was shimmed in the mid-plane. Table 38 summarizes the shimming layout and Figure 48 compares measured and computed harmonics. As expected, field errors are smaller when shimming on the mid-plane. The Jacobians derived to describe the two possible deformation modes due to coil shimming in MQXF assembly predict accurately the change on the harmonics of going from azimuthal to radial shimming, as it can be seen in Figure 49.

Table 38. MQXFS3a coil lay-out, azimuthal excess and shimming lay-out in the second coil pack assembly.

Q.	Coil	Azimuthal excess (L+R), mm (actual)	Azimuthal excess (L+R), mm (rounded)	Mid-plane shim per coil branch, mm	Radial shim, mm
1	106	-0.145	-0.150	0.150	0

2	7	0.030	0.050	0.050	0
3	105	0.130	0.150	0.000	0
4	107	0.047	0.050	0.050	0

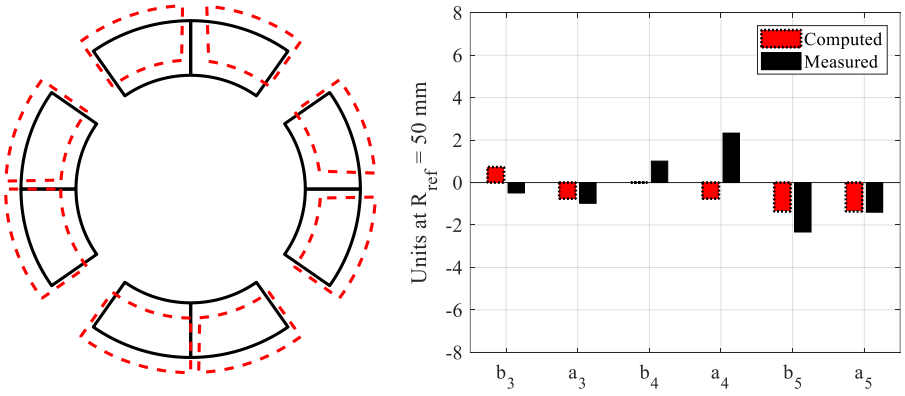

Figure 48. Coil deformed shape for the second coil pack assembly of MQXFS3a (left) and measured and computed field errors (right)

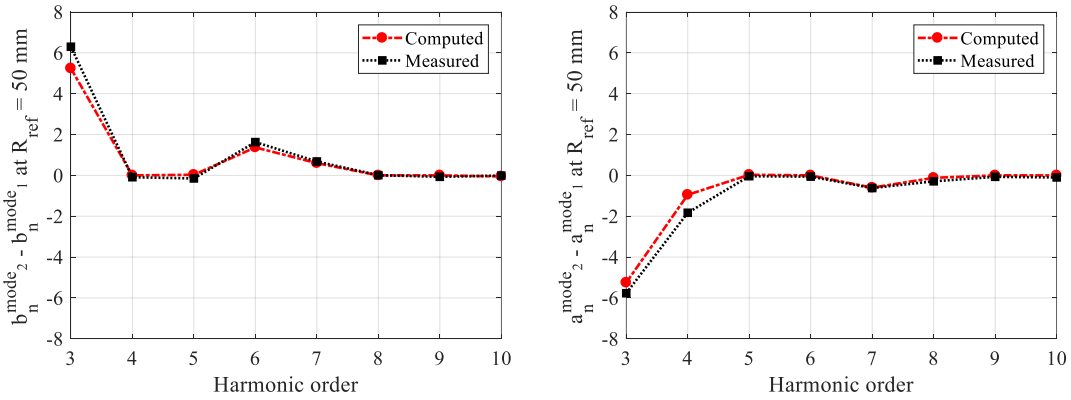

Figure 49. Expected and measured change on the harmonics from radial to azimuthal shimming.

3.3.2.2 Assembly

As discussed before, in the MBH-11 T dipole, magnetic measurements are performed after collaring, meaning that at the stage of the measurements the main pre-load is already applied. In MQXF, the first set of measurements is taken after bolting the coil pack, whereas the pre-load is applied at a later stage during the magnet pre-loading and the cooling down. During loading, the turns are pushed towards the mid-plane and radially inwards. Figure 50 shows the radial, azimuthal and total displacement map of the coil at nominal room temperature pre-load level.

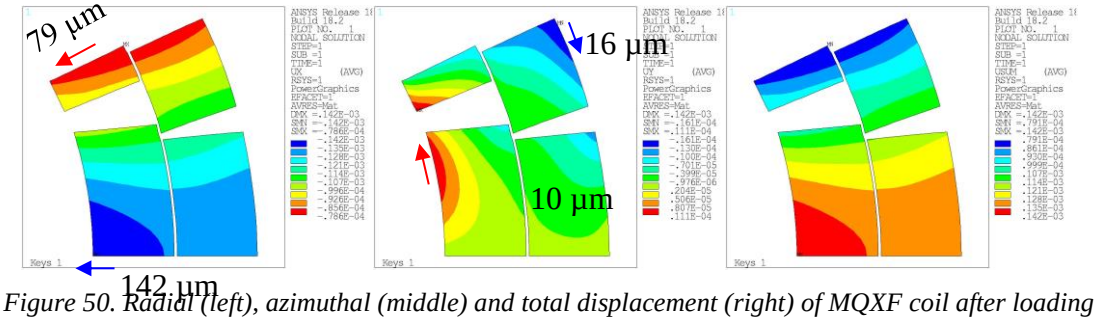

Figure 50. Radial (left), azimuthal (middle) and total displacement (right) of MQXF coil after loading under with nominal loading parameters.

In order to estimate the impact of loading, the coil displacements of the 2-D finite element model in ANSYS were exported to the 2-D magnetic model implemented in ROXIE, to assess the effects of coil deformation on field quality. The displacement map corresponds to the state of the coil after loading. The computed displacements in ANSYS were applied to every strand of the magnetic model. Due to the room temperature loading, an increase of the main field of 30 units and 0.9 units of b_6 is expected for the nominal target pre-load. The average measured change in the MQXFS and MQXFB magnets assembled so far is 1.2 units of b_6 and 40 units of the main field as it can be seen in Figure 51. The difference between measured and expected values is 25 %, which could indicate that the coil is slightly softer than assumed in the FE model. The stiffness of the coil blocks in the FE models is assumed to be 20 GPa, with a linear-elastic behavior. Published results in simplified geometries, the so-called ten stacks, showed that the behavior is highly non-linear and orthotropic, and for virgin loading the E-modulus is in the range of 10-20 GPa [3.11]. The change of the rest of the harmonics with the loading is negligible, meaning that the main source of field errors is the position of the coil turns within the impregnated coil cross section and not its alignment in the structure. For illustration, Figure 52 shows the correlation between the normal and skew sextupole components before and after room temperature loading showing not significant impact.

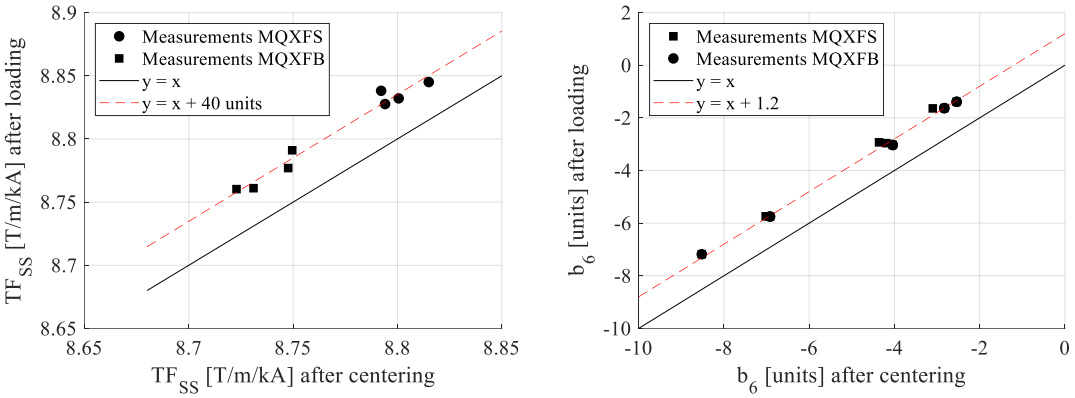

Figure 51. Correlation plot between the transfer function and b_6 component after centring the coil pack and after room temperature loading for MQXFS and MQXFB magnet assemblies.

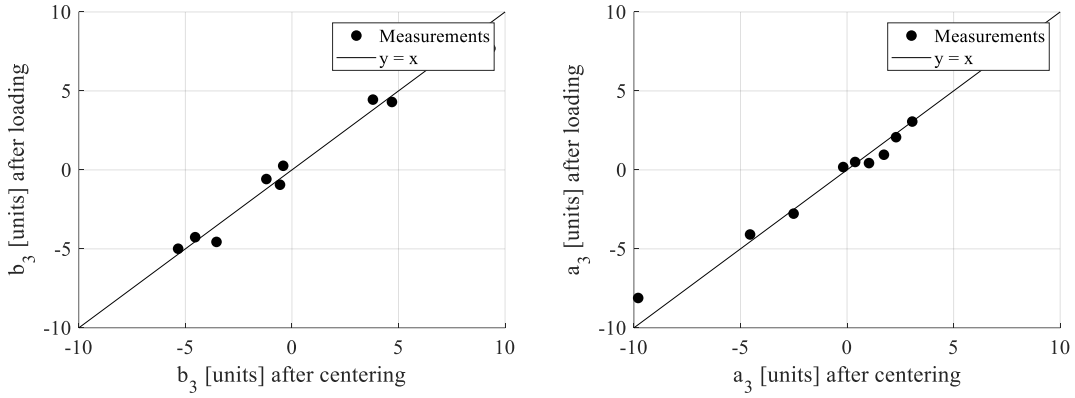

Figure 52. Correlation plot between the sextupole normal (left) and skew (right) component after centring the coil pack and after loading for MQXFS and MQXFB magnet assemblies.

3.4 Cool down and powering

During cool down, the coils move radially inwards with an expected increase on the main field of ≈ 100 units for the case of MQXF and ≈ 25 units for MBH-11T. Further details will be discussed in Chapter 0, combining with the impact of the iron saturation. For MQXF, at nominal current, b_6 is around one unit more that at warm after loading and the rest of the harmonics do not change from loading to operation conditions (see Figure 53) showing a very good cold to warm correlation, important for the definition of the location of the magnetic shims to correct field errors that will be discussed in section 4.3.

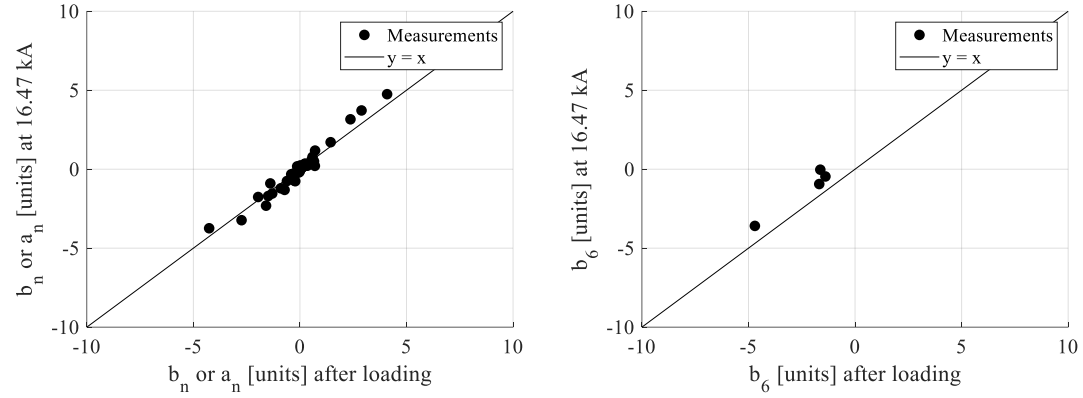

Figure 53. Cold to warm correlation in MQXFS magnets for the non-allowed harmonics (left) and the first allowed harmonic (right)

In the presence of electromagnetic forces, the pole turn is expected to move towards the mid-plane. To investigate the impact of the electromagnetic forces on field quality, we use the MQXFS6 short model. The magnet was tested under an azimuthal pre-load ranging from 50 % to 100 % of the electromagnetic forces at nominal current to assess the impact of mechanical stress on the quench performance [3.12], keeping the same axial preload to fully compensate electromagnetic forces in this direction. Due to the lower pre-load in the MQXFS6c assembly, in the presence of electromagnetic forces the pole turn is expected to detach more than in MQXFS6b assembly and move towards the mid-plane with a wider amplitude. This is inducing a variation of b_6 that can be measured using rotating coils. The difference on coil pre-stress at cold between MQXFS6b and MQXFS6c is 45 MPa. Assuming a coil elastic modulus of 20 GPa and an infinitely rigid structure, the angle of the pole θ_0 shall vary of 1.2 mrad. This corresponds to 0.110 mm pole displacement and 1.8 units of b_6, i.e. well above the sensitivity of the magnetic measurement system. To have a more refined estimate of the coil displacement during powering, the coil displacements of the 2-D finite element model in ANSYS were

exported to the 2-D magnetic model implemented in ROXIE for the MQXFS6b and MQXFS6c pre-load conditions. Figure 54 shows the coil displacement at nominal current for MQXFS6b loading conditions and Table 39 shows the average displacement of the coil block sides due to the electromagnetic forces at 16.47 kA for MQXFS6b and MQXFS6c, as estimated by the mechanical model. Δr_1 and Δr_2 are the average radial displacements of the inner and outer radius of the block, and $\Delta l_{\theta 1}$ and $\Delta l_{\theta 2}$ the average azimuthal displacement of the top and bottom side of the block. The results indicate an azimuthal displacement of the coil blocks in MQXFS6b of 0.020-0.040 mm and a radial displacement lower than 0.05 mm. In MQXFS6c, with 45 MPa lower preload, the azimuthal displacement at 16.47 kA is 0.05-0.08 mm and the radial displacement is 0.05-0.11 mm. The difference on azimuthal displacement during powering between the two assemblies is 0.03-0.04 mm, which is around one third of the analytical estimation assuming an infinitely rigid structure.

Table 39. Average displacement of the coil blocks sides due to electromagnetic forces at 16.47 kA

	Layer	Block	Δr_1 mm	Δr_2 mm	$\Delta l_{\theta 1}$ mm	$\Delta l_{\theta 2}$ mm
S6b	Inner	Mid-plane	0.049	0.043	0.000	-0.039
	Inner	Pole	0.006	-0.008	-0.037	-0.021
	Outer	Mid-plane	0.049	0.037	0.000	-0.030
	Outer	Pole	0.004	0.000	-0.030	-0.018
S6c	Inner	Mid-plane	0.113	0.107	0.000	-0.071
	Inner	Pole	0.055	0.044	-0.076	-0.069
	Outer	Mid-plane	0.114	0.101	0.000	-0.051
	Outer	Pole	0.061	0.056	-0.054	-0.052

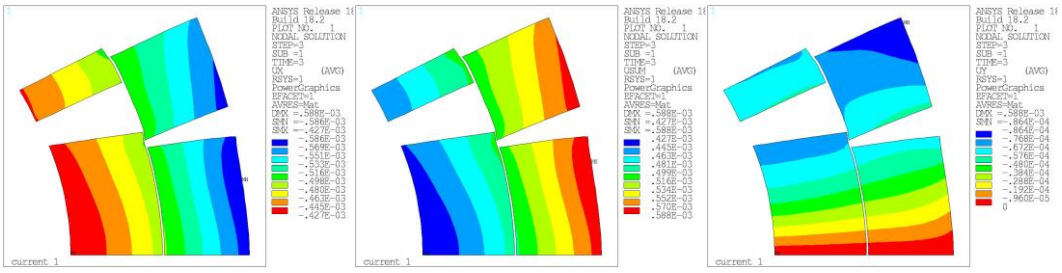

Figure 54. Radial (left), azimuthal (middle) and total displacement of MQXF coil at 16.47 kA with nominal loading parameters (MQXFS6b)

The measured and computed b_6 as a function of the square of the current is compared in Figure 55. The magnetic model predicts a difference in the normalized b_6 harmonic after cool-down of 0.37 units due to the different pre-load level, and 0.47 units larger increase during powering in MQXFS6c due to its lower pre-load. The measured geometric difference after cooling down is 0.25 units, and the difference in increase during powering is 0.30 units, 30 % less than predicted by the model.

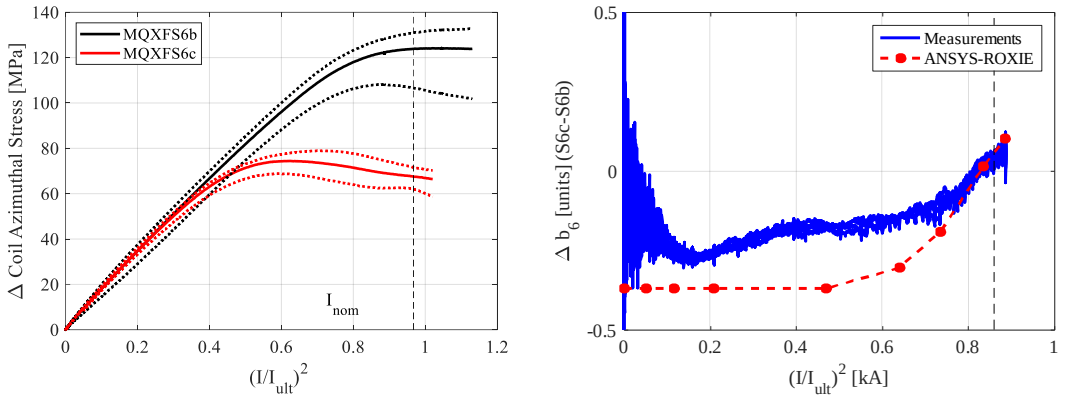

Figure 55. Left: Coil unloading during powering measured with strain gauges installed in the winding pole. Average (continuous lines) and variation across the four coils (dashed lines). Right: Measured difference on b6 in between MQXFS6b and MQXFS6c as a function of the square of the current, normalized to the ultimate current (17.5 kA) compared to the ANSYS-ROXIE model

During loading, cool down and powering, the coil undergoes a plastic deformation. The total arc length of the coil (Left + Right) is typically 0.05-0.1 mm smaller after loading and test. This corresponds to a mid-plane shift of 0.025-0.050 mm for each coil, and a radial shift of 0.03-0.06 mm. The expected impact on field quality, based on the Jacobians presented in Table 34 is 6-12 units on the transfer function and 0.4-0.7 units of b_6. Measurements show 1.1 unit increase of b_6 in average and 15 units increase of the transfer function (see Table 40, with a summary of the impact of cold powering test in the transfer function and integral field, the uncertainty of the measurements is 1 units), with no significant impact in the rest of the harmonics as expected from the symmetry. Figure 56 shows the correlation plot before and after cold powering test for the non-allowed harmonics and b_6 for MQXFS3, MQXFS5, MQXFBP2 and MQXFBP3 magnets.

Table 40. Impact of cold powering test in the transfer function and integral field

	Before cold test		After cold test		Diff [Units]	
	TF, T/m/kA	Int.,T/kA	TF, T/m/kA	Int.,T/kA	TF	Int
MQXFS5	8.813	10.599	8.836	10.619	26	19
MQXFBP2	8.832	63.359	8.844	63.440	14	13
MQXFBP3	8.860	63.548	8.867	63.610	8	10

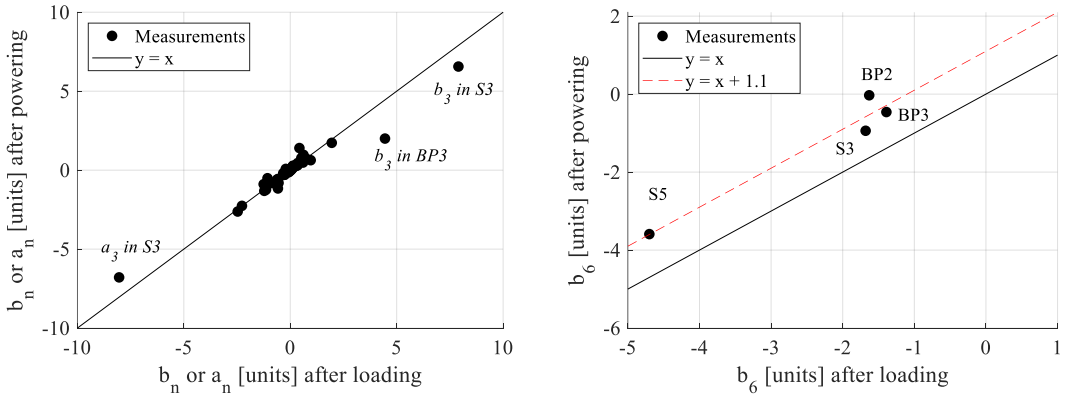

Figure 56. Change on the harmonics from warm measurements after loading to warm measurements after magnet powering cycle.

The increase of transfer function and b_6 occurs during the first thermal and cold powering cycle. Afterwards, the coils are plastically deformed, and the system is stable. This is also observed in the mechanical measurements, where the measured stress in the aluminium

shell stress decreases by 20 MPa in average with the first cool down. In subsequent cool downs, the shell stress does not vary (Figure 57).

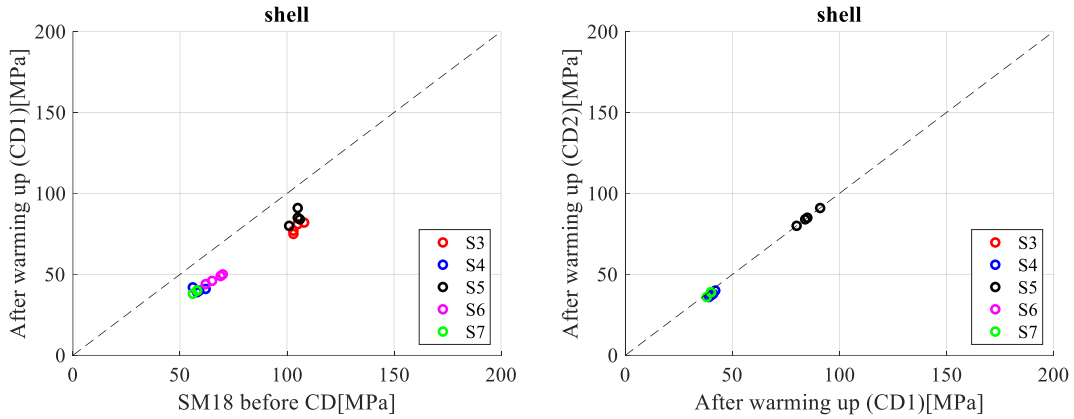

Figure 57. Measured stress in the aluminium shell before cooling down and after warming up in the first thermal cycle (left) and second thermal cycle (right) in MQXFS short model magnets.

3.5 Production monitoring

Magnetic measurements are a powerful tool for the detection of manufacturing errors, and it has been intensively used for the control of magnet production for many years. There are not intrinsic differences in between NbTi and Nb_3Sn in this aspect. Although the available statistics in MQXF is limited to work out control limits for production, the assembly of the short models and first prototype magnets provide valuable experience for the series magnets. This section summarizes the faulty assembly procedures detected up to date through magnetic measurements and the improvements implemented in the production based on the feedback from magnetic measurements.

3.5.1 Pole key to collar over-shimming

A strong anomaly of 13 units of a_4 and 1 unit of a_8 was found in the coil pack assembly measurements of MQXFS5a. Inverse analysis showed that a radial misalignment of the coils of about 0.20 mm would give this effect on the multipoles. The coil pack was dismounted and revealed excessive shimming between the pole key and the collars. The coil pack was reassembled with the appropriate shims and the strong a_4 and a_8 disappeared.

3.5.2 Coil pack squareness

In MQXF, a G11 key is inserted in the coil poles, to center the coils with respect to the aluminium collars. The goal during assembly is to provide sufficient clearance key to collars to avoid intercepting any force during room temperature loading. According to FEM computations, described in [3.13], the proper contact condition at cryogenic temperature between the aluminium collars and the G11 key is achieved by assembling the coil pack at room temperature with a collar to pole-key gap of 0.20 mm per side (see Figure 58).

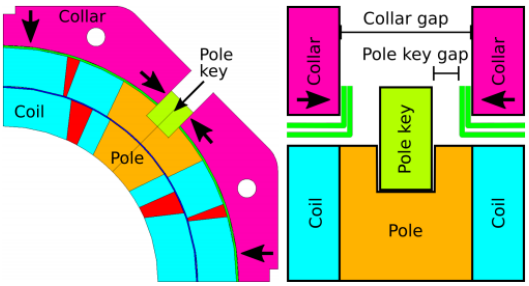

Figure 58. Schematic view of the collared coil (left) and of the pole key (right)

Once the bolting operation is completed, the gap between the pole key and the collars is measured. For MQXFB prototype magnets, the pole key gap was inferred from the measured distance between collars or pads. The first magnets were assembled aiming at an average pole gap among the four quadrants of 0.25 mm ± 0.10 mm (see Figure 59). After the assembly of MQXFBP3, the process was optimized in order to have a maximum difference among the quadrants of 0.2 mm and from MQXFB02 the clearance per side in the pole key was increased by 0.2 mm. Table 41 shows the a_4 has a greater change during centring for the magnets with larger spread on the pole key gap per quadrant, meaning that a more squarish coil pack minimizes the movements during the initial settling of the coils in the centring operation.

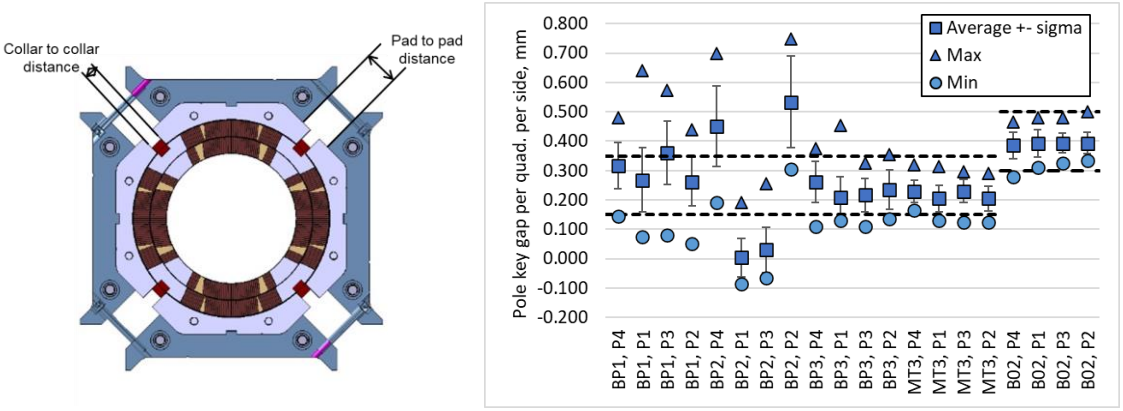

Figure 59. Measured pole key gap per quadrant per side in magnets BP1, BP2, BP3, MT3 and B02. The square solid markers represent the average over the full length, with ±1 σ error bars; the triangle and round markers represent the maximum and minimum values over the full length.

Table 41. Range of average pole key gap per quadrant and measured change on a_4 during centering

Magnet	Average pole key gap per quadrant, mm	Δa_4 during centering
MQXFBP1	0.26-0.36	1.30
MQXFBMT2	0.15-0.6	2.84
MQXFBP2	0.00-0.53	5.94
MQXFBP3	0.26-0.20	2.32
MQXFBMT3	0.23-0.21	0.89
MQXFB02	0.37-0.39	0.63

3.5.3 Magnet straightness

MQXFB yoke-shell subassembly (see Figure 18) is built of 5 modules that are assembled vertically. When the five modules are assembled together in horizontal position, if the surfaces of the four yokes in the module are not in the same plane, when the yoke-shell subassembly is loaded longitudinally the modules are tilted resulting on a bad alignment of the structure in the horizontal plane.

Figure 60 shows the top view of the outer surface of MQXFBP3 magnet measured with the laser tracker, with a misalignment in the order of 1.5 mm. This feature was cured in later assemblies through the machining of the yoke surfaces, achieving an alignment along the full magnet length of ± 0.2 mm. The straightness of the structure is defined by the initial yoke-shell subassembly structure and does not change significantly with the loading and cold mass assembly [3.14]. The magnetic axis was measured in MQXFBP3 using a 0.1 m mole. Figure 61 shows that the shape of the field is consistent with the measured shape of the outer surface of the aluminium cylinders but with an attenuation factor of 2-3. As it can be seen in the image, the shape of the field does not change after the cool down and powering cycle, which was also confirmed with geometrical measurements on the outer surface of the aluminium cylinders after cold mass disassembly.

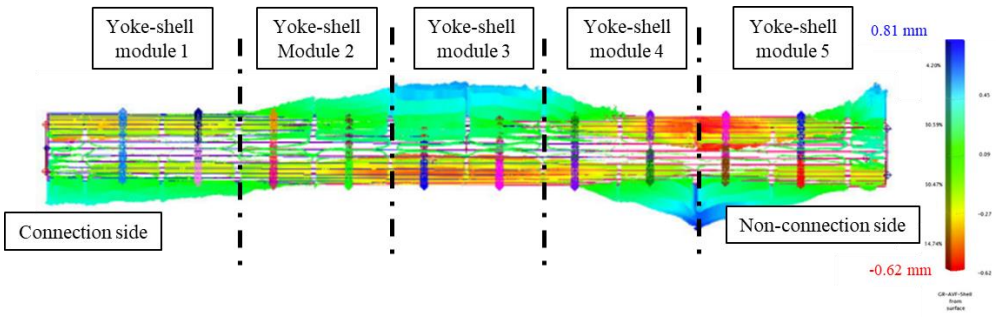

Figure 60. View from the top of the outer surface of the yoke-shell subassembly of MQXBP3 magnet.

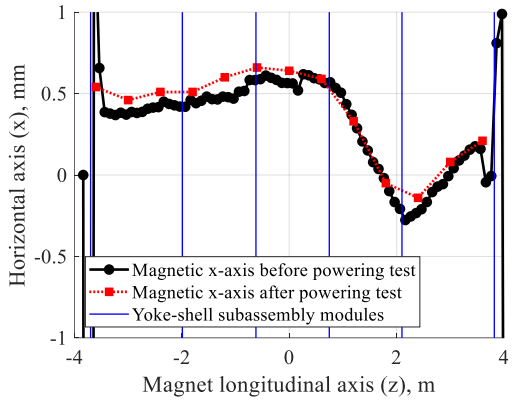

Figure 61. Measured horizontal magnetic axis in MQXFBP3 before and after cold-powering test

3.5.4 b_6 correction

Magnetic measurements from the short model magnets and first prototypes from CERN and the US show a systematic b_6 outside the target of 0 units at collision energy. In order to reach the target, an iteration of the cross section was introduced to fine tune the allowed harmonics increasing the pole insulation thickness before the beginning of the winding

by 0.125 mm and reducing the mid-plane shim thickness by 0.125 mm before coil impregnation. A Δb_6 = +5.3 units and Δb_{10} = +0.3 is expected. These actions take place during coil fabrication, and they allow to keep the same quantity of material in the same impregnation cavity. The cross-section iteration was introduced after the construction of the first prototype at CERN. Table 42 summarizes the measured b_6 in MQXFB prototype, with a difference of 5.6 to 5.7 units of b_6 due to the change of cross section, very close to the expected 5.3 units.

Table 42. Integral b_6 [units] measured after loading for MQXFB built magnets

Magnet	Cross section	b_6
MQXFBP1	Before b_6 correction	-6.52
MQXFBP2	After b_6 correction	-0.89
MQXFBP3	After b_6 correction	-0.81
MQXFB02	After b_6 correction	-0.90

3.6 Conclusions

The author studied the reproducibility that can be obtained in positioning the coil in superconducting magnets made with Nb_3Sn conductor. In spite of the intrinsic challenges of Nb_3Sn technology, with the need to accommodate the expansion of the conductor due to heat treatment, results are encouraging since the accuracy on the position of the conductors has nearly reach the standards of the NbTi technology. Reaching a 0.1 mm control on the azimuthal coil size is one of the main challenges for Nb_3Sn. In the initial phase of development, the spread in azimuthal coil size was in the order of 0.4 mm. For series production long coils, the average size and variation along the straight section length stabilized to ± 0.125 mm. The author assessed the precision of the placement of the conductors using the Monte-Carlo analysis developed for NbTi magnets: the relation between the spread in the coil position and the spread in the field harmonics is evaluated with ROXIE that implements the Biot-Savart law. Then, the spread in the integral field harmonics measured over a homogeneous series of magnets is associated with a spread in the coil position through a best fit. The variability of the field harmonics along the magnet axis shows that MQXF and MBH reached 0.030 – 0.050 mm accuracy, close to the 0.025 mm of accuracy in the NbTi main bending dipoles of the LHC. For the spread among magnets, a great improvement is found from the short model magnet program to the long prototypes and series. The author obtained a spread of 0.209 mm for MBHS and 0.057 for the MBH series collared coils, only a factor 2 times larger than the 0.025 mm of the LHC-MB. As observed for NbTi magnets, the random movements are not equally spread along the different degrees of freedom: one systematically observes that the spread in odd normal multipoles is 2–3 times larger than in the skew, and vice versa for the even ones. For MQXF, the accuracy in the placement of the conductors is 0.079 mm for the short model magnets and 0.040 mm for the prototypes and first series, to be compared to 0.029 mm reached in the LHC-MQ production. The larger spread in the short models is expected due to the differences in coil parameters and pre-loaded level. The impact of the different deformation modes is assessed by means of Jacobians and compared to measurements.

MQXF is the first accelerator magnet based on an aluminium shrinking cylinder pre-loaded using bladders and keys, and the detailed analysis of the geometric field errors is an important validation of the suitability of this structure for accelerators. The main findings are:

- the dominant source of field errors is the coil geometry and not its alignment on the magnet structure, with no change on the non-allowed harmonics with the loading. The room temperature magnet loading increases the main field and b_6 by 40 and 1.2 units respectively, close to the 30 units in the transfer function and 0.9 units of b_6 expected when imposing in the magnetic model the computed coil displacement in the mechanical FE model. The difference between measurements and computations could be due to an overestimation of the coil stiffness in the FE model
- in order to have a uniform pre-load, the difference in coil azimuthal size can be compensated using radial or azimuthal shims. The use of azimuthal shims allows to have a better alignment of the inner diameter of the coils, which results in a better field quality
- good cold to warm correlation, important for the correction of field errors through magnetic shimming based on the room temperature magnetic measurements after loading
- during loading, cool down and powering, the coil undergoes a plastic deformation which is measurable not only on the coil geometrical measurements after powering but also in the field with an increase of the transfer function of 10-20 units and 1 unit of b_6
- the initial squareness of the coil pack is important to limit the movements of the coil pack during centring, visible in the skew octupole
- the straightness of the field is defined by the straightness of the initial yoke-shell subassembly structure, which does not change significantly with the magnet loading, cold mass assembly, cool down and powering cycles.

The results are very encouraging for Nb_3Sn since in terms of geometric field errors has nearly reach the standards of the NbTi technology. It is important to point out that we are comparing a production of a stable series production of a well-stablished technology with a new technology used in few magnets. MQXF has also demonstrated that the tight requirements of field quality are reachable using an innovative structure based on an aluminium shrinking cylinder pre-loaded using bladders and keys.

3.7 References

[3.1] P. Ferracin, W. Scandale, E. Todesco, and R. Wolf, Phys. Rev. STAB, vol. 3, p. 112403, 2000.

[3.2] B. Bellesia, C. Santoni, and E. Todesco, in European Particle Accelerator Conference, 2006, p. 2601.

[3.3] B. Bellesia, J. P. Koutchouk, and E. Todesco, Phys. Rev. STAB, vol. 10, p. 062401, 2007.

[3.4] F. Borgnolutti et al., "Reproducibility of the Coil Positioning in Nb3Sn Magnet Models Through Magnetic Measurements," in IEEE Transactions on Applied Superconductivity, vol. 19, no. 3, pp. 1100-1105, June 2009, doi: 10.1109/TASC.2009.2018530.

[3.5] E. Rochepault et al., "Dimensional Changes of Nb_3Sn Rutherford Cables During Heat Treatment," in IEEE Transactions on Applied Superconductivity, vol. 26, no. 4, pp. 1-5, June 2016, Art no. 4802605, doi: 10.1109/TASC.2016.2539156.

[3.6] H. Felice et al., "Impact of Coil Compaction on Nb_3Sn LARP HQ Magnet," in IEEE Transactions on Applied Superconductivity, vol. 22, no. 3, pp. 4001904-4001904, June 2012, Art no. 4001904, doi: 10.1109/TASC.2012.2183843.
[3.7] S Izquierdo Bermudez *et al* 2019 *Supercond. Sci. Technol.* **32** 085012
[3.8] J. Ferradas Troitino et al., "Applied Metrology in the Production of Superconducting Model Magnets for Particle Accelerators," in IEEE Transactions on Applied Superconductivity, vol. 28, no. 3, pp. 1-6, April 2018, Art no. 4002106, doi: 10.1109/TASC.2017.2786262.
[3.9] J. Herrera et al., in Particle Accelerator Conference, 1987, p. 1477.
[3.10] P. Ferracin et al., "Mechanical Analysis of the Collaring Process of the 11 T Dipole Magnet," in IEEE Transactions on Applied Superconductivity, vol. 29, no. 5, pp. 1-5, Aug. 2019, Art no. 4002705, doi: 10.1109/TASC.2019.2899284.
[3.11] C. Fichera, A. Bertarelli, P. Ferracin, M. Guinchard, O. Sacristán de Frutos and G. Vallone, "New Methodology to Derive the Mechanical Behavior of Epoxy-Impregnated Nb3Sn Cables," in IEEE Transactions on Applied Superconductivity, vol. 29, no. 7, pp. 1-12, Oct. 2019, Art no. 8401912, doi: 10.1109/TASC.2019.2905224.
[3.12] S. I. Bermudez et al., "Performance of a MQXF Nb_3Sn Quadrupole Magnet Under Different Stress Level," in IEEE Transactions on Applied Superconductivity, vol. 32, no. 6, pp. 1-6, Sept. 2022, Art no. 4007106, doi: 10.1109/TASC.2022.3167369.
[3.13] E Takala et al 2021 Supercond. Sci. Technol. 34 095002
[3.14] B. Arias Alonso et al, CERN Internal Report, Misalignment between shells in MQXFBP3, EDMS 2477740

4 FERROMAGNETIC MATERIALS CONTRIBUTION

4.1 Introduction

The field quality in the aperture of a superconducting magnet is dominated by the layout of the cross section and distribution of the current in the coil. Nevertheless, the coils are enclosed in a ferromagnetic material, the so-called iron yoke, which has several important functions: (i) to keep the magnetic flux within the magnet, (ii) to prevent fringe fields in the tunnel that may endanger the electronics, and (iii) to reduce the current density in the magnet via the creation of virtual coils. Its design needs also to take into account all auxiliary elements: handling or welding housings, holes for heat exchangers, powering, etc. Assuming that all the field lines in the aperture go through the iron (and not for instance through the collars) the iron thickness required to shield the field can be easily estimated considering that the iron saturates at 1.5-2 T,

$$rB \approx t_{iron} B_{sat} \qquad \textit{Eq. 24}$$

where r is the aperture radius, B is the field in the aperture, t_{iron} is the iron thickness and B_{sat} is field is the iron saturation field (see Figure 62). For the case of quadrupole, the shielding condition is

$$\frac{r^2 G}{2} \approx t_{iron} B_{sat} \qquad \textit{Eq. 25}$$

In the case of the 11 T, r = 30 mm and B_1 = 11.2 T, resulting in $t_{iron} \approx 168$ mm. The actual iron thickness is 163.5 mm for the single aperture magnet. In MQXF, r = 75 mm and B = 132.2 T/m, so the shielding thickness is $t \approx 186$ mm whereas the actual design has an iron thickness of ≈ 145 mm.

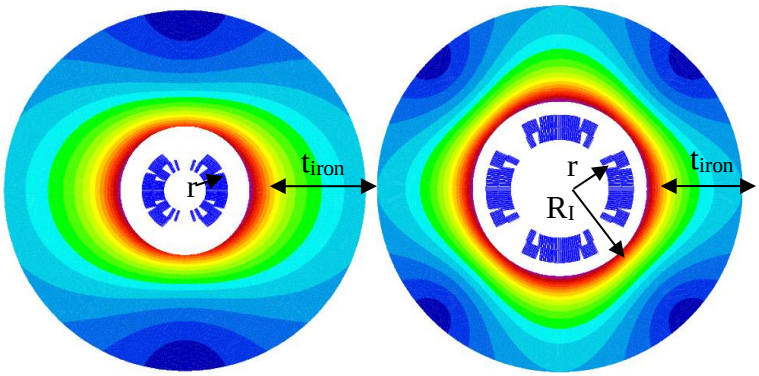

Figure 62. View of the field lines in a non-saturated iron yoke around the 11 T and MQXF coils assuming the iron is a perfect thick ring.

If the iron is not saturated, a thick ring of iron at a distance R_I from the center of the aperture produces an image current of a current line ρ, which is at a distance ρ' and carries a current I' ([4.1], page 53),

$$\rho' = \frac{R_I^2}{\rho}; I' = \frac{\mu-1}{\mu+1} I \sim I \qquad \textit{Eq. 26}$$

Figure 63, left, shows the image of a single line current. For non-saturated iron, integrating over a 60˚sector coil of width w in an aperture r, leads to a virtual coil of inner radius R_1 and outer radius R_2 (Figure 63, right), giving an additional field of [4.1],

$$\Delta B_1 = \frac{2\mu_0}{\pi} sin\left(\frac{\pi}{3}\right) J(R_2 - R_1) = 4\sqrt{3} \cdot 10^{-7} J(R_2 - R_1) \qquad \textit{Eq. 27}$$

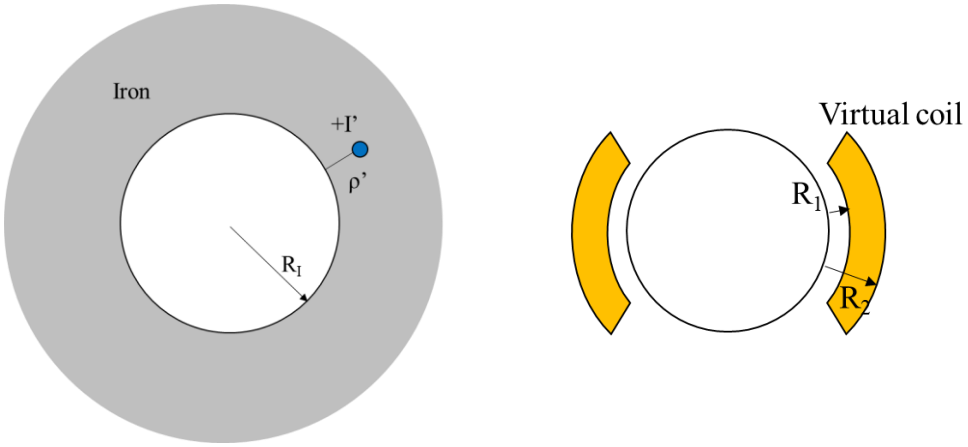

Figure 63. Impact of iron: current image produced by iron at R_I (left), and virtual coil provided by iron (right).

The total current of the virtual coil I' and the sector coil of width w and aperture r is the same, but the area of the virtual coil is much larger.

$$j[(r+w)^2 - r^2] = J(R_2^2 - R_1^2) \rightarrow J(R_2 - R_1) = j\frac{(r+w)^2 - r^2}{R_2 + R_1} \qquad \textit{Eq. 28}$$

Therefore, the field produced by the virtual coil is

$$\Delta B_1 = 4\sqrt{3} \cdot 10^{-7} j \frac{(r+w)^2 - r^2}{R_2 + R_1} \quad \textit{Eq. 29}$$

$R_2 = R_I^2/r$ and $R_1 = R_I^2/(r+w)$, thus the iron increases the field by a fraction which is a function of the aperture, the coil width and the inner radius of the iron. The thinner is the coil and the smaller are the collars, the larger is the gain. For accelerator magnets, typical gains are in the range of 10-50 %. For the MBH-11 T the gain is 18 % and for MQXF is 19 %.

$$\frac{\Delta B_1}{B_1} = \frac{r(r+w)}{R_I^2} \quad \textit{Eq. 30}$$

Above 2 T, the iron saturates, and the non-liner contribution of the iron yoke and other ferromagnetic materials needs to be considered for an accurate modelling of the field. For Nb_3Sn magnets operating at high field, a good modeling of the iron saturation is essential. Here we use the field computation program ROXIE (**R**outine for the **O**ptimization of magnet **X**-sections, **I**nverse field calculation and coil **E**nd design) [4.2], which couples the Finite Element Method and the Boundary Element Method in the so-called BEM-FEM method. The advantage of the method is that it allows the treatment of non-linear material with FEM and the accurate modelling of superconducting coils with BEM [4.3]. Figure 64 shows the elementary model problem for the BEM-FEM computation. As it can be seen in the figure, the computing area of a superconducting accelerator magnet comprises different domains. In case of the BEM-FEM method, the superconducting coil is positioned inside the non-meshed air domain (boundary element domain) Ω_3. Additional magnetic subdomains of different material parameters (Ω_1 and Ω_2) exist. These magnetic subdomains can be arbitrarily shaped and can present a coil protection sheet or tuning shims, for instance. Non-linear material parameters are allowed for all subdomains. The evaluation point is positioned in the boundary element domain, which is free from magnetic material and source currents (symbolized by the dashed circle). Only the magnetic domains have to be meshed in finite elements. The field arising from the superconducting coil can be computed analytically by means of the Biot-Savart's Law, since the coil is positioned in the air subdomain Ω_3 of the BEMFEM area. Single currents in the coil are accurately described by single line currents at the position of the superconducting strands in the coil cross-section. From the source currents, the source vector potential A_Γ on the coupling boundary between the FEM domains and the air domain is determined. The resulting vector potentials $A_{\Gamma 1}$ and $A_{\Gamma 2}$ are found from the iterative solution of the system of linear equations that results from the BEM-FEM coupling method. In this case, the right-hand side of the system of equations is the vector potential $A_{\Gamma S}$, which can again be calculated by Biot-Savart type integrals [4.4]. The reduced magnetic inductions B_{R1} and B_{R2} can be computed by means of Kirchhoff-Integrations, once the A_Γ are determined. The magnetic induction at the evaluation point is found by superimposing the source field B_S and the iron contributions B_{Rn}.

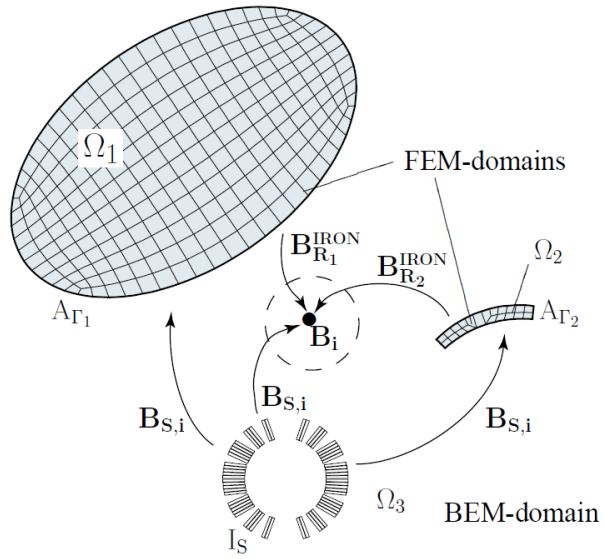

Figure 64. Elementary model problem for BEM-FEM computation of superconducting magnets.

This chapter summarizes the main aspects where the saturation of the ferromagnetic materials plays a key role. First of all, the impact of iron saturation in the transfer function and integral field is discussed together with the actions taken along the production of the MBH-Dipoles and MQXF-Quadrupoles in order to reach the required field. Due to the iron saturation effect, the gain in field at nominal current is 12 % and 8 % for the MBH-11 T and MQXF respectively, instead of the 18-19 % gain at low current where the iron is not saturated. The second part of the chapter focuses on the magnetic additions of other components, first the magnetic shims used in the MQXF quadrupoles to correct field errors and then the beam screen. The final section of the chapters describes some assembly errors detected through magnetic measurements where the presence of ferromagnetic materials in the assembly played a role.

4.2 Transfer function and integral field

The integral field provided by the magnet needs to be accurately reached. For example, in the MQXFB quadrupoles, the difference in integral gradient among magnets shall be lower than 20 units of the main field. The MBH-11 T dipoles needs to closely follow the integral field of the MB dipoles to avoid orbit distortions. Due to the high field in the iron in these magnets, iron saturation needs to be precisely modelled and measured. This section provides an overview of the measurements and requirements in terms of integral field and transfer function for MQXF and MBH-11 T magnets. The electromagnetic model is compared to measurements, to have a careful monitoring of the production and implement the required measures to reach the ambitious targets from the beam physics.

4.2.1 MBH-11T Dipole

The requirement of the MBH-11 T full cryo-assembly is to provide the same integral field at nominal current (I_{nom} = 11.85 kA) than a standard LHC-MB dipole, i.e., 119.2 Tm (59.6 T/m per magnet). Figure 65 shows the measured field divided by the current during a cycle to nominal current in a central segment of the magnet in the short model single and double aperture magnets, the so-called transfer function. In order to remove the persistent current effects, the average between the ramp up and ramp down cycle is shown. The transfer function decreases by ~ 5 % from injection level to nominal current due to the iron saturation effect, which is in very good agreement with ROXIE model. In the LHC-MB dipole magnets, the decrease due to iron saturation effect is less than 1 %

and therefore a trim power converter is added to the circuit to have the same integral value of the transfer function across the entire range of current during ramping up to nominal current. It is important to point out that in the MBH-11T single aperture short model magnets, the field in the middle of the magnet is 0.7 % higher at nominal when including the 3-dimensional effects. This effect is not present in the double aperture. The measured field is within 10 units the expected value for all current levels.

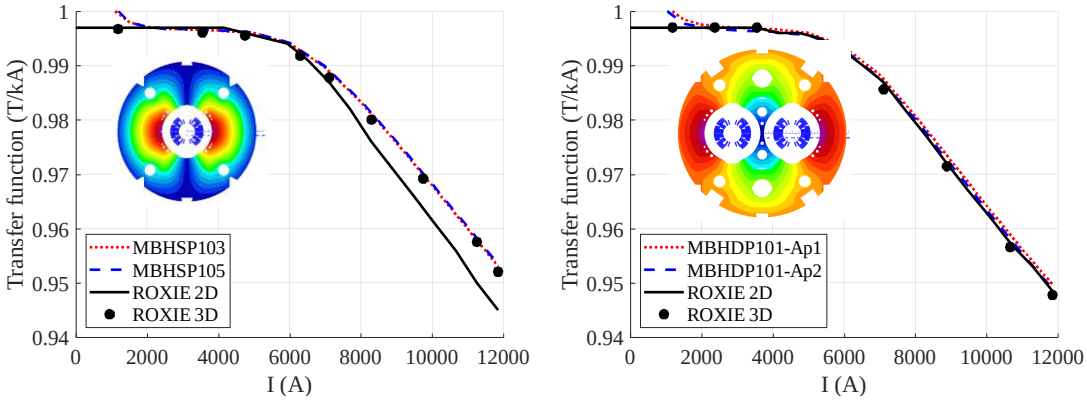

Figure 65. Transfer function (ratio between the main field and current) in the magnet center as a function of the magnet current in the single aperture (left) and in the first double aperture magnet (right) short model magnets

After the construction of the first short model magnets, a set of modifications were introduced on the design which have an impact on the integral field:

- Magnetic iron laminations on the magnet extremities were replaced by non-magnetic laminations to reduce the peak field on the coil ends
- The outer radius of the iron yoke was reduced from 275 mm to 270 mm in order to have the same outer diameter of the cold mass of the LHC-MB dipoles. The aim of this change it was to be able to re-use the existing tooling from the MB production. Few other details such as the yoke handling holes were also modified, as it can be seen in Figure 66.

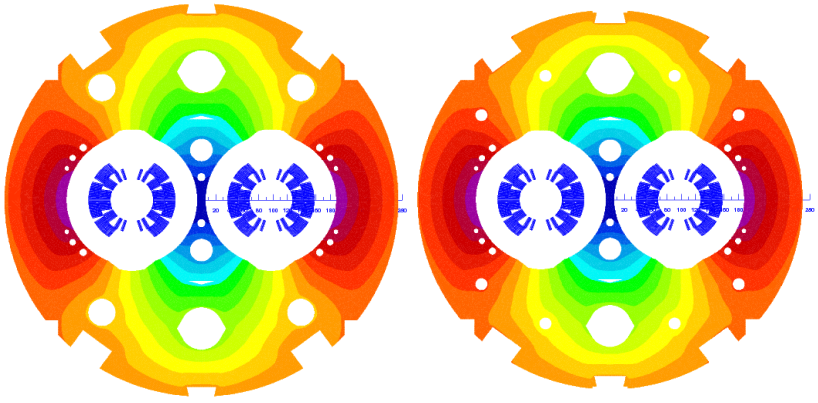

Figure 66. Left: Iron yoke geometry for the first short model double aperture magnet (MBHDP101) Right: Iron yoke geometry for the second short model double aperture (MBHDP102), prototype and series magnets.

Due to time constrains and additional uncertainty on the final coil length (mainly due to the lack of experience in terms of dimensional changes during heat treatment in 5.5 m long Nb_3Sn coils), the coil length of the first prototype coils was not modified to account for the design changes described above. A fine tuning of the coil length was done after

the construction of the first prototype magnet to reach the target integral field of the series magnets based on all existing data (i.e. room temperature measurements after collaring (CC), room temperature measurements after shell welding (CM) and measurements at 1.9 K in operation conditions).

A total of six short model and three prototype collared coil apertures were built at the time of fine tuning the coil length. The transfer function on the centre of the magnet, integral field and magnetic length is within 10 units of the expected values for the short models and the prototype-collared coil apertures (see Table 43). The standard deviation on the measured integral field is ~ 20 units for the short models and ~ 10 units for the prototype coils.

Table 43. Summary on measured collared coil transfer function in the straight section (TF_{ss}), integral field and magnetic length (l_m) for the short model and prototype magnets

Collared coil	Short models			Prototype		
	TF_{ss} (T/kA)	Integral (Tm/kA)	l_m (mm)	TF_{ss} (T/kA)	Integral (Tm/kA)	l_m (mm)
Ave. all single apertures	0.7969	1.3460	1689	0.7940	4.2221	5317.8
STD (units)	7	23	21	2	6	7
ROXIE 3D	0.7972	1.3473	1690	0.7947	4.2272	5319
diff to ROXIE 2D (units)	28	n.a	n.a	-10	n.a	n.a
diff to ROXIE 3D (units)	-4	-10	-7	-10	-12	-2

In terms of cold mass, five single aperture short model magnets (MBHSP101-105), one double aperture short model magnet using the original yoke cross section (MBHDP101) and one double aperture short model magnet using the final yoke cross section (MBHDP102) were built before the fine tuning of the series magnets coil length. Consistent with the collared coil measurements, the transfer function in the central segment is within 10 units the expected value (σ = 10 units). Larger dispersion is measured in the integral field for the single aperture models (σ = 40 units), with an offset with respect to the expected field of around 50 units (see Table 44). For the double aperture models, there is only one magnet of each type, so there are not enough statistics to evaluate the magnet-to-magnet repeatability (see Table 45). Nevertheless, measured integral field was closer to expected value (25 units), partly due to a better control during assembly of the iron laminations packing factor.

Table 44. Summary on measured cold mass transfer function in the straight section (TF_{ss}), integral field and magnetic length (l_m) for the short model single aperture models.

Cold mass (single aperture)	TF_{ss} (T/kA)	Integral (Tm/kA)	l_m (mm)
Average all single apertures	0.9929	1.6829	1693
STD (units)	9	40	16
ROXIE 3D	0.9924	1.6725	1685
diff to ROXIE 2D (units)	-20	n.a	n.a
diff to ROXIE 3D (units)	4	62	45

Table 45. Summary on double aperture short model cold mass magnetic measurements

Cold mass (double aperture aperture)	TF_{ss} (T/kA)		Integral (Tm/kA)		l_m (mm)	
Magnet	DP101	DP102	DP101	DP102	DP101	DP102
Average two apertures	0.9903	0.9910	1.6772	1.6627	1694	1678
STD (units)	1	5	18	6	17	1
ROXIE 3D	0.9912	0.9909	1.6732	1.6587	1688	1674
diff to ROXIE 2D (units)	-20	-12	n.a	n.a	n.a	n.a
diff to ROXIE 3D (units)	-9	1	24	24	33	23

At cold, the measured field is within 10 units the expected value for all current levels (see Figure 65). Since measurements in the short models are performed using a rotating shaft at cold, there is not an accurate evaluation of the integral field and magnetic length available. Based on the existing data, the coil length had to be increased by 33-48 mm in order to achieve the target integral field. The coil physical length was increased for the first series magnet by 40 mm on the straight section, with minor impact in the cold mass assembly and coil production process. In case the target field is not reached with the implemented modification, the deviation on the integral field can still be corrected by:

- Increasing or reducing the number of non-magnetic laminations in the magnet extremities. Maximum increase of the magnetic length is 14 mm, and increases the peak field in the coil ends by 0.2 T.
- Modifying the trim circuit current profile. 10 mm deviation on the magnetic length corresponds to ~ 20 A shift at nominal current.

During the cold powering test of the first series magnet, the integral field was precisely measured to validate the design of the trim. Figure 67 shows the measured difference in the integrated field with respect the LHC-MB dipole and the required trim current to have the same integrated field across the entire range level. The design considered a maximum required trim current of - 230 A, close to the - 216 A measured. At nominal current, 10 A

were required in the trim circuit to reach the LHC-MB integral field, close to the 0 A expected from the model so no further actions were required to correct the integral field.

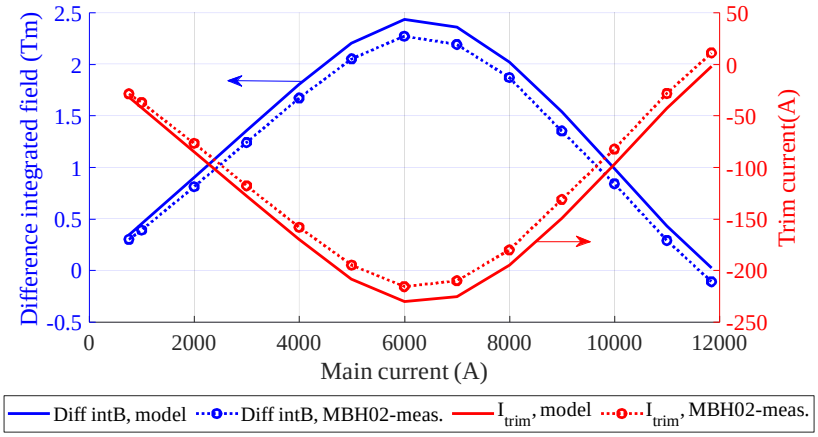

Figure 67. Difference in the integrated field in between the LHC-MB dipoles and the MBH-11 T magnets and required trim current in the 11 T to have the same integrated field across the entire range of current during ramping up to nominal current. Continues lines correspond to ROXIE model predictions. Dotted lines are measurements in the MBH02 dipoles.

4.2.2 MQXF Low-beta quadrupole

The requirement for the MQXF magnet is to provide an integrated gradient at nominal current (i.e, 7 TeV collision energy) of 557 T and 948 T for MQXA and MQXFB respectively. One of the main challenges for MQXFB magnets is to have an integral field at nominal current within 20 units for the different magnets. For MQXFA, thanks to the presence of a trim in the circuit, the requirement is slightly less stringent, with a maximum allowed difference of 50 units. Contrary to the MBH-11 T dipoles that had to be connected in series to the LHC-MB dipole circuit, MQXF magnets are independently powered, and the current can be fine tuned at a later stage to reach the required integral gradient. The original design considered conservative assumptions for the computation of the gradient (no radial deformation due to loading and cool down, expected to increase the field by ≈ 1 %), such that if a fine tuning of the current is needed in a later stage the magnets are qualified to a higher current level. The transfer function, defined as the ratio between the gradient and the magnet current, decreases by ≈ 9 % from injection level to nominal due to the iron saturation effect, which is in very good agreement with ROXIE model (see Figure 68).

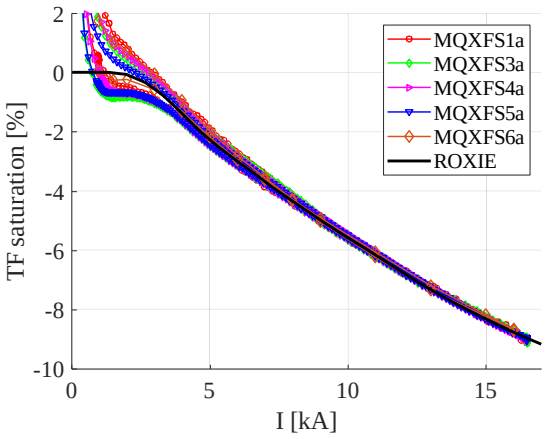

Figure 68. Current dependence of the transfer function measured during a machine cycle to nominal current compared to ROXIE 2D model.

Table 46 summarizes the transfer function in the magnet straight section for all short models and MQXFB magnets tested at room temperature, after room temperature loading, and at nominal operation conditions. The uncertainty of the measurements is on the order of 0.2 %. Accurate measurements on the absolute value of the transfer function at nominal current are not available for few magnets that did not reach performance requirements. The influence of coil deformation due to loading, cool down and powering is analysed imposing in ROXIE the deformed geometry computed in ANSYS.

Table 46. Transfer function (T/m/kA) in the magnet straight section at room temperature after loading and at 16.37 kA

	After loading (RT)		16.47 kA (1.9 K)	
	TF (T/m/kA)	Diff to Ref. (Units)	TF (T/m/kA)	Diff to Ref.
ROXIE (Reference)	8.84	--	8.051	--
ROXIE + 3 mm/m rad. cool down	--	--	8.093	52
ROXIE + ANSYS Deformation	8.86	23	8.134	103
MQXFS1a	8.865	28	8.145	117
MQXS3a	8.884	50	--	--
MQXS4a	8.865	28	8.13	98
MQXS5a	8.868	32	8.146	118
MQXS6a	8.806	-38	8.196	180
MQXS7a	8.779	-69	8.179	159
MQXFBP1	8.828	-13	--	--
MQXFBP2	8.832	-9	--	--
MQXFB01	8.828	-14	8.163	139
MQXFB02	8.845	6	--	--

The iron saturation effect is also visible in the magnetic length, defined as the ratio between the integral field and the main field in the straight section. Figure 69 compares the magnetic length as a function of the current for the magnets measured at CERN with the 3D model predictions. Measurements are done following a stair-step cycle. A pre-

cycle with a flattop current of 16.47 kA and a reset current of 100 A preceded the measurements. The model correctly predicts the iron saturation effect on the magnetic length but under-estimates the absolute value by 5 mm when assuming a longitudinal thermal contraction of 3 mm/m.

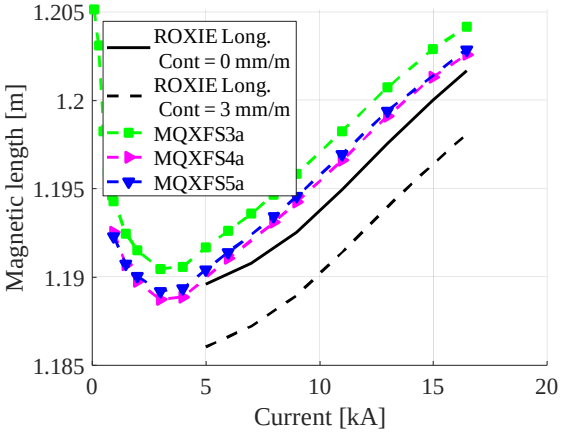

Figure 69. Current dependence of the transfer function measured during a stair step cycle to nominal current compared to ROXIE 3D model.

The magnetic length at nominal operation conditions is summarized in Table 47, showing a magnet-to-magnet reproducibility of 1 mm. The difference between MQXFS1 and the rest of the magnets is expected to be due to the differences in coil geometry between the first- and second-generation design.

Table 47. Magnetic length [mm] at nominal current. Computed values assume 3 mm/m of longitudinal thermal contraction.

Magnet	Measured	Computed
MQXFS1	1198	1192
MQXS3	1204	1198
MQXS4	1203	1198
MQXS5	1203	1198
MQXBP3	7170	7150

In September 2020, based on the available measurements at the time the nominal and ultimate current of MQXFB magnets was updated. The measured integral gradient was ≈ 2 % higher than required, with ≈ 1.5 % coming from the azimuthal and radial direction and ≈ 0.5 % due to a mismatch in the longitudinal direction. In order to keep the same integral field keeping the same mechanical lengths (no impact on coil design, tooling, magnet and cold mass construction), the 1.5 % higher field from the azimuthal and radial direction was corrected decreasing the nominal current. The 0.5 % coming from the length was corrected decreasing the target gradient in the straight section from 132.6 T/m to 132.2 T/m. Nominal current, integrated gradient and magnetic length in the original and updated design is summarized in Table 48.

Table 48. Nominal current, integral gradient, magnetic length and central gradient for 7 TeV collision energy.

	I (A)	Integral gradient (T)	Magnetic length (m)	Central gradient (T/m)
Original design	16470	557 (MQXFA)/ 948 (MQXFB)	4.200 (MQXFA)/ 7.150(MQXFB)	132.6
2020 update	16230	557 (MQXFA)/ 948 (MQXFB)	4.213(MQXFA) /7.172 (MQXFB)	132.2

Figure 70 shows the measured transfer function the three MQXFB prototype magnets. The measured integral transfer function is within 20 units, as required, already in this early stage of the development phase. The measured magnetic length MQXFBP3, the only magnet that reached nominal current at 1.9 K so far, is 7170 mm, very close to the 7172 mm target.

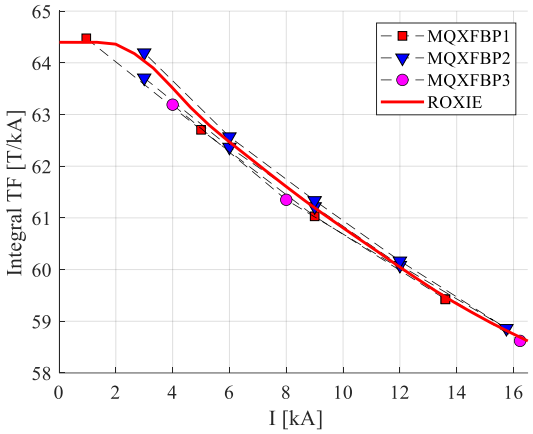

Figure 70. Measured transfer function in the three MQXFB prototype magnets.

4.3 Magnetic shimming

Correction of low order not allowed multipole using magnetic shims is a technique that has extensively been studied and tested in the past ([4.5],[4.6]). The idea is to excite different configurations of field harmonics through an asymmetric placing of magnetic shims to compensate the coil geometric imperfections. A very careful assessment of the correlations between measurements at 300 K and in operational conditions is needed to carry out effective corrective actions. Figure 71 shows the three different locations for magnetic shims that have been studied for MQXF. Electromagnetic computations show that shims on the collar rods have a strong impact at low current, but they quickly saturate and get transparent at high field values. Shims on the yoke alignment slot are too far from the beam so their correction capability is small. Ferromagnetic shims placed on the bladder slots can correct up to ± 5 units of b_3 and a_3, ±3 units of b_4 and ±1 units of a_4, and they were selected for the correction of low order not allowed multipoles in MQXF magnets. The impact to the harmonics of a magnetic shim inserted in the bladder slot number 1, as indicated in Figure 71, is shown in Table 49. The impact of a combination of shims can be derived using the symmetry rules defined in Table 50.

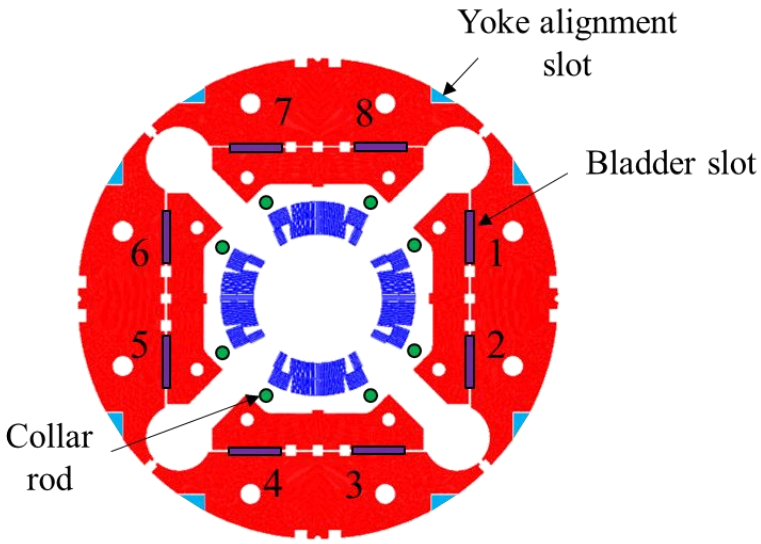

Figure 71. Location of ferromagnetic shims on the magnet cross section

Table 49. Impact on field quality of a magnetic shim inserted in bladder slot # 1 using the nomenclature defined in Fig. 71 (first quadrant), units at R_{ref} = 50 mm

Order	b_n	a_n
3	1.79	0.11
4	0.59	-0.26
5	0.16	-0.11
6	-0.35	-0.04

Table 50. Symmetry rules for normal, and skew multipoles (n=0...∞) generated by the magnetic shim inserted in the bladder slot using the nomenclature defined in Fig. 71. A "+" entry in the table means that the multipole generated has the same signs as the one computed for the first quadrant, a "-" entry means that the multipole generated in the quadrant has the same amplitude as the one computed for the first quadrant, but sign inverted

Shim	b_{4n+1}	a_{4n+1}	$b_{2(2n+1)}$	$a_{2(2n+1)}$	b_{4n+3}	a_{4n+3}	$b_{2(2n+2)}$	$a_{2(2n+2)}$
1	+ b_{4n+1}	+ a_{4n+1}	+ $b_{2(2n+1)}$	+ $a_{2(2n+1)}$	+ b_{4n+3}	+ a_{4n+3}	+ $b_{2(2n+2)}$	+ $a_{2(2n+2)}$
2	+ b_{4n+1}	- a_{4n+1}	+ $b_{2(2n+1)}$	- $a_{2(2n+1)}$	+ b_{4n+3}	- a_{4n+3}	+ $b_{2(2n+2)}$	- $a_{2(2n+2)}$
3	+ a_{4n+1}	- b_{4n+1}	+ $b_{2(2n+1)}$	+ $a_{2(2n+1)}$	- a_{4n+3}	+ b_{4n+3}	- $b_{2(2n+2)}$	- $a_{2(2n+2)}$
4	- a_{4n+1}	- b_{4n+1}	+ $b_{2(2n+1)}$	- $a_{2(2n+1)}$	+ a_{4n+3}	+ b_{4n+3}	- $b_{2(2n+2)}$	+ $a_{2(2n+2)}$
5	- b_{4n+1}	- a_{4n+1}	+ $b_{2(2n+1)}$	+ $a_{2(2n+1)}$	- b_{4n+3}	- a_{4n+3}	+ $b_{2(2n+2)}$	+ $a_{2(2n+2)}$
6	- b_{4n+1}	+ a_{4n+1}	+ $b_{2(2n+1)}$	- $a_{2(2n+1)}$	- b_{4n+3}	+ a_{4n+3}	+ $b_{2(2n+2)}$	- $a_{2(2n+2)}$
7	- a_{4n+1}	+ b_{4n+1}	+ $b_{2(2n+1)}$	+ $a_{2(2n+1)}$	+ a_{4n+3}	- b_{4n+3}	- $b_{2(2n+2)}$	- $a_{2(2n+2)}$
8	+ a_{4n+1}	+ b_{4n+1}	+ $b_{2(2n+1)}$	- $a_{2(2n+1)}$	- a_{4n+3}	- b_{4n+3}	- $b_{2(2n+2)}$	+ $a_{2(2n+2)}$

Magnetic shims were inserted in most of the MQXF magnets during the initial assembly based on the warm magnetic measurements. Figure 72 shows the shim configuration for the different assemblies, and Table 51 compares the measured and expected variation of the multipoles. The intended correction is achieved within 10 %, confirming the capability to correct low order harmonics through magnetic shims.

Table 51. Measured and computed impact of the magnetic shims in MQXF magnets. Units at R_{ref} = 50 mm.

Magnet	Bladder slots with magnetic shims	Computed impact on harmonics	Measured impact on harmonics at Inom
MQXFS1c	1,2,7,8	Δb_3 = 3.58; Δa_3 = -3.58	Δb_3 = 3.51 Δa_3 = -3.92
MQXFS3a	3,4,7,8	Δb_4= -2.38	Δb_4 = -2.55
MQXFS5a	2,3,6,7	Δa_4 = 1.04	Δa_4 = 0.71
MQXFS4a	1,2,3,8	Δb_3 = 3.37	Δb_3 =3.30
MQXFS6b	1,6,7,8	Δa_3 = -3.37	Δa_3 = -3.59
MQXFS7a	3,4,5,6	Δb_3 = -3.58; Δa_3 = 3.58	Δb_3 = - 3.59; Δa_3 = 3.60

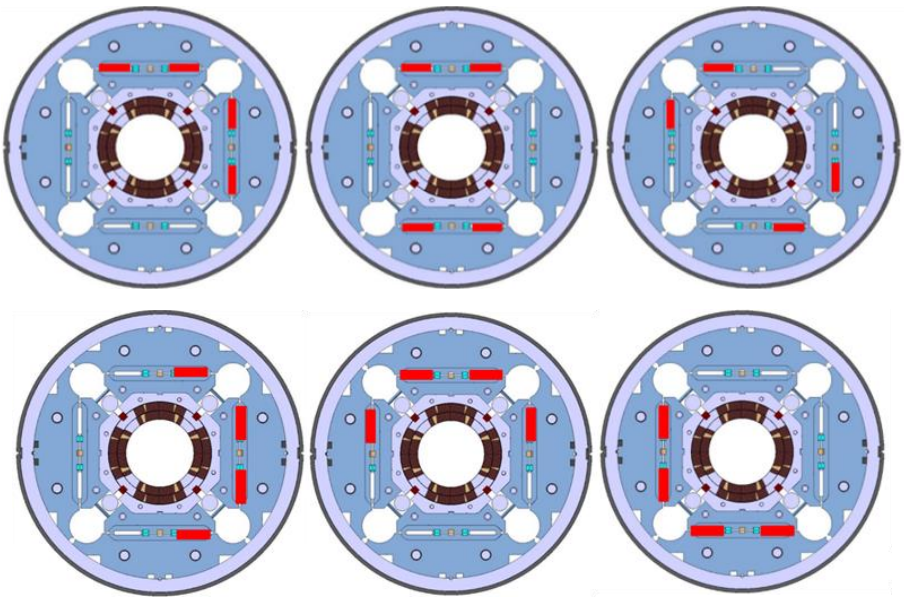

Figure 72. Magnetic shim configuration form left to right in MQXFS1c, MQXFS3a, MQXFS5a (top), MQXFS4a, MQXFS6b and MQXFS7a (bottom)

Magnetic shims have a negligible impact in the transfer function at collision energy. Nevertheless, they are visible at intermediate current levels and its effect is well reproduced by the electromagnetic model in ROXIE as it can be observed in Figure 73.

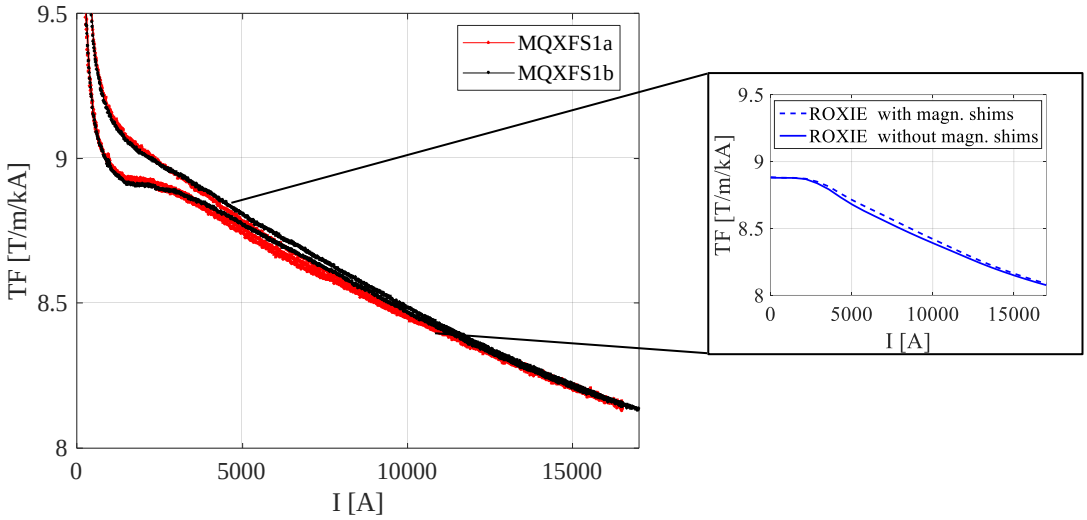

Figure 73. Measured transfer function in MQXFS1a (without magnetic shims) and MQXFS1b (with magnetic shims). The difference on transfer function an intermediate current level is well reproduced by ROXIE model when including or not the magnetic shims.

4.4 Beam screen effect

In the LHC, a beam screen shields the magnet cold bore from the synchrotron radiation emitted by the circulating proton beam and its internal copper layer decreases the wall impedance for the image currents. Due to the proximity of the circulating beam, the screen must be non-magnetic. Larger and more heavily shielded beam screens will be installed in the beam pipe of MQXF magnets. The beam screen is a complex assembly that guarantees the vacuum requirements while shielding the magnet cold mass from the induced heat loads. The HL-LHC beam screen, shown in Figure 74, is made of 1-mm thick high-nitrogen high-manganese stainless steel, colaminated on the inner surface with 75 μm thick high-purity copper to lower the beam impedance. On the longitudinal flat surfaces of the beam screen, four series of tungsten alloy blocks and four cooling tubes are alternately placed. The blocks, also referred to as heat absorbers, intercept the collision debris; they are laid on the octagonal pipe to avoid residual stress during cool-down [4.7]. The mechanical behavior of the beam screen during a quench was verified in a short model magnet[4.8], and here we focus on the impact on field quality.

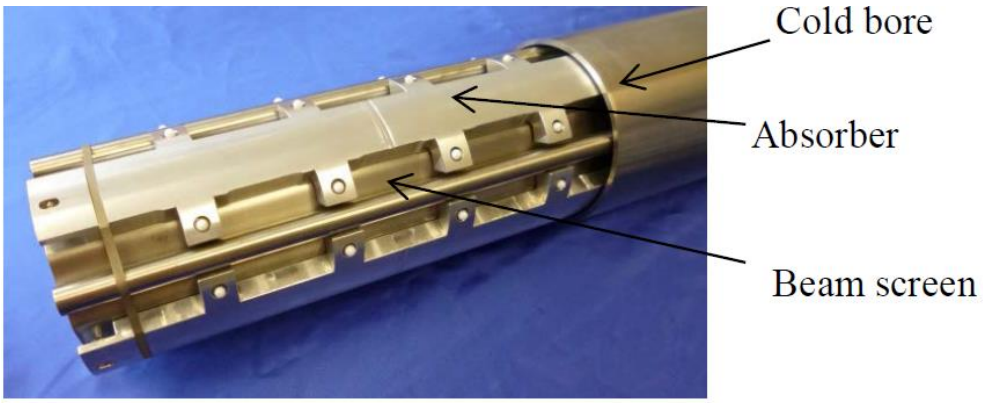

Figure 74. HL-LHC beam screen [4.7]

Two different types of beam screens are being built for HL-LHC. The main difference among them is the thickness of the tungsten alloy blocks. For the MQXFA quadrupoles closer to CMS and ATLAS experiments, the tungsten blocks are 16 mm thick, whereas for the rest of the magnets the tungsten blocks are 8 mm thick. The cross section of the beam screen model implemented in ROXIE for the two geometries is shown in Figure 75. Beam screen and cooling channels are made of high-nitrogen high-manganese stainless steel (P506), with a very low magnetic permeability (1.0025) at all temperature ranges. The cold bore is made of stainless steel 316LN, with a magnetic permeability of 1.01 at low temperature. For the tungsten blocks, the first computations were done with a magnetic permeability ranging from 1.00012 to 1.00028 based on the measurements available at the time. Figure 76 shows the magnetic properties for the different materials implemented in the model.

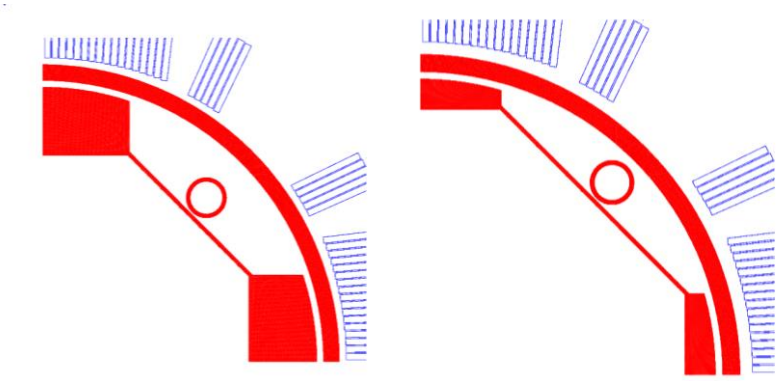

Figure 75. Beam screen geometry implemented in ROXIE. Left: 16-mm thick tungsten (Q1); Right: 8-mm thick tungsten (Q2, Q3 and D1)

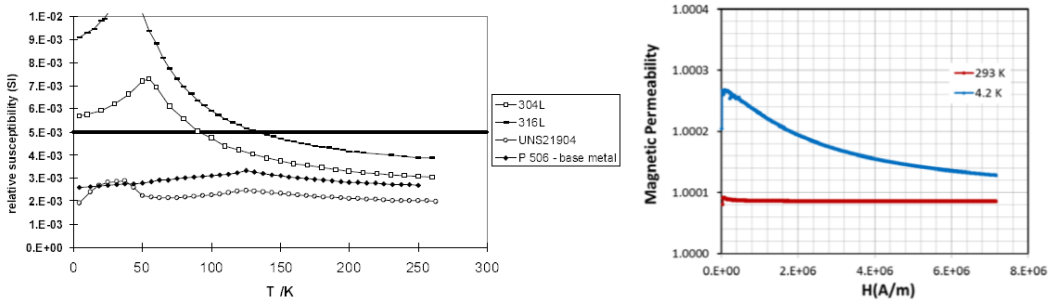

Figure 76. Left: Magnetic susceptibility of different steels of the 300 series (Mn content up to 2 %), compared to P506 (Mn = 12 %) and UNS 21904 (Mn = 9 %). Measurements performed at CEN – Grenoble, [4.9]. Right: Magnetic permeability of tungsten, measurements performed at CERN

The computed effect of the thick tungsten beam screen at 7 TeV collision energy was - 0.65 units of b_6, 0.37 units of b_{10}, -0.08 units of b_{14} and 0.10 units of b_{18}. The contribution of each of the single component to the harmonics was studied separately, showing that the larger source of field errors are the cooling channels (see Table 52).

Table 52. Impact on field quality at 7 TeV of each individual component for the 16 mm thick tungsten beam screen, units at R_{ref} = 50 mm.

		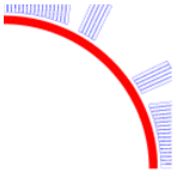	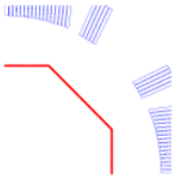	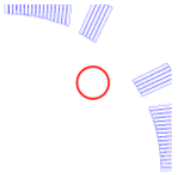
	Absorber	Cold Bore	Beam Screen	Cooling Channels
Δb_6	-0.07	0.00	-0.14	-0.44
Δb_{10}	0.05	0.00	0.00	0.32
Δb_{14}	0.02	0.00	0.09	-0.20
Δb_{18}	-0.01	0.00	0.00	0.11

An intense qualification campaign on different suppliers for tungsten was carried out, in order to select the material for the series production. Samples with a permeability ranging from 1.065 to 1.0006 at low field and 1.0006 to 1.0002 at high field were received [4.10]. The material specification was set to assure the tungsten absorber contribution to the field quality is negligible, using a conservative approach:

- $\mu_r < 1.0003$ at $H > 6 \cdot 10^6$ A/m
- $\mu_r < 1.0015$ at $H > 1 \cdot 10^6$ A/m

The first series samples show that the material was significantly better than specified with $\mu_r < 1.00011$ at all field levels. ROXIE model was updated accordingly with the final beam screen geometry and material properties. Table 53 summarizes the impact of the beam screen to the field harmonics at injection and collision energy. The field map at collision energy is shown in Figure 77.

Table 53. Impact of beam screen on the field quality at injection and collision energy (units at R_{ref} = 50 mm)

	Q1 (thick tungsten)		Q2/Q3 (thin tungsten)	
	Δ @ Inj.	Δ @ 7 TeV	Δ @ Inj.	Δ @ 7 TeV
b_6	-0.88	-0.70	-0.50	-0.42
b_{10}	0.64	0.50	0.17	0.18
b_{14}	-0.16	-0.22	-0.11	-0.12
b_{18}	0.19	0.23	0.08	0.08

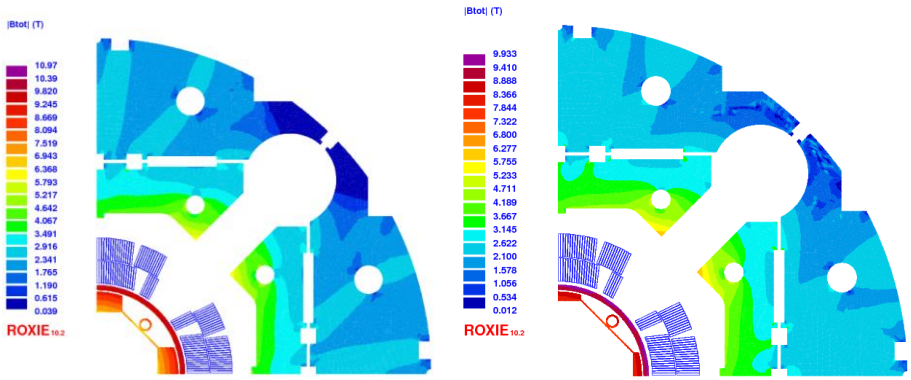

Figure 77. MQXF field map at collision energy, including the beam screen. Left: thick tungsten beam screen (Q1); Right: thin tungsten beam screen (Q2 and Q3).

The impact of the beam screen on field quality was measured in MQXFS4d. The beam screen was Q2-Q3 type (thin tungsten), 2 m length, using nominal cross section and materials. Specific supports were designed to hold the beam screen in the magnet and host the standard rotating shaft that is used during the vertical cold powering test. Figure 78 shows a schematic view of the set up and Figure 79 some pictures of the actual implementation. In the first thermal cycle, both beam screen and rotating shaft are installed. The shaft is supported in the top independently from the beam screen. In the bottom, the shaft is supported from inside the beam screen. Once the first set of measurements are completed, the magnet is warmed up and removed from the cryostat. The bottom support is removed to allow the extraction of the beam screen at ambient temperature without dismounting the measurement head. After the extraction of the beam screen the bottom support piece is installed to hold the rotating shaft. The measuring precision is 0.1 units.

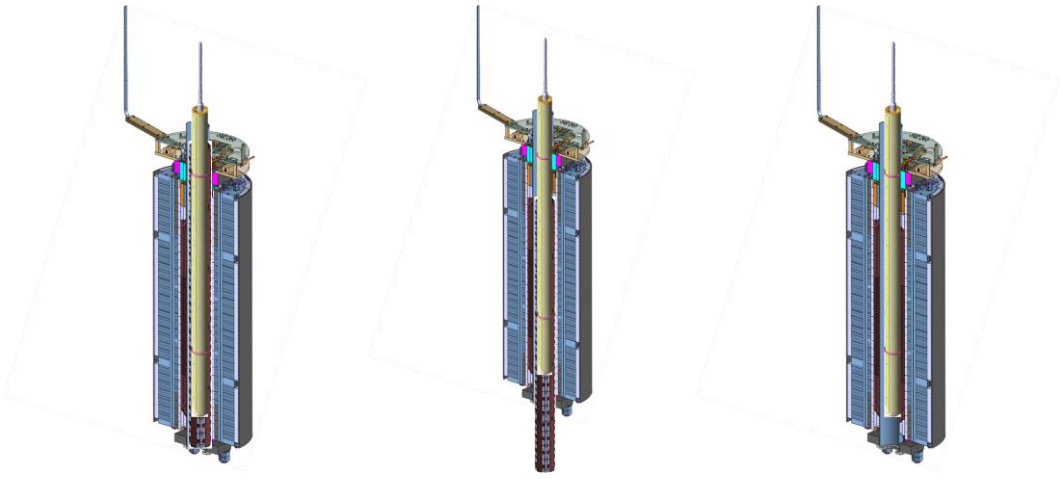

Figure 78. Schematic view of the set up for the beam screen magnetic measurement set up. Left: first thermal cycle with beam screen and rotating shaft installed in the magnet. The shaft is supported in the top independently form the beam screen. In the bottom, the shaft is supported from inside the beam screen. Middle: Extraction of the beam screen at room temperature without dismounting the measuring head, after removal of the bottom support piece. Right: Second thermal cycle without beam screen. Courtesy of Lucio Fiscarelli.

Figure 79. MQXFS4d magnet with the beam screen installed.

Table 54 summarizes the change of harmonics with and without beam screen. As predicted by the model, the effect of the beam screen is barely visible on the measurements. As expected, b_6 shows the larger different (-0.32 units measured vs -0.42 units expected).

Table 54. Measured impact of the beam screen in field quality at 7 TeV collision energy. Units at R_{ref} = 50 mm

n	Δb_n	Δa_n
3	0.22	-0.07
4	-0.02	0.06
5	0.18	-0.07
6	-0.32	--
10	0.11	--

4.5 Assembly errors

As introduced in section 3.5, magnetic measurements are a powerful tool for the detection of manufacturing errors, and it has been intensively used for the control of magnet production. Several cases along the production of the Nb_3Sn short model magnets show the presence of unwanted ferromagnetic material. This section summarizes the faulty assembly procedures detected up to date through magnetic measurements.

4.5.1 Magnetic screws

Large variation of multipoles along the axis were found in the second coil pack assembly of MQXFS5a. The spikes were in three positions along the magnet axis and had an amplitude of 15 units in b_3/a_3 and four units in b_5/a_5. After inspection, it was found that three pre-assembly screws were not removed from the pole. These screws, made of ferromagnetic material, were the source of the large spikes. MQXFS5a was reassembled after removal of the screws and the large spikes disappeared (see Figure 80).

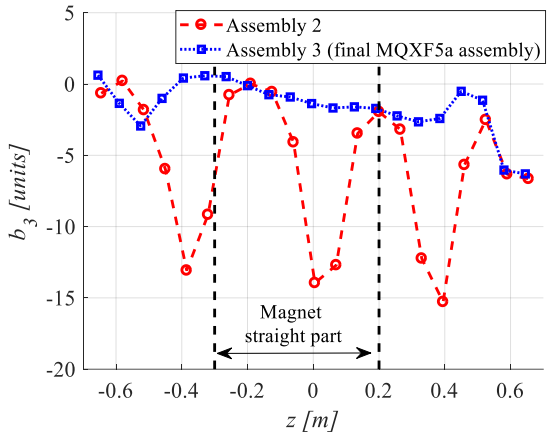

Figure 80. Warm magnetic measurements after loading for MQXFS5a faulty assembly (Assembly 2) and the final MQXFS5a assembly (Assembly 3).

4.5.2 Wrong positioning of the magnetic shims

After the cold powering test of MQXFS1a, it was decided to install magnetic shims to correct around +4 units of b_3 and –4 units of a_3. The obtained correction MQXFS1b had the correct amplitude and direction in a_3, but inverted sign in b_3. The source of the error was a 180 degrees rotation on the reference frame for magnetic measurements. In addition, the shims were inserted around the coil in quadrant 4 instead of around the coil in quadrant 1. The error was corrected for MQXFS1c where the desired correction was achieved.

4.5.3 Wrong material for the pole shimming

The room temperature measurements of MBHSP104 collared coil show 10-20 units of b_2, a_2, b_3 and a_3. At nominal current, the large harmonics disappeared which was an indication of a presence of a ferromagnetic material saturating at high field. After analysis, it was found that the material of the 0.2 mm pole shim in the first quadrant of the collared coil (see Figure 13 for a schematic of the collared coil assembly) was made of stainless steel 301 (1.4310) instead of 316LN. The magnetic permeability of 301 is orders of magnitude higher than the permeability of stainless steel 316LN, and strongly dependent on the state of deformation, as it can be seen in Figure 81. Table 55 compares the measured harmonics after collaring to the expected harmonics with and without magnetic shim. Two cases of material properties were studied: 301LN-5% deformed, 301LN-26% deformed. Measured harmonics are in between the two cases, demonstrating that the source of the errors was the wrong material of one of the pole shims.

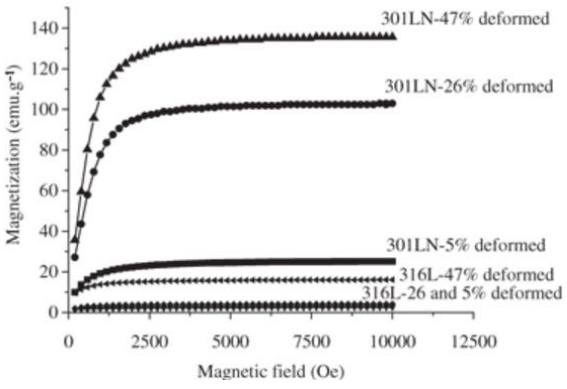

Figure 81. Magnetization of different stainless steels, courtesy of Stefano Sgobba.

Table 55. Measured harmonics in MBHSP104 at room temperature (20 A) compared to the expected harmonics without magnetic shim in the pole and with a magnetic shim in the first quadrant for two different cases of magnetic permeability. Units at R_{ref} = 17 mm.

	n	ROXIE, no magnetic shim	ROXIE, 301 5 % deformed	ROXIE, 301 26 % deformed	Measured
b_n	2	0.00	7.21	16.40	10.07
	3	6.76	-0.48	-10.38	-4.36
	4	0.00	-4.96	-11.43	-6.23
	5	0.08	1.16	2.77	3.89
a_n	2	0.00	-12.60	-30.84	-19.35
	3	0.00	-6.70	-15.29	-8.72
	4	0.00	3.12	7.62	4.38
	5	0.00	3.29	7.57	3.92

4.6 Conclusions

In a superconducting magnet, the field is dominated by the coil. The iron yoke around the coils has several important functions. It increases the field in the aperture by 10-20 % and shields the magnetic flux within the magnet preventing fringe fields in the tunnel. The author has performed detailed analysis on the main field measurements to fine tune the coil length in the case of the MBH-11 T and the operating current in the case of MQXF in order to reach the operation requirements. In addition, and based on room temperature field measurements, the author defined the location of the ferromagnetic shims in order to correct low order harmonics in MQXF. Last but not least, she implemented a detailed model of the beam screen, including the measured BH-characteristics of the material to assess the impact on the field errors. The model has been validated experimentally with the measurements on a short model magnet at cold. The detailed follow up of the production and magnetic measurements allowed to identify assembly errors where ferromagnetic materials were present in unwanted locations.

4.7 References

[4.1] K.H. Mess, P. Schmuser and S. Wolff, *Superconducting Accelerator Magnets* (World Scientific, Singapore, 1996).

[4.2] cern.ch/roxie

[4.3] S. Kurz and S. Russenschuck. The application of the BEM-FEM coupling method for the accurate calculation of fields in superconducting magnets. Electrical Engineering - Archiv fuer Elektrotechnik, 82(1), 1999.

[4.4] Stefan Kurz, Joachim Fetzer, and Günther Lehner. A novel iterative algorithm for the nonlinear BEM-FEM coupling method. In IEEE Transactions on Magnetics, volume 33, pages 1772–1775, 1997.

[4.5] R. Gupta et al., "Tuning shims for high field quality in superconducting magnets," in IEEE Transactions on Magnetics, vol. 32, no. 4, pp. 2069-2073, July 1996, doi: 10.1109/20.508569.

[4.6] G. Sabbi et al., "Correction of high gradient quadrupole harmonics with magnetic shims," in IEEE Transactions on Applied Superconductivity, vol. 10, no. 1, pp. 123-126, March 2000, doi: 10.1109/77.828191.

[4.7] C. Garion, L. Dufay-Chanat, T. Koettig, W. Machiocha, M. Morrone. Material characterisation and preliminary mechanical design for the HL-LHC shielded beam screens operating at cryogenic temperatures.
[4.8] M. Morrone, C. Garion, O. Sacristan de Frutos, "Mechanical behaviour of the HL-LHC beam screen (Q1 type) during a quench test of the MQXFS-4b magnet". EDMS 2228587.
[4.9] S. Sgobba and G. Hochoertler: A New Non-Magnetic Stainless Steel for Very Low Temperature Applications, Proc. Int. Congress Stainless Steel 1999: Science and Market, Chia Laguna /IT, 6-9 June 1999, 2, p. 391-401
[4.10] Nicolaas Kos, Qualification tests of tungsten absorber suppliers, EDMS 1973451

5 PERSISTENT AND COUPLING CURRENTS EFFECTS

5.1 Introduction

Superconductors react to external magnetic field changes through several mechanisms that tend to screen the superconducting filaments, strands, and cables from the field variation. We neglect any skin effect related to the field expulsion (Meissner effect), whose amplitude and range of existence are too small for the field range of interest in accelerator magnets. With this assumption, the mechanism dominating field screening is akin to eddy currents, with the particularity that depending on the scale considered (e.g. filament, strand or cable) the current can flow either partially or totally in the superconductor, without resistance. Indeed, we can distinguish current loops that are fully superconducting, in which case we refer to the induced currents as *persistent currents* [5.1], from loops where the currents couple superconducting paths through resistive portions, referred to as *coupling currents*. In practice, persistent currents shield the superconducting filaments from the external field change. Being fully superconductive, the persistent currents in the filament only change if the external field is changed and remain constant otherwise (we neglect here the effect of flux creep, whose magnitude is also not relevant for accelerator magnets). This is not the case for coupling currents that can flow among the filaments in a multi-filamentary strand, crossing through the stabilizer matrix, or among the strands in a cable, crossing through the contact resistances. The resistive component in the current loop makes that coupling currents decay with a time constant given by the ratio of the inductance of the current loop over its resistance.

Whether persistent or coupling currents, their screening effect translates in the generation of a magnetic field inside the superconductor that opposes the change of the external field. As an example, in a superconducting filament exposed to an externally applied magnetic induction the persistent current is arranged in the filament cross-section to produce an approximate dipole field. The case is similar for multifilamentary strands and cables, where the loops of coupling currents are arranged in the cross section to cancel the change in the applied field. As an alternative view, one may regard screening currents as the source of a diamagnetic field in the interior of the superconductor which results in a superconductor magnetization on the macroscopic scale. The diamagnetic moment associated with the screening currents produce field errors which are particularly important at injection level, where the effect is stronger compared to the field generated by the transport current. In the range of field and field ramp rate considered here, the dominating effect tends to be that of the filament magnetization generated by persistent currents. As we will discuss later, the errors are in the range of a few 10^{-4} to a few 10^{-3} of the main field at 2/3 of the aperture, which is significant compared to the field quality

requirements, and hence require precise knowledge and correction. An additional challenge is that one of the options for the next generation of particle accelerators, requiring magnetic fields higher than 10 T, is the use Nb_3Sn as superconductor. Due to the larger filament size (typically 10 times larger than in the Nb-Ti LHC dipoles), strand magnetization effects are even larger, and in some instances exhibit a non-reproducible behaviour associated with sudden flux jumps. This is the main motivation and justification for the comprehensive and careful evaluation reported in this chapter. Further reduction of the effective filament size is challenging, although world-wide efforts are on-going to improve the performance of the superconductor [5.2].

In addition to the distortion of the field, the hysteretic nature of the magnetization associated with persistent and coupling currents results in a net energy loss when the magnet is subjected to a field ramp. This ac loss can impact conductor performance and stability. The loss is deposited in the superconductor itself and needs to be removed by the cooling system. Under the influence of the ac loss, the temperature of the magnet coil rises, leading to a reduction of operating margin on the equilibrium of ac loss deposition and the cooling capacity, the magnet may hit its operating limits and thus runaway in a premature quench.

This chapter focuses on the analysis of the field mainly generated by filament magnetization associated with persistent currents, leading to field distortions that degrade the accelerator performance, in particular at the injection energy. First, the methods to compute strand and cable magnetization are discussed briefly, to provide relevant orders of magnitude and focusing on a semi-analytical model to describe the filament magnetization in the LHC NbTi dipoles. Flux jumps in Nb_3Sn at 1.9 K introduce a degree of uncertainty in the contribution of the magnetization, so an approach to account for the flux jumps through a reduction of the effective filament size is discussed. The computation method is described and validated against measurements. Related to persistent and coupling current magnetization, we will also consider the hysteresis and coupling losses arising from the magnetization of the filaments, strands and cables.

5.2 Persistent and Coupling Currents in a Superconductor

As anticipated in the introduction, persistent currents develop to shield the interior of a superconducting filament from external field changes. They are distributed at the periphery of the filament; in a region whose dimension and shape depends on the excitation history. C. P. Beam developed in 1964 the Critical State Model [5.4], where the superconductor is treated macroscopically considering only two possible states of current density: The density is either zero or equal to the maximum current density $\pm Jc(B,T)$ [5.1], i.e., the field and temperature-dependent critical current density. The filament is fully penetrated or in critical state if the persistent currents fill the totality of the filament cross section. Figure 82 shows a qualitative representation of the screening currents in a superconducting slab for an applied magnetic field H. H^* corresponds to the maximum field that can be screened. Above this value, the superconductor is fully penetrated.

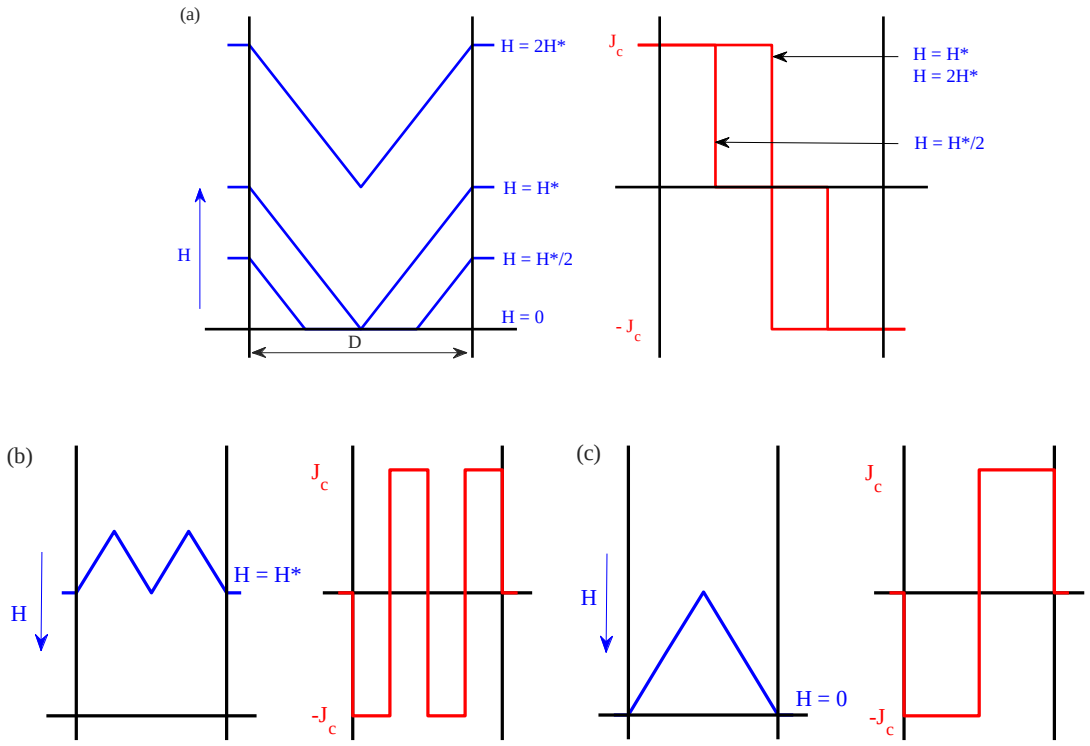

Figure 82. Critical State Model [5.4]. (a) Left: Superconducting slab of width D with an external magnetic field H. H denotes the maximum screenable field, reached when the material is fully penetrated. Right: Current density distribution for the H distribution shown in the left. (b) Reduction of external field when the field previously has been increased from 0 to a value above H*. (c) Fully penetrated state after reducing the external field to zero. The axis is perpendicular to the applied field orientation.*

The maximum screenable field, H^*, corresponds to the magnetic induction B_p/μ_0, where B_p corresponds to the penetration field, and can be derived from Maxwell's Equations of magnetostatics $\nabla \times H = J_c$. In case of constant J_c, the first penetration field is given by:

$$B_p = \mu_0 J_c \frac{D}{2} \qquad \text{Eq. 31}$$

where D is the dimension of the slab.

When the applied magnetic field changes orientation, additional current layers are generated, as shown schematically in Figure 82. The field reversal generates layers of induced currents with reversed direction, which enter the filament from the periphery until the cross section is again fully penetrated. For a constant value of J_c this happens at a field 2 H^*.

In the general case, the persistent current profile impressed depends on the field changes experienced by the filament. As we have shown schematically above, the history of field reversals is *stored* in layers of persistent currents, responsible for the hysteretic behaviour. The diamagnetic moment of the filaments can have a rather complex functional dependence on powering history. Matters are made even more complex by the fact that the filaments have 2D geometry, and the critical current density is a function of the applied field. Several approximations and techniques were developed in the past to obtain a good representation of the persistent currents.

Assuming round filaments and constant J_c, M. Wilson proposed a model [5.3] which approximates the inner boundary of the current distribution with an ellipse, whose ellipticity changes as a function of the external field change (see Figure 83). Although the

screening field produced by this arrangement will not produce a perfectly uniform dipole field, the deviations are small. Similar models were proposed by other authors [5.5]-[5.8].

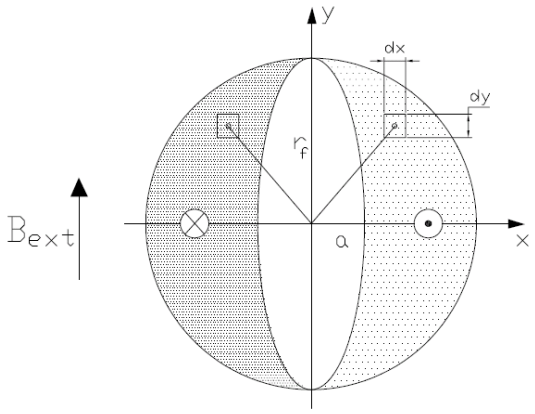

Figure 83. Calculation of the magnetization from the model of Wilson. The model integrates the surface of equivalent induced currents. The currents are oriented in ±z-direction [5.3].

With the above hypotheses, the penetration field for a filament radius r_f can be computed as follows

$$B_p = \mu_0 J_c \frac{2r_f}{\pi} \qquad \text{Eq. 32}$$

As for the slab, the filament is said to be partially or fully penetrated depending on whether the persistent currents fill only a portion or the totality of the filament cross-section available for screening (i.e., excluding the portion occupied by the transport current).

The magnetic moment in the center of the filament of two infinitely small currents applied symmetrically using the coordinate axis in Figure 83 is,

$$dm_f = J_c l_f 2x\, dxdy \qquad \text{Eq. 33}$$

where l_f is the length of the filament in the z-axis and $2x$ the distance between the two currents. Thus, the magnetization depends on the filament geometry and on the persistent current intensity and distribution. Assuming that all filaments inside the strand have identical behaviour, meaning that they have identical geometry (perfectly round filament of radius r_f, for the sake of simplicity) and critical current density J_c, the average strand magnetization, defined as the strand magnetic moment per unit volume is,

$$M = \frac{4}{3\pi} J_c r_f \sum \left(1 - \left(\frac{a}{r_f}\right)^2\right) \qquad \text{Eq. 34}$$

where r_f and a are the semi-major axis and the semi-minor axis of the elliptic inner contour of the current density (see Figure 83). For the case of fully penetrated filaments, the magnetization is:

$$M_p = \frac{4}{3\pi} J_c \lambda r_f \qquad \text{Eq. 35}$$

where λ is the fraction of superconductor in the strand.

The above model was adjusted in [5.7] to account for the postulate of Bean, considering that the current density in the persistent current layers is $J_c(B,T)$, i.e., the field and temperature-dependent critical current density. To this aim, the critical current density can be assumed to be constant J_C^{eff} in the layer of persistent current corresponding to a given applied field, but its value J_C^{eff} is made field (and temperature) dependent [5.9]. The above expression can still be used for the calculation of the penetration depth and the magnetic moment.

The dependence of the critical current density on the external field value is determined by means of the current fit [5.10] based on extracted strand measured data,

$$J_c = \frac{C(T)}{B_p} b^{0.5}(1-b)^2 \qquad \text{Eq. 36}$$

$$B_{c2}(T) = B_{c20}(1-t^{1.52}) \qquad \text{Eq. 37}$$

$$C(t) = C_0(1-t^{1.52})^{\alpha}(1-t^2)^{\alpha} \qquad \text{Eq. 38}$$

Where $t = \frac{T}{T_{c0}}; b = \frac{B_p}{B_{c2}(t)}$ with B_p as peak field on the conductor. T_{c0}, B_{c20}, α, C_0 are fitting parameters computed from the analysis of measurements on the conductor.

The calculation of persistent current with the above approximations gives good results and can be used to understand measurements. However, the accuracy that can be achieved is not sufficient to suitably describe persistent current magnetization effects in accelerator magnets. For this reason, it is common to resort on numerical methods. Several numerical methods were developed in the past, and the following references only give an idea of their variety [5.11]-[5.15]. These models vary in scope and complexity and can cover a great range of conditions, including arbitrary filament geometry, current density, and field variations. The simulation tends to be relatively heavy in terms of computational effort and time, and with the present state-of-the-art it is not easy to see how it could be applied to model the several hundred thousand filaments in a magnet cross section.

A pragmatic approach, more adapted to magnet simulation, was followed by C. Vollinger, who derived the Nested Ellipses model [5.16]. This is a method that approximates current distribution in a round filament by a series of pairs of concentric intersecting ellipses that are nested into each other (see Figure 84). By assigning a different critical current level to each pair of ellipses, the Nested Ellipses model can consider not only the average dependence of the critical current on the applied field and temperature, but also the effect of the field variation in the interior of the superconducting material, i.e. effectively introducing the appropriate $J_c(B,T,r)$ dependence. In the case of Nb_3Sn, critical current density is also dependent on the strain, but the impact of strain is not studied in this work.

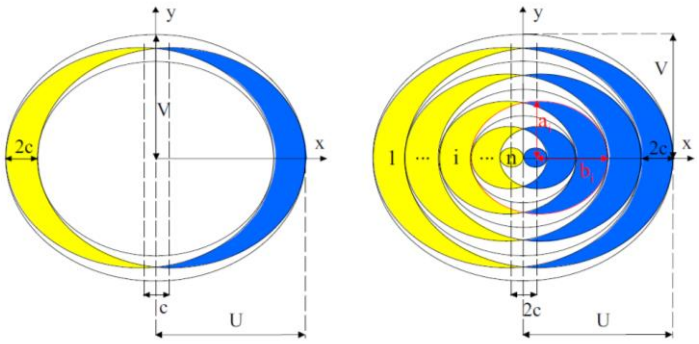

Figure 84. Calculation of the magnetization from the Nested Ellipse Model. Left: one set of nested ellipses with inscribed ellipse in the current free area. Right: set of five nested ellipses for illustration. In the model, n → ∞. Figure taken from [5.16].

Figure 85 shows the magnetization curve for a 0.7 mm strand with an effective filament diameter of 46 µm and a Cu/Sc ratio of 1.2, using the Nested Ellipses model. The plot shows a sweep in applied magnetic induction from 0 T → 6 T → - 6 T → 0 T. Starting from zero, the magnetization follows the initial state curve. The superconducting filaments shield their interior against the applied magnetic induction in the so-called shielding branch. The decrease of magnetization with increasing field results from the dependence of the critical current density with the field. At 6 T, the direction of the applied magnetic field changes arising a reversely oriented current layer penetrating the filament from the outside. The magnetization follows the trapping branch, with a hysteresis behaviour due to the already existing currents in the interior which remain, the so-called trapped currents.

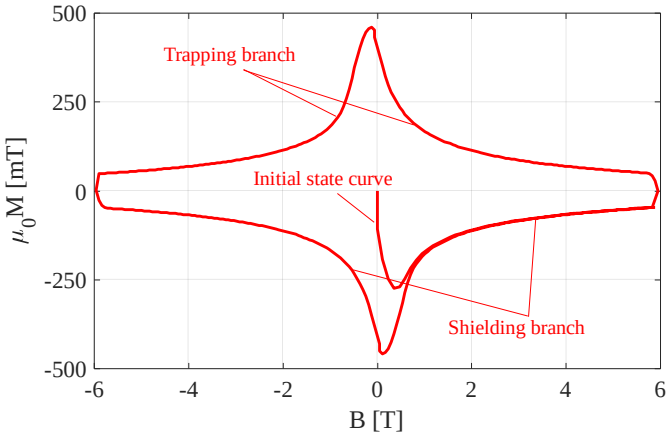

Figure 85. Magnetization curve for a 0.7 mm strand with an effective filament size of 46 µm and a copper to superconductor ratio of 1.2 using the nested ellipses model.

The difference between the modified model of Wilson and the Nested Ellipse Model is small in case of field values above the penetration field B_p. However, below the penetration field, the Nested Ellipse model produces a higher screening effect since the currents induced in the outer part of the filament cross-section screen the interior, reducing the applied magnetic induction with increasing penetration depth (see Figure 86). This is because the modified Wilson model only considers an average dependence of J_c on the applied field, but not on the varying field in the filament cross-section.

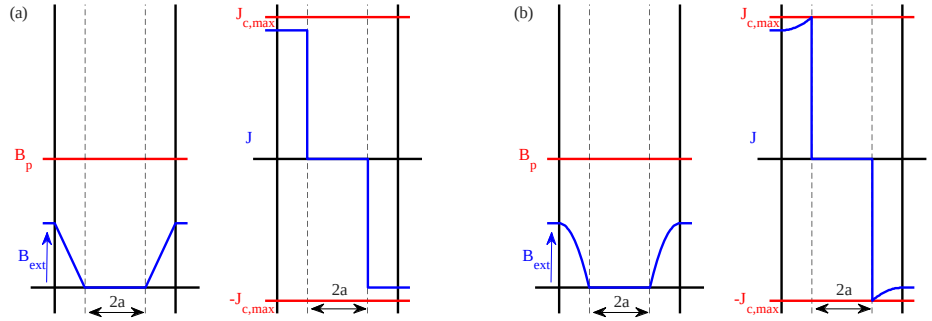

Figure 86. Distribution of the magnetic induction and the critical current density along the cylinder axis in the cross section of a round superconducting cylinder in a homogeneous external magnetic induction B_{ext} according to the Wilson magnetization model (left, a) and the Nested Ellipse model (right, b). a is the minor axis of the elliptic contour of the current densities (see Figure 83). Plot from [5.16].

The magnetization curve for a 0.7 mm strand with 46 µm effective filament size and 1.2 copper to superconductor ration computed using the nested ellipses model and the Wilson model is shown in Figure 87. Above penetration, in the case of round filaments fully penetrated, the difference among the two models is small. A detailed comparison of the models is given in [5.16].

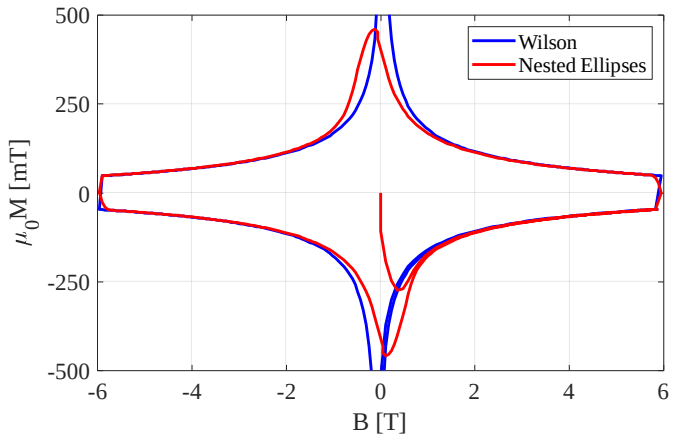

Figure 87. Magnetization curve for a 0.7 mm strand with an effective filament size of 46 µm and a copper to superconductor ration of 1.2, computed with the Wilson and the Nested Ellipses Model.

There are several sources of uncertainty in the estimate of strand magnetization with the equations derived above. The filament size and geometry is one of the main sources of uncertainty. In addition, filaments can be hollow, depending on their manufacturing process. Figure 88 shows the cut through a MQXF Nb_3Sn cable with strands and filaments of different shapes. The deformations can be seen specially on the strands close to the thin cable edge (left side of the picture). The influence of deformed filament shapes was studied in [5.16]. Filament deformation causes an increase of the apparent filament diameter resulting in larger magnetization [5.17].

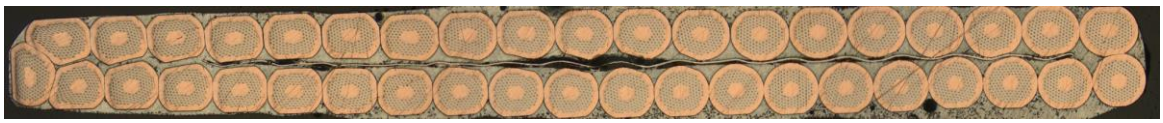

Figure 88. Cut-through a MQXF Nb3Sn cable strand showing strand and filaments with non-uniform cross section. Strands in the thin edge of the cable are strongly deformed. Image courtesy of Jerome Fleiter, CERN.

Nb_3Sn filaments have a typical filament radius one order of magnitude larger than NbTi. Both Bruker Powder-in-tube (PIT) and Bruker-OST Restacked-Rod-Process (RRP) conductors were developed in the framework of the HL-LHC upgrade. Figure 89 and Figure 90 summarize the strand layouts tested during the short model magnet development phase. For MQXF, new variant of the PIT conductor was also developed in collaboration with CERN, which introduces an additional Nb barrier around the whole bundle of filaments that allowed drastically reducing the effect of mechanical deformation and of the heat treatment cycle on the residual resistivity ratio (RRR) of the stabilizing wire copper [5.18]. In all the cases, the center of the strand is not filled with superconductive material. The filaments are hollow, with a non-superconductive filament core (see Figure 91). Filament distortion, growth and bridging during heat treatment will affect the Nb_3Sn strands (see [5.19] for an example).

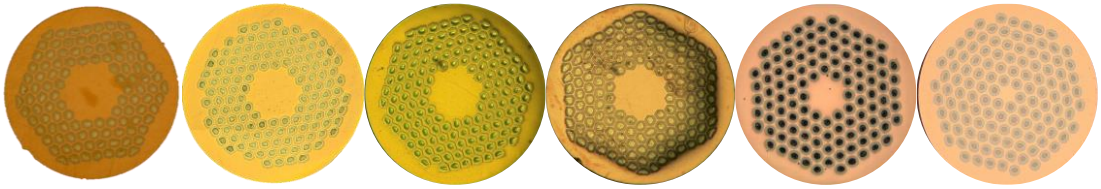

Figure 89. Strand layout in 11 T short model program, from left to right RRP108/127, RRP 132/169, RRP 144/169, RRP 150/169, PIT 114 and PIT 120. Image courtesy of B. Bordini.

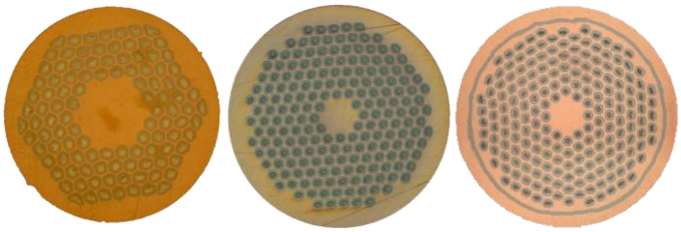

Figure 90. Strand layout in MQXF short model program, from left to right RRP 108/127, PIT 192, PIT 192 with bundle. Image courtesy of B. Bordini.

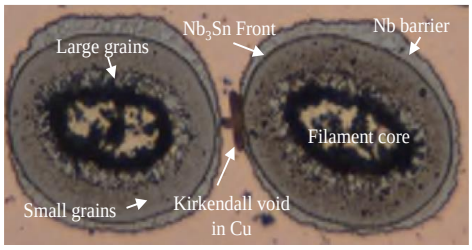

Figure 91. Cut through a PIT Nb_3Sn strand showing deformed hollow filaments. Image courtesy of B. Bordini.

Another source of uncertainty is the fraction of superconductor in the strand, λ, which has an important impact on the average magnetization, with a tolerance range along the production of ± 10 %. Table 56 summarizes the layout, copper to non-copper ratio and sub-element size for the strands developed for the 11T and MQXF programs. For the series production, RRP 108/127 was chosen for both magnets.

Table 56. Strand layout, copper to non-copper ration and sub-element size for MQXF and 11 T strands.

	Layout	Cu to non-Cu	Sub-Element size (μm)
0.7 mm RRP	108/127	1.19	46
	132/169	1.28	41
	144/169	1.08	41
	150/169	1	41
0.7 mm PIT	114	1.25	44
	120	1.15	44
0.85 mm RRP	108/127	1.19	55
	132/169	1.22	50
0.85 mm PIT	PIT 192	1.22	41
	PIT 192 Bundle	1.15	39

The temperature and field dependence of the critical current density is a further source of uncertainty. At low field, the current density is not controlled accurately. In the state-of-the-art Nb_3Sn wires, below 3 T there are flux jumps which limit the conductor magnetization. At 1.9 K, the conductor is so unstable that the jumps are continuous, and their amplitude gets smaller and smaller when reducing the field. When increasing the temperature there are fewer jumps with larger amplitude. Figure 92 compares the measured magnetization in MQXF RRP wire at 1.9 K, 3 K and 6 K. Due to the flux jumps at low temperature, the magnetization at low field is larger at 6 K than at 1.9 K.

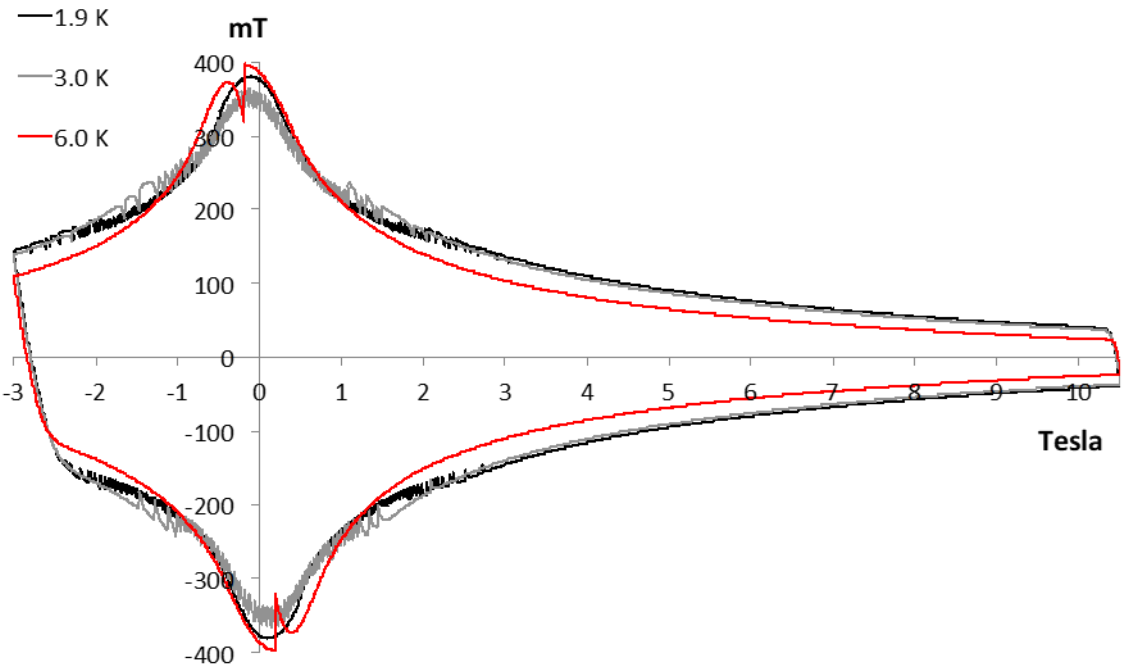

Figure 92. Magnetization of a MQXF RRP wire at different temperature levels. Measurements courtesy of D. Richter, image courtesy of B. Bordini.

In order to include this effect in the strand magnetization model, the author of this thesis proposes to introduce a reduction of the effective filament size D_{eff} as a function of the field for $B < B_0$,

$$D_{eff\,LF}(B) = D_{eff}\left(\chi + (1-\chi)\frac{B}{B_0}\right) \qquad \text{Eq. 39}$$

where $D_{eff\,LF}$ is the equivalent filament size in the flux jumps region, which is a function of the field. B_0 is the highest field where flux jumps are observed (typically ≈ 2 T at 1.9 K for the state-of-the-art Nb_3Sn strands) and χ is the ratio between the effective filament size at 0 T and B_0. This modification is applied to the nested-ellipses model, but can be also applied to the Wilson model. The model lacks microscopic rigor, aiming to calculate and predict the macroscopic behaviour of the magnet rather than finding a theory to be used by material scientist. Figure 93 compares the measured magnetization to the computed values for 0 %, 25 % and 50 % of reduction of the equivalent filament size for B< 2 T. Measurements correspond to a 0.7 mm diameter RRP 132/169 strand. Size sub-element is 41 μm, with a non-copper fraction of 45% and critical current density of 2640 A/mm^2 at 12 T and 4.2 K. Good agreement is shown between measurements and computations except for the region of B close to 0 where the computed magnetization is twice the measured magnetization for χ = 1. Thanks to the reduction of the effective filament size, better agreement is found in the low field region for measurements and computations.

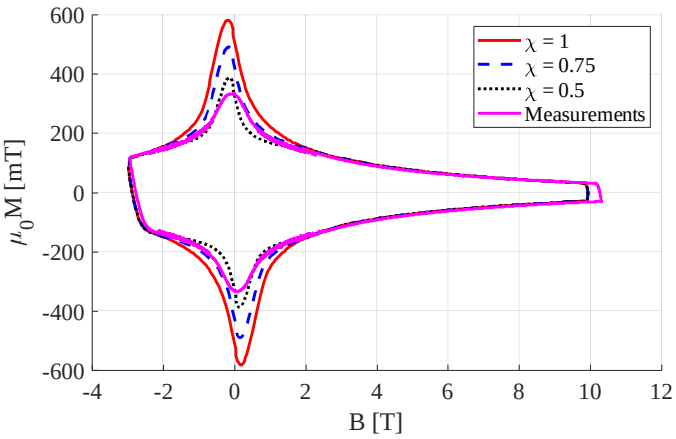

Figure 93. Magnetization as a function of applied field for a RRP 132/169 0.7 mm strand at 1.9 K, with D_{eff} = 41 μm, J_c(12 T, 4.5 K) = 2640 A/mm^2 and 1.25 copper to superconductor ratio. Computed magnetization assuming three different levels of reduction of equivalent filament size for B < 2 T.

As described in the introduction, in addition to the current loops that are fully superconducting, the so-called *persistent currents*, loops where the currents couple superconducting paths through resistive portions, referred to as *coupling currents* contribute as well to the distortion of the field. The inter-filament currents circulating between filaments in the strand normal matrix, were described in [5.21] to a first approximation in terms of two parameters. One is the shape of the coil, the other (which contains most of the material parameters) is the time constant. The coupling currents in any wire is proportional to the internal rate of change of flux density, *dB/dt*, averaged over a volume containing many filaments. Therefore, the internal field is proportional to dB/dt and related to the external field B_0 by

$$B = B_0 - \tau\frac{dB}{dt} \qquad \text{Eq. 40}$$

The magnetic moment associated is then

$$M = -\frac{n\tau}{\mu_0}\frac{dB}{dt} \qquad \text{Eq. 41}$$

where τ is the time constant of the system containing the parameters of the superconductor. In the case of a round filament wire, n = 2 and the time constant is

$$\tau = \frac{\mu_0}{2\rho_e}\left(\frac{L_{pf}}{2\pi}\right)^2 \qquad \text{Eq. 42}$$

L_{pf} is the strand twist pitch and ρ_e the effective transverse resistivity of the strand which depends on the field level due to the magneto-resistivity of the copper matrix. $\tau \sim 30$ ms for the HL-LHC strands, and *dB/dt* 0.01 T/s for a typical ramp, so the magnetization generated by the inter-filament coupling currents is three orders of magnitudes lower than the persistent current magnetization and can be neglected. The inter-strand coupling currents, circulating between strand in the cable can be described using the same approach. [5.22] derived the time constant for a flat cable as,

$$n\tau = \mu_0 \frac{N^2 L_p^2 w^2}{120 R_c} \qquad \text{Eq. 43}$$

where w is the cable width, L_p the twist pitch (≈ 100 mm), N the number of strands (40) and R_c the contact resistance (≈ hundreds of μΩ for cored cables). With a *dB/dt* 0.01 T/s, the magnetic moment generated by inter-strand coupling currents is orders of magnitude lower than the persistent current effect.

5.3 Impact of persistent and coupling currents in the field errors

As described in section 5.2, the magnetic moment generated by coupling currents is an order of magnitudes lower than the persistent current magnetization effect. The measured sextupole during MBHSP103 ramp rate cycles is shown in Figure 94, where the current is ramped at 10 A/s (nominal), 20 A/s, 40 A/s and 80 A/s. Measurements are done following a stair-step cycle. A pre-cycle at 50 A/s with a flattop current of 11.85 kA and a reset current of 100 A preceded the measurements. As it can be seen in the plot, coupling currents, dependent on the ramp rate, have a negligible impact on the field quality compared to the persistent currents. For that reason, the rest of the section focuses on the impact of persistent current magnetization effects in field quality.

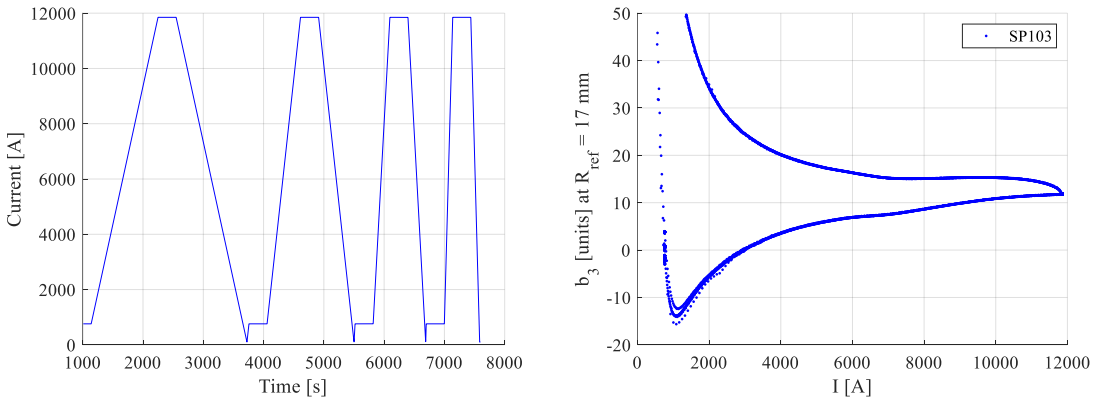

Figure 94. Right: time versus current profile for a ramp rate cycle in MBHSP103 at 10 A/s (nominal), 20 A/s, 40 A/s and 80 A/s, a pre-cycle at 50 A/s with a flattop current of 11.85 kA and a reset current of 100 A preceded the measurements. Right: measured sextupole component of the field during the cycles at different ramps, showing a negligible impact of the ramp rate on the measured field errors.

The magnetization of each filament contributes to the field in the bore. Several methods have been used in literature to predict the impact of magnetization currents in the aperture field [5.23]-[5.26]. The main difference among them is the model of the strand

magnetization. Most of the methods compute the field map in the coil due to the transport current, then compute the persistent current magnetization induced by the local field change in the strand and integrate the elementary contribution of the persistent currents over the coil cross section. In principle, the field in the coil depends on the persistent current magnetization, so the process shall be iterative. In practice, the field is dominated by the transport current so the contribution of the persistent current to the field is small and iteration is not needed. In this work, we modify the method developed in [5.16] implemented in ROXIE (Routine for the Optimization of magnet X-sections, Inverse field calculation and coil End design) [5.27]. The method includes this effect, iterating to consider the field from the transport current, the iron yoke and the persistent currents. The field arising from the coil is calculated analytically by means of the Biot-Savart-Law. As described in section 0, from the source currents, the source vector potential on the coupling boundary between the non-meshed air domain (boundary element domain, BEM) and the finite element domain (FEM) with non-linear magnetic properties is calculated. The system of linear equations is solved iteratively to get the vector potential from the FEM domain. The total magnetic induction is obtained by superposing the source fields from the coil, the iron contribution, and the filament magnetization. Details of this coupling are described in [5.16]. Figure 95 shows the sextupole component in the MBH-11 T single aperture magnet as a function of the current, iterating the transport current, the iron yoke, and the persistent currents, compared to the sextupole component without M(B) iteration. Since the distance between the coil and the inner yoke is large, the iteration with the iron yoke is not needed. The iteration of the persistent currents with the transport current has only a small impact at low field. In the more general case where the magnetic induction rotates in the plane of the filament cross-section (for example in orbit corrector magnets), the determination of the magnetization effect is far more complicated, and the iteration is needed for an accurate prediction [5.16].

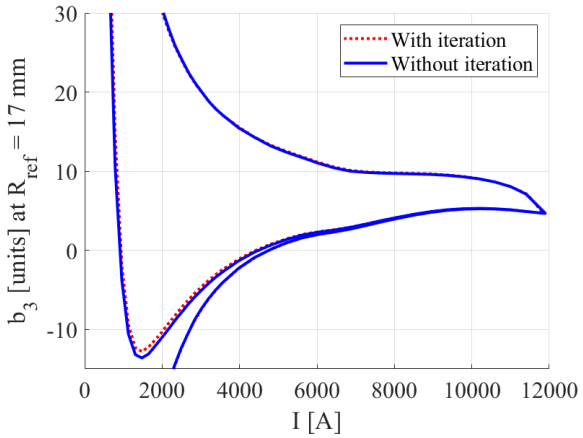

Figure 95. Calculated values of the sextupole multipole in the single aperture MBH-11 T magnet versus the current. Blue curve: without applying the M(B)-iteration; Red curve: The M(B)-iteration is applied.

To further illustrate the effect of the M(B) iteration Figure 96 shows the magnetization in the 11 T coil at injection current (760 A) with and without the iteration. Without the iteration, the repercussion of the magnetic field produced by the induced persistent currents on the external field cannot be considered. With the use of the iteration, after each iteration the external magnet induction increases, resulting in a reduction of the observed induced currents. The persistent currents magnetic field reduces, increasing the region of low induction.

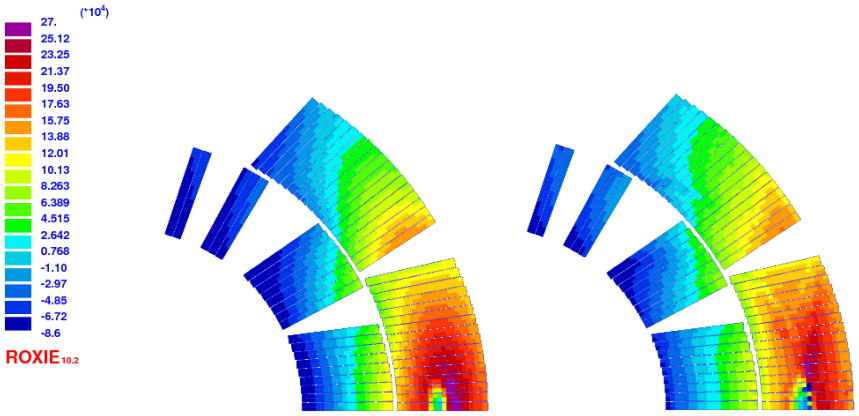

Figure 96. Magnetization (A/m) in the first quadrant of the cross-section of a MBH-11 T dipole coil computed without M(B)-iteration (left) and with M(B)-iteration (right) at injection current

5.4 Persistent current effects in HL-LHC Nb_3Sn magnets

If all strands have homogeneous properties in the magnet cross section, the persistent current magnetization obeys the same symmetry rules as the transport current generating only the so-called allowed multipoles. In a dipole (B_1 main field), allowed multipoles are b_3, b_5, b_7…while in a quadrupole magnet (B_2 main field) allowed multipoles are b_6, b_{10}, b_{14}… Due to the larger filament size and higher current density, strand magnetization effects are about a factor ten larger than in the LHC-NbTi magnets. Figure 97 and Figure 98 show the first allowed multipoles measured in the MBH-11 T and MQXF short model magnets. Coils were wound with different conductor layout during the development phase, which results in a large spread of the measured magnetization effect. The characteristics of the cables used in each coil are summarized in Annex I.

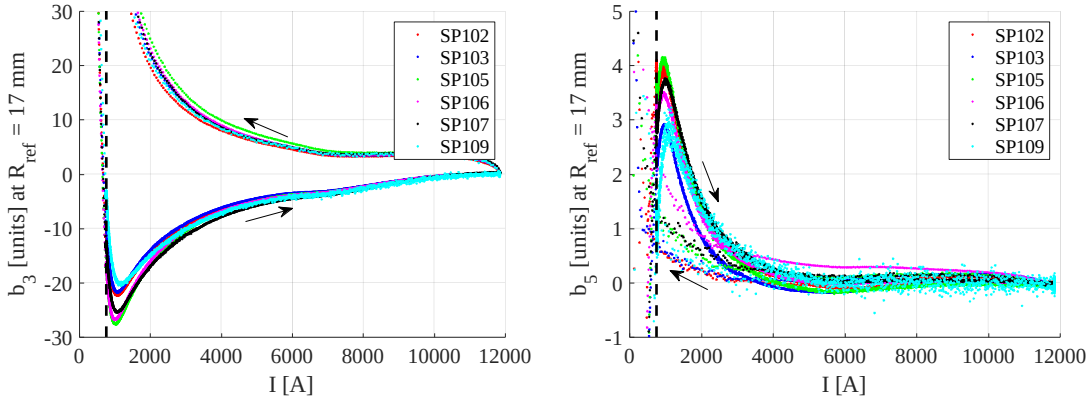

Figure 97. Sextupole and decapole coefficients measured in the MBH-11 T short model dipoles, as a function of current. The data has been shifted to remove the geometric contribution (average value of the multipole at 5 kA). The thick vertical line indicates the injection current.

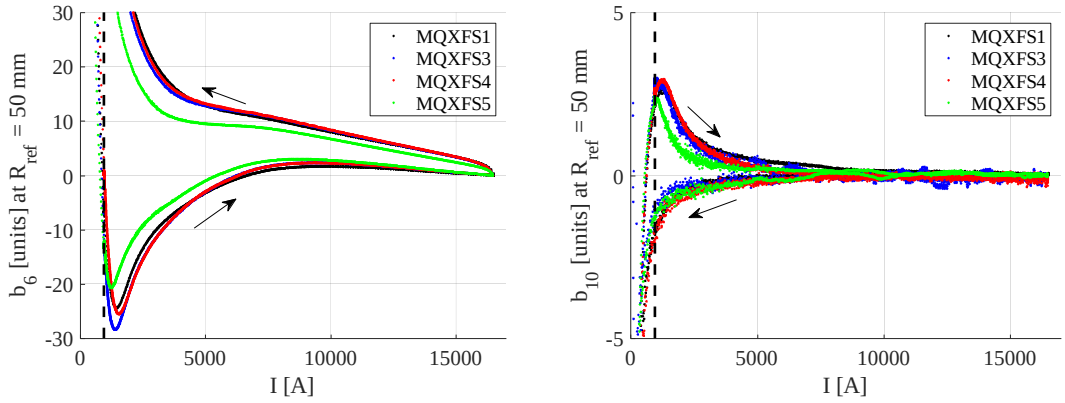

Figure 98. b_6 and b_{10} coefficients measured in the MQXF short model quadrupole, as a function of current. The data has been shifted to remove the geometric contribution (average value of the multipole at 5 kA). The thick vertical line indicates the injection current.

The injection current for the MBH-11 T magnet is 760 A, which corresponds to an injection field of 0.76 T, 0.35 T below the penetration field. The measured persistent current effect at injection is Δb_1^{PC} = -200.1 ± 41.8, Δb_3^{PC} = -87.2 ± 10.4 and Δb_5^{PC} = 4.0 ± 1.1 (all data is quoted as average ± standard deviation, in units at a reference radius of 17 mm). The data above represents averages and standard deviations on the complete magnet sample, irrespective of the cable combinations used to wind the coils. Table 57 summarizes the width of the hysteresis at injection current, 1.5 kA and 5 kA for all the magnets measured.

Table 57. Average width of the hysteresis of the first allowed multipoles measured at 1.9 K in the MBH-11 T Dipoles at 760 A (injection), 1.5 kA and 5 kA. Units at R_{ref} = 17 mm.

	760 A			*1500 A*			*5000 A*		
Magnet	Δb_1^{PC}	Δb_3^{PC}	Δb_5^{PC}	Δb_1^{PC}	Δb_3^{PC}	Δb_5^{PC}	Δb_1^{PC}	Δb_3^{PC}	Δb_5^{PC}
SP102	-188.5	-80.0	3.7	-106.2	-48.9	2.7	-28.2	-11.1	0.3
SP103	-184.4	-77.5	2.4	-90.2	-47.3	2.1	-17.9	-10.5	0.0
SP105	-207.9	-101.5	1.9	-110.0	-58.1	1.1	-9.1	-12.3	-1.7
SP106	-258.4	-96.3	0.2	-138.6	-55.0	-0.7	-20.3	-11.5	-2.9
SP107	-126.4	-93.8	2.1	-123.3	-55.3	1.7	-25.2	-12.2	-0.7
SP109	-235.0	-73.9	0.0	-119.2	-49.2	1.9	-11.2	-11.8	0.2

On the MQXFS quadrupoles measured at cold, the effect at injection is Δb_2^{PC} = -186.2 ± 31, Δb_6^{PC} = 89. 1 ± 4.8 and Δb_{10}^{PC} = 3.5 ± 0.7 units. As in the case of the dipoles, the data represents averages and standard deviations on the complete magnet sample wound with different types of cables. Focusing only in the RRP magnets (MQXFS1, MQXFS3 and MQXFS4), Δb_2^{PC} = -220.2 ± 12.5, Δb_6^{PC} = 85. 3 ± 1.7 and Δb_{10}^{PC} = 4.0 ± 0.2 units. The Δb_2 in the magnets wound with PIT cable (MQXFS5 and MQXFS6) is about 30 % lower than the magnets wound with RRP conductor. Table 58 summarizes the width of the hysteresis at injection current, 2 kA and 7 kA for all the magnets measured.

Table 58. Average width of the hysteresis of the first allowed multipoles measured at 1.9 K in the MQXFS quadrupoles at 960 A (injection), 2 kA and 7 kA. Units at R_{ref} = 50 mm.

	960 A			*2000 A*			*7000 A*		
Magnet	Δb_2^{PC}	Δb_6^{PC}	Δb_{10}^{PC}	Δb_2^{PC}	Δb_6^{PC}	Δb_{10}^{PC}	Δb_2^{PC}	Δb_6^{PC}	Δb_{10}^{PC}
MQXFS1	-229.4	-85.1	3.8	-128.1	-50.6	2.2	-49.6	-10.1	0.3
MQXFS3	-228.8	-87.5	3.9	-121.5	-72.1	2.0	-29.1	-10.4	0.1
MQXFS4	-202.5	-83.3	4.3	-100.9	-73.2	2.4	-26.1	-10.5	0.2
MQXFS5	-153.3	-96.7	3.5	-93.2	-66.1	1.1	-30.6	-9.6	0.2
MQXFS6	-160.0	-89.0	2.3	-90.9	-65.0	1.0	-9.1	-9.8	0.0

The first dipole and quadrupole magnets tested, MBHSP102 and MQXFS1 respectively, are taken as example to validate the model to predict persistent current effect. Measurements are compared in Figure 99 to computed values using two methods: i) the semi-analytical nested ellipses model for strand magnetization implemented in ROXIE [5.16]; ii) the modified version of the nested ellipses model with a reduction of the critical current at low field, method proposed by the author in this thesis. A 50 % linear reduction of the magnetization for field levels below 2 T is assumed to account for the impact of flux jumps on strand magnetization (see Eq. 39). If the reduction of the magnetization due to flux jumps is not included (standard nested ellipses model), there is large discrepancy between model and measurements. Agreement is better when the decrease of the equivalent filament size is included in the model.

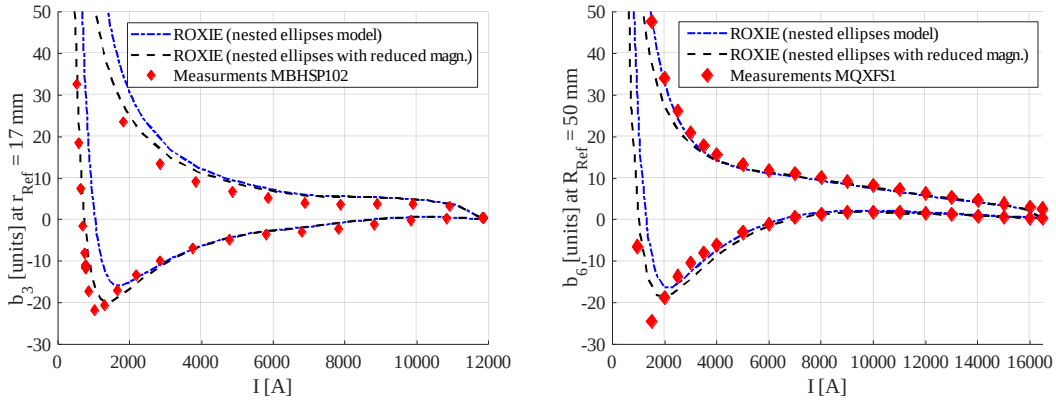

Figure 99. Measured and calculated b_3 field component as a function of the magnet current for the MBHSP102 dipole (left). Measured and calculated b_6 field component as a function of the magnet current for the MQXFS1 (left). Data has been shifted to suppress the geometric component and have 0 harmonics at collision energy.

The next sections will assess the impact of the type of conductor, temperature, magnet symmetry and reset current to the persistent current effect at injection.

5.4.1 Sensitivity to conductor type

As discussed in section 5.2, strand magnetization is proportional to the effective filament size, critical current density, and superconductor fraction. During the development phase, coils with different types of conductors were built and tested (see Annex I), which results in different magnetization. As an example, in MQXF short model program, the magnet

MQXFS5 was built with PIT 192 conductor whereas MQXFS1, MQXFS3 and MQXFS4 were built with RRP coils. Figure 100 shows the measured b_6 as a function of the current during a machine cycle. A geometric offset is applied to the measurements in order to have $b_6 = 0$ at collision energy. The change on b_6 from injection to nominal is 20 units for the MQXFS5 and 25-30 units for the rest of the magnets. The smaller magnetization in MQXFS5 is expected since the sub-element diameter of the superconducting filaments is 41 μm (PIT 192 conductor), to be compared to 55 μm for RRP 108/127 and 50 μm for RRP 132/169.

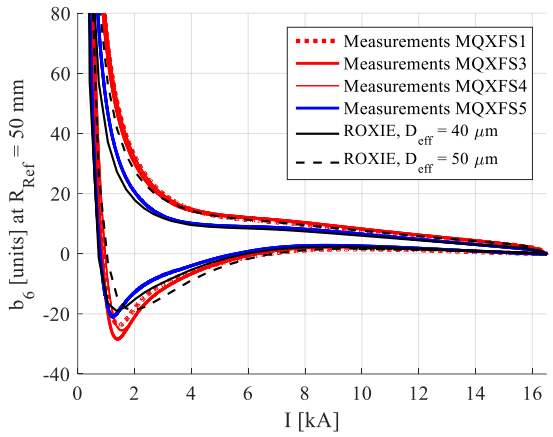

Figure 100. Measured b_6 as a function of the magnet current in MQXFS short model magnets. An offset is applied to all the measurements to have $b_6 = 0$ at collision energy.

To further assess the impact of the conductor type on the persistent current effect, the width of the hysteresis loop is studied at ≈ 40 % of the nominal current, which corresponds to ≈ 5 kA in the MBH-11 T dipole and ≈ 7 kA in MQXF. Figure 101 shows a linear relation between the product of the superconductor fraction and the effective filament size and the width of the hysteresis loop in the first allowed multipole. At injection current, see Figure 102, the dependence is weaker in the case of the DS-11T since the Nb_3Sn strands are affected by partial flux jumps. In MQXFS, the magnets built with PIT conductor have larger magnetization at injection in spite of the smaller filament size (see Figure 102, right). PIT conductor is less affected by flux jumps [5.30], so it has a larger magnetization at low field in spite of the smaller filament.

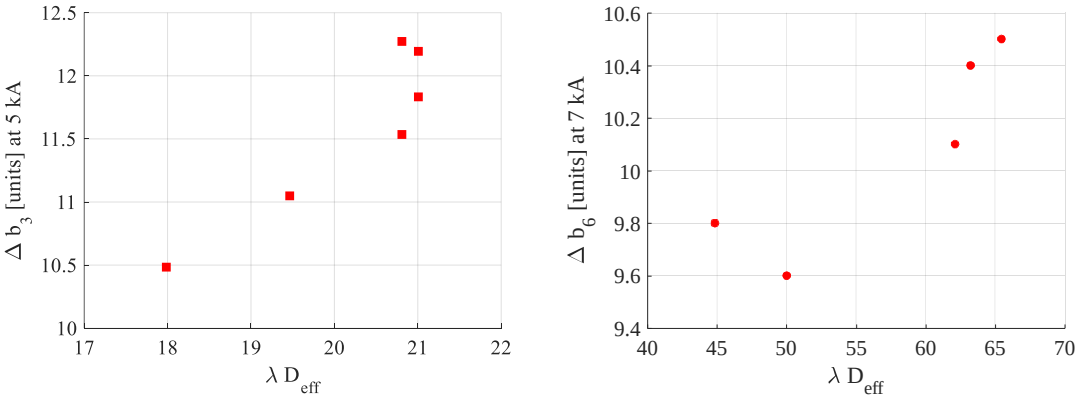

Figure 101. Normal sextupole generated by persistent current in all DS-11T short model magnets (left) and normal duodecuple in MQXFS magnets (right) vs effective filament size and superconductor fraction at 40 % of nominal current.

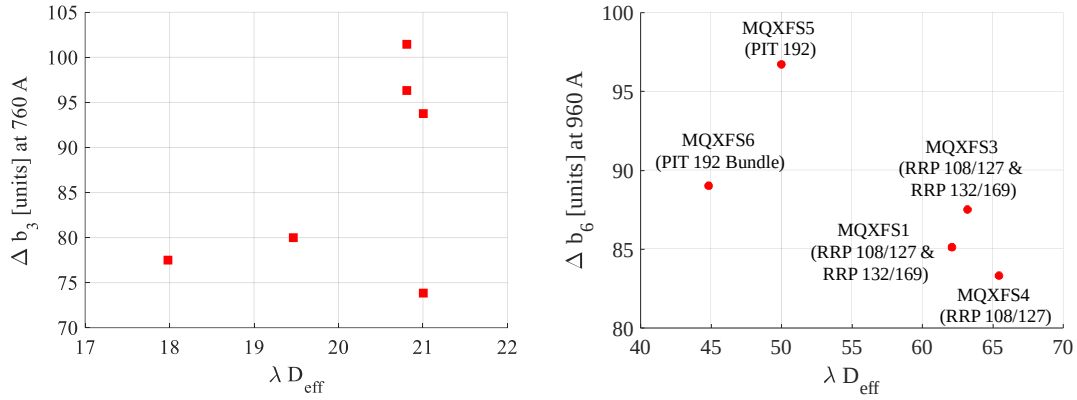

Figure 102. Normal sextupole generated by persistent current in all DS-11T short model magnets (left) and normal duodecuple in MQXFS magnets (right) vs effective filament size and superconductor fraction at injection current.

5.4.2 Sensitivity to temperature

The strand magnetization is proportional to the critical current density. The critical current density of Nb_3Sn is typically 10 % lower at 4.5 K than at 1.9 K, so field distortions due to persistent current effect should be smaller at 4.5 K. Figure 103 shows the first allowed harmonic measured during a machine cycle at 4.5 K and 1.9 K in MBHSP104 and MQXFS3. At high current, the persistent current effects are smaller at 4.5 K as expected due to the lower critical current density. Nevertheless, at low current the persistent currents have a greater contribution at 4.5 K. This is consistent with the measurements on strands that show that due to the flux jumps the magnetization is smaller at lower temperatures (see Figure 92). Table 59 summarizes the width of the magnetization at injection current and 40 % of the nominal current for both magnets. At high current, the magnetization width is 8-10 % smaller at 4.5 K whereas at injection magnetization is 10-20 % larger at 4.5 K.

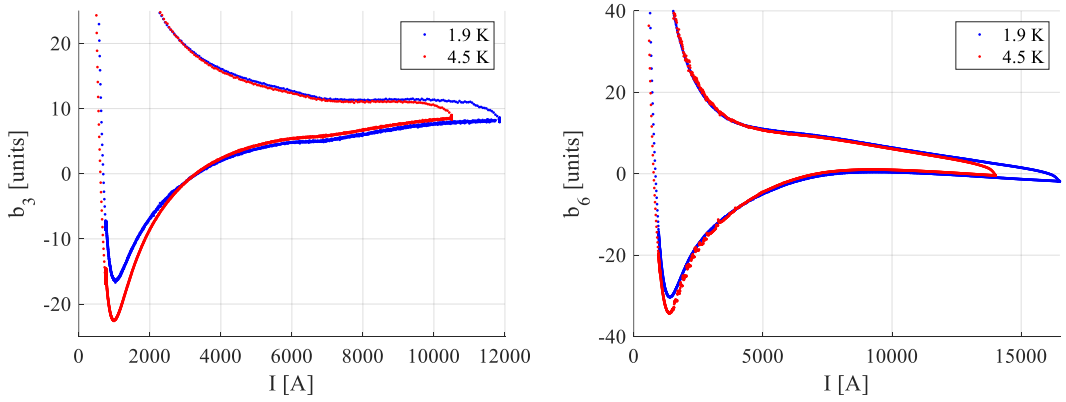

Figure 103. Measured b_3 in MBHSP104 and b_6 in MQXFS3 during a machine cycle at 1.9 K and 4.5 K.

Table 59. Width of the hysteresis of the first allowed multipoles measured at 1.9 K and 4.5 K in MBHSP104 and MQXFS3 at injection and 40 % of the nominal current.

Magnet	Δb_3^{PC} at 1.9 K [units]	Δb_3^{PC} at 4.5 K [units]	Diff [%]
MBHSP104 at 760 A	63.1	78.8	22
MBHSP104 at 5000 A	10.3	9.4	-10
Magnet	Δb_6^{PC} at 1.9 K [units]	Δb_6^{PC} at 4.5 K [units]	Diff [%]
MQXFS3 at 960 A	85.3	95.2	11
MQXFS3 at 7000 A	9.7	9.0	-8

5.4.3 Sensitivity to magnet symmetry

If all strands are perfectly placed and have homogeneous properties in the magnet cross section, the persistent current magnetization obeys the same symmetry rules as the transport current generating only allowed multipoles. Nevertheless, in case of a geometrical error, persistent currents generate also non-allowed multipoles. To illustrate this effect, MQXFS1 is taken as an example where coils with a systematic difference in coil size and different conductor layout were combined. In MQXFS1, two coils were produced by LARP and two coils were produced by CERN. Due to the systematic differences in coil size among CERN and LARP coils and the use of a different stack of superconductor (108/127 for LARP coils and 132/169 for CERN coils), an impact on a_4 is expected. Figure 104 shows that the hysteresis loop can be foreseen when the difference between strand magnetization for CERN and LARP coils is considered. According to ROXIE model, a 6 % difference between strand magnetization for LARP and CERN coils allows to reproduce the measured harmonics.

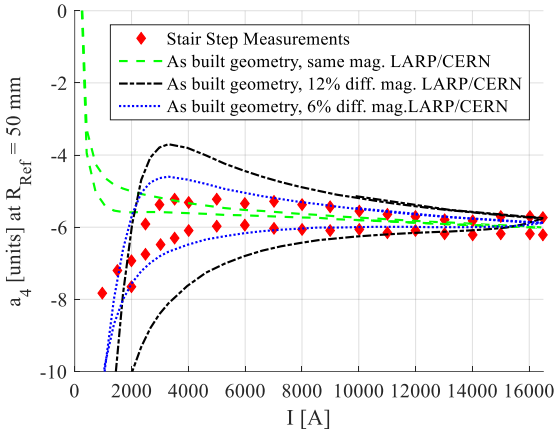

Figure 104. Measured and calculated a_4 field component in MQXFS1 as a function of the magnet current.

5.4.4 Sensitivity to reset current

The minimum field used for cycling has a strong influence on the field errors at injection [5.31]. In the case of the MBH-11 T magnets, the current baseline considers the installation of 300 A bi-polar trim power converters across the 11 T dipoles, meaning that they could be pre-cycled to a different current that the MB dipoles. In order to validate the model, measurements were performed in MBHSP101 at 4.5 K using different reset

currents. Figure 105 shows the dependence of b_3 for different reset currents, suggesting that current profile with a low reset current will significantly simplify the sextupole correction. Measured b_3 at injection current is 10 units for I_{reset} = 100 A, 45 units for I_{reset} = 350 A and 70 units for I_{reset} = 500 A. Computed sextupole with ROXIE does not account for the reduction on magnetization at low field values.

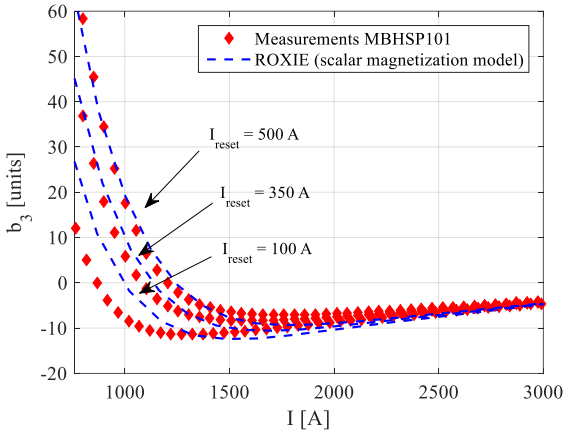

Figure 105. Sextupole field error as a function of the magnet current for different pre-cycles. Measurements on MBHSP101 at 4.5 K.

5.4.5 Scaling

The data presented above summarize an extensive set of measurements for the HL-LHC Nb_3Sn magnets, and it is interesting to put it in perspective with previous experience in accelerator magnets. The main results of the dipole production for the Tevatron [5.33]-[5.36], HERA [5.37]-[5.40], RHIC [5.41] and LHC [5.44]-[5.48], as well as the dipole development for UNK [5.43] and SSC [5.42] are summarized in Table 60. All magnets were built using NbTi superconductor. To achieve a consistent picture, we limit the discussion to the first allowed harmonic in a dipole, the normal sextupole, which is available for all the magnets presented. The data cover a large span of magnet variants with different cross sections, coil inner radius, coil thickness, strands and reference aperture for the beam. We can use them to see whether we can find a general scaling of the effect, a useful tool to interpret and anticipate the properties of different magnet designs. The injection field for the MBH-11 T dipole in the LHC is 0.75 T, i.e., before the penetration field. For this particular analysis, the injection field of the 11 T is considered to be 1.49 T in order to be at injection above the penetration field, as it is the case for the NbTi dipoles.

Table 60. Summary of main magnet features, strand properties and measured persistent current effects in dipoles

	Tevatron	HERA		UNK	SSC	RHIC	LHC	HL-LHC 11 T
		ABB	LMI					
R_{coil} (mm) (1)	38.1	37.5		40	25	40	28	30
B_{inj} (T) (2)	0.66	0.23		0.68	0.66	0.4	0.54	1.49
R_{ref} (mm)	25.4	25	25	35	10	25	17	15
J_c (A/mm^2) (3)	1850	2400	2200	2300	2750	2834	1698	2500
D (μm) (4)	9	14	16	10	6	6	7	43
M_{inj} (mT) (5)	6.4(6)	21.0	22.0	10.3(6)	7.2(6)	6.3	14.2(7)	172
λ (-)	0.35	0.36	0.36	0.42	0.40	0.31	0.38	1.15
σM_{inj} (mT) (8)	0.30	0.21	0.22			0.14	0.33	5
b_3^{PC} (units) (9)	5.54	35.7	36.7	10.1	2	5.7	7.04	26.14
σb_3^{PC} (units) (9)	1.14	1.6	1.2			0.14	0.36	2.00

NOTES:

(1) coil inner radius

(2) bore field at injection. For the HL-LHC 11 T dipoles, the bore field at injection is 0.75 T but 1.49 T is chosen for the analysis to be above the penetration field.

(3) at 5 T, 4.2 K except for LHC, where it is quoted at 10 T, 1.9 K and the HL-LHC 11 T dipole where is quoted at 12 T 4.2 K

(4) geometric filament diameter

(5) magnetization at B_{inj}, as scaled from measured data

(6) computed using Eq. (32) with values of $J_c(B_{inj})$, D and λ

(7) data for the inner layer strand and cable

(8) standard deviation of the magnetization at B_{inj}

(9) b_3 generated by persistent current at B_{inj}

(10) standard deviation of the b_3 generated by persistent current at B_{inj}

The magnetization of a small element of superconducting strand dS in the cross section of a superconducting coil, located at a complex position vector z_m, contributes to any given complex multipole of order n with an amount:

$$dC_n^{coil} = -\frac{n\mu_0 dm^*}{2\pi R_{ref}^2}\left(\frac{R_{ref}}{z_m}\right)^{n+1} \qquad \text{Eq. 44}$$

where dm is the magnetic moment per unit length of strand, related to the magnetization per unit strand volume $M = M_y + iMx$ and the strand surface element dS as follows:

$$dm = \left(M_y + iM_x\right) \qquad \text{Eq. 45}$$

and we indicate the complex conjugate operator by an asterisk. The overall contribution of the persistent current magnetization to C_n is obtained by integration of Eq. 44 over the cross section of the strands in the coil:

$$C_n = -\frac{n\mu_0 R_{ref}^{n-1}}{2\pi}\int_{S_{coil}} \frac{dm^*}{z_m^{n+1}} \qquad \text{Eq. 46}$$

In order to compare different designs, the coil cross section is approximated as a sector of inner radius R_{coil}, thickness ΔR and extending over an angle $\Delta\theta$ from the magnet midplane. Furthermore, we neglect the contribution of the iron yoke. The multipole of order *n* generated by the persistent current magnetization of the strands in this coil is given by:

$$C_n = -4\mathrm{m}\sigma\mu_0 R_{ref}^{n-1}\int_0^{\Delta\theta}\int_{R_{coil}}^{R_{coil}+\Delta R}\left(\frac{M_y - iM_x}{r^{n+1}}\right)e^{-i(n+1)\theta} r dr d\theta \qquad \text{Eq. 47}$$

where the index *m* stands for the order of the main field multipole generated by the magnet, i.e., $m = 1$ for a dipole, $m = 2$ for a quadrupole, etc., and σ is the fraction of strand surface in the total coil area. The integral of the magnetization in Eq. 47 cannot be solved analytically in the general case, as it contains implicitly a dependence on the local field in the coil. Let us assume nonetheless that the result of this integral scales proportionally to the magnetization at the inner coil radius, where the field is approximately equal to the bore field *B*. We expect this to be true only in the case of high order multipoles, that depend mostly on the magnetization of the strands close to the magnet bore, and to hold only approximately for low order multipoles. Under this hypothesis, we can write

$$C_n \propto \mathrm{M(B)}\left(\frac{R_{ref}}{\mathrm{R}_{coil}}\right)^{n-1} \qquad \text{Eq. 48}$$

Using the quantities defined in Table 60, and the relation above, we can define the following scaling relation for the sextupole harmonic in a dipole

$$\mathrm{b}_3^{\mathrm{PC}}\mathrm{B}_{\mathrm{inj}}\left(\frac{R_{coil}}{\mathrm{R}_{\mathrm{ref}}}\right)^2 \propto \mathrm{M(B)} \qquad \text{Eq. 49}$$

Figure 106 shows a scatter plot of the scaled sextupole vs magnetization at injection field as summarised in Table 60. The scaling of Eq. 49 appears to be working reasonably well in the range tested, and thus can be used as desired for b_3^{PC}. This scaling law was developed for NbTi magnets [5.28] and the author of this thesis applied it for Nb_3Sn dipoles.

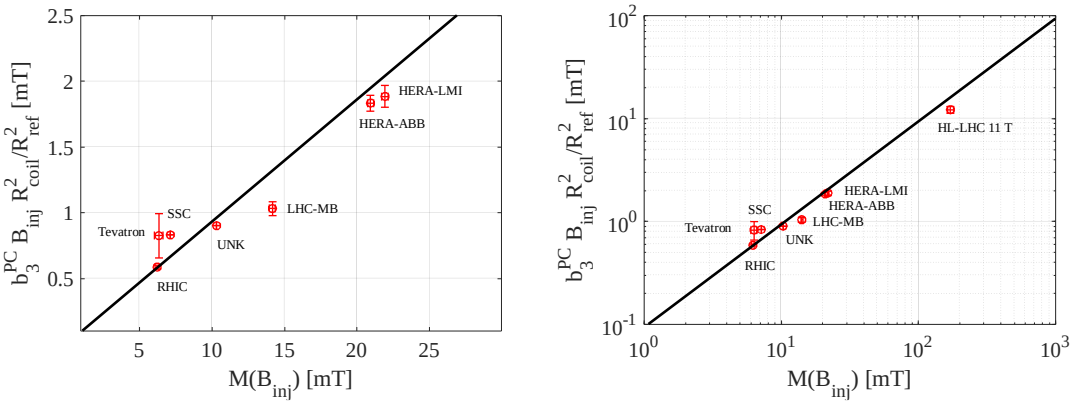

Figure 106. Scaling of normal sextupole generated by persistent currents vs. strand magnetization at injection field. The plot on the left shows only NbTi dipoles whereas the plot in the right includes as well the HL-LHC Nb_3Sn 11 T dipole.

5.5 Impact of persistent and coupling currents in AC losses

In the presence of changing magnetic field, losses due to induced currents are generated in the superconductor. An estimate of the heat deposition into the Helium bath is required to dimension the cryogenic system. Figure 107 shows a typical current cycle in the LHC, with a ramp down from nominal current at 10 A/s after a beam dump, an injection plateau of around 20 minutes followed by a ramp up to nominal. The total duration of the cycle (from beam dump to collision) is around 60 minutes.

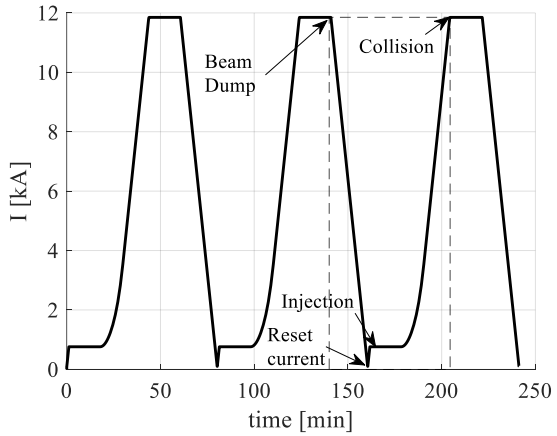

Figure 107. Typical current vs time cycle for a main bending dipole in the LHC.

AC losses come from three sources: i) Magnetization (Hysteresis) losses, P_{hyst}, due to the persistent currents in the superconductor filaments; ii) Inter-Filament Coupling losses, P_{ifcc}, due to the currents circulating between filaments in the strand normal matrix; iii) Inter-Strand Coupling losses, P_{iscc}, due to the induced current loops formed by different strands. Losses on the electromagnetic parts are typically negligible in accelerator magnets due to the slow ramp rate and the use of laminated structures. AC losses have been extensively studied in the literature, and here we present a simplistic assessment to set the appropriate scaling.

The largest source of AC loss heating in HL-LHC Nb_3Sn magnets is the **hysteretic loss** in the superconductor. The energy dissipated per unit strand volume for a fully penetrated filament ($\beta > 1$), for a triangular cycle between B_{max} and B_{min} is [5.3]:

$$E_{\perp} = \frac{2}{3}\frac{B_{max}^2}{2\mu_0}\lambda\left(\frac{2}{\beta} - \frac{1}{\beta^2}\right) \quad \text{Eq. 50}$$

where β is the normalized field change ($\beta = (B_{max}-B_{min})/B_p$). B_p is the penetration field swing (twice the virgin penetration field as defined in Eq. 1), which depends on the effective critical current density and the filament size. Hysteresis losses depend then on the field level but are independent of the ramp rate. If charged to full current, for HL-LHC Nb_3Sn magnets the AC loss is in the order of 1 MJ/m^3.

The second source of loss is the **inter-filament coupling loss** generated by induced currents flowing in normal conducting materials in contact with the superconductor. The IFCC power per unit volume P_{ifcc} during a field sweep with rate *dB/dt* is given by [5.3]:

$$P_{ifcc} = \frac{2\tau}{\mu_0}\left(\frac{dB}{dt}\right)^2 \quad \text{Eq. 51}$$

with $\mu_0 = 4\pi 10^{-7}$ H/m, dB/dt the flux change rate in the conductor and τ is the coupling current time constant for the conductor (see Eq. 42). For the DS-11T magnet, $\rho_e \sim 10^{-10}\Omega$m and L_{pf} is 14 mm, so coupling current time constant is $\tau \sim 30$ ms. The energy dissipated per unit strand volume due to the inter-filament coupling losses during a triangular cycle between extremes 0 and B_{max} at constant ramp-rate *dB/dt* is:

$$E = \frac{4\tau}{\mu_0} B \frac{dB}{dt} \quad \text{Eq. 52}$$

For a ramp from 0 to 11 T and a *dB/dt* of 0.01 T/s, the loss per unit conductor volume is in the order of 1 kJ/m^3, which is three orders lower than the hysteretic AC loss.

The last source of loss in a Rutherford cable is the **inter-strand coupling loss**, generated at the contact points between superconducting strands of a cable due to coupling currents between strands. The eddy current loss in the Rutherford cable due to inter-strand coupling currents per unit cable volume, for a field change perpendicular to the broad face of the cable is [5.29]:

$$P_{iscc,\perp} = \frac{1}{6}\frac{wL_p}{t}\left(\frac{N^2}{20R_c} + \frac{1}{R_a}\right)\left(\frac{dB^{\perp}}{dt}\right)^2 \quad \text{Eq. 53}$$

where w is the cable width, L_p the twist pitch, t the thickness, N the number of strands and R_c and R_a the contact resistance. The energy dissipated per unit cable volume during a triangular cycle (between extremes B_0 and $B_0 + \Delta B_{\perp}$) at constant ramp-rate $\dot{B}_{\perp}$ is:

$$E_{iscc,\perp} = \frac{1}{3}\frac{wL_p}{t}\left(\frac{N^2}{20R_c} + \frac{1}{R_a}\right)\Delta B_{\perp}\frac{dB^{\perp}}{dt} \quad \text{Eq. 54}$$

For a field change in the direction perpendicular to the thin face of the cable, the inter-strand coupling power per unit volume P_{iscc} is given by [5.29]:

$$P_{iscc,\parallel} = 2\frac{tL_p}{w}\frac{1}{R_a}\left(\frac{dB^{\parallel}}{dt}\right)^2 \quad \text{Eq. 55}$$

The energy dissipated per unit cable volume during a triangular cycle (between extremes B_0 and $B_0 + \Delta B_{//}$) at constant ramp-rate $\dot{B}_{//}$:

$$E_{iscc,\parallel} = 4\frac{tL_p}{w}\frac{1}{R_a}\Delta B_\parallel \frac{dB_\parallel}{dt} \qquad \text{Eq. 56}$$

The 40 strands MBH-11 T cable has a width, thickness and twist pitch of 14.7 mm, 1.25 mm and 100 mm respectively. With a transverse inter-strand resistance (R_c) ∼ 300 μΩ and an adjacent inter-strand resistance (R_a) ∼ 3 μΩ, the inter-strand coupling losses are in the order of 5 kJ/m^3 for a triangular ramp from 0 to 11 T at 0.01 T/s, which are negligible compared to the hysteresis losses.

5.6 AC losses in HL-LHC Nb_3Sn magnets

Loss experiments were performed in the 11 T and MQXF Nb_3Sn short model magnets and prototypes. In order to decouple the effect of the inter-filament, which depend on the field level, and the inter-strand coupling currents, AC loss measurements are typically performed at two different field levels. For the low field cycle, the current is changing from $I_{min} = 0.1 \cdot I_{nom}$ to $I_{max} = 0.5 \cdot I_{nom}$ and back to I_{min}. For the high field cycle, the current is changing from $I_{min} = 0.5 \cdot I_{nom}$ to $I_{max} = I_{nom}$ and back to I_{min}, typically with a ramp rate of 10 A/s to 200 A/s. The total energy loss across the whole magnet was obtained by integrating the product between the current and the voltage for the total time of each current cycle at different ramp rates (see [5.26]):

$$W = \int_0^{t_c} VI\, dt \qquad \text{Eq. 57}$$

The dependence of total energy loss with the ramp rate can be fitted using the linear expression:

$$W = W_{hyst} + 2k(I_{max} - I_{min})\frac{dI}{dt} \qquad \text{Eq. 58}$$

Where the energy at $dI/dt = 0$ is the hysteresis loss. The factor k corresponds to the measured slope of the ramp-rate dependent losses. Figure 108 shows the measured AC loss in two 11 T single aperture short models, showing that the main contribution to the losses are the hysteresis losses. As described in section 5.5, inter-strand and inter-filament coupling losses are negligible.

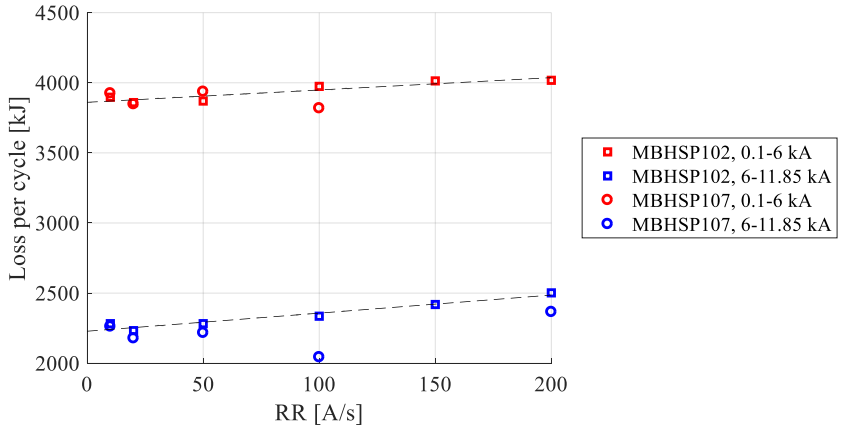

Figure 108. AC loss measured in 11 T single models

Several magnets were measured at 1.9 K, using different current cycles. The results are summarized in Table 61. In all the cases, ISCC and IFCC losses are negligible compared to the hysteresis losses.

Table 61. Measured AC loss in MBH-11 T and MQXF magnets, for trapezoidal current cycles at the specified maximum/minimum currents.

	L_m (m)	I_{min} (kA)	I_{max} (kA)	k [J·s/A^2]	E_{hyst} [kJ]
MBHSP102	1.69	0.1	6	$7.5 \cdot 10^{-5}$	3.86
MBHSP102	1.69	6	11.85	$1.1 \cdot 10^{-4}$	2.29
MBHSP107	1.69	0.1	6	$7.7 \cdot 10^{-5}$	3.88
MBHSP107	1.69	6	11.85	$6.8 \cdot 10^{-5}$	2.20
MQXFBP2	7.15	0.2	8.1	$8.9 \cdot 10^{-3}$	47.36
MQXFBP2	7.15	8.1	14	$6.7 \cdot 10^{-3}$	18.81
MQXFBP2	7.15	0.2	14	$7.9 \cdot 10^{-3}$	74.45

The measured hysteresis per unit length is compared in Table 62 to the computed loss in ROXIE using nominal conductor parameters. The model over-estimates the loss at low field and gives an accurate estimate at high field. The main source of the discrepancy at low field is that the AC-loss computation does not include the reduction of the magnetization due to flux jumps, as it was done for the field quality in section 5.4. Agreement between measurements and computations would improve when including this effect.

Table 62. Comparison of measured and computed hysteresis in MBH-11 T and MQXF magnets

	L_m (m)	I_{min} (kA)	I_{max} (kA)	$E_{hyst, measured}$ [kJ/m]	$E_{hyst, model}$ [kJ/m]	Error [%]
MBHSP102	1.69	0.1	6	2.28	3.01	24
MBHSP102	1.69	6	11.85	1.36	1.27	-6
MBHSP107	1.69	0.1	6	2.30	3.01	24
MBHSP107	1.69	6	11.85	1.30	1.27	-2
MQXFBP2	7.15	0.2	8.1	6.62	6.81	3
MQXFBP2	7.15	8.1	14	2.63	2.67	1
MQXFBP2	7.15	0.2	14	10.41	9.64	-8

Since the field in the coil cross section is not uniform, the energy is not equally distributed in the strands. Figure 109 shows the average power loss per strand, for each of the six blocks in the 11 T coil cross section. The energy deposited in the high field turns (block 4) is around three times the loss in the outer layer mid-plane block (block 5).

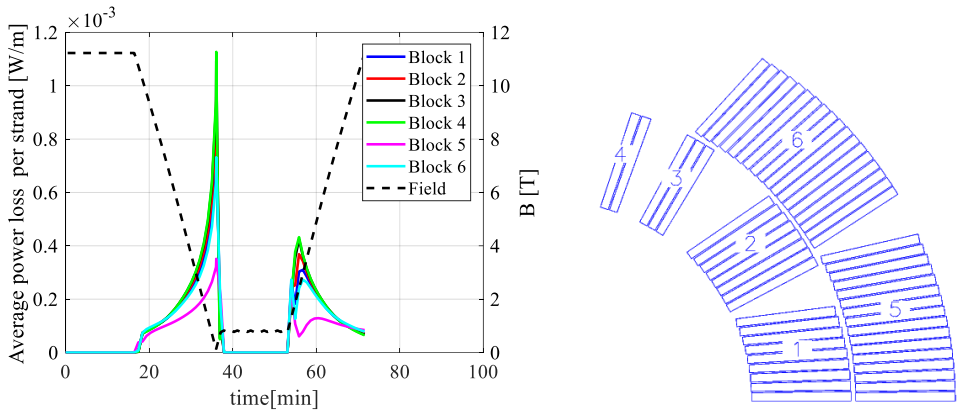

Figure 109. Average power loss in each superconducting strand for the 11 T magnet.

It is important to notice that due to the larger strand magnetization at low field, most of the energy is deposited at the end of the ramp down and the beginning of the ramp up. Figure 110 shows the integral of the energy loss as a function of the time for a typical cycle in the 11 T.

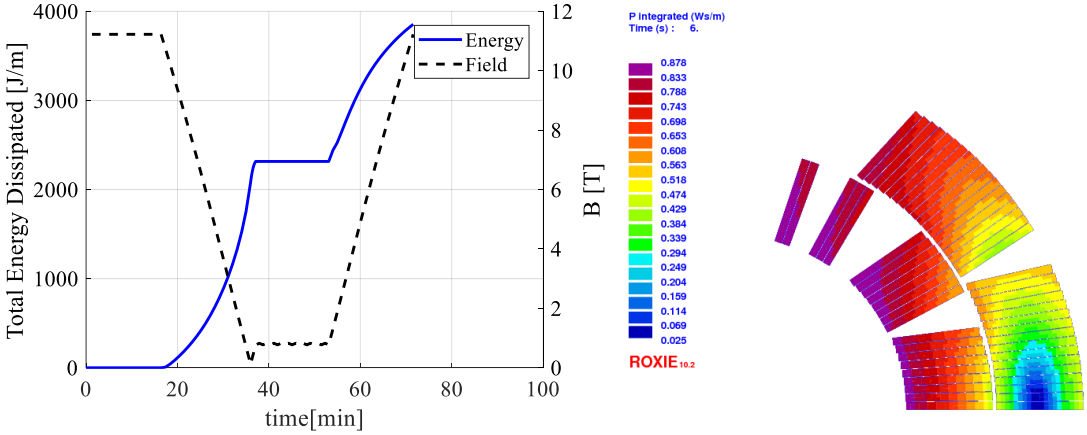

Figure 110. Example of the total hysteresis energy loss for a typical current profile in the 11 T single aperture magnet. Left: total energy deposited and field in the aperture as a function of time. Right: Integrated power per strand in the coil cross section for a ramp down and ramp up cycle.

The additional heat load due to the magnetization cycle of the 11T magnets must be absorbed by the cryogenic system. Each cryogenic sector of the LHC is about 3.3 km, and has available a maximum cooling power of 0.8 W/m when averaged over its full length. Given a static load of about 0.5 W/m, a residual cooling power of about 0.3 W/m is available to deal with sector wide transients. The heat load of the Nb_3Sn-based 11T dipoles contribute an estimated current ramp dissipation of ~ 3.7 W/m each (~ 2207 J/m/aperture x 2 apertures in 1200 s), i.e. ~ 20 W per 11T dipole. In the current LHC, Nb-Ti dipole current ramp dissipation is about 0.18 W/m [5.49]. Since the plan for the HL-LHC is to replace only two 14.3 m LHC-MB dipoles by shorter 11 T dipoles, the impact on the cryogenic system is negligible. Nevertheless, in view of a machine based on Nb_3Sn magnets, the cryogenic system needs to be dimensioned accordingly.

5.7 Conclusions

In the presence of a changing magnetic field, current loops are induced in the conductor: *persistent currents* are fully superconducting whereas *coupling currents* couple superconducting paths through resistive portions. Inter-filament coupling currents are due to currents circulating between filaments in the strand normal matrix and inter-strand coupling currents are induced current loops formed by different strands. For the operation

parameters of the Nb_3Sn magnets for the HL-LHC, inter-strand and inter-filament currents are orders of magnitudes smaller than the persistent currents, so their impact on field distortions and ac loss is negligible when compared to the persistent current effects.

The filament diameter in state-of-the-art Nb_3Sn conductor is ≈ 50 μm, 10 times larger than in the Nb-Ti LHC dipole which has two main implications for the operation of these magnets in an accelerator: i) larger field errors at injection, which in particular for the main bending dipoles in the arc need to be corrected using sextupole and octupole correctors; ii) additional heat load due to the magnetization cycle that must be absorbed by the cryogenic system. Flux jumps at 1.9 K introduce a degree of uncertainty in the contribution of the magnetization. The author proposes in this work an approach to account for the flux jumps through a reduction of the effective filament size. The model is discussed and validated with experimental data on the MBH-11 T dipole and MQXF quadrupole.

To set order of magnitudes, the change of b_3 from injection to nominal current in the MBH-11T is 20-25 units, to be compared to ≈ 7 units in the LHC-MB NbTi dipoles. The heat dissipation during a current ramp is 0.2 W/m for the LHC-MB dipoles, to be compared to 3.7 W/m for the MBH-11 T Nb_3Sn dipoles. For the HL-LHC, the plan is to replace only two 14.3 m LHC-MB dipoles by shorter 11 T dipoles, so larger field errors and cryogenic load can be absorbed by the system. Nevertheless, in view of a machine based on Nb_3Sn magnets, persistent current effects represent a considerable handicap in term of field quality and heat load to the cryogenic system, indicating that a major reduction of the strand magnetization, innovative magnet design and accurate modelling are needed to advance in the quest for improved accelerator magnet performance. The main result of about forty years' experience in the design and manufacturing of accelerator magnets is that today persistent current effects can be predicted and controlled. The author applied a scaling law developed for NbTi magnets in the MBH-11 T magnet. The scaling law that relates the sextupole field distortions in a dipole magnet to the magnetization of the strands used for winding still holds for Nb_3Sn magnets and gives thus confidence in our understanding of the phenomenon.

5.8 References

[5.1] P. Schmüser, "Persistent Current Effects in Superconducting Accelerator Magnets," Vols. 10.1007/978-1-4684-5859-6_3, 1990.

[5.2] L. Cooley, D. Larbalestier and K. Amm, "Challenges and opportunities to assure future manufacturing of magnet conductors for the accelerator sector," DOI 10.48550/ARXIV.2208.12379, 2022

[5.3] M. N. Wilson, Superconducting Magnets., Monographs on Cryogenics, Oxford University.

[5.4] C. Bean, "Magnetization of High Field Superconductors," Rev. Mod. Phys., pp. 36, pp. 31-39, 1964.

[5.5] J. Kato, J. Appl. Phys, vol. 15, pp. 695-702, 1976.

[5.6] Minervini, Analysis of Loss Mechanism in Superconducting Winding of Rotating Electric Generators, MIT: PhD Thesis, 1981.

[5.7] Ashkin, J. Appl. Phys., vol. 50, pp. 7060-7066, 1979.

[5.8] C. Pang, A. Campbell and P. McLaren, "Losses in Nb/Ti multifilamentary composite when exposed to transverse alternating and rotating fields," in IEEE Transactions on Magnetics, vol. 17, no. 1, pp. 134-137, January 1981, doi: 10.1109/TMAG.1981.1061025.

[5.9] Kim, Phys. Rev. Let., vol. 9, no. 7, pp. 306-309, 1962.

[5.10] D. Tommasini, “Baseline specifications and assumptions for accelerator magnet,” CERN-ACC-2016-0030, 2016.
[5.11] E. H. Brandt, “Superconductors of Finite Thickness in a Perpendicular Magnetic Field: Strips and Slabs,” Physical review B,, vol. 54, no. 6, pp. 4246-4263, August 1996.
[5.12] R. A. Hartmann, “A Contribution to the Understanding of AC Losses in Composite Superconductors,” Ph.D. thesis, University of Twente, The Netherlands, 1989.
[5.13] J. V. Minervini, “Two-dimensional analysis of AC loss in superconductors carrying transport current,” Adv. in Cryo. Eng. Materials, vol. 28, pp. 587-599, 1982.
[5.14] C. Y. Pang, “Losses in type II superconducting wires due to alternating and rotating fields,” Ph.D. thesis, University of Cambridge, Cambridge, 1980.
[5.15] P. C. Rem, “Numerical Models for AC Superconductors,” Ph.D. thesis, University of Twente, The Netherlands, 1986.
[5.16] C. Vollinger, “Superconductor Magnetization Modeling for the Numerical Calculation of Field Errors in Accelerator Magnets,” Elektrotechnik und Informatik der Technischen Universitat Berlin zur Erlangung des akademischen Grades.
[5.17] Z. C. R. W. S. Le Naour, “The Enhancement of the Magnetization of Twisted Superconducting Strands due to the Distortion of the Filament Shape,” Proc. of 6th European Conf. Appl. Sup., pp. pp. 440-446, 2003.
[5.18] B. Bordini, “The bundle-barrier PIT wire developed for the HiLumi LHC project,” IEEE Trans. Appl. Supercond., vol. 27, no. 4, p. Art. no. 6000706., 2017.
[5.19] M. S. A.K. Gosh, “Magnetization and Critical Currents of Tin-Core Multifilamentary Nb_3Sn Conductors,” IEEE Trans. Mag., vol. 27, no. 2, pp. pp. 2407-2410, 1991.
[5.20] B. Bordini et al., "Magnetization and Inter-Filament Contact in HEP and ITER Bronze-Route Nb_3Sn Wires," in IEEE Transactions on Applied Superconductivity, vol. 21, no. 3, pp. 3373-3376, June 2011, DOI: 10.1109/TASC.2010.2092733.
[5.21] A.M. Campbell, A general treatment of losses in multifilamentary superconductors, Cryogenics, Volume 22, Issue 1, 1982, Pages 3-16, ISSN 0011-2275, https://doi.org/10.1016/0011-2275(82)90015-7.
[5.22] A.A. Akhmetov, Compatibility of two basic models describing the a.c. loss and eddy currents in flat superconducting cables, Cryogenics, Volume 40, Issue 7, 2000, Pages 445-457, ISSN 0011-2275, https://doi.org/10.1016/S0011-2275(00)00064-3.
[5.23] A. Bossavit, “Numerical Modelling of Superconductors in Three-Dimensions: a Model and a Finite Element Method,” IEEE Trans. Mag., vol. 36, no. 4, pp. pp. 3363-3366, 1994.
[5.24] L. Prigozhin, “The Bean Model in Superconductivity: Variational Formulation and Numerical Solution,” J. Comp. Phys., vol. 129, no. 1996, pp. pp. 190-200.
[5.25] T. Satiramatekul, F. Bouillault, A. Devred and L. Bottura, "Analytical & numerical modelings of elliptical superconducting filament magnetization," in IEEE Transactions on Applied Superconductivity, vol. 15, no. 2, pp. 3680-3683, June 2005, DOI: 10.1109/TASC.2005.849391.

[5.26] J. L. Bottura, “Calculation of Magnetization, Hysteresis and Power Dissipation in a Superconductor During Bipolar Field Cycles,” IEEE Trans. Appl. Sup., vol. 3, no. 1, pp. pp. 460-463, 1993.
[5.27] “cern.ch/roxie,” CERN, [Online].
[5.28] L. Bottura, personal communication
[5.29] V. E. Sytnikov e. al., “Coupling Losses in Superconducting Transposed Conductors Located in Changing Magnetic Fields,” Cryogenics, vol. 29, pp. 926-930, 1989.
[5.30] B. Bordini, D. Richter, P. Alknes, A. Ballarino, L. Bottura and L. Oberli, "Magnetization Measurements of High J_c Nb_3Sn Strands," in IEEE Transactions on Applied Superconductivity, vol. 23, no. 3, pp. 7100806-7100806, June 2013, Art no. 7100806, doi: 10.1109/TASC.2013.2240754.
[5.31] B. Auchmann, “Magnetic Analysis of a Single-Aperture 11 T Nb3Sn Demonstrator Dipole for LHC Upgrades.,” Proceedings of IPAC2012, New Orleans, Louisiana, USA.
[5.32] M. Di Castro, L. Bottura, D. Richter, S. Sanfilippo and R. Wolf, "Coupling Current and AC Loss in LHC Superconducting Quadrupoles," in IEEE Transactions on Applied Superconductivity, vol. 18, no. 2, pp. 108-111, June 2008, doi: 10.1109/TASC.2008.921305.
[5.33] A. Tollestrup, “Superconducting Magnets”, *Physics of High Energy Accelerators*, R.A. Carrigan, F.R. Hudson, M. Month, Eds., AIP Conf. Proc., **87**, pp. 699-804, 1982.
[5.34] A.K. Gosh, W.B. Sampson, P. Wanderer, “Magnetization, Critical Current, and Injection Field Harmonics in Superconducting Accelerator Magnets”, *IEEE Trans. Nucl. Sci.*, **32**, pp. 3684-3686, 1985.
[5.35] G. Annala, et al., “Analysis of the Sextupole Correction in the Tevatron”, FNAL-TD Internal Note TD-03-008, Beamsdoc 480, 2003.
[5.36] P. Bauer, et al., “Tevatron Magnetic Models. Geometric and Hysteretic Multipoles in the Tevatron Dipole”, FNAL-TD Internal Note TD-02-040, 2004.
[5.37] S. Wolff, “Superconducting HERA Magnets”, IEEE Trans. Mag., 24(2), pp. 719-722, 1988.
[5.38] A. Ghosh, W. Sampson, “Magnetization of HERA Quadrupole Cables”, BNL Magnet Division Note MDN-213-4, SSC-MD-158, 1987.
[5.39] H.R. Barton, et al, “Performance of the Superconducting Magnets for the HERA Accelerator”, Proc. of 11th Magn. Tech. Conf., pp. 147-152, 1990.
[5.40] H. Brueck, et al., “Persistent Current Effects in the Superconducting HERA Magnets and Correction Coils”, Proc. of 1990 European Part. Acc. Conf. , pp.
[5.41] A. Greene, et al., “Manufacture and testing of the Superconducting Wire and Cable for the RHIC Dipoles and Quadrupoles”, *IEEE Trans. Appl. Sup.*, **5**(2), pp. 397-399, 1995.
[5.42] Y. Zhao, “Current Dependence of Harmonic Field Coefficients of 5-cm Aperture, 15-m-Long SSC Dipole Magnet Prototypes, IEEE Trans. Appl. Sup., 3(1), pp. 674-677, 1993.
[5.43] A. Zlobin, “UNK Superconducting Magnets Development”, Nucl. Instr. Meth. Phys. Res., A, 333, pp. 196-203, 1993.
[5.44] F. Savary, et al., “Status Report on the Series Production of the Main Superconducting Dipole Magnets for LHC”, IEEE Trans. Appl. Sup., 16(2), 425-428, 2006.

[5.45] R. Wolf, “Persistent Currents in LHC Magnets”, IEEE Trans. Mag., 28(1), pp.374-377, 1992

[5.46] R. Wolf, S. Le Naour, “The Expected Persistent Current Field Errors in the LHC Main Dipole and Quadrupole”, LHC Project Note 230, 2000.

[5.47] S. Le Naour, et al., “Magnetization measurements on LHC superconducting strands”, IEEE Trans. Appl. Superconduct., 9(2), pp. 1763-1766, 1999.

[5.48] J.D. Adam, T. Boutboul, G. Cavallari, Z. Charifoulline, C.H. Denarie. S. Le Naour, D.F. Leroy, L. Oberli, D. Richter, A.P. Verweij, R. Wolf, “Status of the LHC superconducting cable mass production”, IEEE Trans. Appl. Sup., 12(1), pp. 1056-1062, 2002.

[5.49] O. Bruning et al., LHC design report, CERN, Geneva, CERN Yellow Reports: Monographs, 2004, doi 10.5170/CERN-2004-003-V-1, page 160,

6 DECAY AND SNAPBACK

6.1 Introduction

Precise control of the magnetic field uniformity remains a must for the next generation of accelerator magnets, and a good characterization of the so-called dynamic effects at injection is important due to their relative large amplitude and strong time dependence. Dynamic effects at injection, the field "decay" and following "snap-back", have been extensively studied for the Tevatron [6. 1], HERA [6. 2], SSC [6. 3] and the LHC magnets [6. 4]-[6. 8]. Indeed, the database and understanding of dynamic effects are quite well established for magnets built with Nb-Ti cables. The explanation of the mechanism [6. 7] is that during magnet ramps the unavoidable field variations in the coil ends, non-homogeneities in the splice and interstrand resistances induce current imbalance among the strands in the Rutherford cables. The diffusion of the current distribution during injection changes the local field along the cable, with an oscillating pattern. These field changes reduce the magnetization of the single filaments, and cause an apparent field to decrease during injection, the so-called "decay". After the end of injection, the magnet is ramped up again, the filament magnetization is re-established by the background field change, and the magnet field returns to the magnetization branch of the original hysteresis curve. This effect is called "snapback". Figure 111 shows the typical sextupole component as a function of the current in the LHC-MB dipoles, with a zoom of the decay and snapback during injection.

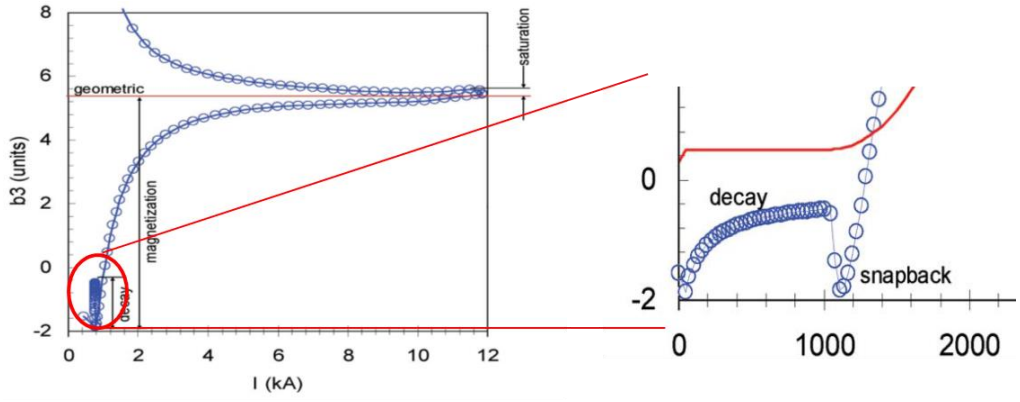

Figure 111. Sextupole component as a function of the current in the LHC-MB dipoles, with a zoom of the decay and snapback during injection. Courtesy of L. Bottura.

While we would expect the basic mechanisms to be identical in Nb_3Sn cables, only little data is available [6. 9]. In this section we present measured dynamic effects in the MBH-11 T and MQXF short models for the LHC High Luminosity upgrade. In order to provide systematic results, we measured the dependence of decay and snapback on the injection field level, powering history and temperature. Table 63 summarizes the current cycles that have been studied and compare the parameters to the LHC cycle profile and the

standard profile for the MB series magnetic measurements. The measurements are always preceded by a quench to erase the memory of the previous powering. The main attention in this paper is restricted to the first allowed multipoles for which the effects are systematic.

Table 63. Current cycle parameters

	dI/dt (A/s)	I_{FT} (A)	t_{FT} (s)	I_{inj} (A)	t_{inj} (s)	T (K)
Standard LHC MB cycle	10	11850	1000	760	1000	1.9
Standard MM MB cycle	50	11850	1000	760	1000	1.9
#01: MBHSP101	50	11250	1800	760	1000	1.9
#02: MBHSP102	50	11850	1800	760	1000	1.9
#03: MBHSP103	50	11850	1800	760	1000	1.9
#04: MBHDP101	50	11850	1800	760	1000	1.9
#05: MBHDP101	50	11850	1800	1100	1000	1.9
#06: MBHDP101	50	11850	1800	1700	1000	1.9
#07: MBHDP101	50	11850	1800	760	6000	1.9
#08: MBHDP101	50	4000	1000	760	1000	1.9
#09: MBHDP101	50	8000	1800	760	1000	1.9
#10: MBHDP101	50	10000	1800	760	1000	1.9
#11: MBHDP101	50	11850	60	760	1000	1.9
#12: MBHDP101	50	11850	900	760	1000	1.9
#13: MBHDP101	50	11850	1800	760	1000	1.9
#14: MBHSP104	50	11850	1800	760	1000	1.9
#15: MBHSP104	50	11850	1800	760	1000	4.5
# 16: MQXFS3	14	16470	1000	960	1000	1.9
# 17: MQXFS3	14	16470	1000	960	1000	4.5
# 18: MQXFS4	14	16470	1000	960	1000	1.9
# 19: MQXFS5	14	16470	1000	960	1000	1.9
# 20: MQXFS6	14	16470	1000	960	1000	1.9

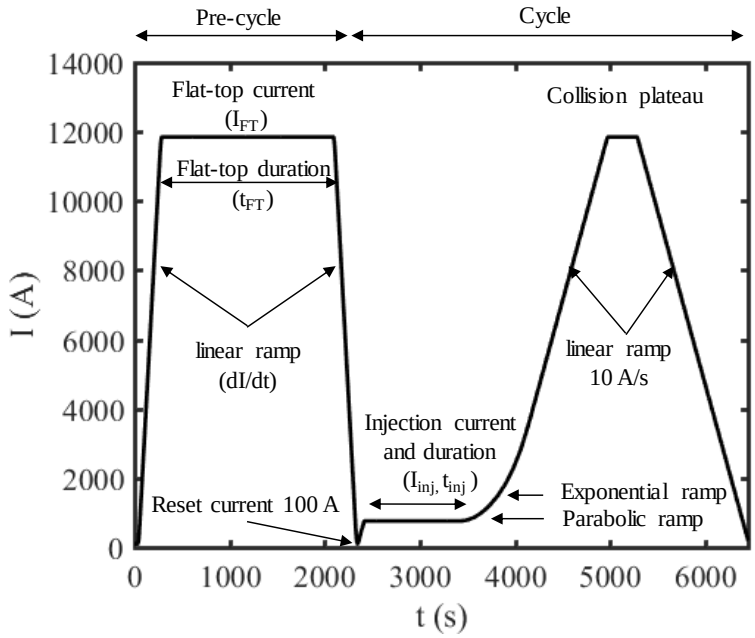

Figure 112. Current profile cycle parameters definition.

6.2 Decay

The multipole decay observed in the LHC Nb-Ti magnets can be characterized using a double exponential fit with a fast and slow mode for the decay [6. 1],

$$\Delta b_n(t, t_{inj}, \tau, d) = \delta(d(1 - e^{(t_{inj}-t)/\tau}) + (1-d)(1 - e^{(t_{inj}-t)/9\tau})) \quad \text{Eq. 59}$$

which holds for $I=I_{inj}$ and $t>t_{inj}$. t is the instantaneous time, t_{inj} is the time when the injections starts, I_{inj} is the current at injection, τ is the time constant and d is the normalized weight of the fast mode of the decay. The long injection plateau cycle performed in the MBH-11 T magnet has been used to characterize the dynamic response of the magnet. Figure 113 shows the variation of b_1, b_3 and b_5 during injection, shifted along the vertical axis to make the initial value at injection equal zero. The parameters used to fit the data using Eq. 59 are summarized in Table 64. Comparing to the LHC-MB [6. 8] the main difference is in the normalized weight of the fast mode of the decay. The amplitude of the decay is comparable to the MB dipoles, but in the case of the 11 T the change on b_3 and b_5 represents a net increase of the average coil magnetization which was never observed in LHC Nb-Ti magnets.

Table 64. Parameters obtained fitting Eq 59. to cycle #07

	Dimension	b_1	b_3	b_5
t	seconds	123.5	131.1	102.6
d	--	0.219	0.136	0.271
δ	units	4.23	-1.18	0.42

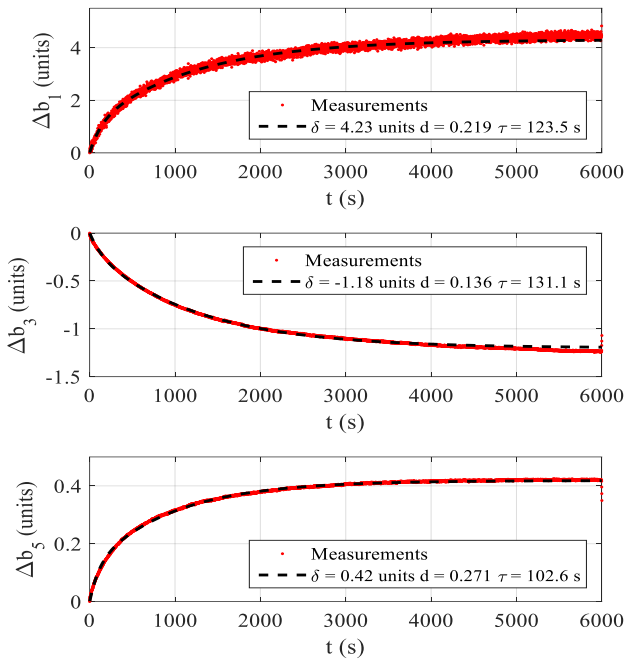

Figure 113. Integral of the decay of b_1, b_3 and b_5 measured during a 6000 ms injection plateau in MBHDP101 (Cycle #7).

Figure 114 shows the integral of the decay of b_6 measured in the MQXFS3 short model magnet. A net increase of the strand magnetization is observed, consistent with the findings in the MBH-11T short model magnets.

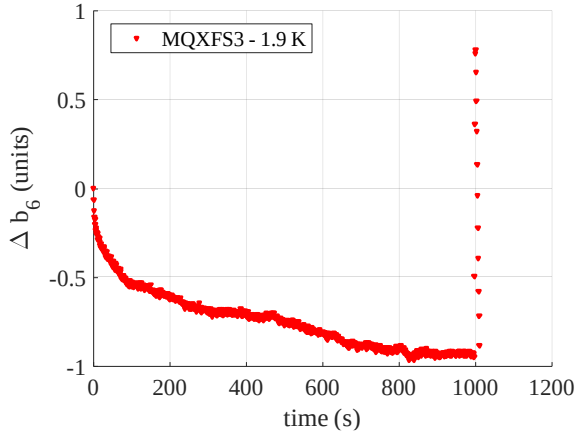

Figure 114. Integral of the decay of b_6 during the injection plateau in MQXFS3 (Cycle #18).

6.2.1 Longitudinal dependence

Figure 115 shows the strong longitudinal dependence of the amplitude of the decay. Larger decay and snapback is observed in the segments close to the magnet ends. The same behavior is observed in b_5.

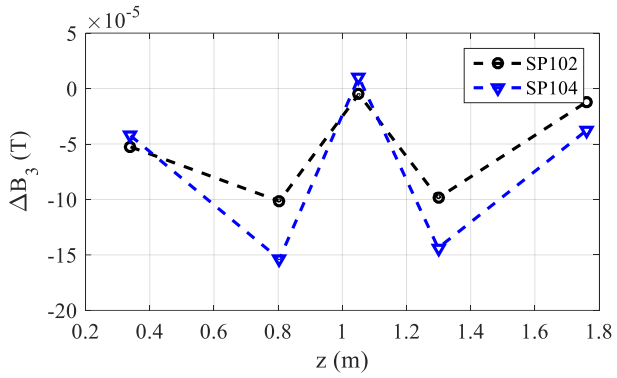

Figure 115. Amplitude of the decay at t = 1000 s as a function of the longitudinal magnet location for the standard measurement cycle.

6.2.2 Powering history dependence

The decay amplitude and snap-back of the allowed multipoles in the LHC magnets is known to be affected by the powering history of the magnet [6. 4], [6. 6]-[6. 8]. A systematic study of the impact of the flat-top current and duration on the decay has been performed in MBHDP101. Figure 116 shows the dependence of the flattop current and duration on b_1, b_3 and b_5. The amplitude of the decay increases at increasing the flat-top current and the flat-top duration. This is consistent with the large sample of Nb-Ti magnets measured at the LHC.

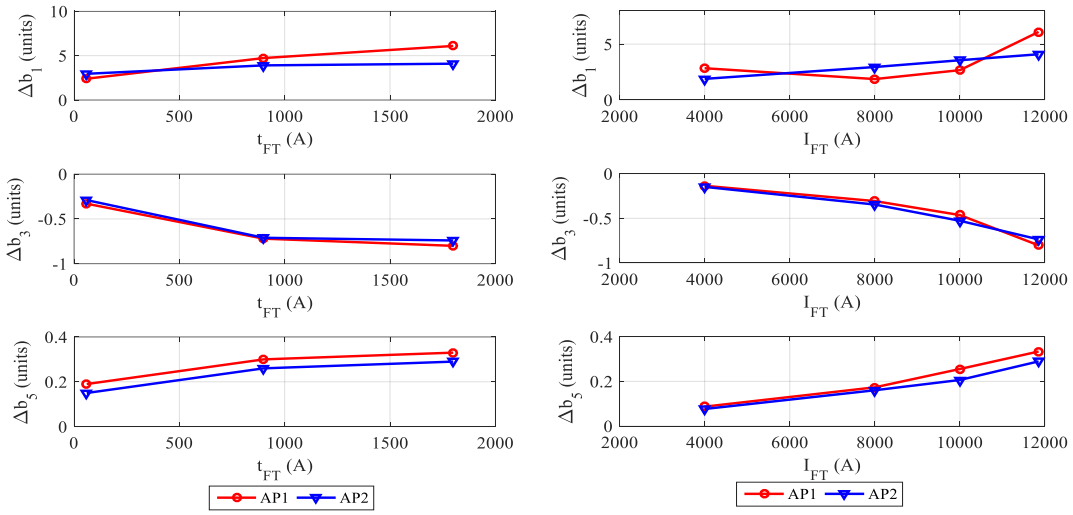

Figure 116. Left: Variation of the integral decay amplitude at t = 1000 s with the flattop duration for b_1, b_3 and b_5 for the two magnets apertures (AP1 and AP2). Right: Variation of the integral decay amplitude at t = 1000 s with the flattop current for b_1, b_3 and b_5 for the two magnets apertures (AP1 and AP2)

6.2.3 Magnet to magnet repeatability

Figure 117 compares the decay in MBHSP101, MBHSP102 and MBHDP101 for the standard measurement cycles. Measurements correspond to the integral decay along the longitudinal magnet axis, except for MBHSP101, where magnetic measurements were performed only in one half of the magnet (lead side). As expected, very similar behavior is observed in the collared coil tested in MBHSP102 when re-assembled in the double aperture MBHDP101. The close resemblance of the results points to the fact that the effects are systematic, and that the sign inversion observed in the decay is not a single anomaly.

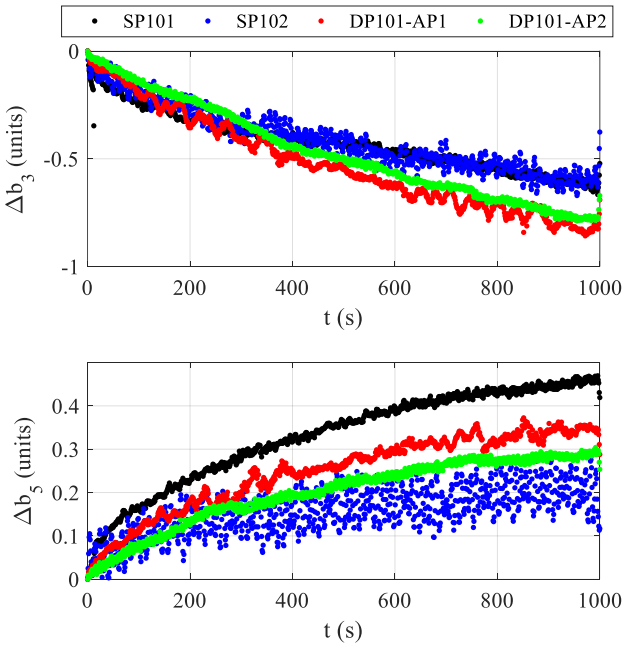

Figure 117. Integral decay for the standard measurement cycle in MBHSP101, MBHSP102 and MBHDP101 (cycles #1, #2 and #4).

The behaviour in MQXFS is less systematic. Figure 118 shows the measured decay in MQXFS short model magnets tested at CERN. The curve is vertically shifted so that b_6 is zero at injection. The left plot shows the integral decay whereas the plot on the right shows the behaviour of the magnet straight section. MQXFS3, built with RRP conductor (132/169 and 108/127) shows a behaviour consistent with the observations in 11 T models with a net increase of the filament magnetization. Measurements on strands showed that flux jumps are fewer and have smaller amplitude for PIT than for RRP conductor [6. 13], which could explain the difference in MQXFS5 and MQXFS6b. MQXFS6b shows no significant change on b_6 during the injection plateau and MQXFS5 shows a net decrease of the magnetization with a jump in the middle of the injection plateau. MQXFS4, built with RRP conductor shows an integral increase of the magnetization followed by a decrease. When focusing on the magnet straight section (right plot), the two RRP magnets show a very different behaviour with a negative/positive delta b_6 in MQXFS3/MQXFS4, respectively. Figure 119 shows the measured decay and snapback as a function of current. In both cases there is an initial increase of the magnetization when approaching the injection plateau, but the change of b_6 during the injection plateau has opposite behaviour in the two magnets.

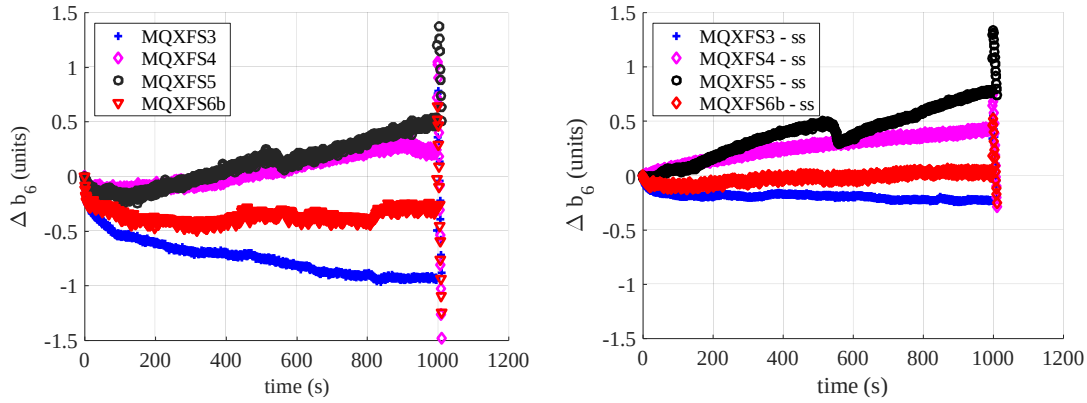

Figure 118. Measured decay in the MQXFS magnets tested at CERN. The curve is vertically shifted so that b6 = 0 at injection (960 A). Measurements performed at 1.9 K (cycle #16, #18, #19 and #20)). The plot on the left shows the integral decay and the plot on the right shows the decay in the magnet straight section.

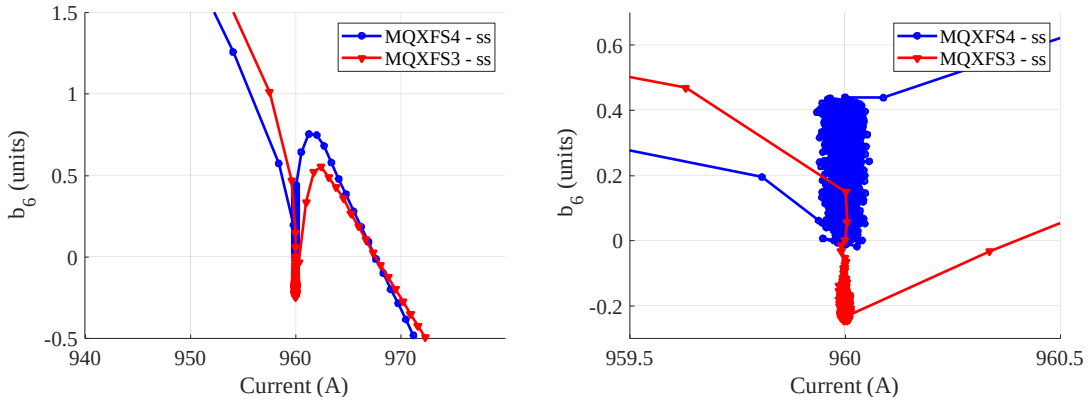

Figure 119. Measured decay and snapback as a function of current in the straight section of MQXFS3 and MQXFS4 magnets, both built with RRP conductor. The curve is vertically shifted so that b6 = 0 at injection (960 A). Measurements performed at 1.9 K (cycle #16 and #18).

6.2.4 Dependence on the injection level

Due to the larger filament size and higher current density, strand magnetization effects are about a factor ten larger than in the LHC-MB dipoles and at injection (I_{inj}=760 A), the magnet is operating before penetration (see Figure 6). In order to study the impact of the injection current level on the decay, different cycles varying the injection current level were performed in MBHDP101 (cycles #5 and #6 in Table I). As it can be observed in Figure 120, the direction of the decay does not change for an injection current level above penetration. The amplitude of the decay at the three field levels is comparable, 0.06 mT for I_{inj} = 760 A, 0.04 mT for I_{inj} = 1100 A and 0.05 mT for I_{inj} = 1700 A.

To further explore the effect of the current on the decay, we have examined the multipole changes at the flat-top currents. Figure 121 compares the decay at the injection plateau and the collision plateau for cycles #8, #9 and #10, where the flattop and collision current is 4 kA, 8 kA and 10 kA respectively. The sextupole is expressed in T for comparison showing that for high plateau current levels the change on b_3 represents a net decrease of the average magnetization, consistent with LHC-MB dipoles.

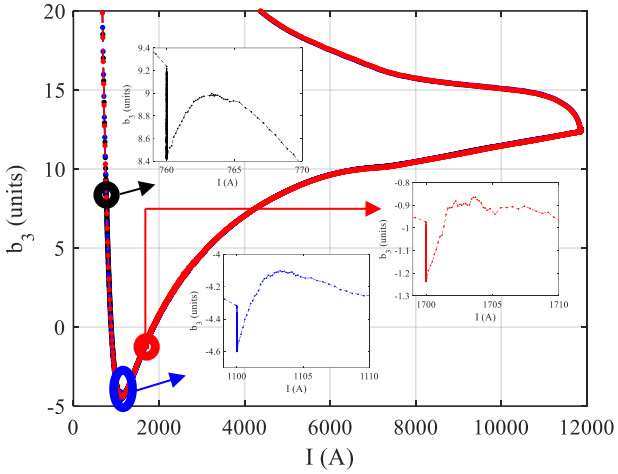

Figure 120. Integral decay for different injection current level in MBHDP101 (Cycles #4, #5 and #6).

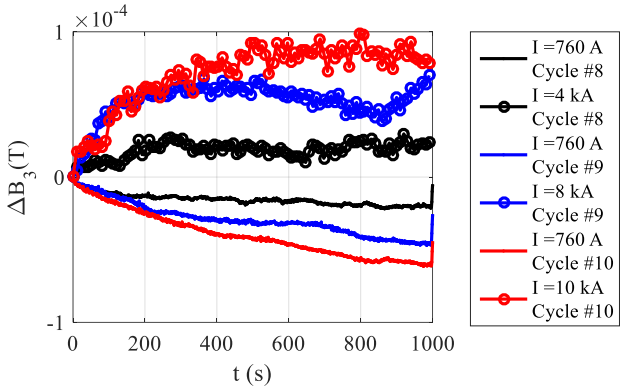

Figure 121. Measured integral decay amplitude for cycles #8, #9 and #10 during the injection plateau at 760 A and during the collision plateau at 4, 8 and 10 kA respectively.

6.2.5 Temperature dependence

The temperature dependence was studied in MBHSP104 by performing a standard measuring cycle at 4.3 K. Temperature has a large impact on the decay, with an inversion of the sign of the amplitude of the decay (see Figure 122). The same behaviour is visible in b_5. This is a very significant result, as the only difference between 4.2 K and 1.9 K is the magnetization of the filaments (including the effect of flux jumps). The same effect is present in MQXFS3 (Figure 123).

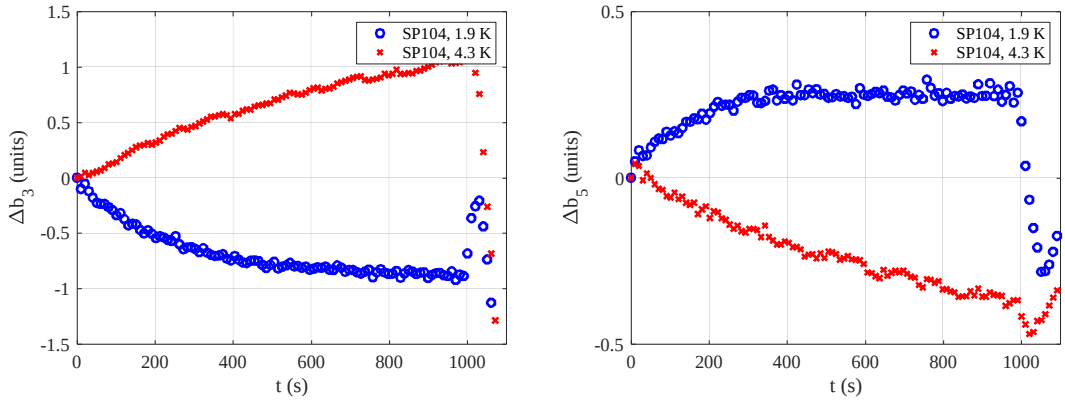

Figure 122. Impact of the operation temperature on the integral decay in MBHSP104.

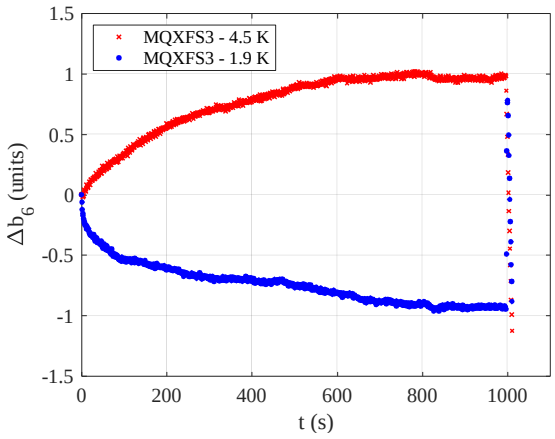

Figure 123. Impact of the operation temperature on the integral decay of b_6 in MQXFS3

6.3 Snapback

Figure 124 (left) shows the typical snap-back curve for b_3 in the 11 T magnets. The vertical line at 760 A corresponds to the decay at constant current, while the snap-back is the change in b_3 that takes place during the first 5 A of the acceleration ramp, when the b_3 is observed to return to the hysteresis branch that would have been measured without the injection stop (dashed line). In some cases, a decrease of magnetization is observed when ramping up the current before reaching the up-magnetization branch (see Figure 124, right). This atypical behavior, with first a very rapid increase (negative to decay), followed by a longer decrease (as we would expect in Nb-Ti magnets) is also visible in all rest of the magnets (see Figure 125, where the snapback amplitudes are plotted as a function of the current after subtracting the underlying hysteresis branch). The effect changes significantly with the longitudinal position of the measuring probe, so only integral values are reported (not available for MBSHP103, where two out of the seven segments of the probe where not acquiring data).

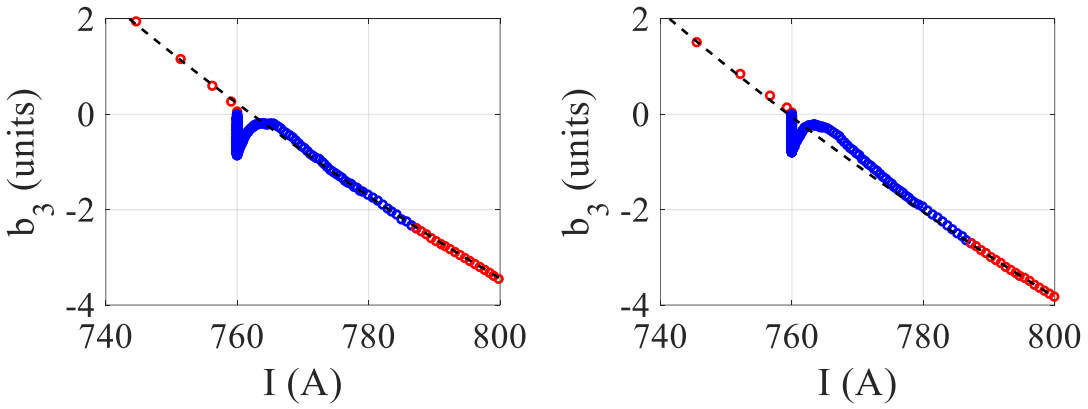

Figure 124. Snapback in MBHDP101 for cycle #4 in Aperture 1 (left) and Aperture 2 (right). The curve is vertically shifted so that $b_3 = 0$ at injection (760 A). The dashed line corresponds to the hysteresis branch that would have been measured without the injection plateau.

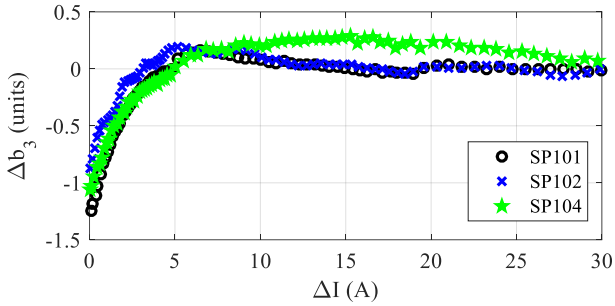

Figure 125. Snapback after subtracting the underlying hysteresis branch.

Figure 126 shows snap-back curve for b_6 in the MQXFS magnets. MQXFS5, the magnet built with PIT conductor, shows a very different behaviour: during the injection plateau, a net decrease of the average filament magnetization is measured, followed by a very slow recovery of the initial magnetization curve.

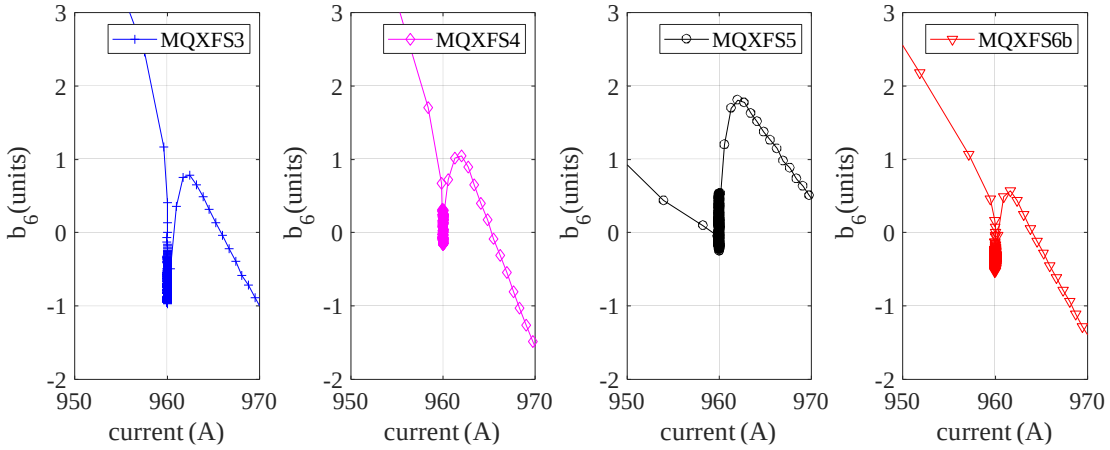

Figure 126. Snapback in MQXFS3 (RRP 108/127&132/169), MQXFS4 (RRP 108/127), MQXFS5 (PIT 192) and MQXFS6b (PIT192 & PIT 192 with bundle). The curve is vertically shifted so that b6 = 0 at injection (960 A).

For the LHC-MB dipoles it was found experimentally [6. 10], and proven analytically in[6. 11], that during the snap-back the first allowed harmonics follow an exponential law,

$$\Delta b_3{}^{snap-back}(t) = b_3{}^{decay} e^{-(I(t)-I_{inj})/\Delta I} \qquad \text{Eq. 60}$$

where $b_3{}^{decay}$ is the amplitude of the snapback, which depends on the powering history parameters, I_{inj} is the injection current and ΔI is the fitting parameter. In the LHC-MB dipoles, there is a linear correlation between the snapback amplitude and its decay constant,

$$g_3{}^{SB}(t) = \frac{b_3{}^{decay}}{\Delta I} \qquad \text{Eq. 61}$$

where $g_3{}^{sb}$ is the correlation coefficient to predict the value of ΔI for a given decay amplitude. To quantify this effect in the 11 T magnet, the standard machine cycles (Cycles #1, #2, #4 and #14) and the cycles performed in MBHDP101 to study the impact of the flat-top current and duration (Cycles #8, #9, #10, #11 and # 11) are analysed. Figure 127 shows the linear correlation between the snapback amplitude and its decay constant. Comparing to the LHC-MB dipoles, where a $g_3{}^{sb}$ = 0.1782 units/A is found in [6. 11], the snapback in the MBH -11 T magnet is about four times faster. A systematic variation of $g_3{}^{sb}$ with the longitudinal position of the measuring shaft was found, with a snapback 25 %

faster in the central segments than in the coil ends. Figure 128 shows the variation on b_3 when ramping up the magnet after injection for two different operation temperatures. The behaviour at 4.3 K is closer to the LHC-MB behaviour reported in [6. 8].

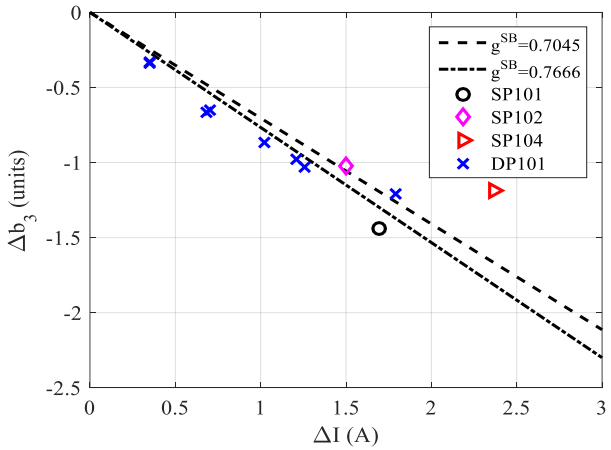

Figure 127. Scatter plot of the sextupole fit parameters for the sextupole Δb_3 and ΔI in the 11 T cycles analyzed.

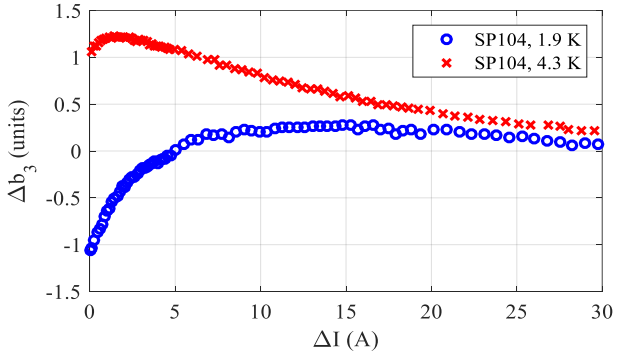

Figure 128. Impact of the operation temperature on the snapback in MBHSP104

6.4 Conclusion

As we discussed briefly earlier, the present understanding of the decay is that the local field changes due to current redistribution during a constant current plateau cause a decrease of the average filament magnetization. In the case of the 11 T dipoles, the changes on b_3 and b_5 during a standard operation cycle at 1.9 K appear as a net increase of the average filament magnetization. As soon as the field is ramped up again after the end of injection, the magnetization rapidly recovers and in most of the cases follows the original hysteresis curve. This snap-back is about four times faster than the one observed in LHC-MB dipoles. In some cases, an overshoot with respect to the original hysteresis curve is visible. In addition, when the cycles are performed at an operating temperature of 4.3 K, an inversion of the sign of the amplitude of the decay on b_3 and b_5 is observed, and the ΔI needed to recover the original hysteresis branch increases to values comparable to the LHC-MB. Finally, decay at high field shows a behavior as expected from the experience in Nb-Ti magnets. The values tested, in the range of 4 kA to 10 kA operating current, are such that a large portion of the coil is well above the penetration field of the superconducting filaments. The above results, and the observed dependencies cannot be the explained through the differences on the inter-strand resistance between the Nb-Ti coils and the Nb_3Sn coils as put forward in [6. 1]. Measurements on the MQXF quadrupole shows a similar behaviour, in particular in the RRP magnets. We point to two possible causes for the “anomalous” behavior observed:

Partial magnetization of the filaments. HEP-grade Nb_3Sn strands have filaments of 40 to 50 μm, to be compared to 5 to 10 μm for Nb-Ti, and the penetration field is up to an order of magnitude larger in Nb_3Sn (approximately 1 T) vs. Nb-Ti (approximately 150 mT). At the typical injection fields of the LHC (0.54 T in the MB dipole, 0.76 T in the 11 T dipole) all strands in the Nb_3Sn coil are still in partially penetrated state. It has been observed that decay and snap-back can be totally suppressed in partially penetrated or de-magnetized Nb-Ti filaments [6. 12]. However, partial penetration does not obviously lead to the observed inversion of the decay direction.

'Undefined' magnetization state induced by jumps. Because of the large filaments, HEP-grade Nb_3Sn strands are affected by partial flux jumps up to background field of 2 T. As demonstrated experimentally [6. 13] the behavior is very different at 1.9 K, where the magnetization is reduced by frequent micro-jumps, and at 4.3 K, where the amplitude of the jumps is significantly larger, the frequency much reduced, and flux jumps are suppressed at lower background field. This effect is taken into account in the simulation of persistent currents (the effect of DC magnetization on field quality) assuming a linear reduction of the effective filament size as a function of the field below a given field value [6. 14][6. 13]. For dynamic effects the situation is less evident. The magnetization in a filament following a partial flux-jump is most likely in an intermediate state between the virgin and partially penetrated ones. As such, it is not clear how an oscillating change of background field will affect the average coil magnetization. Pending further analysis and more data (an experiment of the type described in [6. 7] could be performed), we consider that flux jumps are a potential reason for the observed anomaly.

A systematic study to characterize the dynamic behavior of the CERN 11 T short magnet models has been done in view of understanding this phenomenon in Nb_3Sn accelerator magnets and establishing target values for decay and snapback for future colliders such as the FCC. Although we find that there are similarities in the amplitudes and functional dependencies with the statistics established on LHC-MB dipoles, there is a striking difference in that the sign of the measured decay in the Nb_3Sn dipoles is opposite with respect to the one observed in Nb-Ti magnets and would suggest an average increase of the magnetization of the filaments during constant field plateau. The decay amplitudes are comparable among the measured models, they are reproducible from cycle to cycle, and have general dependencies on powering history that recall similar behaviour in Nb-Ti magnets (apart for the sign inversion). This is why we believe that this anomaly is an inherent feature of Nb_3Sn dipole magnets built with present HEP-grade strands. The fact that the sign anomaly disappears at higher temperature and high background field in the coil, suggests that this effect is related to the specific features of a very large penetration field and flux jumps as typically observed in HEP-grade Nb_3Sn strands for fields below 2 T. The study was less extensive in the MQXF quadrupoles, and the results are less systematic. MQXFS3, built with RRP conductor (132/169 and 108/127) shows a behaviour consistent with the observations in 11 T models with a net increase of the filament magnetization. At 4.5 K, the decay has opposite direction as observed in the 11 T dipoles. The magnets built with PIT conductor show different behaviour. MQXFS6b shows no significant change on b_6 during the injection plateau and MQXFS5 shows a net decrease of the magnetization with a jump in the middle of the injection plateau. Measurements on strands showed that flux jumps are fewer and have smaller amplitude for PIT than for RRP conductor [6. 13], which could explain the difference in MQXFS5 and MQXFS6b.

6.5 References

[6. 1] G. V. Velev et al., "Measurements of the Persistent Current Decay and Snapback Effect in Tevatron Dipole Magnets," IEEE Transaction on Applied Superconductivity, vol. 17, no. 5, June 2007.

[6. 2] H. Brück, et al., "Time Dependence of Persistent Current Effects in the Superconducting HERA Magnets," Contribution to the 11th International Conference on Magnet Technology - MT-11, Tsukuba, Japan, Aug. 28-Sep. 1, 1989 and HERA 90-01, January 1990.

[6. 3] A. Devred et al., "Time Decay Measurements of the Sextupole Component of the Magnetic Field in a 4-cm Aperture, 17-m-long SSC Dipole Magnet Prototype," Proc. of 14th Particle Accelerator Conference, San Francisco CA, May 6-9, 1991.

[6. 4] L. Bottura et al., "Field Errors Decay and "Snap-Back" in LHC Model Dipoles," IEEE Trans. on Appl. Supercond., vol. 7, no. 2, June 1997.

[6. 5] R. Wolf, "The Decay of the Field Integral in Superconducting Accelerator Magnets wound with Rutherford Cables," Proc. of 15th Int. Mag. Tech. Conf., Beijing, pp. 238-241, Science Press, 1997.

[6. 6] M. Schneider, Ph.D. dissertation, Technischen Universitaet Wien, 1999.

[6. 7] M. Haverkamp, Ph.D. dissertation, Twente University, Enchede, 2003.

[6. 8] N. J. Sammut, Mathematical formulation to predict the harmonics of the superconducting Large Hadron Collider magnets. II. Dynamic field changes and scaling laws. Phys. Rev. ST Accel. Beams 10, 082802 (2007)

[6. 9] G. V. Velev et al., "Summary of the Persistent Current Effect Measuremenst in Nb3Sn and NbTi Accelerator magnets at Fermilab," IEEE Trans. Appl. Supercond., vol. 26, no. 4, Jun. 2016.

[6. 10] L. Bottura, T. Pieloni, S. Sanfilippo, G. Ambrosio, P. Bauer, and M. Haverkamp, Proceedings of European Accelerator Conference, Lucerne, Switzerland, 2004, pp. 1609–1611.

[6. 11] L. Bottura, G. Ambrosio, P. Bauer, M. Haverkamp, T. Pieloni, S. Sanfilippo, and G. Velev, "A scaling law for the snapback in Superconducting accelerator magnets," IEEE Trans. on Appl. Supercond., vol. 15, no. 2, June 2005.

[6. 12] M. Venturini et al, "Degaussing and decay reduction in the short superconducting dipole models for the LHC," IEEE Trans. Appl. Supercond. vol. 22, no. 1, March 2012.

[6. 13] B. Bordini et al., "Magnetization Measurements of High-Jc Nb3Sn strands," IEEE Trans. Appl. Supercond., vol. 23, no. 3 , Jun. 2013.

[6. 14] S. Izquierdo Bermudez et al., "Persistent-Current Magnetization Effects in High-Field Superconducting Accelerator Magnets," IEEE Trans. Appl. Supercond. vol. 26, no. 4, Jun. 2016.

7 CONCLUSIONS AND FUTURE DEVELOPMENTS

Nb_3Sn is very different from NbTi. The geometry of the conductor changes during the reaction heat treatment performed after winding, increasing the difficulty to keep the precise position of the conductors. Due to the larger filament size and critical current density, the magnetization is 10 times larger than in the NbTi LHC MB dipoles. This translates into larger field errors at injection and additional heat load that needs to be absorbed by the cryogenic system. Nb_3Sn magnets for the HL-LHC operate at a field level below the penetration field of the superconductor at injection, which has implications for the decay and snapback. However, and in spite of these intrinsic difficulties of Nb_3Sn, the experience from the 'mini-series' production of the magnets for HL-LHC is very encouraging. This thesis provides a comprehensive picture of the attainable field quality in Nb_3Sn accelerator magnets through a systematic study of the Nb_3Sn magnets under construction for the HL-LHC.

7.1 Main conclusions

As stablished in the introduction, the goal of this thesis is to assess the magnetic behaviour of Nb_3Sn accelerator magnets by means of:

- Modeling of the behaviour with analytical and numerical models.
- Analysis of the magnetic measurements performed at ambient and cryogenic temperature.
- Analysis of conductor magnetization, coil geometry and stress measurements, to evaluate and describe the source of the measured effects in the field.

The main conclusions are divided in four groups, corresponding to the different contributions to field errors in an accelerator magnet.

- Geometric field errors

In terms of geometric field errors, the accuracy on the positioning of the conductor for the Nb_3Sn HL-LHC series magnets is $\sim$ 0.05 mm, only a factor 2 the value for the NbTi LHC-MB dipoles (0.025 mm). Larger spread is observed in the short models ($\sim$ 0.2 mm) due to the differences in coil parameters and pre-loaded level, pointing to the importance of having a well stablished production before an assessment of the potential of the technology.

MQXF has also demonstrated that field quality targets are reachable using an innovative structure based on an aluminium shrinking cylinder pre-loaded using bladders and keys. The dominant source of field errors is the coil geometry and not its alignment on the magnet structure, with no change on the non-allowed harmonics with the loading. The straightness of the field is defined by the straightness of the initial yoke-shell subassembly structure, and measures have been implemented at the level of the assembly to achieve a precision of ± 0.2 mm along the 8 m magnet length. Due to the large axial stiffness of the structure compared to traditional laminated structures, the straightness of the field does not change significantly with the magnet loading, cold mass assembly, cool down and powering cycles.

- Ferromagnetic materials contribution

Available tools to model iron saturation effect are very precise. To reach the tight operation requirements, a careful monitoring of the early-stage production (short models and prototypes) was important to fine tune the coil length in the case of the MBH-11 T and the operating current in the case of MQXF. Iron saturation has been also used to cure low order field errors in MQXF, by placing ferromagnetic shims in the iron yoke.

- Persistent and coupling currents effects

The filament diameter in state-of-the-art Nb_3Sn conductor is ≈ 50 μm, 10 times larger than in the Nb-Ti LHC dipole which has two main implications for the operation of these magnets in an accelerator: i) larger field errors at injection; ii) additional magnetization heat load that must be absorbed by the cryogenic system. For the operation parameters of the Nb_3Sn magnets for the HL-LHC, and thanks to the use of cored cables, inter-strand and inter-filament currents are orders of magnitudes smaller than the persistent currents, so their impact on field distortions and AC-loss is negligible when compared to the persistent current effects. Flux jumps at 1.9 K introduce a degree of uncertainty in the contribution of the magnetization. The scaling law developed for NbTi magnets that relates the sextupole field distortions in a dipole magnet to the magnetization of the strands used for winding still holds for Nb_3Sn magnets and gives thus confidence in our understanding of the phenomenon.

- Dynamic effects at injection: decay and snapback

A systematic study to characterize the dynamic behavior of the Nb_3Sn HL-LHC short magnet models has been done in view of understanding this phenomenon in Nb_3Sn accelerator magnets. Although there are similarities in the amplitudes and functional dependencies with the statistics established on LHC-MB dipoles, there is a striking difference. The sign of the measured decay in the Nb_3Sn dipoles is opposite with respect to the one observed in Nb-Ti magnets and would suggest an average increase of the magnetization of the filaments during constant field plateau. The decay amplitudes are comparable among the measured models, they are reproducible from cycle to cycle, and have general dependencies on powering history that recall similar behavior in Nb-Ti magnets (apart for the sign inversion). This is why we believe that this anomaly is an inherent feature of Nb_3Sn magnets built with present HEP-grade strands. The fact that the sign anomaly disappears at higher temperature and high background field in the coil, suggests that this effect is related to the specific features of a very large penetration field and flux jumps as typically observed in HEP-grade Nb_3Sn strands for fields below 2 T. The study was less extensive in the MQXF quadrupoles, and the results are less systematic, showing a big difference for the two conductor technologies (PIT and RRP).

7.2 Main contributions and future developments

The main contributions of this thesis are highlighted below along with the possible developments to which they could lead in the future:

- The main contribution of the thesis has been to provide a comprehensive and complete picture of the attainable field quality in Nb_3Sn magnets, showing that the stringent field quality requirements in accelerator magnets are reachable with Nb_3Sn. The tools developed in this thesis and validated against measurements are valuable to define the target field quality in future accelerators.
- The derivation of the Jacobians allowed to establish the theoretical dependence of the geometrical multipoles with the typical modes of deformations. The tool was powerful for manufacturing control, intercepting assembly errors and helping on the understanding of the precision in the construction process. This tool will be used for MQXF series production and can be used in future productions after an assessment of the expected modes of deformation based on the magnet features.
- The Monte-Carlo analysis developed for NbTi magnets to define the precision of the placement of the conductors shows that Nb_3Sn has nearly reach the standards of the NbTi technology. In this thesis, the author limited the study to the magnets built at CERN, but it can be extended in the future to the MQXFA magnets which are being fabricated by the US Accelerator Research Program (AUP) [8. 1]. In view of future accelerators, if other coil layouts such as block or common coil configurations are considered [8. 2], a study of the accuracy on the placing of the conductors and tolerances considering the specific magnet features could provide an early-stage assessment of the expected geometrical errors.
- Ferromagnetic shims placed in the iron yoke have become for MQXF a standard tool to correct low order field errors at collision energy. As a future development, the placement of ferromagnetic shims close to the aperture could be used to compensate the allowed harmonics arising from persistent current effects at injection. This idea was already proposed in the past, but it was not further developed and implemented in HL-LHC Nb_3Sn magnets due to the limited interest for these specific magnets: field errors in MQXF are critical only at collision energy; only few units of MBH-11T were planned to be installed, so the additional sextupole component at injection due to persistent currents is not affecting the accelerator performance.
- The author of this thesis proposed a method to account for the impact of flux jumps in persistent currents through a reduction of the effective filament size at low field. Agreement between measured field errors and computations improved with this approach, and the same methodology could be applied in the future for a more accurate assessment of the magnetization loss. Sustainability and energy efficiency will be important in future accelerators. The load to the cryogenic system of a 16 T magnet with state-of-the-art conductor is at least a factor 20 the magnetization loss in the current LHC. Developments on the conductor to minimize the loss to the cryogenic system will pay-off. In addition, heat extraction mechanism in non-standard coil configuration shall be studied in detail. In the cos-theta coil layout, the inner radius of the coil is in direct contact with the superfluid helium. For the coil block configuration, there is an internal support structure, typically in Titanium, so the heat extraction efficiency might have an impact on the operational margin of the magnet.
- The study of the dynamic behavior of the Nb_3Sn short magnet models show that there are similarities in the amplitudes and functional dependencies of the decay and snapback with the statistics established on LHC-MB dipoles, but there are also striking differences. As a future development, the study shall be extended to

the prototypes and series magnets, pursuing the collection of data, and possibly perform dedicated experiments to characterize the behavior of the magnetization of a strand submitted to oscillating field variations after a flux jump.

- A Future Circular Collider (FCC) [8. 3], or an energy upgrade of the LHC (HE-LHC) [8. 4], would require bending magnets operating at up to 16 T. This is about twice the magnetic field amplitude produced by the Nb-Ti LHC magnets, and about 5 T higher than the one produced by the Nb_3Sn magnets being developed for HL-LHC. To explore the design and manufacture of these magnets, several development programs have been initiated [8. 2]. Together with CERN, European Laboratories are working on the development of these magnets. INFN explores the cos-theta design [8. 5], CEA the block coil design [8. 6] and CIEMAT the common coil design [8. 7]. Even if new measurements and methods are required, this thesis paved the way towards the next step in High Energy Physics.

7.3 Closing remarks

The HL-LHC marks a new era in superconducting magnet technology, installing for first time Nb_3Sn magnets in an accelerator. The next step is to demonstrate Nb_3Sn magnet technology for large-scale development, pushing it to its practical limits in terms of ultimate performance and moving towards production scale through robust design, industrial manufacturing process and cost reduction. The stringent field quality requirements in accelerator magnets are reachable with Nb_3Sn, and this thesis provided an exhaustive study of the available data and challenges. The data and analysis presented span the worldwide largest-ever sample of Nb_3Sn high field magnets. This sample is unique, it is based on the major effort in magnet design and engineering associated with the High Luminosity Upgrade of the LHC, and will not be replicated for years, possibly decades. As such, the work is a unique reference in field quality for superconducting accelerator magnets built with Nb_3Sn, the baseline superconductor for one of the preferred options of a next step in High Energy Physics. To go above the perceived limit of 16 T, the most promising High Temperature Superconductors (HTS) today are Bi2212 and REBCO. Bi2212 is available in round isotropic wires and can generally follow the design and fabrication approach developed for Nb_3Sn. REBCO is produced by deposition on thin tapes that include layers of metals, oxides and ceramics for crystal plane alignment, mechanical strength, and electrical stability. The conductor features very large magnetic moment, so achieving a high dynamic field quality is a main concern. This requires the development of new tools and methods (see for example [8. 8]), innovative magnet designs and/or additional tools to cancel field errors (see for example the passive and self-regulating HTS screens proposed in [8. 9]). Promising materials are emerging, and worldwide efforts are on-going to provide a proof-of-principle of HTS magnet technology.

7.4 References

[8. 1] G. Ambrosio et al., "Lessons Learned From the Prototypes of the MQXFA Low-Beta Quadrupoles for HL-LHC and Status of Production in the US," in IEEE Transactions on Applied Superconductivity, vol. 31, no. 5, pp. 1-5, Aug. 2021, Art no. 4001105, doi: 10.1109/TASC.2021.3058597.

[8. 2] D. Tommasini et al., "Status of the 16 T Dipole Development Program for a Future Hadron Collider," in IEEE Transactions on Applied Superconductivity, vol. 28, no. 3, pp. 1-5, April 2018, Art no. 4001305, doi: 10.1109/TASC.2017.2780045.

[8. 3] M. Benedikt et al., 'FCC-hh: The Hadron Collider', Eur. Phys. J. Spec. Top. 228, 755–1107 (2019). https://doi.org/10.1140/epjst/e2019-900087-0

[8. 4] F. Zimmermann et al., 'HE-LHC: The High-Energy Large Hadron Collider', Eur. Phys. J. Spec. Top. 228, 1109–1382 (2019). https://doi.org/10.1140/epjst/e2019-900088-6

[8. 5] V. Marinozzi et al., "Conceptual Design of a 16 T cos θ Bending Dipole for the Future Circular Collider," in IEEE Transactions on Applied Superconductivity, vol. 28, no. 3, pp. 1-5, April 2018, Art no. 4004205, doi: 10.1109/TASC.2018.2795533.

[8. 6] C. Lorin, M. Segreti and M. Durante, "Design of a Nb3Sn 16 T Block Dipole for the Future Circular Collider," in IEEE Transactions on Applied Superconductivity, vol. 28, no. 3, pp. 1-5, April 2018, Art no. 4005005, doi: 10.1109/TASC.2018.2800692.

[8. 7] F. Toral, J. Munilla and T. Salmi, "Magnetic and Mechanical Design of a 16 T Common Coil Dipole for an FCC," in IEEE Transactions on Applied Superconductivity, vol. 28, no. 3, pp. 1-5, April 2018, Art no. 4004305, doi: 10.1109/TASC.2018.2797909.

[8. 8] J. Van Nugteren, 'High Temperature Superconductor Accelerator Magnets,' PhD Twente U., Enschede, Enschede : 2016-09-01

[8. 9] L. Bortot et al., Supercond. Sci. Technol. 34 (2021) 105001

APPENDIX 1: COIL AND CONDUCTOR PARAMETERS FOR MBHS AND MQXFS

Table 65. Coil and conductor parameters of MQXF and 11 T magnets. Critical current density parameters (C and Bc_2 at 1.9 K, with $I_c = C \cdot b^{0.5}(1-b)^2/B_p$ and $b = B_p/B_{c2}$) are given for the witness samples reacted with the coils. For some of the early production coils, J_c fitting parameters are not available.

Magnet	Coil ID	Cross section	Manufac.	Conductor	Deff [μm]	Cu/sc	C (1.9 K) [kA·T]	B_{c2} (1.9 K) [T]
MQXFS1a/b/c	3	1st	LARP	RRP 108/127	55	1.19		
	5	1st	LARP	RRP 108/127	55	1.19		
	103	1st	CERN	RRP 132/169	50	1.22		
	104	1st	CERN	RRP 132/169	50	1.22		
MQXFS3a/b	7	2nd	LARP	RRP 108/127	55	1.19		
	105	2nd	CERN	RRP 132/169	50	1.22	54.0-56.8	26.4
	106	2nd	CERN	RRP 132/169	50	1.22	54.0-56.8	26.4
	107	2nd	CERN	RRP 132/169	50	1.22	57.2-60.0	25.2
MQXFS3c	8	2nd	CERN	RRP 144/169				
	105	2nd	CERN	RRP 132/169	50	1.22	54.0-56.8	26.4
	106	2nd	CERN	RRP 132/169	50	1.22	54.0-56.8	26.4

	107	2nd	CERN	RRP 132/169	50	1.22	57.2-60.0	25.2
MQXFS5a	203	2nd	CERN	PIT 192	41	1.22	37.3-45.0	27.7
	204	2nd	CERN	PIT 192	41	1.22	42.5-44.6	28.3
	205	2nd	CERN	PIT 192	41	1.22	38.6-44.1	28.4
	206	2nd	CERN	PIT 192	41	1.22	40.1-44.7	28.4
MQXFS4a/b/c	108	2nd	CERN	RRP 108/127	55	1.19	48.5-58.3	27.9
	109	2nd	CERN	RRP 108/127	55	1.19	51.6-58.1	27.7
	110	2nd	CERN	RRP 108/127	55	1.19	54.7-60.6	27.2
	111	2nd	CERN	RRP 108/127	55	1.19	53.5-59.0	27.6
MQXFS6a	208	2nd	CERN	PIT 192 Bundle	39	1.15	45.2-56.6	27.4
	209	2nd	CERN	PIT 192 Bundle	39	1.15	42.5-48.6	28.4
	210	2nd	CERN	PIT 192 Bundle	39	1.15	38.9-44.5	28.9
	212	2nd	CERN	PIT 192 Bundle	39	1.15	39.5-44.2	29.0
MQXFS6b-d	203	2nd	CERN	PIT 192	41	1.22	43.8-45.0	27.7
	204	2nd	CERN	PIT 192	41	1.22	42.5-44.6	28.3
	210	2nd	CERN	PIT 192 Bundle	39	1.15	38.9-44.5	28.9

	212	2nd	CERN	PIT 192 Bundle	39	1.15	39.5-44.2	29
MQXFS7a-e	113	2nd	CERN	RRP 108/127	55	1.19	52.6-59.0	28.4
	114	2nd	CERN	RRP 108/127	55	1.19	53.2-58.9	27.5
	207	2nd	CERN	PIT 192	41	1.22	43.4-45.3	28.6
	211	2nd	CERN	PIT 192 Bundle	39	1.15	37.7-41.0	29.3
MBHSP101	106	1st	CERN	RRP 108/127	46	1.19	38.66	24.7
	107	1st	CERN	RRP 108/127	46	1.19	39.8	24.10
MBHSP102	106	1st	CERN	RRP 108/127	46	1.19	38.66	24.7
	108	1st	CERN	RRP 132/169	41	1.25	37.72	25.8
MBHSP103	109	1st	CERN	RRP 132/169	41	1.28	35.96-45.31	25.0
	111	1st	CERN	RRP 132/169	41	1.28	34.84-43.90	24.8
MBHSP104	112	1st	CERN	RRP 132/169	41	1.28	34.80-36.16	26.1
	113	1st	CERN	RRP 132/169	41	1.28	33.72-35.04	26.1
MBHSP105	114	1st	CERN	RRP 150/169	41	0.97	37.90-39.50	25.9
	115	1st	CERN	RRP 150/169	41	0.97	37.90-39.60	25.3
MBHSP106	116	1st	CERN	RRP 150/169	41	0.97	38.1	26.3

	117	1st	CERN	RRP 150/169	41	0.97	39.70-40.60	25.9
MBHSP107	120	1st	CERN	RRP 108/127	46	1.19	34.68-42.07	25.8
	121	1st	CERN	RRP 108/127	46	1.19	33.37-40.00	26.6
MBHSP109	119	1st	CERN	RRP 108/127	46	1.19	34.14-40.19	26.4
	123	1st	CERN	RRP 108/127	46	1.19	35.91-43.29	26.7

APPENDIX 2: GEOMETRIC FIELD ERRORS

Table 66. Average and standard deviation of the measured harmonics in the straight section after loading in MQXFS (MQXFS3 to MQXFS7, 5 magnets)

n	Average		σ	
	b_n	a_n	b_n	a_n
3	-1.50	-0.22	3.18	1.93
4	0.63	1.45	0.91	2.68
5	-0.35	-0.43	1.64	0.94
6	-3.96	0.66	1.74	0.44
7	-0.51	0.04	0.46	0.71
8	-0.07	0.16	0.07	0.36
9	0.09	-0.01	0.10	0.05
10	0.09	0.01	0.26	0.07

Table 67. Average and standard deviation of the measured integral harmonics in MQXFB (MQXFBP1-P2-P3-B02, 4 magnets)

n	Average		σ	
	b_n	a_n	b_n	a_n
3	0.37	0.83	2.23	1.15
4	-0.05	-0.92	0.64	0.36
5	0.15	-0.49	0.45	0.73
6	-0.87	-0.09	0.04	0.22
7	-0.21	0.15	0.31	0.17
8	-0.01	0.01	0.14	0.10
9	0.*02*	0.04	0.13	0.05
10	-0.26	-0.04	0.07	0.05

Table 68. Average and standard deviation of the measured harmonics in MBHS single aperture cold masses (MBHSP101 to SP109, 9 magnets)

n	Straight Section				Integral			
	Average		σ		Average		σ	
	b_n	a_n	b_n	a_n	b_n	a_n	b_n	a_n
2	0.41	-0.52	4.09	8.33	0.52	-0.99	3.88	7.83
3	6.37	-1.54	5.04	2.96	10.44	-2.34	7.40	2.90
4	-0.83	0.64	2.24	1.93	-0.81	0.29	2.11	2.01
5	1.33	0.35	1.27	1.47	1.49	0.62	1.38	1.50
6	0.26	0.07	0.81	0.54	0.24	0.06	0.77	0.54
7	0.24	-0.19	0.07	0.43	0.28	-0.21	0.14	0.43
8	-0.15	0.00	0.45	0.12	-0.13	0.00	0.43	0.10
9	0.85	-0.01	0.10	0.19	0.76	-0.01	0.14	0.18
10	-0.01	-0.01	0.02	0.03	0.00	0.00	0.01	0.01
11	0.40	-0.04	0.03	0.06	0.36	-0.03	0.06	0.06
12	0.00	0.00	0.04	0.02	-0.01	-0.01	0.04	0.02
13	-0.10	0.00	0.02	0.01	-0.10	-0.01	0.02	0.01
14	0.00	0.00	0.01	0.01	0.00	0.00	0.01	0.01
15	-0.02	0.00	0.00	0.00	-0.02	0.00	0.00	0.00

Table 69. Average and standard deviation of the measured harmonics in MBH series collared coil (CC01 to CC11, 11 apertures)

n	Average		σ	
	b_n	a_n	b_n	a_n
2	-0.81	0.27	1.68	1.85
3	5.67	-0.38	1.15	0.58
4	0.03	0.03	0.19	0.23
5	1.27	-0.27	0.35	0.10
6	-0.04	-0.05	0.05	0.14
7	0.14	-0.08	0.08	0.04
8	0.00	-0.07	0.05	0.08
9	1.10	-0.15	0.05	0.01
10	-0.01	-0.04	0.03	0.05
11	0.51	-0.09	0.02	0.01
12	0.00	0.01	0.01	0.01
13	-0.12	0.02	0.01	0.00
14	0.00	0.00	0.00	0.00
15	-0.03	0.01	0.00	0.00

LIST OF TABLES

LIST OF FIGURES